Reversible

Self-Assembled Monolayers

as Biosensor Platforms

Dissertation

by
Annabell Tenboll
from Marl

In Partial Fulfillment of the
Requirements for the Degree
Doctor of Chemistry
(Dr. rer. nat.)

Department of Chemistry
University Duisburg-Essen

June 2013

Die vorliegende Arbeit wurde im Zeitraum von April 2011 bis Juni 2013 im Arbeitskreis von Priv. - Doz. Dr. Börje Sellergren am Institut für Umweltforschung der Technischen Universität Dortmund angefertigt.

Gutachter:	Prof. Dr. Thomas Schrader
	Prof. Dr. Börje Sellergren
Vorsitzender:	Prof. Dr. Stephan Schulz

Tag der Disputation: 11. September 2013

meiner Mutter Anna-Maria und meinem Freund Domenic

Table of content

Summary

The development of ultra-sensitive sensors is a prerequisite for better diagnostic tools. One approach that addresses this issue is the development of reversible self-assembled monolayers. In this work the synthesis and stepwise assembly of self-assembled monolayers is presented. In contrast to the well established covalently bound alkanethiols on gold, reversible SAMs (rSAMs) are attached via non-covalent interactions. This property provides some important advantages. Firstly, functionalized samples can be reused by easily washing away the bound molecules, e.g. by a pH change. Secondly, their dynamic nature renders the SAM adaptable for an optimal packing of the adsorbed probes and enhanced sensing.

Previously, it had been demonstrated that α,ω-bis(4-amidinophenoxy)alkanes form reversible layers of carboxylic acid functionalized thiol SAMs on gold. The interaction between the negatively charged carboxylic acid function and the positively charged amidinium are based on the protonation status of the acid. Alkaline pH media lead to cyclic, directed, stable hydrogen bonds. Hence, in case of a lowered pH the amphiphile layer can be removed from the carboxylated surface.

By introducing a biological function to the α,ω-bis(4-amidinophenoxy)alkanes a novel biosensor platform should be developed. The first sensor platform used biotin to anchor streptavidin. Streptavidin can in turn act as an anchor for biotinylated antibodies. Two different antigens specific for the used antibody were detected and implemented to proof the selectivity and sensitivity of the sensor. The detected analytes were human serum albumin - as a proof of concept - and prostate specific antigen (PSA) for detection of a real sample. PSA was detected from human serum samples in a pM range. By diluting the biotinylated amphiphiles with hydroxylated spacer molecule the head group sensor sensitivity increased, reflecting a better match with the streptavidin topology.

The second biological function introduced was sialic acid (SA). SA can specifically bind hemagglutinin (HA), which is involved in the infection by influenza viruses. This second sensor consisted of the sialic acid terminated amphiphile, which was reversibly attached on the carboxylated gold substrate. In a first series of experiments, the hemagglutinin protein was detected. Then the detection of influenza virus like particle (VLP) was performed. The different molar ratios of spacer molecule to functional molecule were explored for optimal binding conditions. Reusability of the sensor was tested by switching the pH and rinsing

off the reversible attached molecules under acidic pH conditions. The kinetics for the assembly and disassembly processes were followed by *in-situ* ellipsometry. With this method the film growth on the substrate could be displayed. Other methods for characterization were infrared reflection absorption spectroscopy (IRRAS), contact angle measurements and atomic force microscopy (AFM).

Zusammenfassung

Die Entwicklung von ultrasensitiven Sensoren ist eine Voraussetzung für eine bessere Diagnostik in der Medizin. Ein Ansatz, dieses Problem anzugehen, ist die Entwicklung von reversiblen, selbstorganisierten Monoschichten. In dieser Doktorarbeit wird die Synthese und der schrittweise Aufbau dieser Schichten entwickelt. Im Gegensatz zu den etablierten, kovalent gebunden Alkanthiolen auf Gold, sind reversible SAMs (rSAMs) über nicht-kovalente Wechselwirkungen gebunden. Diese Eigenschaft bietet ihnen einige wichtige Vorteile. Erstens können die gebundenen Moleküle durch einfaches Waschen entfernt und wiederverwendet werden, und zweitens macht ihre dynamische Natur die SAMs anpassungsfähig, so dass eine optimale Packung der adsorbierten Sonden vorliegt und verbesserte Sensoreigenschaften generiert werden.

In früheren Arbeiten dieser Arbeitsgruppe konnte gezeigt werden, dass α, ω-bis (4-Amidinophenoxy)alkane reversible Schichten auf carbonsäurefunktionalisierten Thiol SAMs auf Gold bilden. Diese Wechselwirkungen entstehen zwischen der negativ geladenen Karbonsäurefunktion und dem positiv geladenen Amidin, aufgrund des Protonisierungsgrades der Säure. Es entstehen in alkalischen pH-Medien zyklische, gerichtete, stabile Wasserstoffbrücken. Aufgrund diesen pH-abhängigen Verhaltes kann nach Absenken des pH-Werts die Amphiphilschicht von der karboxylierten Oberfläche entfernt werden.

Durch die Einführung einer biologischen Funktion an die α,ω-bis (4-Amidinophenoxy) alkane sollte eine neuartige Biosensor-Plattform entwickelt werden. Die erste Sensor-Plattform nutzte Biotin, um Streptavidin zu verankern. Streptavidin kann wiederum als Anker für biotinylierte Antikörper wirken. Es konnten zwei verschiedene Antigene spezifisch für die verwendeten Antikörper mit dem Sensor mit hoher Empfindlichkeit detektiert werden. Die detektierten Analyten waren humanes Serumalbumin - als „proof of concept“ - und Prostata-spezifisches Antigen (PSA) zur Detektion in biologischen Proben. PSA konnte in pM Konzentration in einer menschlichen Serumprobe nachgewiesen werden. Durch Verdünnen der biotinylierten Amphiphile mit hydroxylierten Spacermolekülen wurde die Kopfgruppen-Sensor-Empfindlichkeit erhöht, was einer besseren Übereinstimmung mit der Streptavidin-Topologie entspricht.
Die zweite biologische Funktion die eingeführt wurde, war Sialinsäure (SA). SA kann Hämagglutinin (HA) spezifisch binden. HA ist an der Infektion durch Influenzaviren

beteiligt. Dieser zweite Sensor besteht aus dem Sialinsäure-terminierten Amphiphil, das reversibel an das carboxylierte Goldsubstrat angebracht wird. In einer ersten Reihe von Experimenten wurde reines Hämagglutinin-Protein detektiert, bevor die Detektion der influenzavirusartigen Partikeln (VLP) durchgeführt wurde. Die verschiedenen Molverhältnisse von Spacermolekül zu funktionellem Molekül wurden für die optimalen Bindungsbedingungen untersucht. Die Wiederverwendbarkeit des Sensors wurde getestet, indem das Substrat mit pH 3-Puffer gespült und somit die reversibel angelagerten Moleküle abgelöst wurden. Die zeitabhängige Anlagerung und Regenerierung wurde mittels in-situ Ellipsometrie aufgezeichnet. Mit dieser Methode konnte das Filmwachstum auf dem Substrat nachgewiesen werden. Andere Methoden zur Charakterisierung waren Infrarot-Reflexions-Absorptions-Spektroskopie (IRRAS), Kontaktwinkelmessungen und Rasterkraftmikroskopie (AFM).

1 Introduction

1.1 Self-assembled monolayers (SAMs)

Self-assembly is an important tool for creating structurally well defined organic surfaces. The use of those organic films reaches from chemistry over biology to physics and material science. In nature, self-assembly can, for example, be found when phospholipids self-assemble into lipid bilayers or when long chains of amino acids fold into the secondary and tertiary structure of functional proteins. Self-assembled monolayers (SAMs) of chemically adsorbed assemblies represent modules for the design of complex structures on solid surfaces. SAMs formed on a substrate can tailor the physical properties of a sample, e.g. the hydrophobicity or wet ability. SAMs are used in different fields as structural or functional parts. They can be used in sensor devices to detect analytes by a recognition reaction from liquid or gaseous phase.

Self-assembled monolayers (SAMs) are molecular assemblies of organic molecules, which form spontaneously on surfaces by adsorption. SAMs can not only be formed by adsorption from solution but also from the gas phase. They can build ultra thin organic films according to their molecular length. Abraham Ulman and colleges provide an excellent overview about the basics of molecular assemblies in their book "Ultrathin Organic Films".[1] They explain that self-assembled molecules can be separated into three parts. The first part is the head group, which can chemisorb on the substrate within a chemical reaction. Commonly used head groups are alkanethiols for adsorption on gold[2,3,4,5,6], copper[6], silver[6,7,8], palladium[9,10], platinum[11] and mercury[12].

The second part of the SAM forming molecule is the alkyl chain. The SAM formation is mainly driven by van der Waals interactions between these chains. The third part is the terminal group (Scheme 1). The latter can have different functionalities, e.g. it can be a simple methyl group or a more complex group with biological functionalities like biotin.

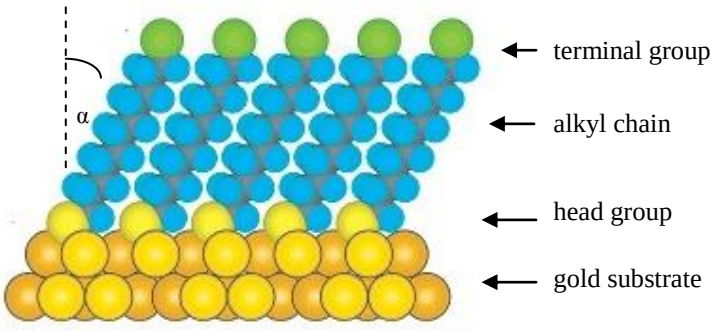

Scheme 1: Schematic representation of an alkanethiol SAM on gold with a tilt angle of α = 30°[13]

The assembly of alkanethiols on gold was studied intensively over the last decades. Already in 1983, Allara and Nuzzo published one of the first papers in this area.[14] They found that dialkylsulfides can form ordered SAMs on gold. The reaction mechanism established for the chemisorptions of alkanethiols is not fully understood yet.[15] In here the most common explanation is mentioned involving the formation of hydrogen.

$$R–S–H + Au^0 \rightarrow R–S–Au^I + ½\ H_2$$

The sulfur atom forms a sp^3-hybrid orbital, and hence can covalently bind three gold atoms with a symmetrical bond length of 0.245 nm.[16] The adsorption of the alkanethiol on gold is a so called chemisorption (ΔH = - 40 kJ/mol).[1,17] Gold is used for studying SAMs because of this high binding affinity. Other reasons are that the substrates are easy to prepare via physical vapor deposition or sputtering; that gold is an inert metal and does not oxidize below its melting point; and that it can be used in optical methods due to its reflection properties.[13] Next to SAMs of alkanethiols on metals, monolayers can also be deposited on nonmetallic surfaces such as glass. This method is called silanization. For silanization trichlorosilanes or alkoxysilanes are used. Fatty acids are common compounds for functionalization of aluminiumoxide substrates (Scheme 2).

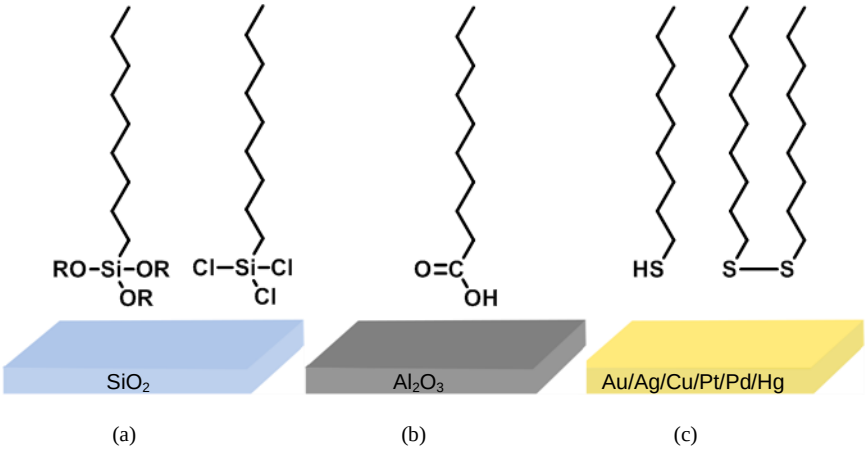

Scheme 2: Surface functionalization with a) alkoxysilane, trichlorosilane b) fatty acid c) thiol, disulfides

Since self-assembly is a spontaneous process, the Gibbs free energy (ΔG_0) is negative. The thermodynamics of an assembly is given by the Gibbs free energy equation:

$$\Delta G_0 = \Delta H_0 - T\Delta S_0 \quad (1)$$

ΔH_0 is the enthalpy in the system. The enthalpy is defined as the energy of a thermodynamic system, e.g. the intermolecular potentials. ΔS_0 is the entropy; it represents the order or disorder of the system. In a self-assembly process the entropy is decreasing; the molecular assemblies are arranging on a surface; the order is increased. Since self-assembly is a self-driven process, ΔH_0 is negative and in excess of ΔS_0. If the temperature (T) is above a certain critical limit, the spontaneous process becomes unlikely.[18]

Bain et al. found that the self-assembly process consists of two steps.[5] The first step takes a few minutes and the density reaches about 80 - 90% of its maximum. The second step takes several hours and is driven by lateral diffusion on the substrate to reduce defects, kink healing and packing optimization. After this time, densely packed layers are assembled on the substrate. They establish an ordered, crystalline like structure. Bain and coworkers also studied the effect of the alkyl chain length on the absorption kinetics.[5] Longer alkylchain lead to a better order in the monolayer and less defects. They attribute this observation to the fact that the van der Waals interaction is a function of the chain length. Short alkanethiols only show small van der Waals interaction. This leads to a small order in the layer, which consequently lowers the packing density. However, longer alkanethiols assemble with a tilt angle (α) of 30° on the substrate, which is a result of van der Waals interaction among the chain (Scheme 1).[4,13,19] Molecular SAMs carrying phenyl

rings in their structure, e.g. benzylmercaptan, also show a high ordering even if they are short chained.[20] This is a result of the perpendicular orientation of the phenyl ring stabilized by π-stacking.

Several characterization techniques for thin films are known. Most common are methods which give information about the thickness of the films. Those methods are for example ellipsometry or surface plasmon resonance spectroscopy (SPR). Information about the functional groups on the surface can be achieved with infrared reflection absorption spectroscopy (IRRAS). Contact angle measurements provide information about the wettability of the substrate. Atomic force microscopy is used to determine the 2D structure of the surface.

SAMs of alkanethiols are important tools in molecular recognition and biosensing.[21,22,23,24] Different functionalities of those films allow an application in various fields, e.g. optoelectronics[25], molecular electronics[26] or nonlinear optics[27]. A closer look is taken at the applications in the chapter called “Biosensing with SAMs”.

1.2 Reversible self-assembled monolayers (rSAMs)

Small molecules which are able to self-assemble onto substrates are widely used to modify surface.[28,29,30] Those molecules have useful properties due to their molecular order, orientation and functionality. Amphiphilic molecules, which self-assemble at a liquid-solid interface are one example.[1,31] Amphiphiles can be adsorbed on substrates *non-covalently* forming stable and ordered SAMs.[32,33,34] Sellergren and colleagues improved this *non-covalent* system, and introduced a switching function to the amphiphile.[24,35] This function allowed them to repetitively assemble and disassemble a the second layer of a two-layered SAM structure. The reversibility is achieved by controlling the interactions between the molecules from the first and the second layer, e.g. by a change in pH.[24]

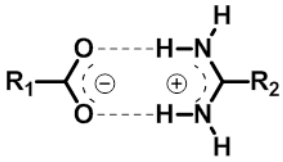

Scheme 3: Schematic representation of the cyclic hydrogen bonded ion pair formed between amidines and oxoacids

Amidinium groups can form cyclic hydrogen bounded ion pairs with the carboxylate (Scheme 3). The directed interaction of carboxylic acid and amidine offers stable bonds which were investigated by Wulff et al.[36] concerning their association constants in aqueous media. Wulff et al. found readily soluble complexes with very high association constants in the order of 8.9 $*10^7$ M.[36] The strong interaction and the switchability make these compounds very interesting for reversible attachable systems. Herein the amidine can be removed from the surface by switching the protonation status of the acid. The interactions are stable in aqueous media and have been used for the assembly of supramolecular structures.[37] The first publication in this field came from Sellergren et al. in 1999, where they demonstrated the reversible assembly of α,ω-bis(4-amidinophenoxy)alkanes on carboxylic acid functionalized SAMs on gold substrates (Scheme 4).[24] Herein the first layer consist of 11-mercpatoundecanoic acid and the second layer of α,ω-bis(4-amidinophenoxy)alkane. They found stable and ordered monolayers whereas the stability and orientation were depending on the alkylchain length of the amidine. They also found that with increasing alkylchain length the order increased due to the same van der Waals argument. The amphiphilic amidine molecules were oriented perpendicular to the substrate.[1,38,39]

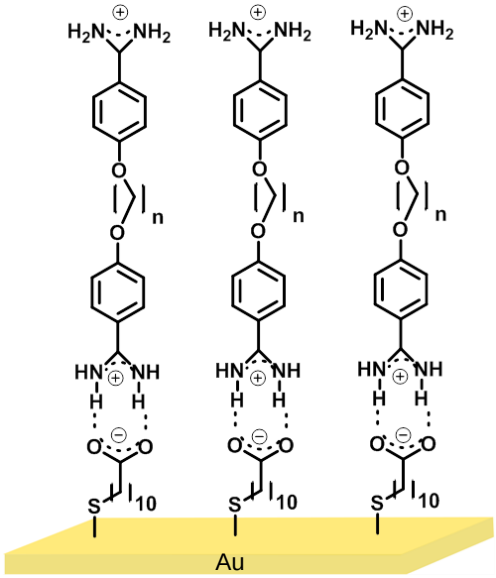

Scheme 4: Schematic representation of assembly of α,ω-bis(4-amidinophenoxy)alkane on carboxylic acid functionalized SAMs on gold substrate[24]

Auer et al. proofed this by evaluating the phenyl ring orientation to the substrate by infrared refection absorption spectroscopy (IRRAS).[24] Evans et al. found that faster adsorption kinetics appear, when bulky groups like phenyl rings are present in the SAM.[31] The position of the phenyl ring as well as the total number of alkyl carbons influences the kinetics and result in faster assembly. Further investigation of the rSAM showed that the second molecular layer is subject to the same condition as the chemisorbed SAMs of alkanethiols. This means with increasing alkyl chain of the carboxylic acid terminated thiol the stability and orientation on the gold increase.

A later publication from Auer et al. focuses on the so called "odd-even effect" of bisbenzamidines.[35] They found that the order, orientation and tendency to form bilayers of the amphiphile layer is depending on the position of the amidine substituent and the alkyl chain length of the amidine amphiphile (rSAM) and the layer underneath (SAM). They found that with an odd number of carbon atoms in the alkyl chain of the second layer the amphiphiles tend to form bilayers, whereas an even number shows only monolayer assembly (Scheme 5). They explained this effect with a more tilted arrangement of the head groups in the molecules with odd numbers of alkyl chain carbons. The π-stacking arrangement allows further lateral hydrogen-bond stabilization between the amidine groups. The increased orientation of the second layer's head groups promotes the formation of a third layer (Scheme 5).

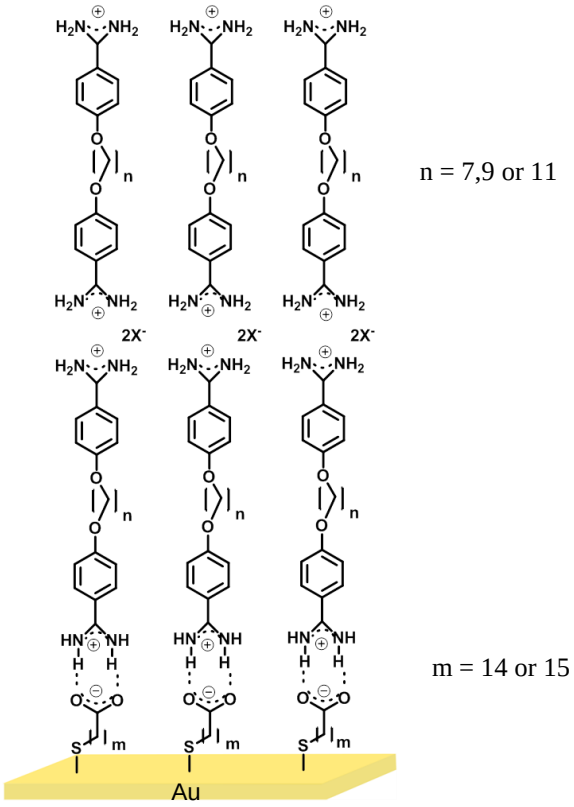

Scheme 5: Assembly of amphiphiles with an odd number of carbon atoms in the alkyl chain tend to form bilayers on carboxylic acid terminated SAMs[24]

The reversibility of the amphiphile assembly Sellergren et al. demonstrated is based on the pH-switchability of the amidinium-carboxylate bond. They assembled α,ω-bis(4-amidinophenoxy)decane on mercarcaptoundecanoic acid and adjusted the pH with small addition of 0.1 M HCl and 0.1 M NaOH. In Scheme 6 the thickness measured by ellipsometry is decreasing to zero after acidification to pH 2-3. When the pH is basified, the thickness increased and the amidine layer seems to be reassembled.

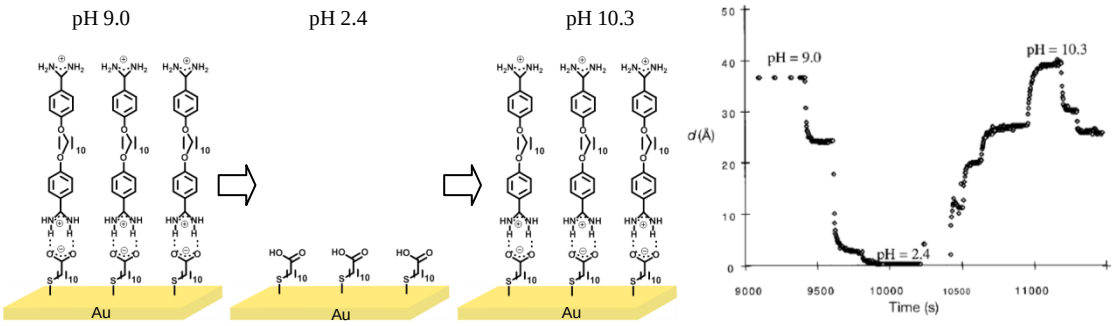

(a) (b)

Scheme 6a) Schematic representation showing a reversible assembly of α,ω-bis(4-amidinophenoxy)decane on mercarcaptoundecanoic acid, and b) the ellipsometric results from Sellergren et al.[24]

The system was applied to selectively bind olinucleotides on rSAMs. Sellergren et al. adsorbed nucleic acids rapidly and selectively on pH switchable layers of bisbenzamidines on modified gold substrates.[40] Another application of bisbenzamidines is the formation of nanocomposides, which could possibly be used in optoelectronics or semiconductors.[41] Herein the authors introduce a system where the bisbenzamidines are used as linkers for the formation of gold nanoparticle assemblies on planar gold modified with carboxylic acid functions. The optical properties of this system were similar to the ones of solid gold. Another interesting publication is the thesis written by Ravi Deshmukh, which focuses on the head group functionalization of amidines.[42] Deshmukh introduces different terminal groups to the amphiphiles, which produce high, intermediate and low energy surfaces. Those surfaces can be used for further assembly of hydrophobic or hydrophilic molecules. By introducing biological active compounds as terminal groups to the amphiphile, one can achieve surfaces, which can be used as biosensor platforms.

1.3 Biosensing with SAMs

Biosensors can be used for the detection of essential biomolecules such as pregnancy hormones[21], cancer biomarkers[43], pathogens[44] and many others. They offer a straightforward analytical method where only small amounts of reagent are needed. Immobilization of biomolecules on a substrate is an fundamental part for the development of biosensors in the form of chips.[45] In a biosensor, the molecule which should be detected is recognized by the sensor. For example, an antibody can be immobilized on the sensor and the antigen is detected by a recognition reaction. The attachment is then monitored by a detectable change of physical properties of the sensor.[1]

Why are SAMs useful as a recognition unit in a sensor device?

In Love et al.'s[13] review it is pointed out that self-assembled monolayers are especially interesting for studying biological processes. Love et al. introduces SAMs, which are nanometer sized materials, as mimicking biological membranes. SAMs can include organic functionalities which make the adsorption of proteins possible. The molecules used to form SAMs can be modified with biologically active ligands during synthesis. Screening the literature on biosensors using SAMs as recognition element, show that the functional group of SAMs can be chemically modified in several ways. *Covalent* and *non-covalent* approaches are known for this modification method. One of the covalent approaches is the "Click" reaction. Song et al. studied this reaction type by immobilizing an azide terminated SAM on a substrate and reacted the later with an alkyne terminated molecule to mimic a cell surface for pathogen detection.[46] A schematic representation of this reaction can be found in Scheme 7.

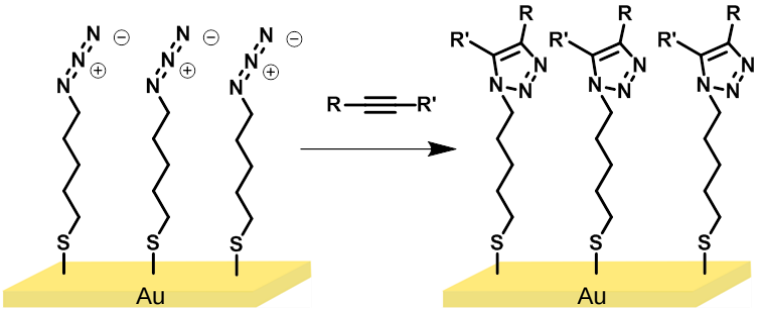

Scheme 7: Click reaction on a gold substrate containing azide functionalities

Another covalent approach is the reaction of amine groups of lysine residues of proteins with a *N*-hydoxysuccinimide (NHS) esters of the SAM. This reaction forms a stable amide bond. Herrwerth et al. describe the activation of a carboxylic acid terminated SAM with an NHS ester and bound antibodies covalently (Scheme 8).[47]

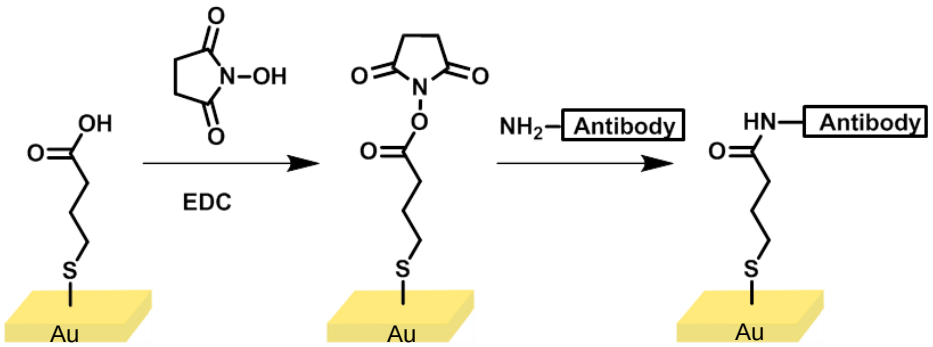

Scheme 8: Covanlent immobilization of an antibody to a self-assembled monolayer of carboxylated thiol on gold via NHS coupling. Adapted from Sarkar and Samanta[45]

Detection of pathogens such as influenza viruses were studied by Charych[48] and Narla[49] using glycan functionalized SAMs to covalently bind viral hemagglutinin. This approach is explained in detail in chapter 1.3.2.

One of the strongest *non-covalent* interactions know in nature is the interaction between biotin and streptavidin (STV). This interaction is a well-established system in biosensor research. More details about this system can be found in chapter 1.3.1.

Further focusing on the advantages of self-assembled monolayers as biosensor platforms one needs to mention that SAMs are less affected by mass transport than for example relatively thick gel films.[13] In the case of gels which are assembled on a substrate, the biomolecules have to diffuse in and out through the layer, which decreases the speed of the response. Thinner layers can advance the efficiency of the sensor device. However, the simple preparation of SAMs is also an advantage. Herein the substrate is immersed in a solution containing the organic molecule for a certain amount of time, and afterwards rinsed with the same solvent and dried under nitrogen flow. The concentration of chemicals needed for creating a monolayer is very small (0.02 mM - 2 mM).[50] Sarkar and Samanta proposed that even expensive compounds are economically viable to use in this context.[45]

The biggest advantage next to the one described above is that the SAMs are easy to be characterized with a number of techniques. Those techniques are optical ellipsometry,[51,52] surface plasmon resonance (SPR) spectroscopy,[53,54] infrared reflection absorption spectroscopy (IRRAS)[55,56] or QCM (quartz crystal microbalance).[57,58] Optical ellipsometry has been used by Malmsten et al. as a biosensing device to detect different proteins on a

methylated gold surface, e.g. human serum albumin (HSA). This technique can be used to analyze the thickness of the adsorbed layer and the amount of bound protein in mg/m^2.[51] Further explanation of *in-situ* ellipsometry can be found in chapter 2. Recent trends in antibody based sensors by Higson et al.[59] explain that immunosensors, e.g. implementing the quartz crystal microbalance, display changes in the resonance frequency of a quartz crystals due to changes in mass of the adsorbed molecules. This device has been used to detect multiple analytes like influenza or streptavidin.[57,58] SPR spectroscopy is an optical sensing technique, which is dependent on the change in optical thickness, a convolution of thickness and refractive index, due to molecule adsorption on a surface. Jang et al. used this technique to detect prostate specific antigen.[53] These methods can provide information about the layer-thickness and mass coverage. Binding events can be displayed as kinetic measurements in real time.

1.3.1 The biotin - streptavidin interaction in sensor application

Different methods for the attachment of biomolecules using self-assembled monolayers on a sensor device were developed over the last decades. There are two mechanisms relevant in this attachment. First, the attachment via *covalent* bond formation between the functional group of a SAM and the biomolecules and second the attachment via *non-covalen*t interactions such as hydrophobic interactions, electrostatic interactions or polar interactions between the functional group of the SAM and the biomolecules. Methods including affinity interactions such as biotin-streptavidin or antibody-antigen interaction are known to be *non-covalent*. The *non-covalent* interactions involve an attachment at various points of the biomolecule. One of the strongest *non-covalent* interactions know in nature is the interactions between biotin and streptavidin (STV). This interaction is a well-established system in biosensor research. STV is a 60 kDa homo-tetramer, which binds to biotin with an association constant of ~ 10^{14} M^{-1}.[60] The STV molecule has four equal binding pockets for biotin. Biotin can access STV from two sides (Scheme 9). This can be exploited to bind a biotinylated protein to a biotin-functionalized surface.

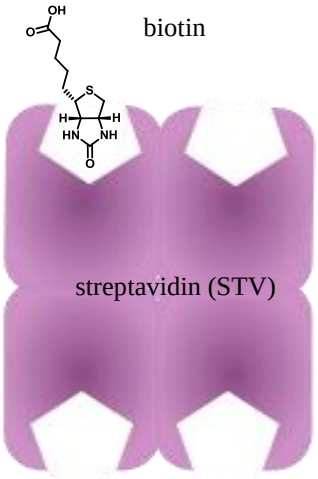

Scheme 9: Schematic representation of the biotin – streptavidin interaction

The biotinylation of biomolecules and chemicals is a standard technique.[21] Biotinylation of antibodies can be done chemically or enzymatically. The enzymatic method has the advantage of no unspecific biotinylation, since only one lysine with a certain sequence is biotinlayted by biotin ligase.[61] The chemical biotinylation involves most of the time NHS-

coupling to primary amines in the protein. Hence, all accessible primary amines in the protein are biotinylated.[62]

The biotinylated antibodies can in turn act as detectors for antigens. Simultaneously, the STV can be anchored by biotinylated SAMs. Spinke et al. used the system upon chemisorbed irreversibly biotinylated SAMs to develop a sensor for the pregnancy hormone human chorionic gonadotrophin (HCG) (Scheme 10).[21] The system using the biotin streptavidin interaction is especially interesting for the detection of very low antigen levels. Biotinylated antibodies are closely packed due to the ordered chemisorbed SAM and the STV layer. The close packing of STV is influenced by the orientation of the SAM and the accessibility to the functional group of the molecules. The accessibility is generated by lateral dilution of the functional molecules with a "spacer" molecule. The spacer should be inert and reduce the steric hindrance for improved functional group accessibility. On SAMs functionalized with biotin groups the antibodies are immobilized in an oriented fashion, which is an optimal condition for antigen binding. This is a great advantage over the antibody being directly immobilized on a surface. The orientation of proteins on bare metal surfaces has been studied by Arnebrandt et al.[52] They found that the flat orientation is favored, due to hydrophobic interaction. Baldrich et al. reported antibody immobilization by NHS coupling on an amine terminated SAM.[63] This two methods achieve randomly immobilized antibodies which are not optimal for antigen detection. The biotin-STV system overcomes this problem and is therefore the method of choice.

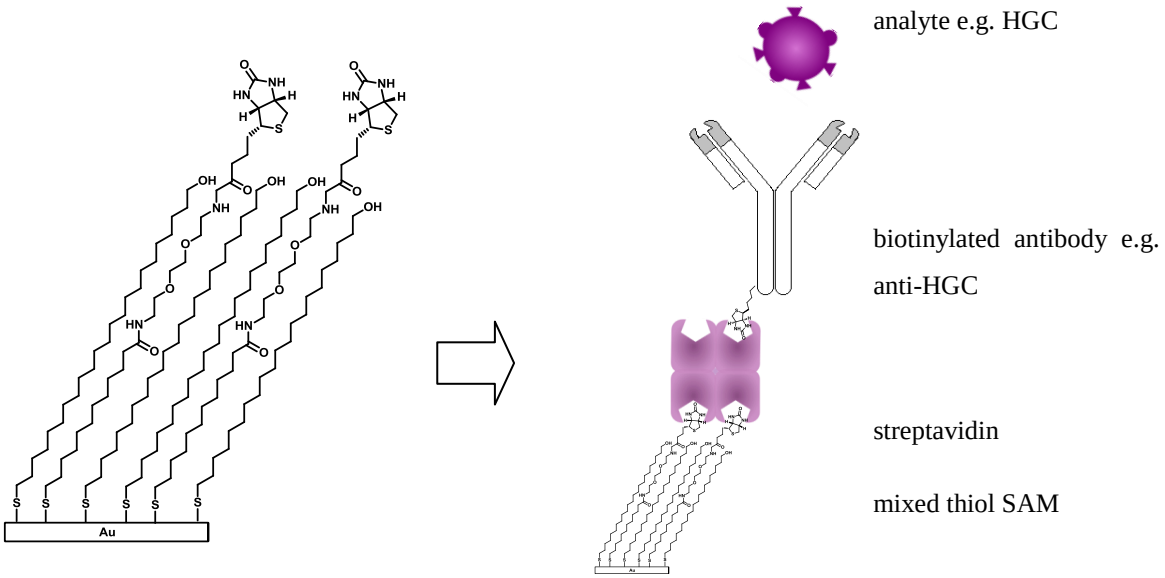

Scheme 10: Schematic representation of the biosensor developed by Spinke et al. upon chemisorbed irreversible SAMs;[21] the sensor consists of biotinylated thiol mixed with hydroxylated spacer thiol, streptavidin, biotinylated HCG and HGC as analyte

Antigen detection via capturing with antibodies has some great advantages. First, the detection is rapid and, second, very sensitive. The antibody/antigen association constant is very high, in the order of ~10^{11} M.[59] Antibodies are mostly produced by immunization of an animal hosts. The animal is immunized with an antigen and produces an immune reaction. The antibodies can be collected from the spleen and furthermore be processed using myeloma cell lines.[64]

One of the most common model analytes in biosensor technology is human serum albumin (HSA). HSA is a plasma protein; one of the most abundant proteins in blood. It is produced in the liver and therefore a marker for liver disease. Its molecular weight is around 66 kDa.[65] The crystal structure[66] and dimensions[67] of HSA can be found in Scheme 11.

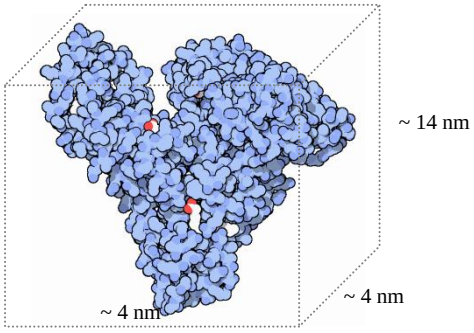

Scheme 11: Human serum albumin protein crystal structure and dimensions[66]

The advantage of using HSA as an analyte is that it is one of the best characterized and low-priced proteins available. HSA detection was extensively tested as the "proof of concept" in SPR,[68,69] nanoparticle based sensors[70] and other applications. In one of these studies, HSA has been used as a model analyte, to test the performance of a biosensor prepared using a biotinylated anti-HSA-antibody immobilized on a SAM.

Further, Prostate Specific Antigen (PSA) is used as an analyte to detect samples of medicinal relevance. PSA is a marker for prostate cancer. The molecular weight of PSA is 32-33 kDa.[71] The size of PSA found in literature is around ~ 4 nm in aqueous media.[72] It is a glycoprotein, which is produced by prostate epithelial cells.[73] PSA belongs genetically to the kallikrein family. Lilija et al. reported that PSA is present in human serum in two isoforms. Those are free-PSA (f-PSA) and complexed-PSA (c-PSA), respectively.[74] Since PSA levels are increased in patients with prostate cancer, it is of immense importance to detect PSA rapidly and sensitively. Current methods are based on immunoassays (ELISA),[75] which often involve techniques with fluorescence labels.[76]

1.3.2 Influenza virus detection via the hemagglutinin-sialic acid interaction

Biosensors cannot only be applied for sensing of free protein, but can also be used to detect proteins in membranes, e.g. on surfaces of cells or viruses like influenza. Influenza virus detection became more and more important in the last 15 years. In 1996 the first case of the so called bird flu in humans was reported.[77] It was caused by the influenza virus H5N1 and caused six deaths in Hong Kong. From 2003 until 2012, the WHO has reported 608 cases of avian influenza H5N1 and 359 deaths. The influenza virus is highly pathogenic and can be considered as a potential pandemic threat to human health.[57] Influenza belongs to the family of orthomyxoviridae and its envelope includes a segmented single strand RNA and nucleoprotein.[78] A review from Amano and Cheng about detection of influenza viruses describes traditional approaches and the development of biosensors in this field.[79] The so called gold standard in virus detection is virus isolation culture with immunocytological confirmation of viral antigens.[80] Current detection methods also include immunoassays with antigen capture. Those methods are poor in sensitivity and have high costs.[81] Another method is ELISA (enzyme-linked immunosorbent assay) which needs several steps and is time consuming.[82] Biosensing technologies based on a change in physical properties upon binding the analyte are rapid, and require only minute amounts of sample. Several of those detection methods are based on antigen capture with prior antibody assembly.[83,84,85] Disadvantages using antibody for capturing are the high cost of antibodies, the sensitivity against heat and the preparation method, which involves animal hosts.[64] Our special interest was to develop a sensor with no need for antibody assembly. Therefore we looked closer at the binding properties of influenza viruses.

A number of glycoproteins are located on the membrane of cells. The two most important proteins involved in virus infection are hemagglutinin (HA), which is localized on the influenza virus and sialidase, which is localized on the host cell. Sialidase has a sialic acid (SA) function, which is present at the carbohydrate side chains of glycoproteins and glycolipdis of the host cells.[86] The schematic representation of the sialic acid molecule can be found in Scheme 12.

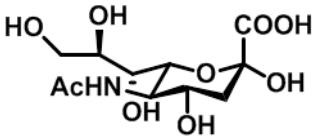

Scheme 12: Structure of the sialic acid molecule

In Scheme 13 the life cycle of an influenza virus is shown. After the hemagglutinin of the influenza virus has bound to the sialic acid on the attacked (host) cell, the virus penetrates the cell and endocytosis starts. Subsequently, the viral RNA and proteins are produced in the nucleus of the host cell. After replication, the viral RNA and proteins are assembled to form the virion. The virion leaves the host cell via budding with assistance of sialidase.

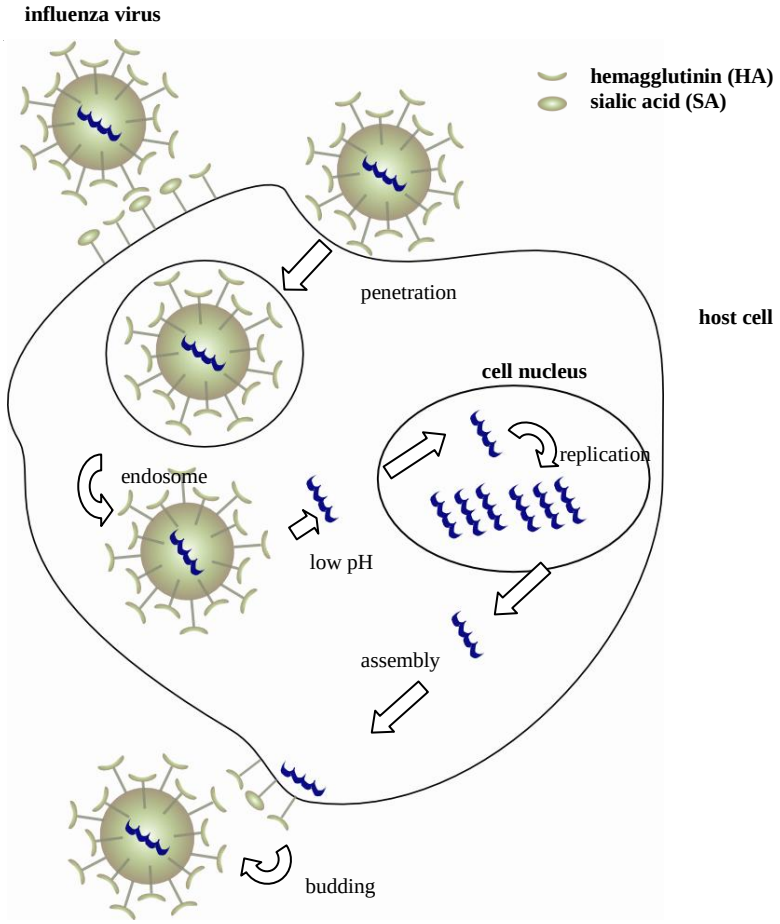

Scheme 13: Schematic representation of an influenza virus life cycle adapted from Among and Cheng;[79] the infection of the host cell starts with binding of hemagglutinin (HA) of the virus to the sialic acid located on the host cell; the virus enters the cell via endocytosis. RNA and viral proteins are replicated by the host cell and are assembled to new influenza viruses (virion); the virions leave the host cell via so called "budding"

The interaction of hemagglutinin with sialic acid (SA) makes SA an interesting tool for virus detection. SAMs with sialic acid as terminal group have been used in virus detection by Charych, Spevak and colleges.[48,87,88] Charych et al. developed a colorimetric influenza sensor functionalized with an analog of SA (Figure 14). A visible response of the layer assembled on a glass microscope slide could be observed with naked eye when the virus was present.

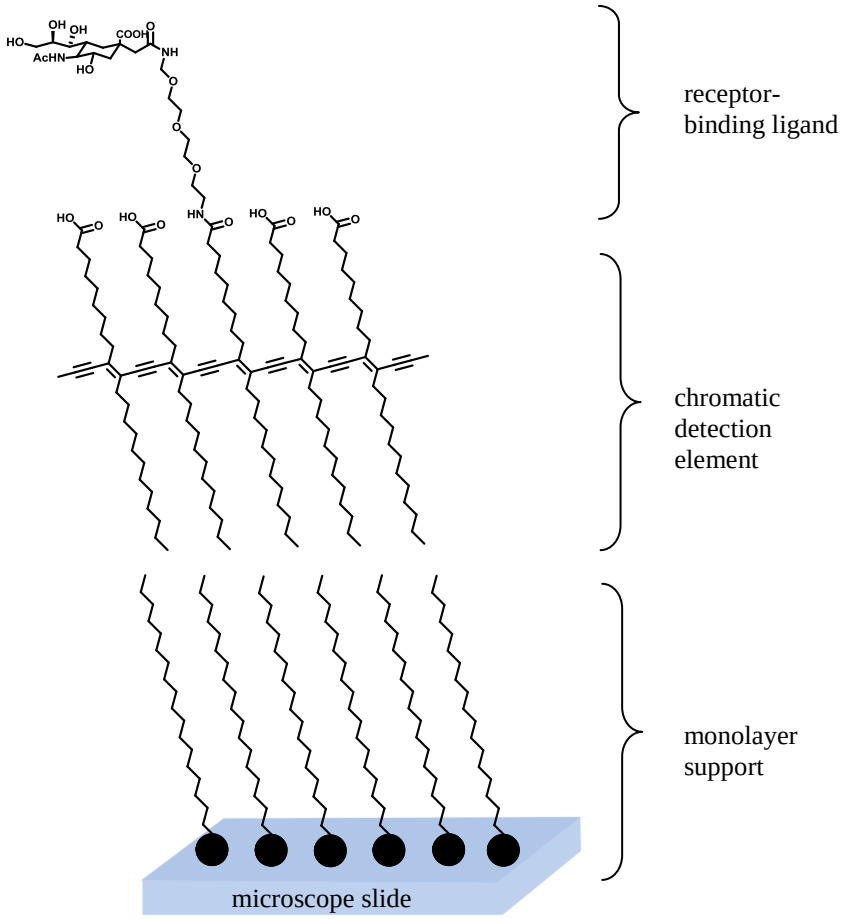

Scheme 14: Colorimetric detector for influenza recognition by sialic acid terminated bilayer. Adopted from Charych et al.[87]

Narla et al. applied this system upon chemisorbed irreversible SAMs in SPR.[49] Our special interest was to develop a reversible version of the chemisorbed SAMs for virus detection. In future, this system might be applied for diagnostic purposes to detect influenza viruses in biological samples.

2 Characterization Techniques

2.1 Ellipsometry

Ellipsometry is an optical method with very high precision, which is mainly used to determine optical characteristics of materials. It is used in particular to determine the refractive index and the thickness of thin films on surface.[89] It is a nondestructive method, which was invented by Drude and Rayleigh in 1889.[90]

When light is reflected or transmitted at a surface, the polarization status of the light changes. The name of the method results from the observation that the incoming linear or circular polarized light is often elliptically polarized upon reflection or transmission. The measured parameters are the changes of the polarization state of the light upon reflection on a surface in dependence of the surface functionalization. Linear polarized light, which has a parallel and a perpendicular component (called p-polarized and s-polarized) changes the phase of both components when reflected at a surface (Scheme 15). Fujiwara et al.[91] gives a good introduction about ellipsometry in his book "Spectroscopic Ellipsometry: Principles and Applications". They explain that the measured values psi (Ψ) and delta (Δ) represent the amplitude ratio and the phase difference between the light waves of p- and s-polarized light waves, respectively. In Scheme 15 the light reflection on a substrate is shown.

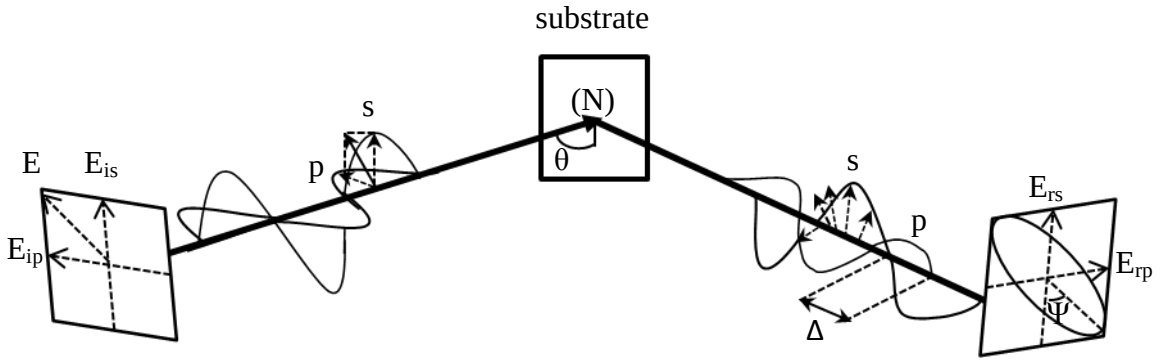

Scheme 15: Measurement principle of ellipsometry adopted from Fujiwara et al.[91]

The basic equation of ellipsometry is

$$\tan\Psi \exp(i\,\Delta) = \frac{E_{rp}}{E_{ip}} \Big/ \frac{E_{rs}}{E_{is}} \qquad (2)$$

The vectors of the electric filed (*E*) stand for the transmission and the reflection of the light. The subscribes E_{ip} and E_{rp} correspond to the incidence and reflection of the p-polarized light, respectively. The subscribes E_{is} and E_{rs} correspond to the incidence and reflection of the s-polarized light, respectively. Equation (2) is based on other parameters like the refractive index (N), which is the interaction of light with the material and will be explained in further detail in the following text.

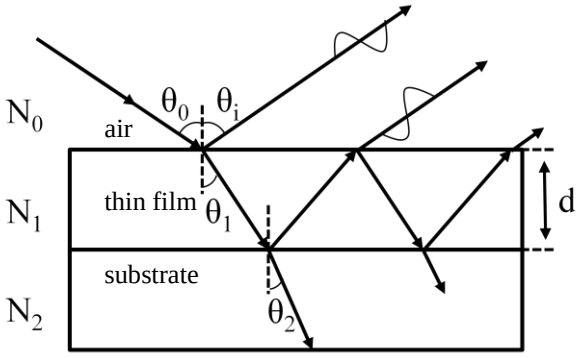

Scheme 16: Schematic representation of the 3 layer optical model of a system consisting of air, a thin film and a substrate adapted from Fujiwara[91]

In the optical model in Scheme 16, we have a closer look at the interaction of light with the substrate. The optical model is defined by the complex refractive indices (N_0, N_1, N_2) and the layer thickness (d). In Scheme 16 the optical three layer model is shown.

The parameters are defined as the complex refractive indices of air (N_0), a thin film (N_1) and the substrate (N_2). θ_0 is defined as the angle of incidence. θ_1 and θ_2 are defined as the transmission angles. In the law of reflection we can find, that the angle of incidence (θ_0) is equal to the angle of reflectance (θ_i).

$$\theta_0 = \theta_i \tag{3}$$

But some of the light is refracted at a different angle (θ_1, θ_2). With Snell's law one can calculate these transmission angles of θ_1 and θ_2.

$$N_0 \sin\theta_0 = N_1 \sin\theta_1 = N_2 \sin\theta_2 \tag{4}$$

The refractive index ($N_{0,1,2}$) is defined by

$$N_{0,1,2} = n_{0,1,2} - ik_{0,1,2} \tag{5}$$

whereas $n_{0,1,2}$, the real part of the refractive index, is defined by the material dependent reduction of light speed of the electromagnetic wave and $k_{0,1,2}$ is the imaginary part of the refractive index, which indicates the absorption when the wave travels through the film.

The measured data points (Ψ, Δ) cannot be directly converted into optical constants. Therefore we have to use an optical model developed by Fresnel, which is described in equation (6) and (7).[91] The reflection coefficient of the s-polarized light is given by r^s and the reflection coefficient of the p-polarized light is given by r^p.

$$r_{0,1}^{P} = \frac{\mathrm{N}_1 \cos\theta_0 - \mathrm{N}_0 \cos\theta_1}{\mathrm{N}_1 \cos\theta_0 + \mathrm{N}_0 \cos\theta_1} \tag{6}$$

$$r_{0,1}^{S} = \frac{\mathrm{N}_0 \cos\theta_0 - \mathrm{N}_1 \cos\theta_1}{\mathrm{N}_0 \cos\theta_0 + \mathrm{N}_1 \cos\theta_1} \tag{7}$$

Within this model, the refractive indices of the different layered system have to be taken into account. The correlation of the measured ellipsometric parameters (Ψ, Δ), the refractive index and the complex ratio of the reflection coefficient rho (ρ) are further defined by the following equations:

$$\tan\Psi \exp(i\,\Delta) = \rho\,(\mathrm{N}_0, \mathrm{N}_1, \mathrm{N}_2, \mathrm{d}, \theta_0) \tag{8}$$

$$\rho\,(\mathrm{N}_0, \mathrm{N}_1, \mathrm{N}_2, \mathrm{d}, \theta_0) = r^p(\mathrm{N}_0, \mathrm{N}_1, \mathrm{N}_2, \mathrm{d}, \theta_0)\ / r^s(\mathrm{N}_0, \mathrm{N}_1, \mathrm{N}_2, \mathrm{d}, \theta_0) \tag{9}$$

$$\frac{r^p(\mathrm{N}_0, \mathrm{N}_1, \mathrm{N}_2, \mathrm{d}, \theta_0)}{r^s(\mathrm{N}_0, \mathrm{N}_1, \mathrm{N}_2, \mathrm{d}, \theta_0)} = \frac{E_{rp}}{E_{ip}} \Big/ \frac{E_{rs}}{E_{is}} \tag{10}$$

The refractive indices for film thickness calculation, used in this thesis were adapted from literature and are summarized Table 1.

Table 1: Refractive indices for different media found in literature

Layer	n_l	k_l
gold[16]	0.20	3.32
air[16]	1.00	-
aqueous media e.g. buffer[16,92]	1.33	-
thiol[93,94]	1.58	-
protein[92,93]	1.45	-

2.1.1 Ellipsometry instrumentation

The experimental setup of an ellipsometer is illustrated in Scheme 17. The light source of the ellipsometer is a HeNe laser at a wavelength λ of 632.8 nm. The laser beam passes a polarizer and is converted into linearly polarized light. The latter is reflected off the substrate and arrives at a quarter wave plate, which converts the reflected and now elliptically polarized light back into linearly polarized light, however with a different polarization direction. The analyzer, a polarizer, is used to determine the change in the polarization direction of the reflected light.

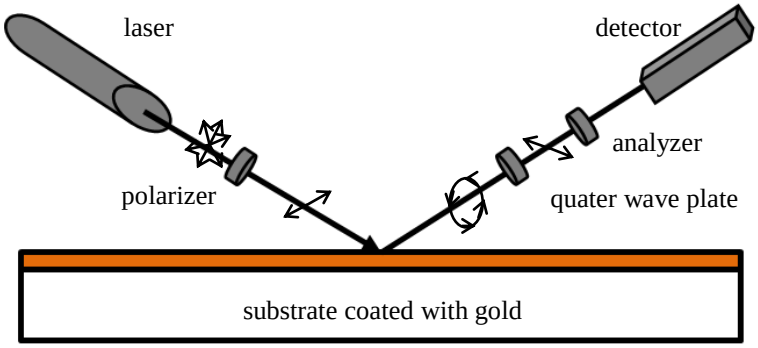

Scheme 17: Schematic representation of an ellipsometer, where denotes the unpoarized light, represents the plane polarized light, and represents the elliptically polarized light. Scheme was adapted from Ulman[1]

For *in-situ* measurements a setup with a cuvette is used. The cuvette is made of teflon as an inert material. The setup shown in Scheme 18 includes a gold-coated substrate.

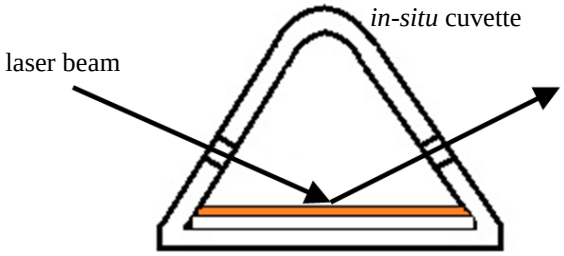

Scheme 18: *In-situ* ellipsometry cuvette with a cuvette volume of 1.7 mL including a substrate coated with gold

2.2 Infrared reflection adsorption spectroscopy (IRRAS)

Infrared reflection adsorption spectroscopy (IRRAS) is a spectroscopic tool to study thin organic films assembled on metal substrates.[2, 4,95] This method provides information about functional groups, their orientation, chain conformation and packing density of a thin film.[1] Infrared light is used to excite particular molecular vibrations in the molecules assembled on the surface. Once the molecular moiety is excited, one can obtain information about the direction of transition dipoles of this vibration within the film. In IR-spectroscopy, light is used which is polarized parallel (p-polarized) to the plane of incidence.[96] This ensures an electrical field vector oscillation at the point of reflection perpendicular to the gold surface. The reflection adsorption is measured at high angles of incidence (θ_1 = 80°) to achieve maximal intensity. The molecule absorbs the energy necessary to excite the molecular vibration, therefore the reflected absorption spectrum is specific for their structure and the orientation of the vibrating molecular moiety.

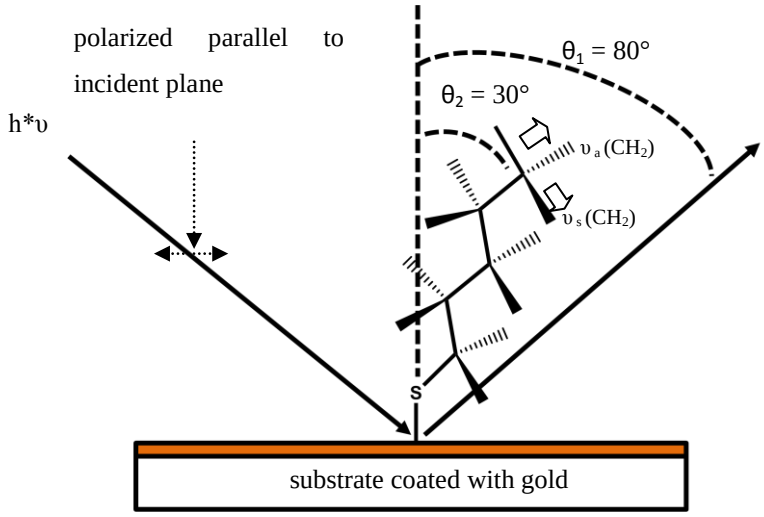

Scheme 19: Schematic representation of the IRRAS experiment. In the point of reflection the electrical field is oscillating perpendicular to the gold surface

In Scheme 19, the IRRAS experimental setup is displayed. Since alkane-thiols are tilted with an angle of $\theta_2 \approx 30°$ on gold substrates,[5] the symmetric and asymmetric methyl vibrations ($\upsilon_s(CH_2)$, $\upsilon_a(CH_2)$) can be detected. If the asymmetric and symmetric vibration of the methylene group of the alkane thiol would have a transition dipole moment (TDM), which is parallel to the surface, the p-polarized light could not excite the vibration.[1,20] This is a consequence of the surface selection rule. If the TDM is exactly perpendicular to the surface the IR bands have the largest intensity, whereas the intensity is reduced when the TDM is oriented differently. We used IRRAS to verify the orientation of the alkane thiols and the further assemblies. By investigating the peak position and intensity of the methylene we could obtain information about the presence and orientation. Pioneering work in this field has been done by Porter et al.[4] and Arndt et al.[97] who showed that the peak position of the $-CH_2$ vibrations is a function of the tilt angle of the molecule on the surface. In order to compare the IRRAS data, we also conducted transmission IR spectroscopy in KBr-pellets.

A Nexus FTIR (Fourier transform infrared spectroscopy) instrument from Thermo Scientific with an SAGA (specular apertured grazing angle) setup for IRRAS investigations was used. The MCT-A detector was cooled with liquid nitrogen, and a sample compartment was purged with N_2.

2.3 Contact angle investigation

Contact angle investigation is an important tool to study the wettability of thin molecular layers. Typically a water drop is applied to a solid/vapor interface. The contact angle θ is the angle between the tangent plane of the surface and the surface of the drop. The drop is exposed to three forces: the surface tension between the solid phase and the liquid phase (SL), the surface tension between the solid and the vapor phase (SV) and the surface tension between the liquid and the vapor phase (LV). The contact angle can be calculated via the Young equation. [98]

$$\cos\,\theta = \frac{\gamma_{SV} - \gamma_{SL}}{\gamma_{LV}} \qquad (11)$$

The measurement here is carried out using a drop of borate buffer. If the contact angle is smaller than 90°, the surface can be considered as hydrophilic, the water spreads above the surface. If the contact angle is higher than 90°, the surface is called hydrophobic, water tries to avoid contact with the surface and tries to form a sphere.

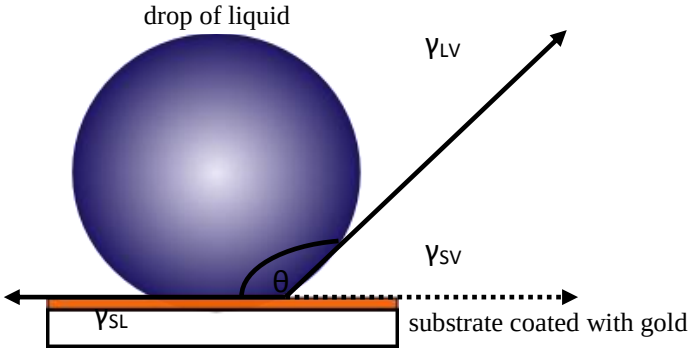

Scheme 20: Schematic representation of a contact angle measurement including the parameters for Young's equation

2.4 Atomic force microscopy (AFM)

With AFM, one can obtain information about the topography of a sample surface. In Scheme 21, the concept of an AFM is shown. The sample is scanned with a tip, which interacts with the atoms of the surface. The resulting attractive or repulsive force deflects the tip, which is stationary mounted on a cantilever.[1] When tapping mode (dynamic contact mode) is applied in the measurement, the cantilever is moving up and down near the sample with specific amplitude. It only has intermittent contact with the sample. When the tip comes close to the sample, forces like dipole-dipol interactions, van der Waals- or electrostatic-forces are interacting with the cantilever and change this specific amplitude.[99] The deflection of the tip is measured by a laser spot reflected off the top of the cantilever and detected by position sensitive photodiodes.

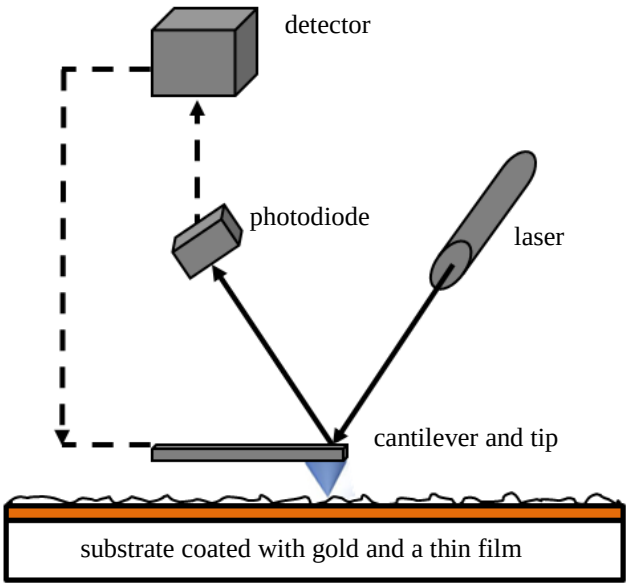

Scheme 21: Schematic representation of an AFM

We used AFM to investigate the topography of the alkane thiols and the further assemblies on the surface. By examining the ultrathin organic layers e.g. thiols and functionalized amidines we wanted to obtain information about the crystallinity of the films.[35,100] Applying AFM to biological functionalized surfaces could offer us information about assembled biological structures, e.g. their shape or size.[99,101] Atomic force microscopy was carried out with a Nanoscope IIIa equipped with a 10 µm scanner from Veeco Instruments.

3 Results and Discussion

3.1 Synthesis of heterofunctionalized amphiphiles

The main objective of this thesis was the development of reversible biosensor platforms. The well-established self-assembled monolayers (SAMs) of alkane thiols on gold were exploited to create the affinity groups for an analyte in those sensors. Apart from allowing the substrates to be reused, the reversibility of the layer assembly can allow a more homogenous and oriented presentation of molecular recognition sites. In the past, Auer et al. could show that α,ω- bis(4-aminophenoxy)alkanes form mono- and bi-layers on carboxylic acid functionalized alkanthiols, which were assembled on gold.[24] Following up on this study, biologically active ligands were introduced at the ω-position of the amphiphiles. The different functionalities offer the possibility to develop biosensors for prostate specific antigen (PSA) and influenza hemagglutinin. To create a sensor for PSA, ω-biotinylated amphiphiles for selective binding of streptavidin were synthesized. The protein streptavidin has four binding pockets for biotin, allowing it to act as a connector between the biotinylated amphiphiles and biotinylated antibodies. Anti-prostate-specific antigen or anti-human serum albumin was used in this study. The antibodies were used for antigen detection, respectively. The sensor including biotin represents a platform and can be applied to any biotinylated antibody or protein. The well-established biotin–streptavidin coupling scheme is used to assemble the sensor. In a second study, amphiphiles modified with sialic acid on the ω-terminus were synthesized to detect hemagglutinin. Sialic acid is a glycan on the surface of erythrocytes and influenza attaches to the cells via binding between sialic acid and hemagglutinin. After this binding, the influenza virus can enter the host cells and initiate the virus' membrane fusion to release the viral genome into the cytoplasm of the host cell.[102]

3.2 Synthesis of ω-functionalized biotinylated amphiphiles

The synthesis route was previously developed in the Sellergren group.[42] The synthetic procedure is shown in Scheme 22.

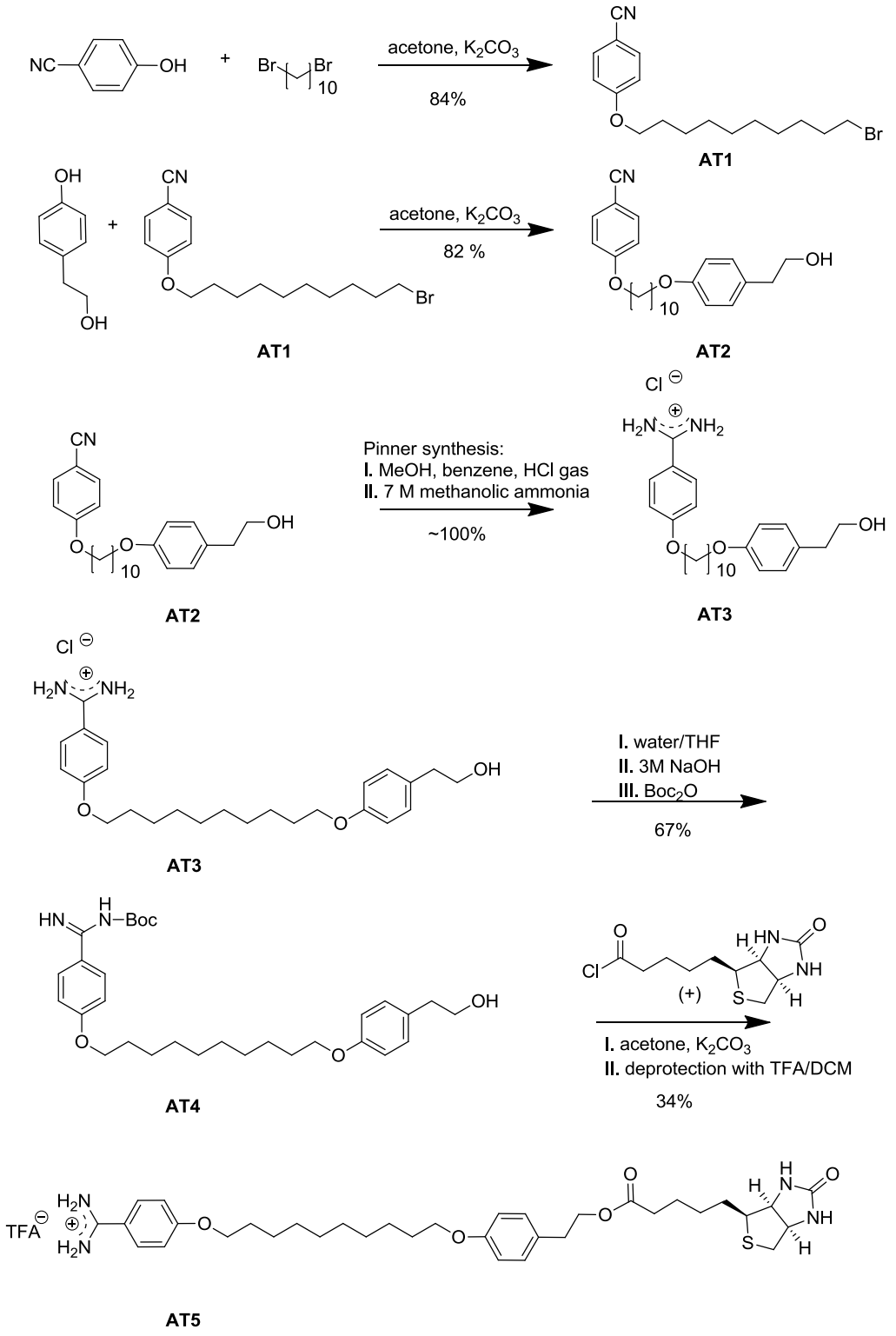

Scheme 22: Synthesis of biotinylated amidine

In Scheme 22, the synthesis route of the biotinylated amidine product is shown. Product (**AT1**) was obtained by refluxing a large excess of 1,10 dibromodecane (10 eq.) with 4-cynaophenol in acetone for 48 h in presence of the base K_2CO_3. After purification by column chromatography, the product 4-((10-bromodecyl)oxy)benzonitrile was obtained in 84% yield. In the second step, 4-((10-bromodecyl)oxy)benzonitrile was refluxed with 4-(2-hydroxyethyl) phenol in presence of the base K_2CO_3. After 24 h the crude product (**AT 2**) was worked up with column chromatography and obtained in 82% yield. The challenge in this 5-step-synthesis was the Pinner-reaction. Gaseous HCl was used in this reaction which was generated by dripping concentrated sulfuric acid into sodium chloride. In the Pinner reaction[103], the cyano-group is first converted to the hydrochloric acid salt of an imino ester in the presence of an alcohol and HCl-gas (Scheme 23). The intermediate is called Pinner salt. In a second step, the Pinner salt can be converted to an amidine. The reaction starts in the presence of methanolic ammonia. The product **(AT3)** was obtained in a quantitative yield.

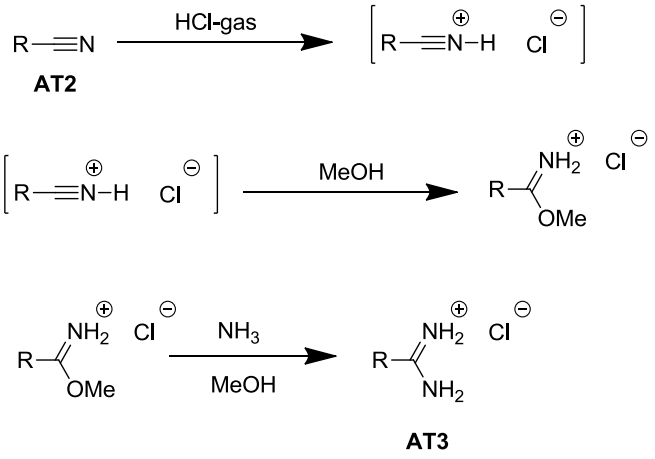

Scheme 23: Pinner mechanism[104]

To couple the biotinchloride to the amphiphile, it was necessary to protect the amidine function. This was done using the Boc strategy.[105] The product **(AT5)** was obtained as yellow solid in 34% yield

In addition to the biotinylated amidine (**AT5**), which is used as an anchor for streptavidine, the OH terminated amidine (**AT3)** served as a spacer. The spacer molecule was separating

the biotin head groups and allows an optimal streptavidin packing by avoiding steric hindrance of too close biotin labels.

In the following paragraphs, the analysis of the monolayer formation using different surface-analytical techniques is described.

3.2.1 In-situ ellipsometry of biotinylated amphiphiles

With in-situ ellipsometry we could display the assembly of the multi-layered system. The layer system consisted of mecaptohexadecanoic acid, which is assembled on the gold via a covalent bond between the sulfur and gold atoms.[106] The successive was formed by different functionalized amidines (**AT3** and **AT5**). Those amidines can bind to mercaptohexadecanoic acid via the pH switchable amidinum carboxylate interaction.[24] The third layer represented the anchor layer for streptavidin (STV). STV can be an anchor for biotinylated antibodies specific for an antigen.

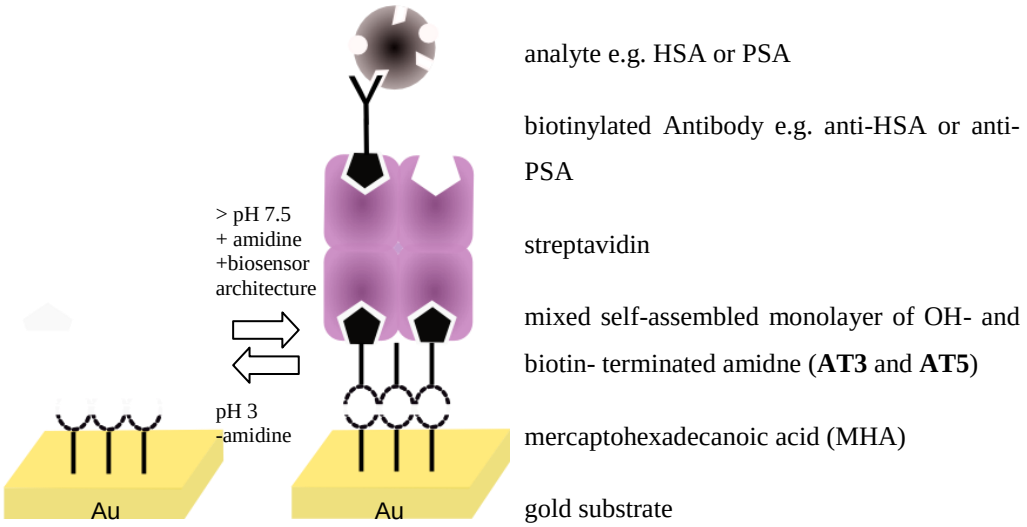

Scheme 24: Reversible biosensor consisting of MHA, amphiphile, streptavidin, biotinylated antibody and analyte.; reversibility is achieved by changing the pH of the environmental solution, and therefore the charge status of the MHA

Before the amphiphiles were assembled, the anchor layer of mecaptohexadecanoic acid (MHA) was assembled on the gold. The gold slides were etched in freshly prepared piranha solution (4:1 H_2SO_4/H_2O_2; **Caution**! reacts violently with organic compounds) for 1 min, washed with copious amounts of Milli-Q water, and dried with N_2 to be cleaned in an appropriate way. Subsequently, the gold slides were immersed in a 0.02 mM solution of

MHA in absolute ethanol for ≥18h. to self-assemble properly. This first layer had a film thickness of ~2.2 nm (ellipsometry). This corresponds to a monolayer of elongated mercaptohexadecanoic acid with a tilt angle of 30°, respectively.[38,54,93,106] This film thickness was investigated via ellipsometry taking a homogeneous refractive index of n(thiol) = 1.58 and n(protein) = 1.45 into account.[107] The kinetics of the formation of the first layer are shown in Figure 1a. Within ~1 min the thiol layer self-assembled on the gold slide. To generate a crystalline-like structure of thiols on gold, the concentration and the adsorption time are important parameters.[2,35,106] Concentrations of 1 mM and lower as well as adsorption times of several hours tend to form closely packed layers.[3] Tamada et al. claim that the first arrangement of the thiol molecules seems to be driven by van der Waals attraction, before the chemisorption between the sulfur and the gold atoms takes place.[106] Figure 1 displays our result of the ellipsometry data. The graph shows the thickness of the layer in nanometers versus the assembly time in seconds. Figure 1 b is a schematic representation of the monolayer. The thickness was calculated via ChemBioDraw (Version 12.0 Ultra) and can be found in Table 2.

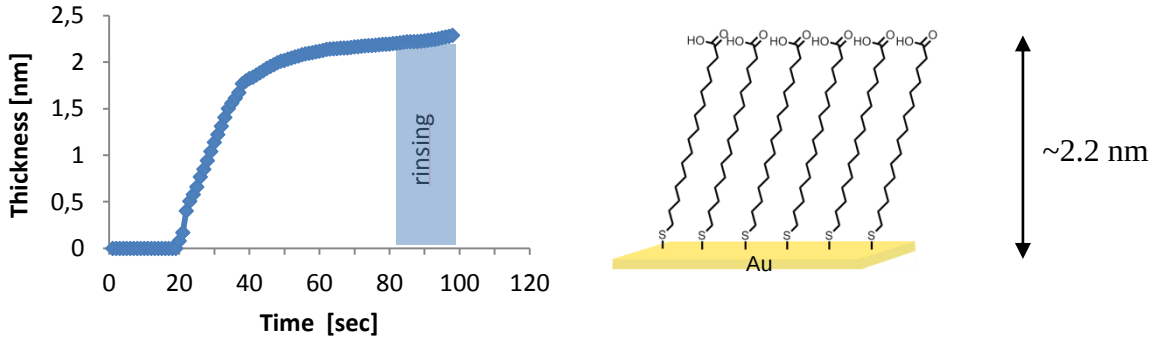

(a) (b)

Figure 1 a) Ellipsometric assembly kinetic of the MHA SAM on gold ; b) scheme of the MHA SAM

For further investigation of the multilayer assembly, several MHA substrates were prepared separately. Therefore, the gold substrates were immersed in 0.02 mM ethanolic MHA overnight. After rinsing the substrate extensively with absolute ethanol and drying it with nitrogen, the MHA functionalized surface was mounted into the teflon cuvette filled with pH 9 borate buffer (0.01 M). Subsequently, the bipolar amphiphil **AT5** or **AT3** was self-assembled on the carboxyl-functionalized surfaces (50 µM, pH 9 borate buffer). This self-assembled layers were oriented nearly perpendicular to the substrate (Scheme 25). We concluded this from the calculated molecule size (Table 2) and the measured ellispometry

results (Figure 2), which are in good agreement with each other. Auer et al. had observed this behavior for bipolar amphiphiles, α,ω- bis(3- or 4-amidinophenoxy)alkanes on carboxylated gold substrates before.[35]

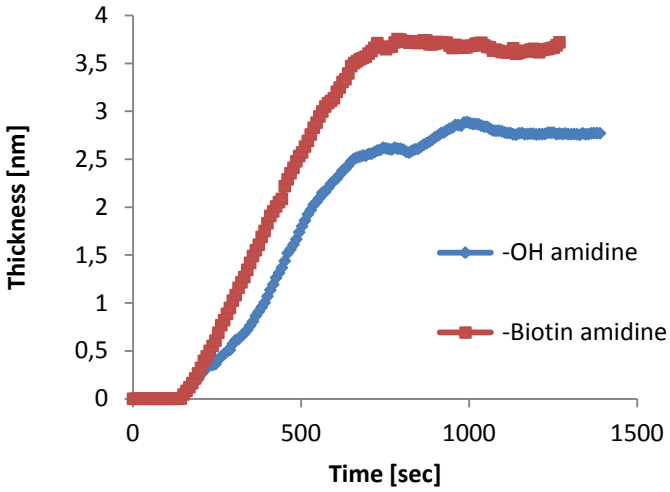

Figure 2: Kinetic of the self-assembly of biotinylated amidine (red) and OH terminated amidine (blue)

To achieve maximal streptavidin binding, experiments were performed with mixtures of the amphiphiles **AT3** and **AT5** in different ratios (Figure 4). The ratios studied were: 100/0, 10/90, 20/80, 40/60, 60/40 and 0/100 biotinylated amidine **AT5** to OH-terminated amidine **AT3**. The different monolayers are shown as a function of the mole fraction X_B of biotinylated amidine to hydroxyl terminated amidine in the adsorption solution. Spinke et al. used this way of plotting data as a function of molecule composition for irreversibly chemisorbed SAMs.[21] The lateral dilution with a spacer-molecule (hydroxylated thiol) to a functional molecule (biotinylated thiol) gave them the chance to find optimal binding properties for further layer assembly. We adapted this method for your investigations.

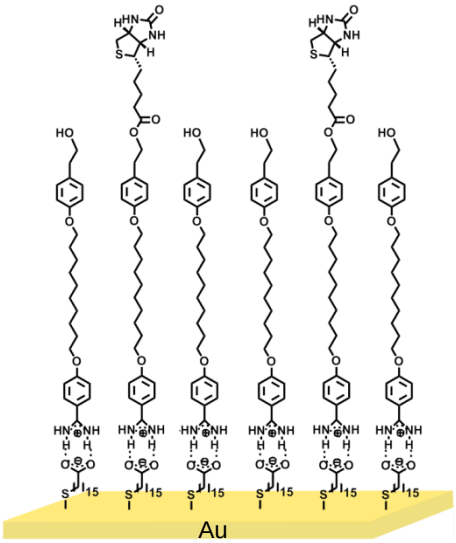

Scheme 25: Mixed self-assembled monolayer of amidines with OH-function (AT3) and biotin-function (AT5) on the carboxylated gold surface

After addition of the hydroxyl terminated amphiphile to the ellipsometry cuvette, an increase in film thickness of 2.9 ± 0.1 nm was observed (error is the standard deviation of three measurements on different substrates). The biotinylated compound increased the film thickness by 3.6 ± 0.1 nm. This matches the size, which was estimated via ChemDraw (Table 2). The amphiphiles mixed in different ratios show similar increases in film thicknesses from ~ 3.5 to ~3.6 nm. The kinetics are depicted in Figure 3 a-c.

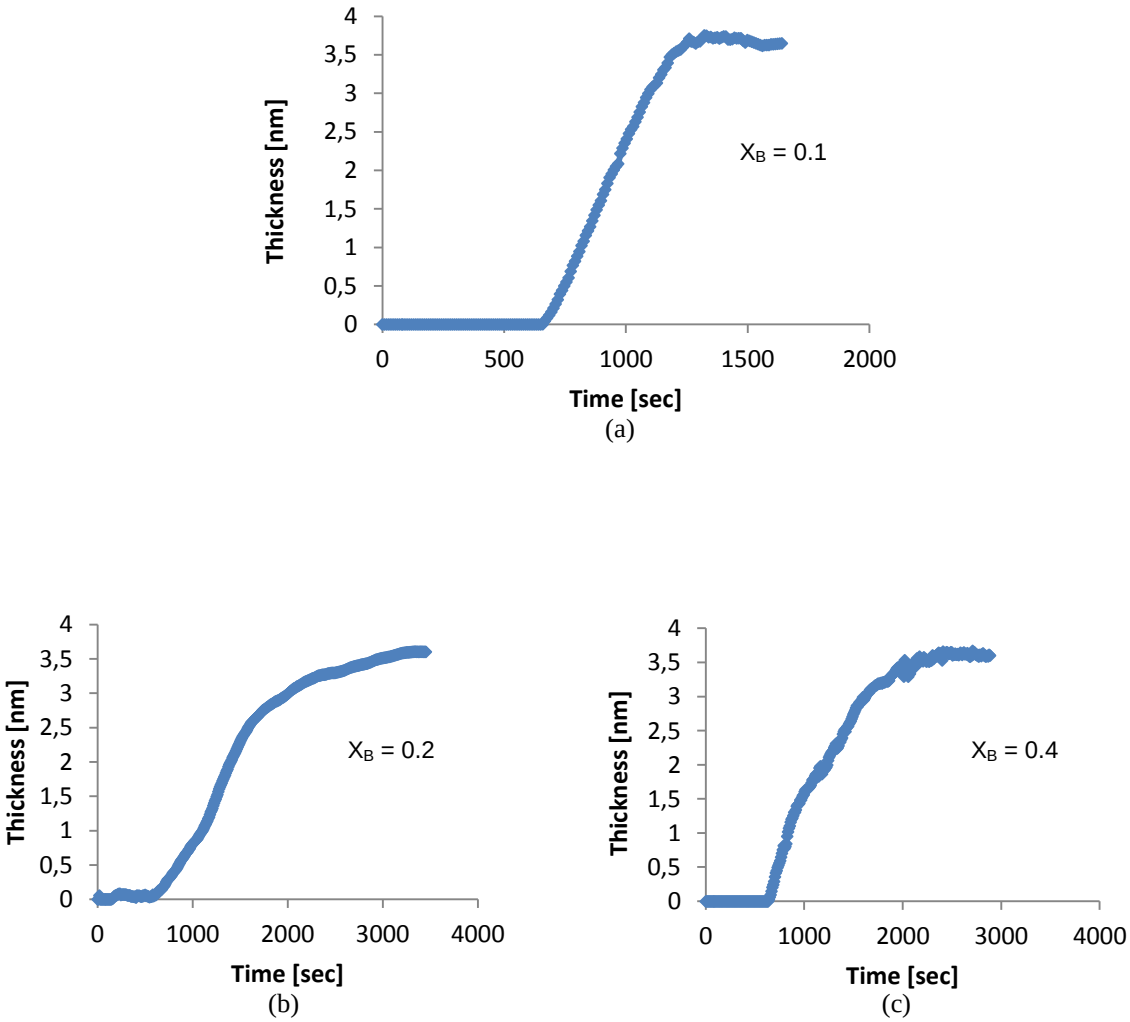

Figure 3: Self-assembly of different mixed amidines on MHA; the different monolayers are shown as a function of the mole fraction of biotinylated amidine to hydroxylated terminated amidine in the adsorption solution X_B; a) biotin content of X_B = 0.1, b) biotin content of X_B = 0.2 and c) biotin content of X_B = 0.4

The next assembled layer was the anchor layer of streptavidin. Subsequently, 5 µM STV was used to bind to the biotin labels on the reversible monolayer of amidine. The exact thicknesses can be found in Figure 4 and Table 2.

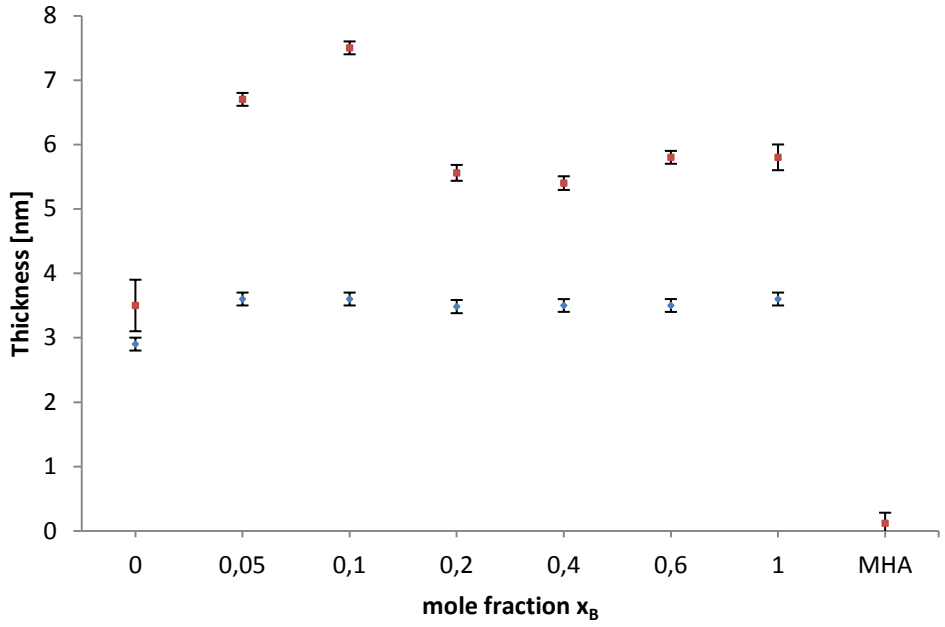

Figure 4: Film thickness measured by in-situ ellipsometry; blue points are the monolayer thickness of the amphiphiles on MHA red points are the assembled streptavidin thickness on the different mixed SAMs; the different monolayers are shown as a function of the mole fraction X_B of the biotinylated amidine to OH terminated amidine in the adsorption solution; the error bars are the standard deviation of three measurements on different substrates

From Figure 4 we could observe that maximum STV binding was achieved with a biotin content of $X_B = 0.1$ with a successive decrease in the STV thickness as the biotin content increased. This is the same observation Spinke et al. made with irreversibly chemisorbed SAMs of biotinylated thiols. It has been well established, that full insertion of biotin heads into STV pockets is favored on diluted biotin SAMs.[21,55] We did not observe significant binding on the pure mercaptohexadecaoic acid (MHA) film. The binding on the pure hydroxylated amidine film was low and it was possible to remove the unspecifically bound STV by rinsing the cuvette with buffer (Figure 5).

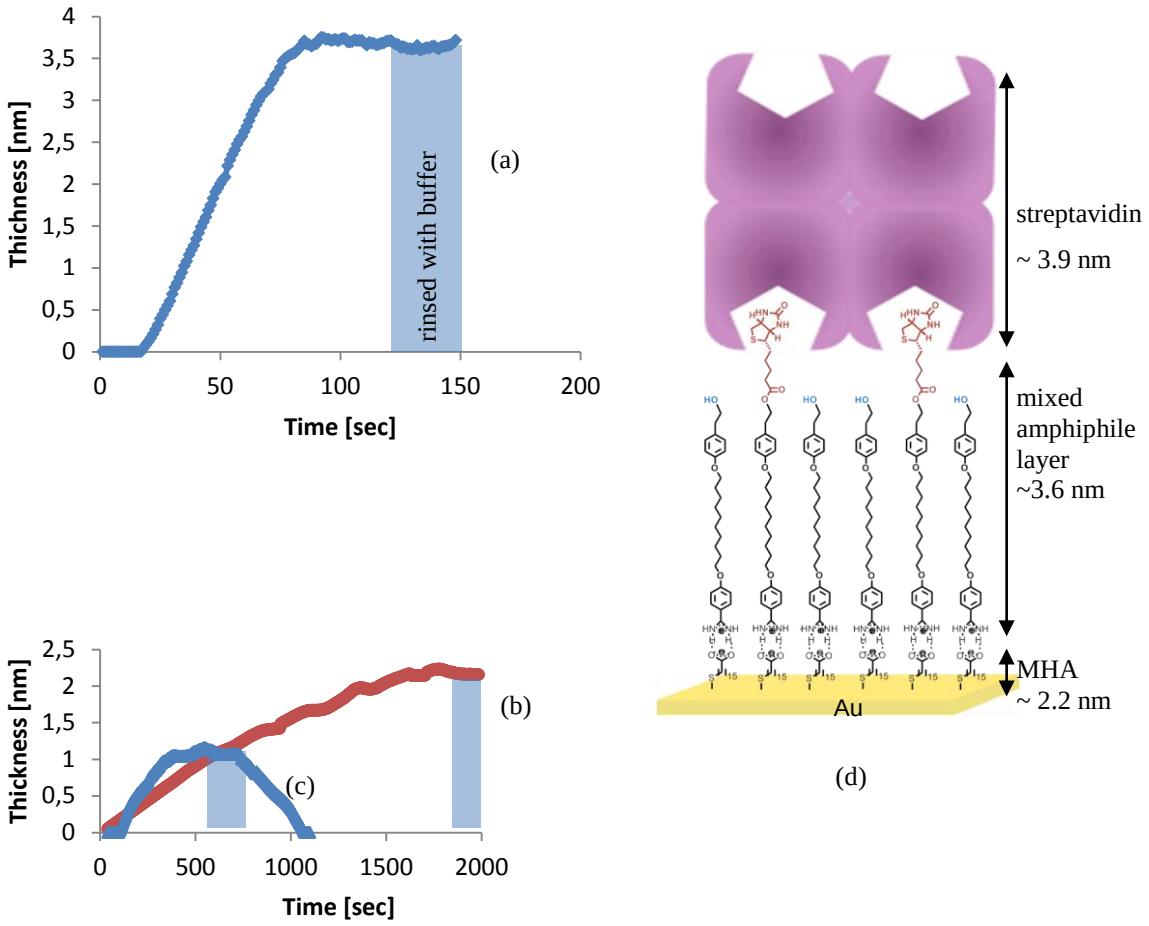

Figure 5: Self-assembly of streptavidin on different mixed amphiphiles with a biotin content of a) $X_B = 0.1$; b) $X_B = 1$; c) $X_B = 0$; d) schematic representation of streptavidin assembled on mixed amphiphile layer .

The low increase of film thickness for the STV adsorption on the hydroxylated SAM can be attributed to weak hydrophobic interaction between the hydroxyl-group on the surface and the STV. The binding of STV on the pure biotinylated amidine film was also low, but some of the STV was bound to the functional head groups, since the rinsing with buffer did not remove all the STV (Figure 5).

There is no binding of STV at the pure mercaptohexadecanoic acid film. The maximum binding of STV was found at a biotin content of $X_B = 0.1$. This behavior indicates high densities of binding sites in one layer produces high adsorption of the next layer. Pure amphiphile **AT5** showed only a small increase of ~2 nm STV film-thickness on the MHA-terminated surface, which was due to the effect of steric hindrance. As explained before, the biotinylated amidine was used as anchor layer for streptavidin, which was subsequently used to bind biotinylated anti-human-serum-albumin (anti-HSA) or biotinylated anti-

prostate-specific-antigen (anti-PSA). The film-thickness increase of anti-HSA was 3.4 nm, which corresponds with the published results by Mittler-Neher et al.[93]

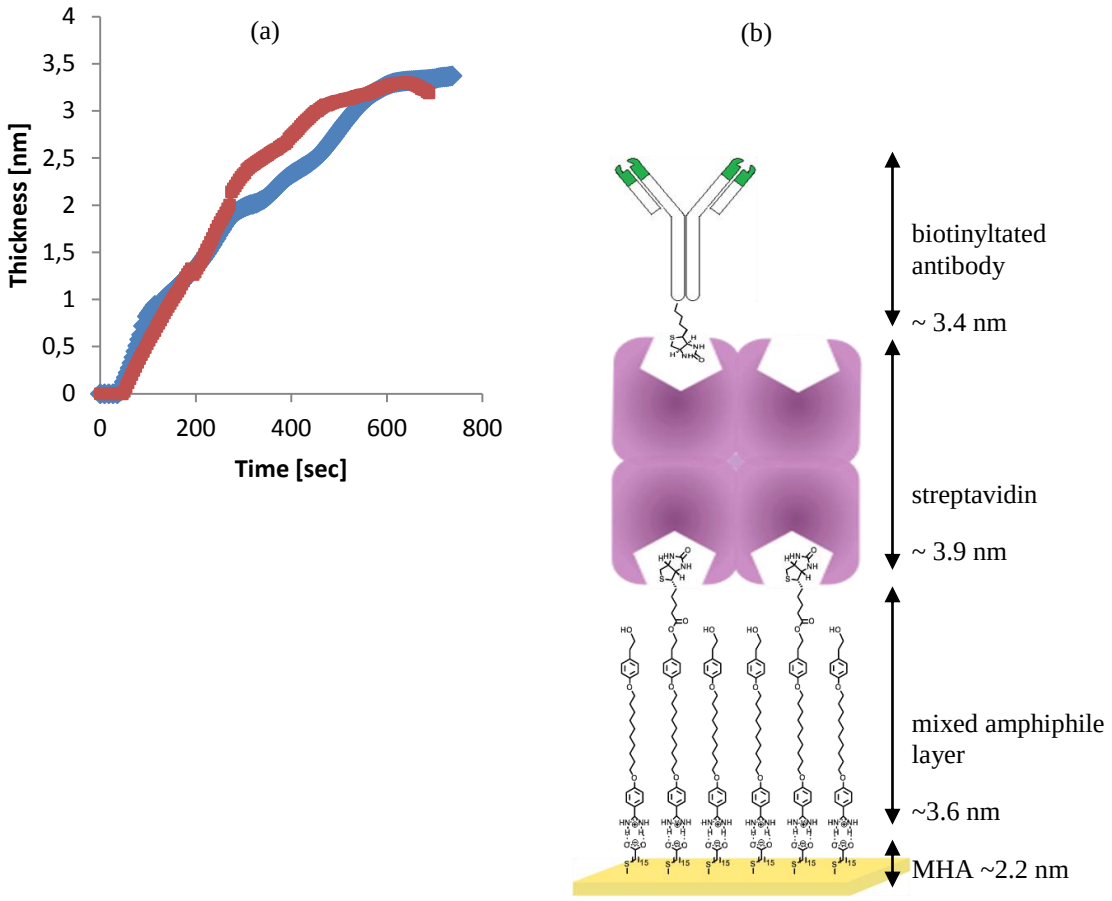

Figure 6 a) Self-assembly of anti-HSA (blue) and anti-PSA (red) on streptavidin assembled on mixed amphiphiles X_B = 0.1; b) schematic representation of biotinylated antibody assembled on STV, mixed amphiphile and MHA

As model analytes PSA and HSA were chosen. HSA is the most abundant protein in the human blood.[70,108,109] A low HSA concentration is a hint for liver disease.[110] Therefore it is important to be able to detect HSA and distinguish it from other proteins present in the blood such as IgG. Different concentrations of HSA (1.5 pM to 5 µM) were added to test the sensor response (Figure 7). Also the non- specific protein IgG was tested in different concentration and mixtures of both proteins on the sensor surface. Low concentrations up to 50 pM did not yield relevant film thickness enhancements. However, starting at 70 pM up to 5 µM concentration ellipsometry yielded the expected film-thickness increase for HSA (Figure 7). In literature a correlation between the analyte concentration and the film thickness was reported by testing biomolecule detection based on irreversible SAMs.[54,69,93,111] In detail, it was found that a decreasing concentration leads to a decreasing film

thickness. This fact the authors attributed to the lower amount of adsorbed molecules onto the SAM. In this thesis thicknesses corresponding to monolayer size were found. Even at a very low concentration of 70 pM a thickness of 4.0 ± 0.2 nm were observed. When lower concentrations were tested, they did not show any significant molecule adsorption. This interesting behavior can be attributed to the fact that the dynamic nature of the reversible SAM layer structure renders the individual SAMs adaptable for an optimal packing of the adsorbed molecules. The amidium-carboxylate is attractive and directional at the same time, respectively.[112,113] Thus assuming the dynamic layer structure proposed, the rSAM is able to preorganize in two dimensions.

Unspecific binding of IgG was not observed. We can attribute this behavior to high binding constant for antigens and antibodies (>10^{-8}M).[21]

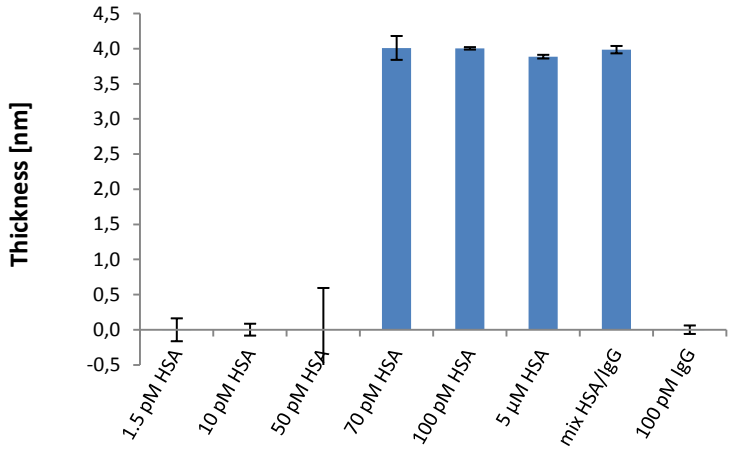

Figure 7: Detected film thickness increase of HSA and IgG with respect to applied concentration

Table 2: Measured and calculated monolayer thicknesses of compounds AT3 and AT5, as well as the thickness of the subsequently assembled layers.

Compound	Theoretical thickness [nm]	Experimental thickness (ellipsometry) [nm]	Experimental thickness of adsorbed STV [nm]	Experimental thickness of adsorbed HSA [nm]
MHA	2.1	2.2 ± 0.1	-	0.5 ± 0.5
X_B = 0.0 -OH (**AT 3**)	2.8	2.9 ± 0.1	0.6 ± 0.4	1.0 ± 0.1
X_B = 1.0 -biotin (**AT 6**)	3.6	3.6 ± 0.1	2.2 ± 0.2	1.4 ± 0.1
X_B = 0.05 mixed SAM	-	3.6 ± 0.1	3.1 ± 0.3	-
X_B = 0.1 mixed SAM	-	3.6 ± 0.1	3.9 ± 0.1	-
X_B = 0.2 mixed SAM	-	3.5 ± 0.1	2.1 ± 0.1	-
X_B = 0.4 mixed SAM	-	3.5 ± 0.1	1.9 ± 0.1	-
X_B = 0.6 mixed SAM	-	3.5 ± 0.1	2.3 ± 0.1	-
streptavidin (STV)	4.0[35]	3.9 ± 0.1	-	-
biotinylated anti-HSA	3.4[35]	3.4 ± 0.1	-	-
HSA	4.0[35]	3.9 ± 0.1	-	3.9 ± 0.1
biotinylated anti-PSA	4.0[71,72]	4.0 ± 0.1	-	-
PSA	4.2 ± 0.2[71, 72]	4.0 ± 0.3	-	-

To estimate the assembled amount of protein (Γ) on the surface the Feijter equation was applied.[114] The equation is based on the assumption that there is a linear behavior between the protein concentration and the refractive index of a protein in solution.[65]

$$\Gamma = d_p \left(\frac{n_p - n_l}{d_n/d_c} \right) \qquad (12)$$

whereas d_P is the thickness of the absorbed protein layer, n_p is the refractive index of the protein layer, n_l is the refractive index of the ambient solution, and d_n/d_c is the refractive index increment of the protein. The refractive index increment d_n/d_c is 0.187 cm^3/g for HSA.[51] For other proteins the increment is varying between 0.1-0.2 cm^3/g.[115] The Feijter model was used in data analysis for in-situ ellipsometry before by Burkert et al. who determined the time–depended adsorption behavior of HSA onto polymer brushes.[65] The calculated amount of HSA and prostate specific antigen on the antibodies is shown (Figure 8 a).

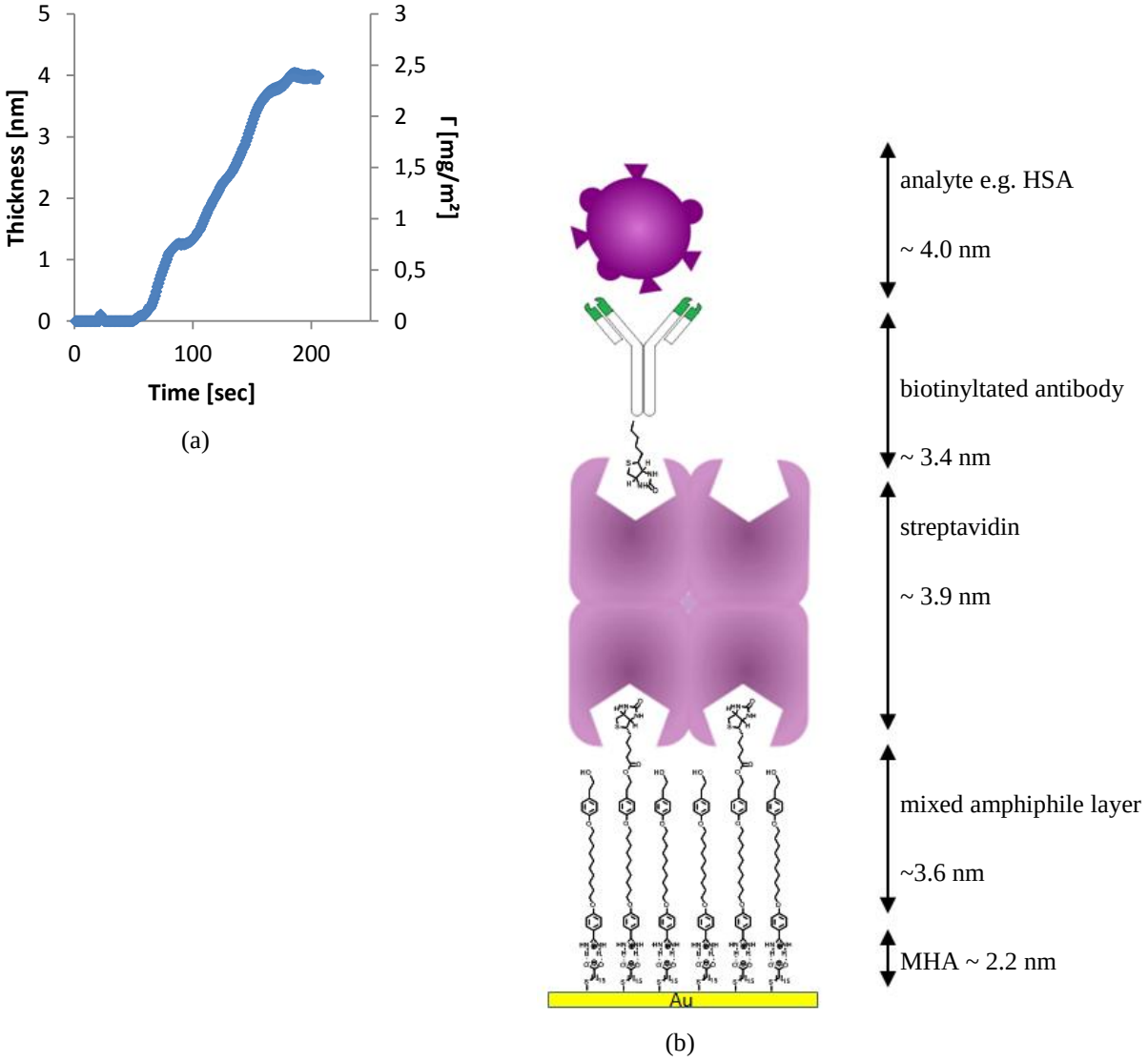

Figure 8 a) Thickness and calculated surface coverage of protein versus time for the assembly of 100 pM HSA on the sensor b) Schematic representation of analyte assembly on biotinylated antibody

For HSA the maximum surface coverage of protein bound to anti-HSA varied between 2.3-2.7 mg/m². The maximum amount Burkert et al. could absorb was 7.2 mg/m² onto a poly(2-vinylpyridine) covered surface. They conclude that these high values can be attributed to a multilayer formation of HSA on the surface.[65] Monolayers on hydrophobic substrates such as methylated silica surfaces, vary between 0.8 and 0.9 mg/m².[116,117] These values can be explained with a flat orientation of the protein on the surface. Arnebrant et al. found coverages between 2.0 mg/m² and 2.3 mg/m² with antibody-based systems for IgG detection.[52] The results for HSA detection show that the lower molecular weight HSA binds with 2.3-2.7 mg/m². To compare these results on different proteins one needs to take

into account that IgG is roughly 17-18 nm in size. [118,119] In conclusion, more HSA is bound in here, since the adsorbed amount of protein is molecular weight and therefore size dependent. Lower concentrations did not yield the estimated film thickness, and therefore did not show an increase in the amount of bound protein (Figure 9). After addition of 1.5 pM HSA we only observed a data fluctuation which was in the error range of the instrument (± 0.1 nm). Unspecific binding of IgG was not observed (Figure 10). We attribute this behavior to the high binding constant for antigens and antibodies (>10^{-8}M).[21]

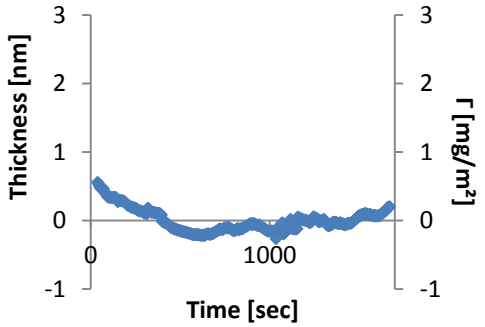

Figure 9: Thickness and surface coverage of 1.5 mM HSA on anti-HSA versus time

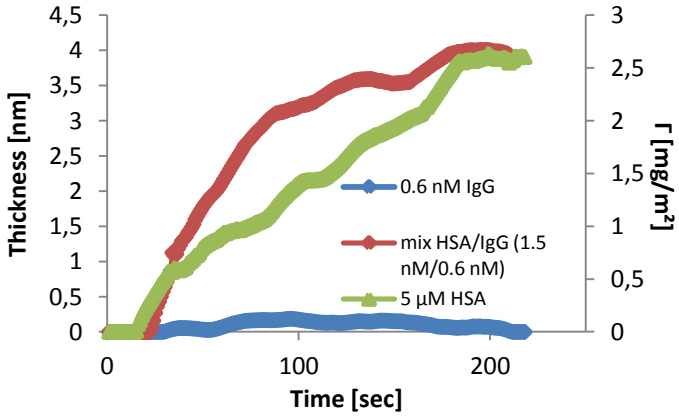

Figure 10: Thickness and surface coverage of HSA, IgG and a mixture of both (mixture 1.5 nM : 0.6 nM) versus time on anti-HSA covered surface

To quantify unspecific binding of HSA on the second film (amphiphile layer) HSA was added to the system (Figure 11). The binding on the hydroxylated amidine film was low, as well as the binding on the pure mercaptohexadecanoic acid (MHA) film and the film with a biotin content of 100% (X_B = 1).

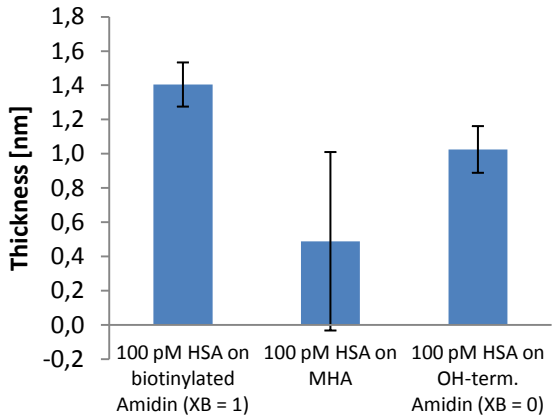

Figure 11: Final film thickness of HSA assembled on the amphiphiles (AT5 and AT3) and the MHA layer

A reconstitution of the multilayer system was achieved by pH dependent washing steps, allowing repeatable multilayer construction and characterization using a single substrate. The directed hydrogen bound of the amidinum-carboxylate interaction is very strong in pH 8-9 and the protonation status of the carboxylic acid can be easily altered by changing to pH 3. A fully reversible biosensor platform was demonstrated (Figure 12).

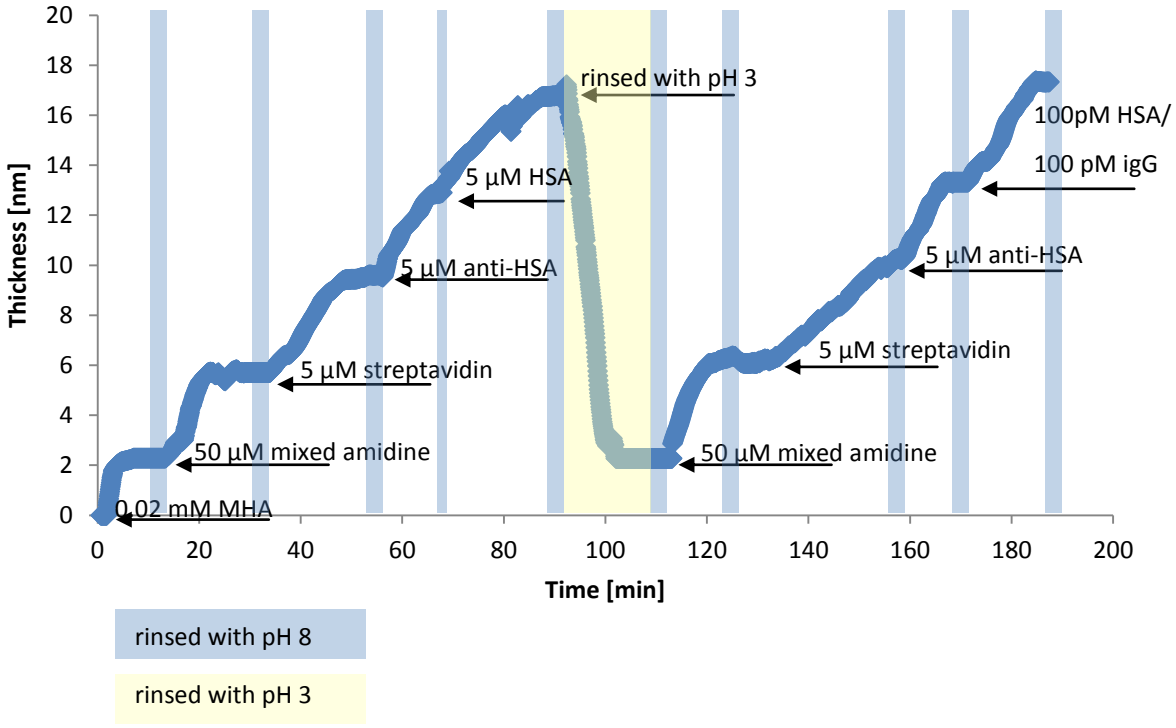

Figure 12: Stepwise assembly of 50 µM mixed biotinylated amidin, 5 µM streptavidin, 5 µM biotinylated anti-HSA and 5 µM HSA; disassembly with pH 3; a second assembly cycle with 50 µM mixed biotinylated amidin, 5 µM streptavidin, 5 µM biotinylated anti-HSA and mixed HSA/igG 100 pM/100 pM on MHA

The system for PSA - detection was prepared identically as the system for HSA detection despite the specific recognition layer. In brief, MHA, the amphiphiles (biotin content: X_B = 0.1) and streptavidin were assembled, followed by adding the biotinylated anti-PSA with a concentration of 5 µM. The PSA was tested for its limit of detection. The sensor could detect PSA from buffer media down to a concentration of 40 fM. In order to correlate the monolayer size of the antigen with the time until monolayer size has reached, even with very low concentrations, we focused on the absorption rate measurement (Figure 13-Figure 14). Figure 13 shows the assembly kinetics of PSA on anti-PSA with respect to PSA concentration. The amount of bound protein can be estimated from this graph. The maximum surface coverage achieved for PSA from buffer media is 2.4 mg/m² ± 0.1 mg/m². The dissociation constant for anti-PSA/PSA is $>10^{-9}$M.[68]

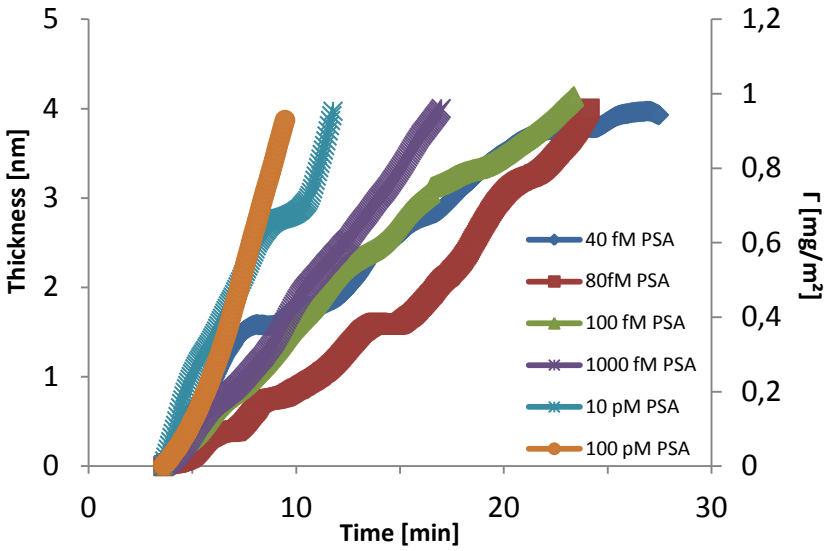

Figure 13: Assembly kinetics for different concentrations of PSA on anti-PSA

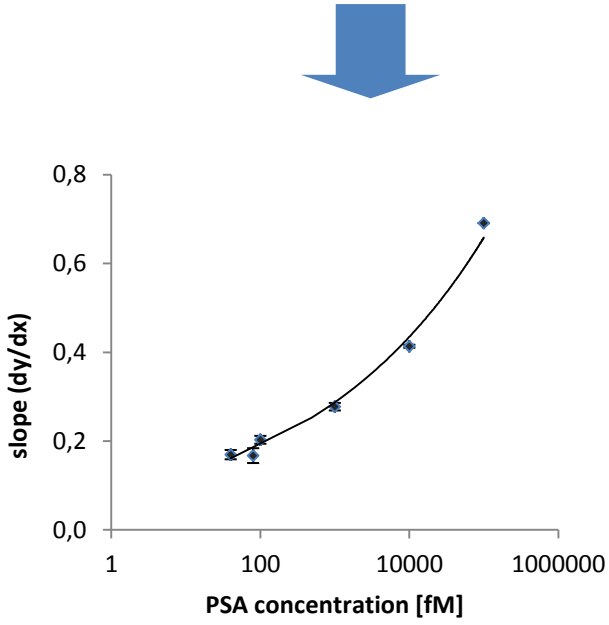

Figure 14: Correlation of the slope (dy/dx) of the antigen adsorption and the concentrations

To test the selectivity of the sensor containing anti-PSA, the non-target protein HSA was added to the system. Here we could only observe low unspecific binding (~ 1 mg/m²) on the PSA antibody (Figure 15).

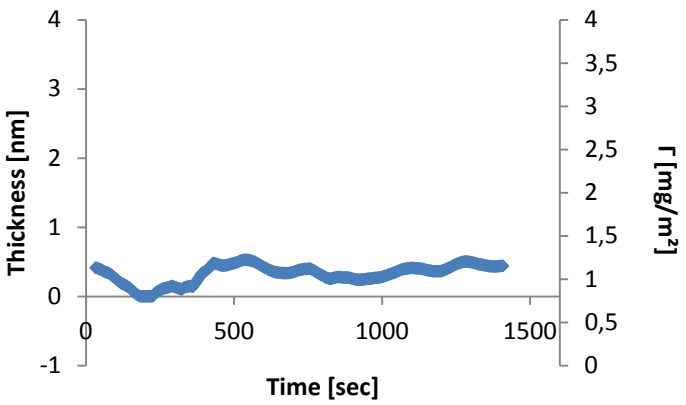

Figure 15: Adsorbtion kinetic (amount and thickness) of 1.5 nM HSA on anti-PSA

The PSA biosensor was also tested for reversibility. Therefore layers were subsequently assembled. Then the solution in the ellipsometer cuvette was acidified to pH 3 with 0.1 M HCl. After acidification, the cuvette was basified to pH 8, with 0.1 M NaOH. However, when acidifying the cuvette to pH 3, the layer thickness decreased to the value measured for the bare carboxylated surface. When the pH was basified again, the layer size returned to its original thickness for the biosensor architecture. In Figure 16 the assembly-disassembly test is displayed. Sellergren et al. observed the same phenomena of reversible layer formation upon cyclic pH change when they attached phosphate biomolecules on a pentamidine-carboxylate-layer. The disassembly-reassembly occurred when they cycled the pH between 8,7 and 3.[113]

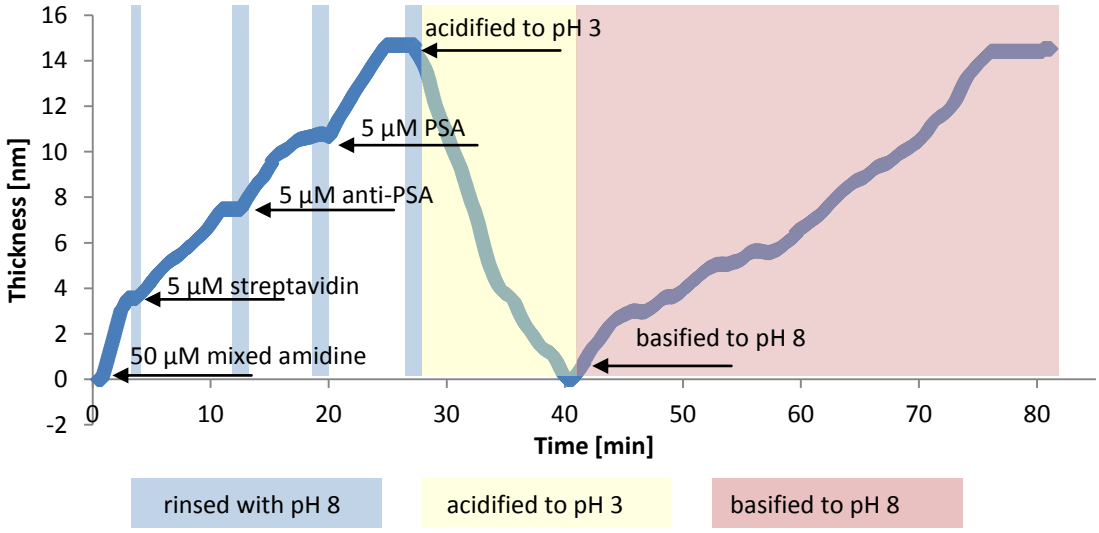

Figure 16: Stepwise assembly of 50 µM mixed biotinylated amidine, 5 µM streptavidin, 5 µM biotinylated anti-PSA and 5 µM PSA, disassembly with pH 3, reassembly with pH 8; the thickness of the MHA layer has been defined as zero

To test the detection in real samples, the multilayer architecture was assembled as explained previously. The human serum samples (commercial available AB plasma) were prepared as follows. The human serum was filtered with a 0.45 µm syringe filter, diluted with HEPES buffer (10 mM, pH 8) 200 times before loaded with different concentrations of PSA. The concentrations to test sensor response were 100 fM to 10 nM.

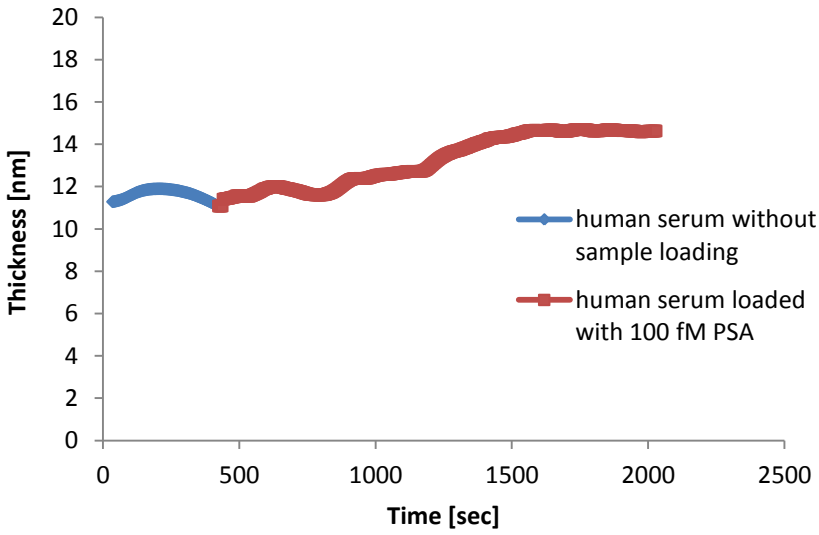

Figure 17: Assembly kinetic of PSA to anti-PSA in human serum. Addition of human serum to anti-PSA, with and without PSA loading. Thickness of ~11 nm before injection of PSA indicates a multilayer architecture consisting of MHA, mixed amphiphiles (X_B = 0.1), streptavidin and anti-PSA

3.2.2 IRRAS of biotinylated amphiphiles

To confirm the results received with in-situ ellipsometry, the spectroscopic behavior of the samples was tested. The monolayers were examined by infrared reflection adsorption spectroscopy (IRRAS). The monolayer- and the transmission-spectra were recorded at 4 cm^{-1} resolution in the reflection mode gathering 2000 scans. The reflection adsorption was measured at high angles of incidence (θ_1 = 80°) to achieve maximal intensity. The molecule absorbs the energy necessary to excite the molecular vibration; therefore the reflected absorption spectra are specific for their structure and the orientation of the vibrating molecular moiety.

The crystalline like structure of the mercaptohexadecanoic acid film was confirmed by the presence of the $v_a(CH_2)$ mode at 2918 cm^{-1} (asymmetric stretching). The $v_s(CH_2)$ mode peak we could find at 2850 cm^{-1} (symmetric stretching (Figure 18)). These peaks correspond to the crystalline polymethylene chain of the compound. Higher peak positions at $v_a(CH_2)$ 2928 cm^{-1} and $v_s(CH_2)$ 2856 cm^{-1} would indicate a liquid like nature of the molecules e.g. for compounds with shorter mesogen length.[4,94] The substrates were prepared as described in the chapter about in-situ ellipsometry. After the substrate was immersed in 0.02 mM MHA overnight it was rinsed with absolute ethanol extensively and dried under a nitrogen flow, respectively.

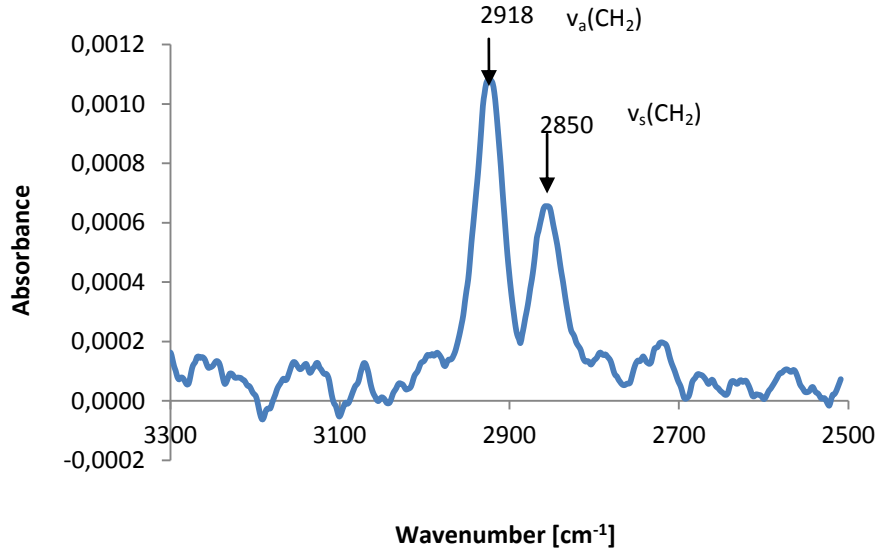

Figure 18: IRRAS spectrum of the high frequency region of the CH_2-symetric and asymmetric stretch vibrations of the mercaptohexadecanoic acid

Wöll et al. found, if MHA SAMs were prepared in these very low concentrations (0.02 mM), it is possible to generate the deprotonated form of the carboxylic acid.[38] The low frequency region of the mercaptohexadecanoic acid spectra shows the presence of the carboxylate head group on the substrate (Figure 19). The peak at 1461 cm^{-1} corresponds to the deprotonated form of carboxylic acid (COO^-). The peak at 1412 cm^{-1} corresponds to ω-CH_2 def. mode of the molecules. Interestingly, a strong peak is observed at ~1700 cm^{-1}. Here, the carbonyl groups form cyclic dimers with each other.

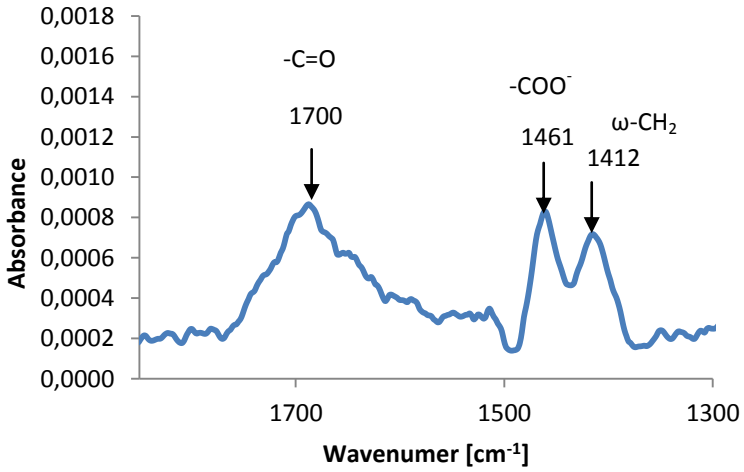

Figure 19: IRRAS spectrum of the low frequency region of mercaptohexadecanoic acid

After the IRRAS data confirmed the well-ordered orientation of the MHA SAM, the next layer, the amphiphile, was assembled, respectively. After immersion in amphiphile solution (50 µM in borate buffer pH 9) for more than 1h, the substrates were rinsed with buffer and dried with nitrogen flow. To compare peaks of the assembled amphiphile layer, transmission spectra were recorded from the biotinylated amidine (**AT5**) and the OH-terminated amidine (**AT3**).

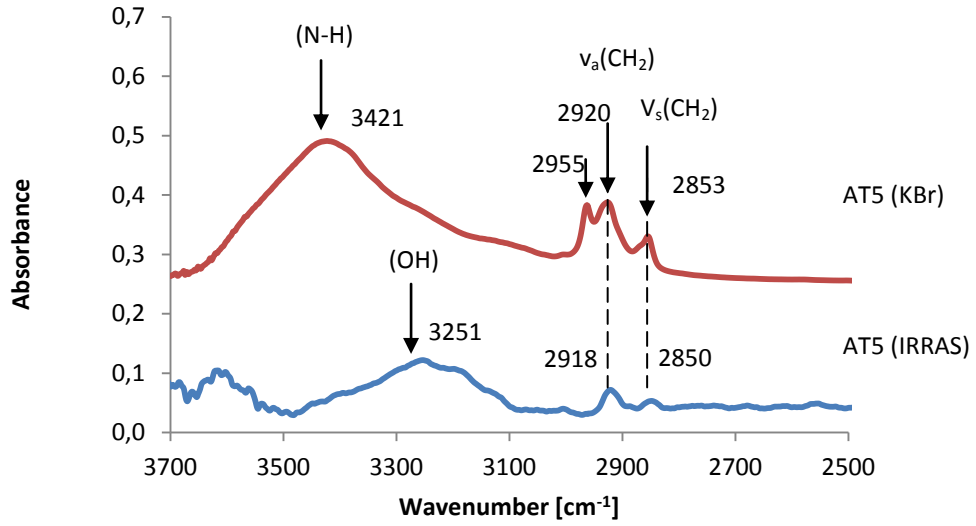

Figure 20: IRRAS (blue) and FTIR (red) spectra of the high frequency region of the biotinylated amidine AT5

The high frequency region of the reflection and the transmission spectra of the biotinylated compound are compared in Figure 20. The -CH_2 asymmetric stretch vibration, found at 2918 cm^{-1} for the compound, self-assembled on MHA, is an indication for the high crystallinity and order of the amphiphile layer.[38] In the transmission spectra (FTIR), this band can be observed at 2920 cm^{-1}. However, the shift of +2 cm^{-1} for the asymmetric stretch vibration in the transmission spectrum suggests a higher disorder of the compound dispersed in the KBr pellet. The same observation is made for the symmetric stretch bond, which shifted +3 cm^{-1}. The peaks were found at 2850 cm^{-1} for the IRRAS and at 2853 cm^{-1} for the FTIR transmission spectrum. The broad IRRAS band between 3100 cm^{-1} and 3500 cm^{-1} indicates hydrogen bond formation of the amidine tail group with the carboxylic acid.[120] The FTIR peak at 2955 cm^{-1} can be attributed to the asymmetric -CH_2 stretch of the amidine.[121]

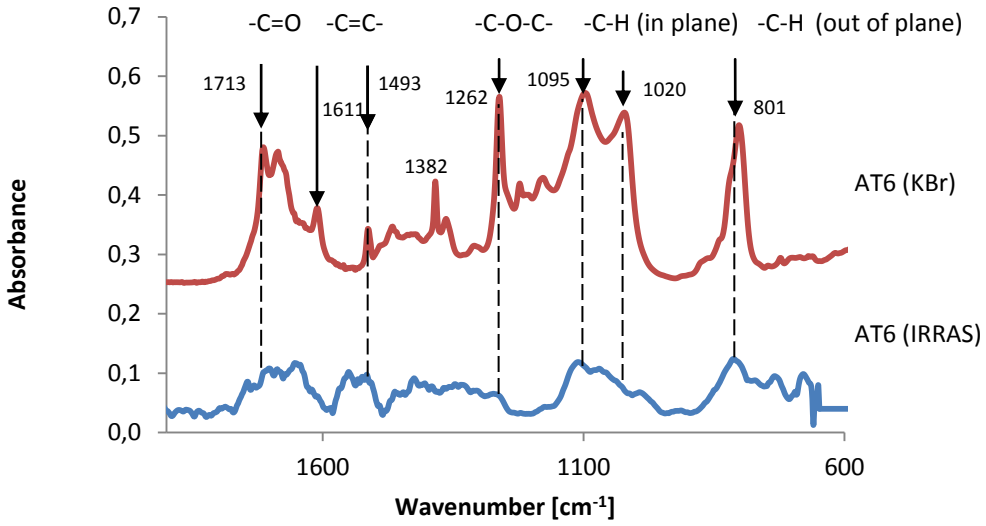

Figure 21: IRRAS and FTIR spectra of the low frequency region of the biotinylated amidine AT5

The low frequency region of the biotinylated amphiphile can be found in Figure 21. We first assign the FTIR signals. The peaks found at 1713 cm^{-1} can be assigned to the carbonyl group of the amphiphile. The peaks at 1611 cm^{-1} and 1493 cm^{-1} were assigned to the C=C stretching modes of the benzene ring of the amidine. The peak at 1262 cm^{-1} can be attributed to the C-O-C mode of the compound. The in-plane bending of the of the -C-H group was found between 1020 cm^{-1} – 1095 cm^{-1}. The out-of-plane bending of the -C-H group was found at 801 cm^{-1}. The IRRAS spectrum shows the presence of all functional groups found in the FTIR data of the pure compound.

The hydroxylated amidine AT3 was also compared in FTIR transmission spectroscopy and IRRAS. The high frequency region is depicted in Figure 22.

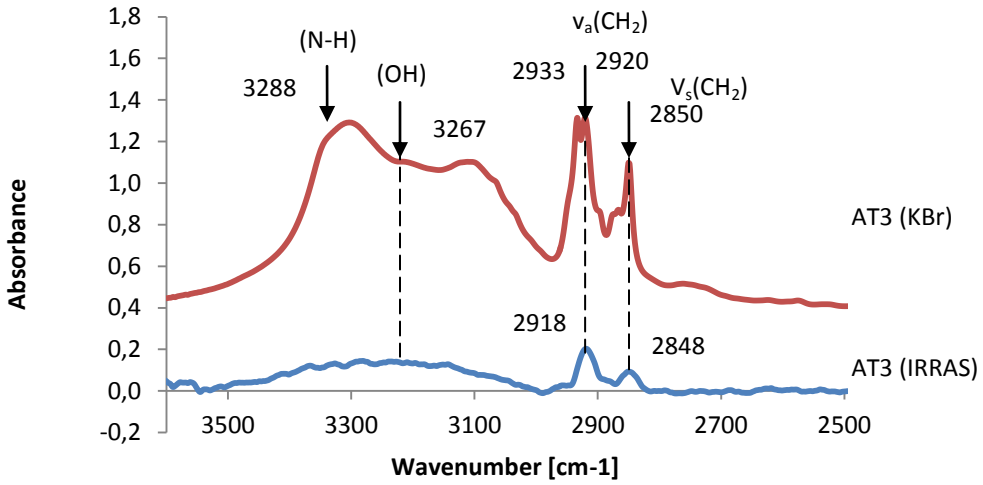

Figure 22: IRRAS and FTIR spectra of the high frequency region of the hydroxylated amidine AT3

The high frequency region of the reflection and the transmission spectra of the hydroxylated compound are compared (Fig.22). The symmetric and asymmetric stretch bonds of -CH_2 were found at 2850 cm^{-1} and 2920 cm^{-1} in the FTIR spectra. In comparison to the symmetric and asymmetric stretch bond of -CH_2 in the IRRAS, the peaks shifted by 2 cm^{-1} to lower wave numbers. This indicates a high ordered amphiphile layer on the MHA. The broad IRRAS band between 3100 cm^{-1} and 3500 cm^{-1} indicates hydrogen bond formation of the amidine tail group with the carboxylic acid.[120] The peaks at 2933 cm^{-1} were attributed to the asymmetric -CH_2 stretch of the amidine.[121]

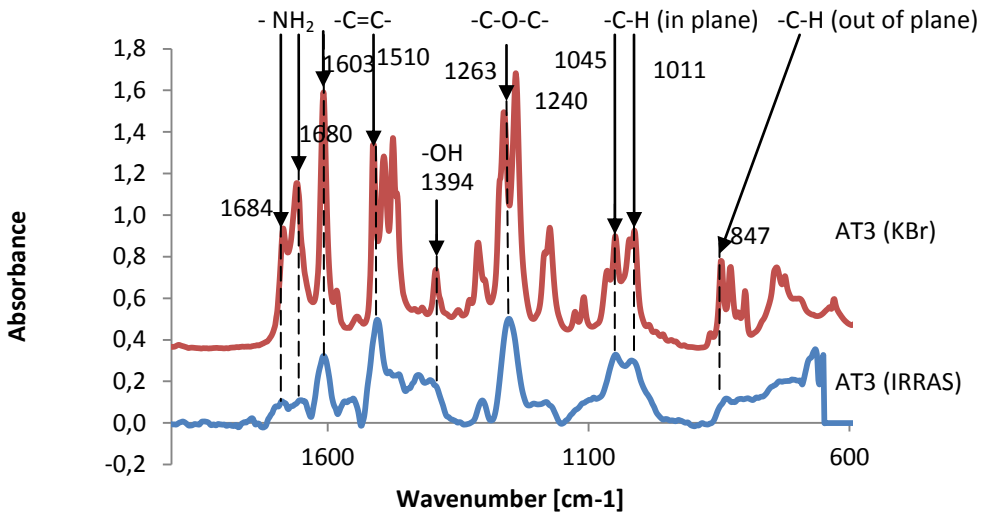

Figure 23: IRRAS and FTIR spectra of the low frequency region of the hydroxylated amidine AT3

The low frequency region of the spectra in Figure 23 compares the IRRAS and the FTIR of compound AT3. The functional groups found in the different spectra are in good agreement with each other. The -NH_2 band at 1684 cm^{-1} and 1680 cm^{-1} were found in both spectra and belong to the amidine function in the compound. The peaks at 1603 cm^{-1} and 1510 cm^{-1} were assigned to the C=C stretching modes of the benzene ring of the amidine. The peak found at 1263 cm^{-1} are attributed to the C-O-C mode of the compound. The in-plane bending of the of the -C-H group was found at 1011 cm^{-1} – 1045 cm^{-1}. The out-of-plane bending of the -C-H group was found at 847 cm^{-1}. The IRRAS spectrum shows the presence of all functional groups found in the FTIR transmission spectra of the pure compound.

The IRRAS spectrum of the mixed amphiphile layer with a biotin content of $X_B = 0.1$ is shown in Figure 24. It contains signals of all functional groups, typical for the hydroxylated amphiphile AT3 and the biotinylated amphiphile AT5. Due to high percentage of hydroxyl functionalized amidine in the mixture (90%), the IR spectrum is very similar to the spectrum of the pure hydroxyl terminated amidine on the surface. The most important functional group is the hydroxyl group, which is present at 3383 cm^{-1}. This peak can be assigned to the -OH stretch mode. The peaks at 2919 cm^{-1} and 2851 cm^{-1} can be assigned to the asymmetric and symmetric stretch mode of the -CH_2 group. These peaks

show once more a crystalline like nature of the film. The peak at 1668 cm^{-1} can be assigned to the NH_2 group of the amidine. The peak at 1601 cm^{-1} and 1456 cm^{-1} was assigned to the C=C stretching mode of the benzene ring of the amidine. The peak found at 1255 cm^{-1} was attributed to the C-O-C mode of the compound. The in-plane bending of the of the -C-H group were found at 1097 cm^{-1}. The out-of-plane bending of the -C-H group were found at 843 cm^{-1}.

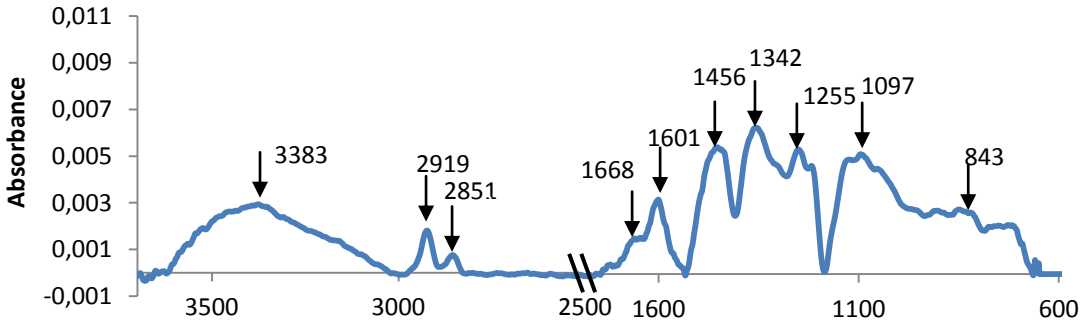

Figure 24: IRRAS spectrum of the mixed amphiphile layer, with a biotin content of X_B = 0.1

Since it was found from *in-situ* ellipsometry that a biotin content of X_B = 0.1 yield in optimal Streptavidin packing, this film was examined with IRRAS. The according spectrum is shown in Figure 25.

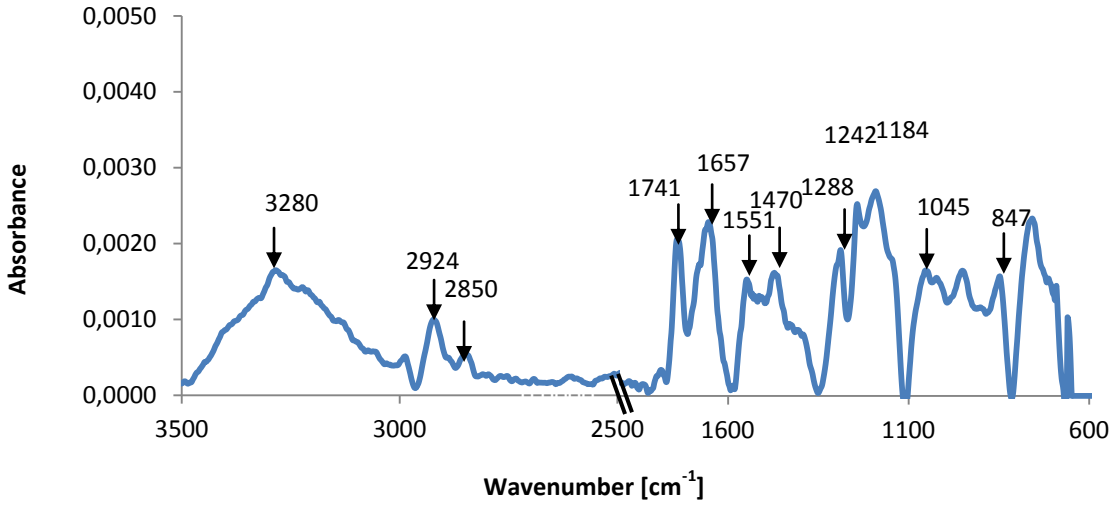

Figure 25: IRRAS spectrum of the streptavidin film assembled on a mixed amphiphile film with a biotin content of $X_B = 0.1$

After the first two layers were assembled on the gold substrate, the sample was immersed in 50 µM streptavidin (STV) solution (pH 8, borate buffer) for more than 1h, rinsed with buffer and dried under nitrogen flow. Apart from the typical functional groups, which were discussed extensively on the above spectra, three new bands appeared when STV was added; the peaks at ~1741 cm^{-1}, ~ 1657 cm^{-1} and ~1551 cm^{-1}. The peaks at ~1657 cm^{-1} and ~1551 cm^{-1} can be assigned to the amide I and amide II vibration of the STV.[55,56] The peak at 1741 cm^{-1} can be assigned to the C=O stretching mode of the carbonyl functional group.[55,56]

The amide I and II bands of the streptavidin were examined closer. The absorption intensities were plotted as a function of the mole fraction X_B of the biotinylated amidine to the OH terminated amidine in the adsorption solution. It can be observed that a biotin content of $X_B = 0.1$ yields in the highest intensity of the amide I and amide II band. This result is in good agreement with the *in-situ* ellipsometry results.

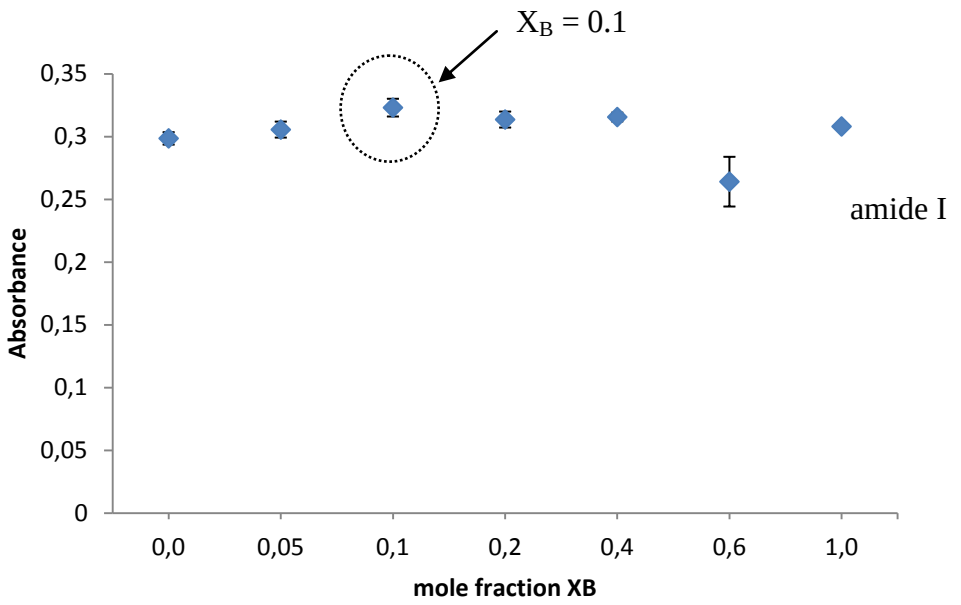

Figure 26: Absorption peak height of the amide I band of streptavidin as a function of the mole fraction X_B of biotinylated amidine to -OH terminated amidine in the adsorption solution

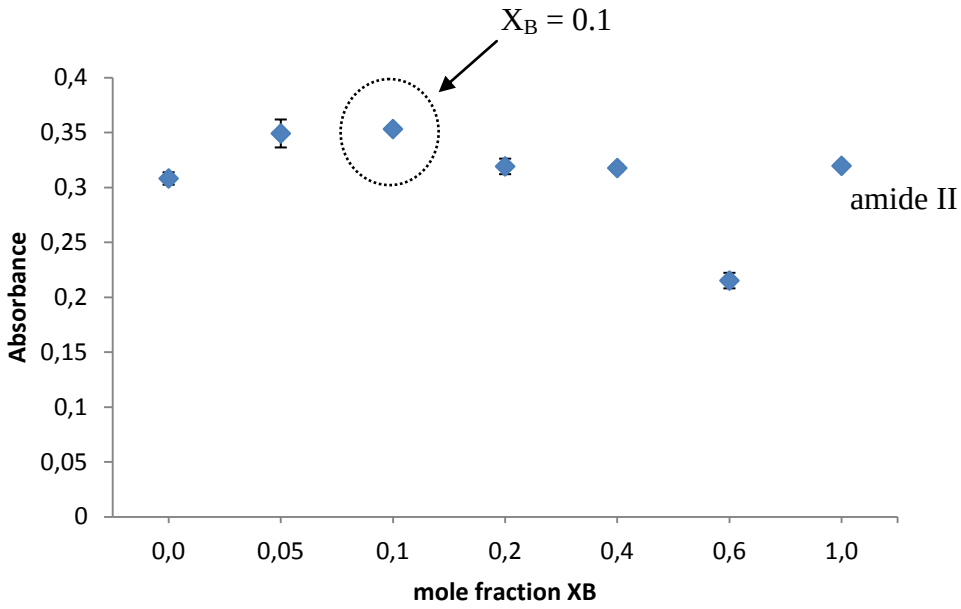

Figure 27: Absorption peak height of the amide II band of streptavidin as a function of the mole fraction X_B of biotinylated amidine to -OH terminated amidine in the adsorption solution

The next assembled layer, was the layer with biotinylated antibody. The substrate was incubated in 50 µM anti-HSA or 50 µM anti-PSA solution (pH 8, borate buffer) for more than 1h, before it was rinsed with buffer and dried under nitrogen flow. Subsequently, the substrate was examined with IRRAS. The spectra are depicted in Figure 28.

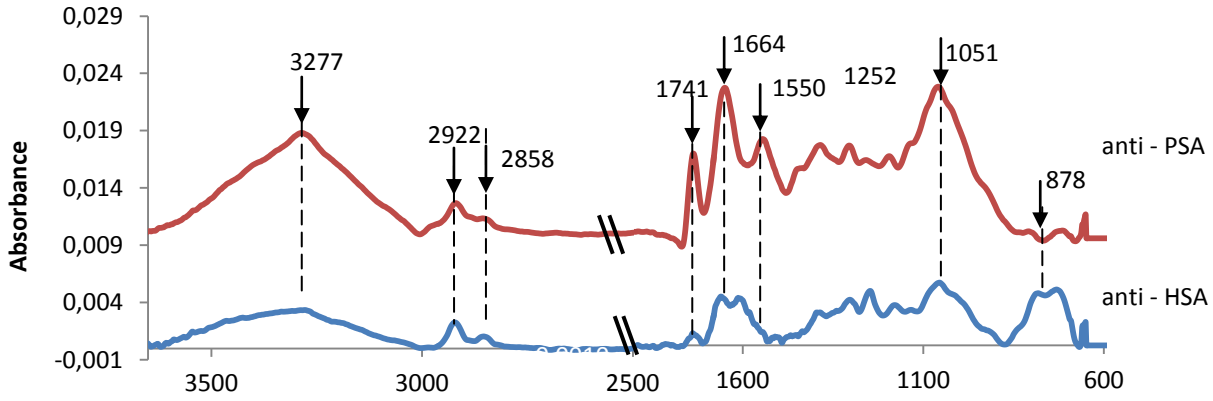

Figure 28: IRRAS spectra of anti-HSA and anti-PSA assembled on STV

In the IRRAS of anti-HSA and the anti-PSA, which were subsequently assembled on streptavidin, mixed amphiphile and MHA, the functional amide bonds, which are characteristic for proteins, could be identified in the low frequency region. The amide I band was assigned to the 1664 cm^{-1} peak, whereas the amide II band could be assigned to the 1550 cm^{-1} peak. The amide II band in the anti-HSA spectra was very weak. The carbonyl band was observed at 1741 cm^{-1}. Those bands are characteristic for anti-HSA and anti-PSA.[111]

Subsequently, the analytes were assembled on the biosensor multilayer structure to test the functionality. After incubation in analyte solution for >1h, the substrates were rinsed with borate buffer (pH 8) and dried under nitrogen flow. These films were examined with IRRAS as well. The IRRAS spectrum of the analyte HSA, which was assembled on anti-HSA, is shown in Figure 29. The peak at 1726 cm^{-1} can be assigned to the C=O stretching mode of the carbonyl functional group. The peaks at 1660 cm^{-1} and 1599 cm^{-1} can be assigned to the amide I and amide II band. The peak found at 1248 cm^{-1} were attributed to the C-O-C mode. The in-plane bending of the -C-H group was found at 1053 cm^{-1}. The out-of-plane bending of the -C-H group was found at 800 cm^{-1}.

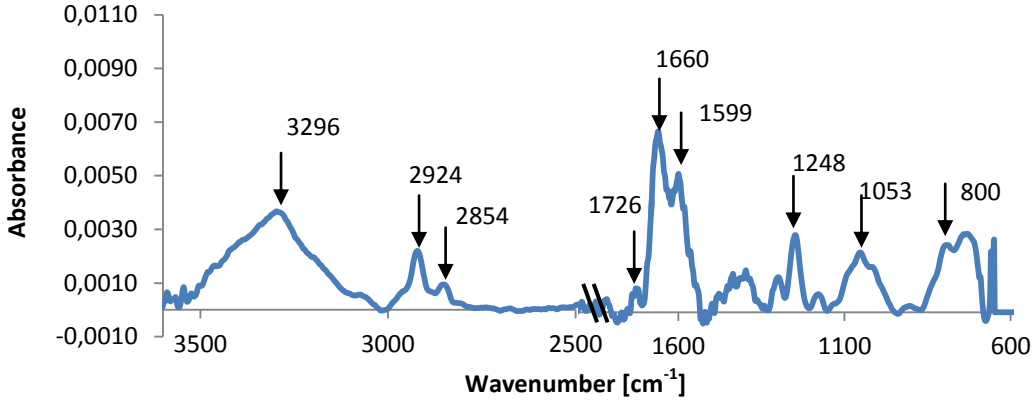

Figure 29: IRRAS spectra of HSA on anti-HSA

The analyte PSA, which was subsequently assembled on anti-PSA, was examined with IRRAS (Figure 30). All bands which are characteristic for proteins, e.g. the amide I and amide II band, were found. Those two bands were found at 1657 cm^{-1} and 1550 cm^{-1} in the low frequency region of the spectrum in Figure 30. The carbonyl peak was found at 1740 cm^{-1}. The peak at 1248 cm^{-1} can be attributed to the C-O-C mode. The in-plane bending of the of the -C-H group was found at 1053 cm^{-1}. The out-of-plane bending of the -C-H group was found at 800 cm^{-1}. The high frequency region of the spectrum shows the OH band at 3296 cm^{-1} and the symmetric and asymmetric -CH_2 bands. Those could be found at 2854 cm^{-1} and 2924 cm^{-1}.

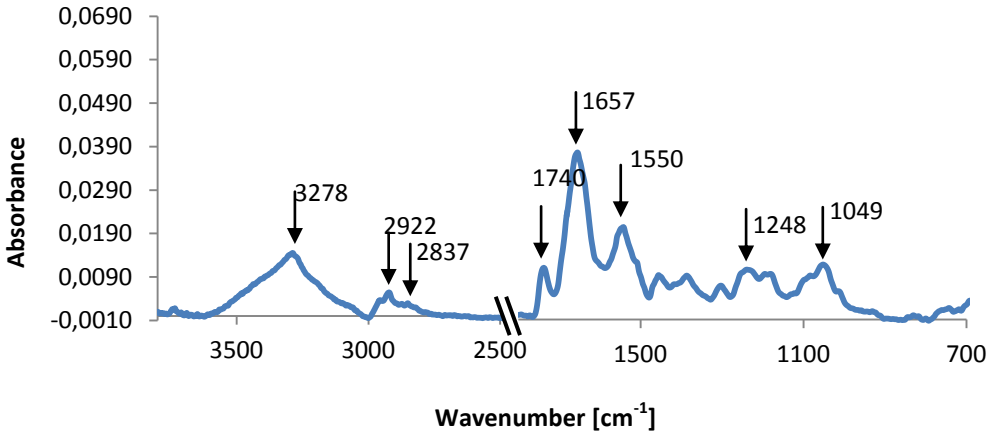

Figure 30: IRRAS spectrum of PSA on anti-PSA

3.2.3 Contact angle investigation of biotinylated amphiphiles

Contact angle measurements with water droplets were used to investigate the hydrophobicity/hydrophilicity of the modified surface. Contact angles lower than 90° indicate a hydrophilic surface. On the other hand, contact angles of more than 90° indicate a hydrophobic surface. Subsequently, the substrates were prepared from 0.02 mM mercaptohexadecanoic acid (MHA) in ethanol immersed in pH 3 for 1h before measuring the angle. This incubation leads to a highly hydrophilic surface with an angle of 23 ± 4°, due to the protonated carboxylated groups on the surface.[94] The relatively low contact angle of the 1:9 biotin- to OH- terminated amphiphile mixed SAMs (X_B = 0.1) was due to the different mesogen lengths of the molecules and the polar behavior of the biotin head group. HSA protein adsorption leads to higher contact angles 65±1° (Figure 31). This contact angle was consisted with Krishnans et al. who also tested HSA adsorption on hydrophilic surfaces (e.g. MHA).[122] The hydrophobic behavior of this protein can be attributed to the hydrophobic interactions and the low polarity of the protein. The lower contact angle for prostate specific antigen indicates that it was less hydrophobic than human serum albumin. Washing the surface with pH 3 disturbed the ionic interaction between the amidin and the carboxylic acid. The same contact angle was observed as MHA only on the surface. This shows the full reversibility of the adsorption on the surface.

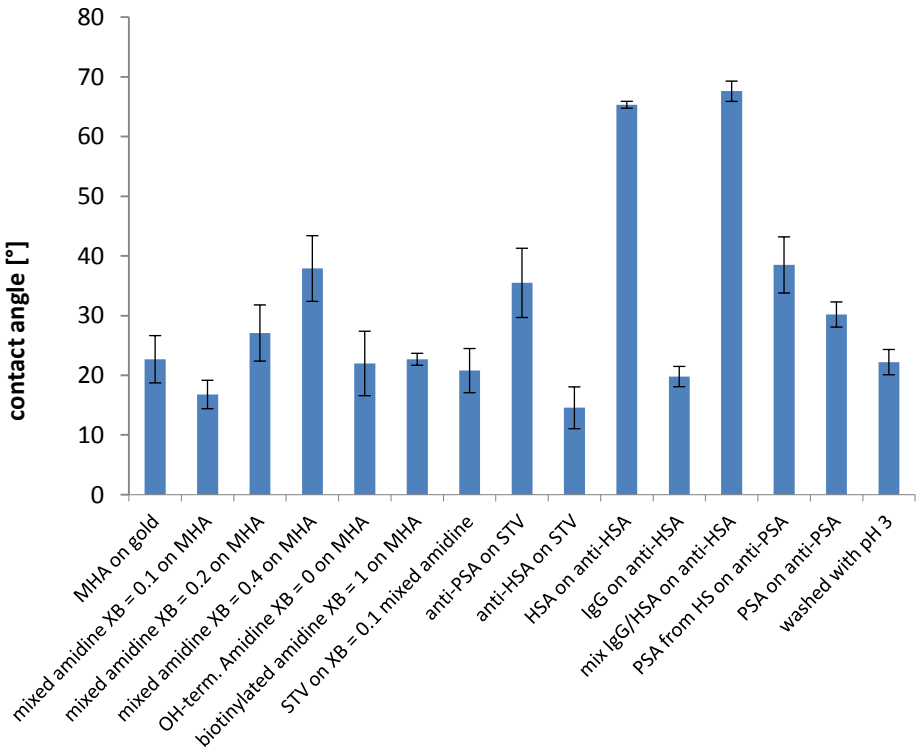

Figure 31: Contact angles of water drops on the system containing biotinylated amphiphile

3.2.4 AFM of biotinylated amphiphiles

To study the two-dimensional structure of the self-assembled monolayers we used Atomic Force Microscopy (AFM). In cooperation with Ulrich Maggraf from ISAS Dortmund, the MICA substrates were coated with ~200 nm gold. Those freshly prepared substrates were immersed in 0.02 mM ethanolic MHA over night, and dried under nitrogen flow. Subsequently, the substrates were coated with the multilayer structures, rinsed with buffer, and dried again under nitrogen flow. The AFM images were taken in dynamic contact mode (tapping mode) at room temperature. First the substrates with pure gold and MHA were examined. AFM images of alkanethiols were studied extensively by Nelles et al. in 1998.[100] They found that alkanethiols and disulfides can form two dimensional crystalline structures on gold. In an AFM image (Figure 32) they show the crystalline domain of bis-[2-(dodecayoyloxy)ethyl] disulfide taken in ethanol. The image shows a centered rectangular lattice of the SAM. It was found here that self-assembled monolayers of mercaptohexydecanoic acid can also form these structures.

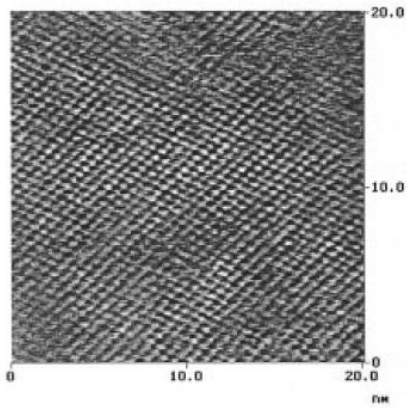

Figure 32: AFM image of the crystalline domain of bis-[2-(dodecayoyloxy)ethyl]disulfide in ethanol, measured by Nelles et al.[100]

The AFM images were recorded with the help of Dr. Franzka from the University of Essen and Nico Zammarelli from Technische Universität Dortmund. The AFM images of the pure gold are displayed in Figure 33. The height of the peaks (lines called (1) in Figure 33 a, Figure 35 a and Figure 37) were analyzed with the program ImageJ of the National Institute of Health (USA).

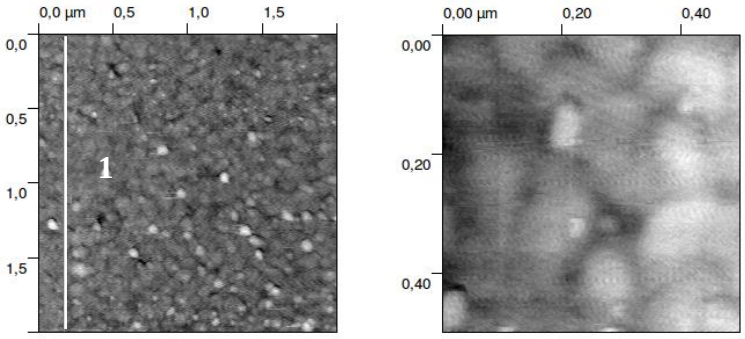

(a) (b)

Figure 33: AFM image of a surface section of 2 µm x 2 µm (a) and 500 nm x 500 nm (b) of pure gold on mica

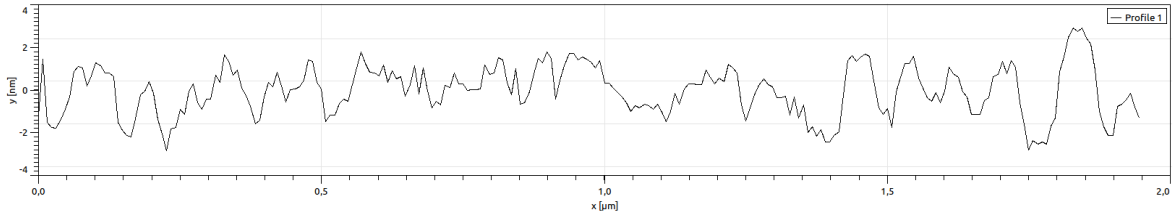

Figure 34: Roughness of the pure gold surface detected by AFM. Roughness is about 1-4 nm. No.1 in Figure 33

First we examined the bare gold substrates (Figure 33). In a review from Love et al. it is pointed out that gold formation on glass or mica is substantially depending on the deposition method.[13] Love et al. write that metal films deposited with electron sputtering, tend to form islands of gold. This behavior we also observe in our AFM images Figure 33 a and b.

Comparing the bare gold slide with the mercaptohexadecanoic acid (MHA) functionalized slides, we can observe the gold island formation (Figure 33 b and Figure 35 b) but also slightly different topographies (Figure 34 and 36). The roughness of the pure gold slide shows values of 1-4 nm (Figure 34), whereas the roughness of the MHA functionalized slide varies between 1-2 nm (Figure 36). This might be attributed the effect that alkanethiols form very dense packed, ordered layers on gold with only a view defects.[5]

The AFM image of MHA is shown in Figure 35. These images do not show crystalline order as observed in Nelles et al's work. The main reason for not showing a crystalline structure could be the preparation method for the gold coated mica substrates. Our substrates were coated via electron sputtering as explained before. The substrates from Nelles and Buriak were prepared via vapor deposition and subsequently the gold was

annealed. In the annealing step the gold substrate is heated to 400°C for 1 min and quenched in methanol to generate ultra smooth surfaces.[100,123] Only when the substrates are that smooth, it is possible to observe crystalline ordered structures. Another reason, next to the gold preparation can be the environment in which we measured. The group of Nelles and Buriak measured in a liquid environment. Our investigations were carried out in air. This has a big influence on the contrast in the AFM measurements.[99]

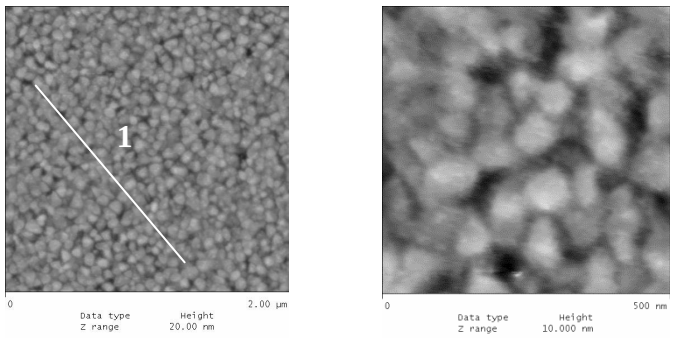

(a) (b)

Figure 35: AFM image of a surface section of 2 µm x 2 µm (a) and 500 nm x 500 nm (b) of MHA on gold/mica

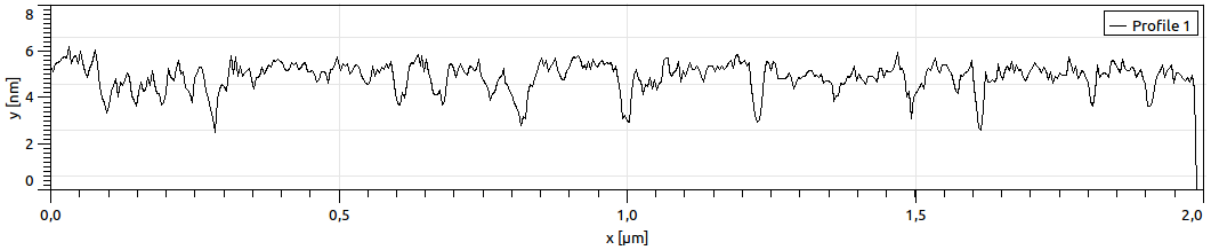

Figure 36: Roughness of the MHA-coated surface detected by AFM. Roughness is about 1-2 nm. No.1 in Figure 35

However, in a second experiment the amphiphile layer was assembled on the MHA coated substrate. Subsequently, the substrate was immersed in amphiphile solution (X_B = 0.1) over night, rinsed with pH 9 buffer and dried under nitrogen flow. The AFM image is depicted in Figure 37. The section analysis of the second film is shown in Figure 38.

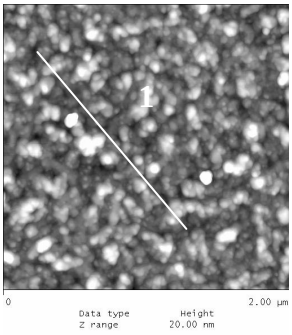

Figure 37: AFM image of surface section of 2 µm x 2 µm of a mixed amphiphile on Au/mica

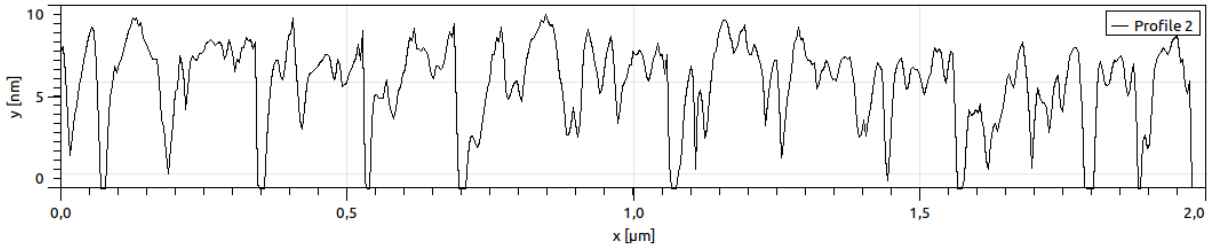

Figure 38: Roughness analysis of the mixed amphiphile film. No 1 in Figure 37

The roughness analysis shows the topography of the 1/9 biotinylated/OH-terminated amidine covered surface. Peaks between 2 nm and 10 nm were found. The peaks indicate the presence of amphiphile on the MHA coated substrate. The film thickness obtained via *in-situ* ellipsometry shows values of 3.9 ± 0.1 nm for the mixed amphiphile film. The size of MHA has to be taken into account. The size of MHA plus amphiphile is ~ 6.1 ± 0.2 nm. Higher peaks indicated multilayer formation. The next assembled layer was the streptavidin-layer. The substrate was immersed in 50 µM STV solutions overnight, before rinsed with buffer and dried under nitrogen flow (Figure 39).

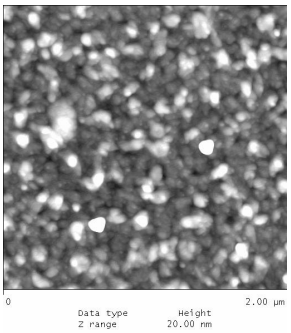

Figure 39: AFM image of surface section 2 µm x 2 µm of streptavidin on Au/mica

Figure 39 does not show any difference to the AFM image of the amidine layer (Figure 37). The topography of the AFM images several steps from STV binding to analyte binding show also very similar structures (Figure 39 to Figure 41). The layer with anti-HSA was prepared the same way as described above. The substrate was examined with AFM (Figure 40). The layer, containing the analyte HSA is shown in Figure 41. The substrate was prepared using 5 µM HSA solution.

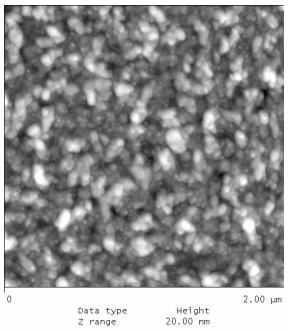

Figure 40: AFM image of surface section 2 µm x 2 µm of anti-HSA on Au/mica

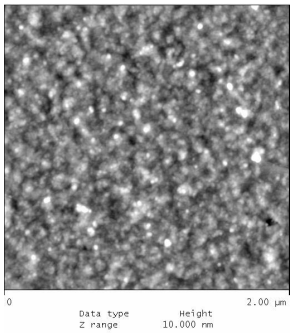

Figure 41: AFM image of surface section 2 µm x 2 µm of HSA on Au/mica

In conclusion, crystalline order of the MHA layers could not be observed. It was also not possible to gain information about the two-dimensional structure of the MHA film. Films at all assembly stages (amphiphile layer to analyte layer) showed very similar structures.

We removed the assembled layers by rinsing the samples with HEPES buffer at different pH. First the biosensor consisting of MHA, mixed amphiphile (X_B = 0.1), streptavidin, anti-HSA and HSA was rinsed with copious amounts of HEPES buffer (10 mM) at pH 7. The topography of the surface treated with buffer at pH 7 shows a “sponge-like” structure.

If higher cantilever force was used, the surface collapsed (Figure 42 (C)). This was an indication that the carboxylate amidinium bond was broken on some parts of the sample.

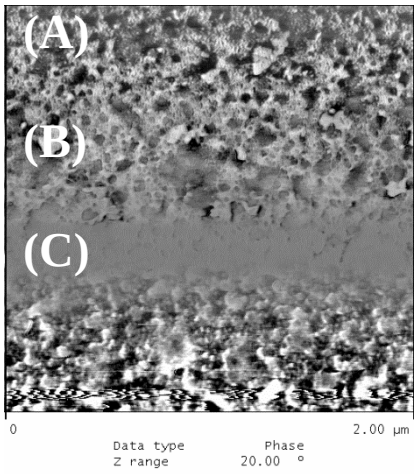

Figure 42: AFM image of a surface section of 2 µm x 2 µm of the multilayers on Au/mica surface after treatment with a buffer at pH 7 (A) low cantilever force (ca. 1 nN), (B) middle force (ca. 5 nN) (C) for the high force (ca. 10 nN)

Decreasing the buffer's pH to 3 resulted in topographies similar to the ones found where only MHA had been assembled. This indicated a full remove of the multilayer biosensor structure and a reusable, pH switchable system. In Figure 43 the AFM image of the pH 3-buffer treated surfaces is shown.

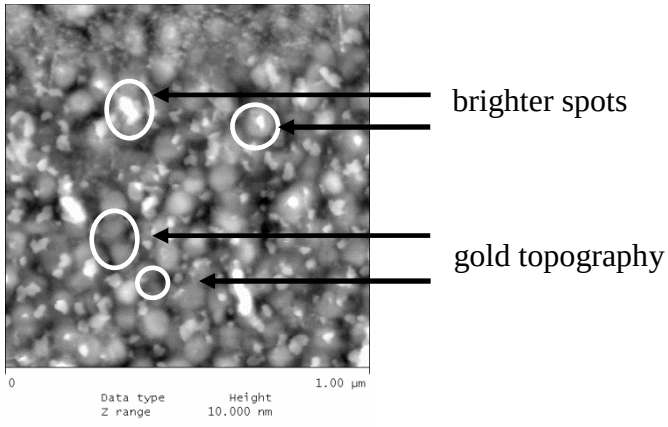

Figure 43: AFM image of a surface section 2 µm x 2 µm of the multilayers on Au/mica after a treatment with a buffer at pH 3

The image shows some brighter spots, which can be identified as precipitation of salt on the surface.[124]

With AFM measurement we could proof that the assembly of the multilayers is reversible via pH change. The assembly-disassembly cycle is shown in Figure 44.

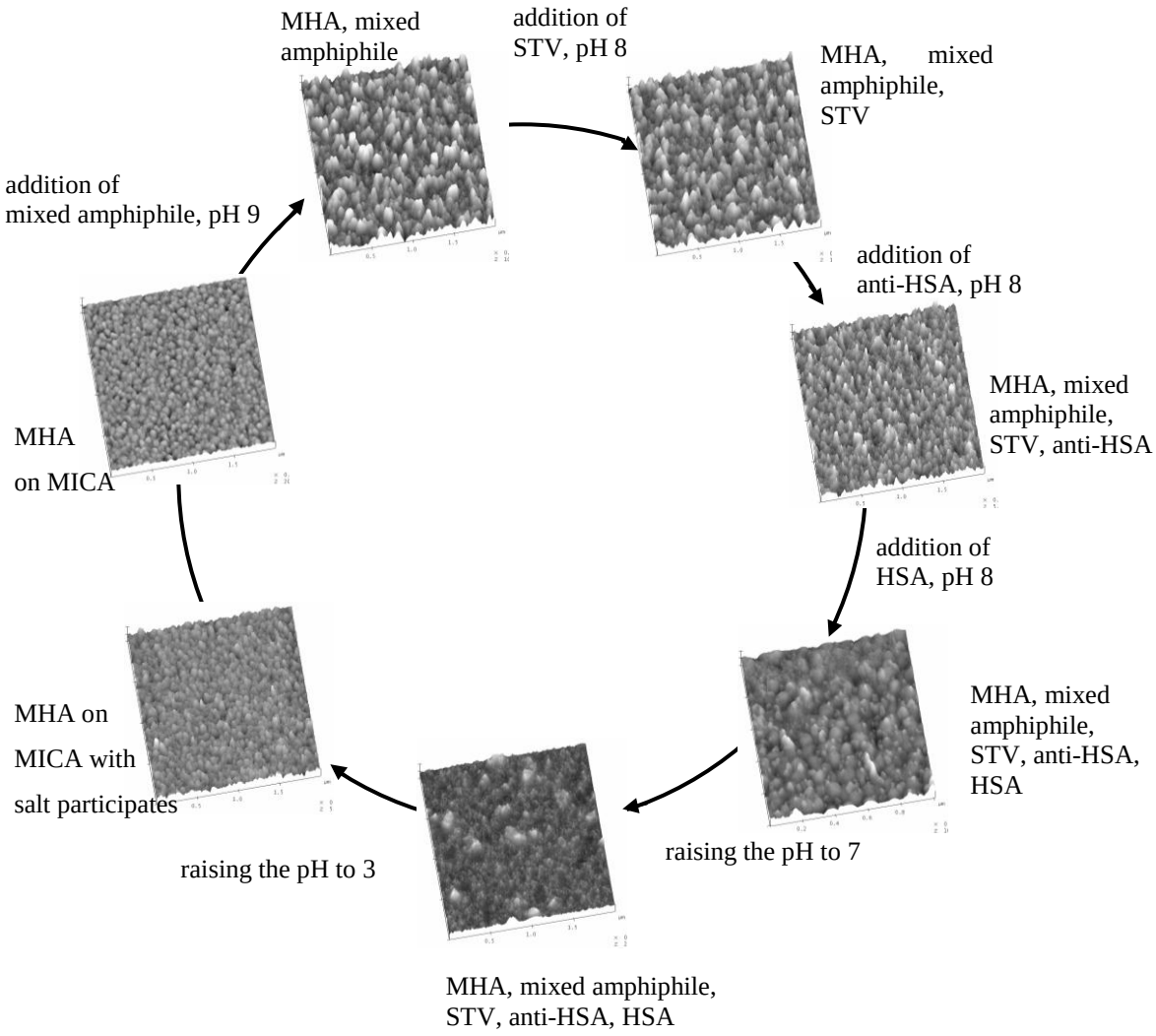

Figure 44: AFM images (tapping mode) of surface sections (2 µm x 2 µm) before and after stepwise assembly of layers on a SAM of MHA on a gold-modified mica surfaces a) MHA on mica b) 1:9 mixed amidine (AT5 and AT3) assembled on a), c) streptavidin on subsequently assembled prior layers d) biotinlyated anti-HSA e) HSA f) layers rinsed with pH 7.5 borate buffer g) layers rinsed with a buffer at pH 3

3.2.5 Conclusion biotinylated amphiphiles

In this study, two ω-functionalized amphiphiles with the ability to self-assemble on a SAM of mercaptohexadecanoic acid via the reversible amidinum carboxylate bond were studied. The amphiphiles were synthesized via a multi-step synthesis and it was possible to reuse the sensor surface by changing the protonation status of the acid. By introducing the biologically active ligand biotin to the amphiphile an anchor for streptavidin was generated. Subsequently, STV was used to anchor two different biotinylated antibodies. The second amphiphile with a hydroxyl function was used as spacer molecule to achieve optimal STV binding. In the first series of measurements the analyte HSA (human serum albumin) was detected and in a second series PSA (prostate specific antigen) was studied in order to define the limits of detection. The stepwise buildup of this multilayer sensor was monitored by in situ ellipsometry, IRRAS, contact angle measurement and AFM.

The *in-situ* ellipsometry results indicated a stepwise assembly of the above described biosensor. The thicknesses measured with this method were in agreement with the thicknesses found in literature and calculated via ChemDraw. This suggested that next to the assembly of mercaptohexadecanoic acid on gold, the amphiphiles formed closely packed monolayers via amidinium carboxylate interaction. After testing different ratios of biotinylated to hydroxlated amidine, a ratio of 1 to 9 (X_B = 0.1) was found to be optimal for close STV packing which is in excellent agreement with Spinke et al. After the assembly of STV, the biotinylated antibodies were assembled and the kinetics of analyte binding displayed. The sensor was able to distinguish between the unspecific binding of the protein IgG and the analyte HSA. Beside the detection of PSA from buffered media, PSA was successfully detected from real samples. The 200x diluted human serum samples were loaded with PSA with a LOD of 100 fM. This LOD is similar to detection limit of 80 fM from fluorescence labeled antibodies[19]. There was also low unspecific binding of non-target proteins on the PSA antibody. The stability of the multilayers was confirmed by rinsing the films with pH 8 after every addition. Decreasing the pH of the rinsing solution to 3 showed a disassembly of the biosensor architecture. The covalently bound mercaptohexadecanoic acid SAM was stable and the sensor could be reused several times.

The enhanced sensitivity was attributed to the multilayer architecture using the strong biotin-avidin interaction. Another reason might be the high surface density, which is given by the lateral mobility of the amphiphilic film. This selectivity led to the low detection

limit. The protein absorption on the anti-PSA proved to be concentration and time dependent.

IRRAS measurements indicated crystalline like structure of the MHA SAM on gold, due to the presence of the asymmetric stretch vibration of -CH_2 at 2918 cm^{-1} and the symmetric stretch vibration at 2850 cm^{-1}. The peak at 1461 cm^{-1} corresponds to the deprotonated form of carboxylic acid (COO^-).[10] The presence of the mixed amphiphile layer was proven by the observation of the broad band between 3100 cm^{-1} and 3500 cm^{-1}, which indicates hydrogen bond formation of the amidine tail group with the carboxylic acid.[31] The peak at 2955 cm^{-1} could be attributed to the asymmetric -CH_2 stretch of the amidine.[121] Further studies with transmission FTIR were in good agreement with the IRRAS results. The assembly of streptavidin, anti-HSA, anti-PSA and the analytes HSA and PSA were proven by the presence of the protein typical amide I and amide II bands.[32,33] The amide I band was assigned at ~1664 cm^{-1}, whereas the amide II band could be assigned at ~1550 cm^{-1}. The comparison of the intensities of the amide I and amide II bond to the molar ratio of mixed amphiphlic solution also indicate an optimal streptavidin binding with a biotin content of $X_B = 0.1$.

Contact angle measurements of the MHA layer showed a highly hydrophilic surface. The measured angle was 23 ± 4°. This indicated protonated carboxylated groups on the surface.[30] The low contact angle of the 1:9 biotin- to OH- terminated amphiphile mixed SAMs ($X_B = 0.1$) was due to the different mesogen lengths of the molecules and the polar behavior of the biotin headgroup. Protein adsorption leads to more hydrophobic surfaces. The hydrophobic behavior of this protein can be attributed to the hydrophobic interactions and the low polarity of the protein.[35] The prostate specific antigen was less hydrophobic than human serum albumin, due to the lower contact angle. Washing the surface with a buffer at pH 3 disturbed the ionic interaction between the amidin and the carboxylic acid and led to the disassembly of the multilayer structure. The same contact angle was observed as before for the MHA functionalized surface. This shows the full reversibility of the surface.

Investigation of the sensor with Atomic Force Microscopy needs further improvement. The topography of the different films could be displayed, but it is hard to distinguish between the assembled protein layers. The samples should be measured in liquid environment and need smoother gold substrates for further research. However, the optimization of the AFM condition need to be conducted in future investigation.

3.3 Synthesis of ω-functionalized sialic acid amphiphiles

The sialic acid terminated amidine was synthesized in 12 steps, the last step was the click reaction between an azide terminated amidine (**AT11**) and the sialic acid terminated alkyne (**AT16**). In Scheme 26 the synthesis whole route is displayed.

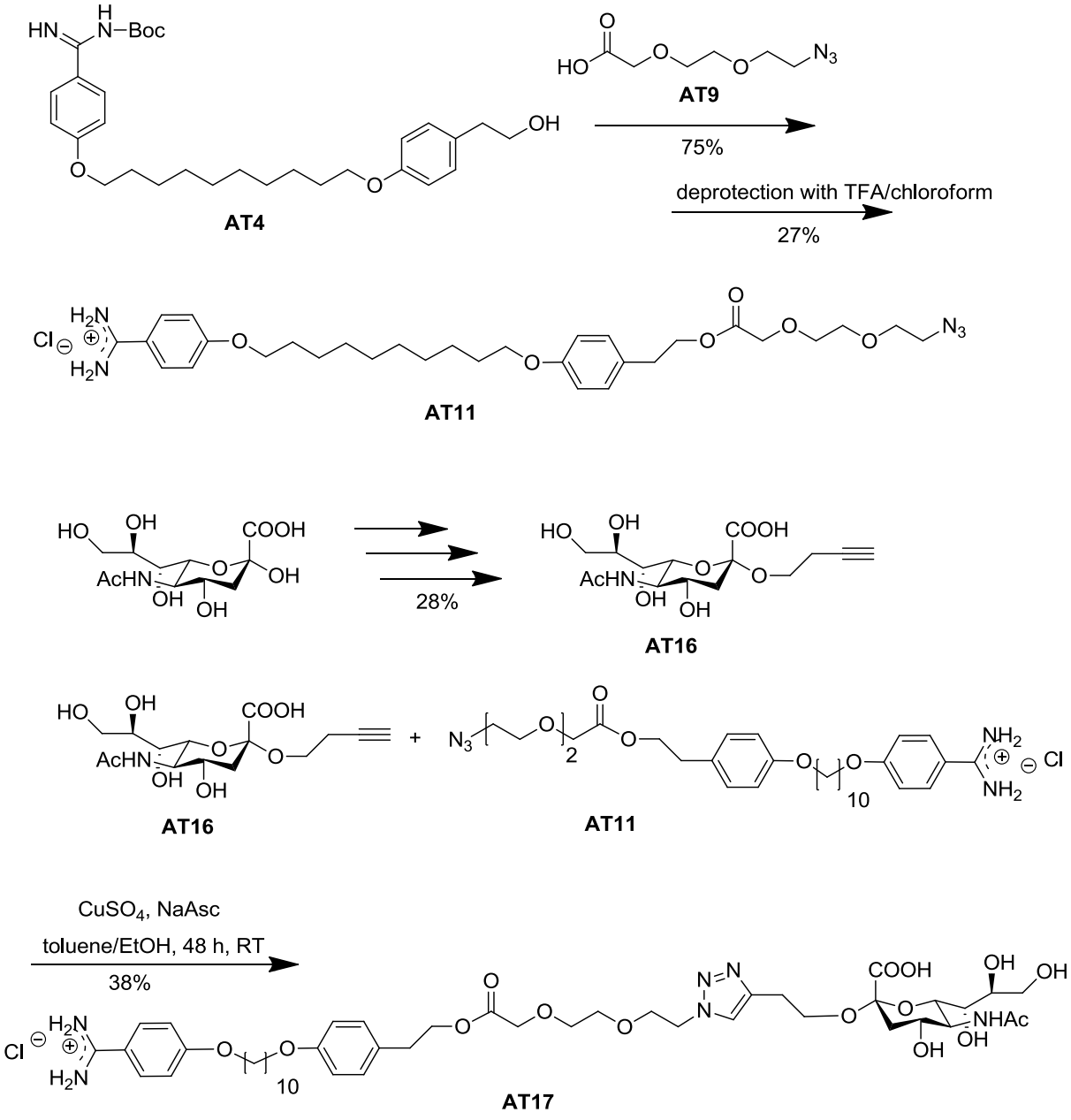

Scheme 26: Click reaction of sialic acid terminated alkyne and azide terminated amidine

The different synthesis steps will now be described. To synthesize the final compound **AT17**, it was necessary to start with the synthesis of the reactants **AT11** and **AT16**. We chose to synthesize an azide containing compound **AT11**, which would be able to be coupled to every alkyne containing compound via a click reaction.[125,126] This compound also needed to be able to bind on a carboxylated surface via the amidinium-carboxylate interaction. This is necessary to have a switchable bond. [24,35] The compound **AT11** was synthesized starting by two different routes. First, the Boc- protected amidine (**AT4**) with an -OH function was synthesized (described in the previous chapter); afterwards the spacer molecule **AT9** with the azide function was produced.

The synthesis followed the description of Hirsch et al.[127] (Scheme 27):

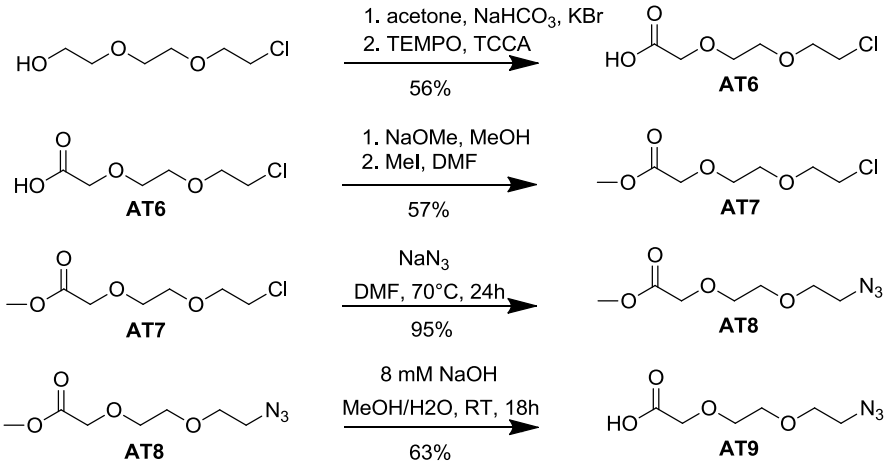

Scheme 27: Spacer molecule for azide synthesis

The curtail step in the synthesis of the spacer molecule (**AT9**) was the first step. To achieve the carboxylated compound (**AT6**), 2-[2-(2-Chloroethoxy)ethoxy]ethanol was dissolved in ice cold acetone. To oxidize the alcohol function of the compound to a carbonyl function, TEMPO (2,2,6,6-tetramethyl-1-Piperidinyloxy) and TCCA (trichloroisocyanuric acid) were added as oxidizing agents (Scheme 28).[128] TEMPO is a mild, non-toxic oxidizing agent and it is well known to be a stabile nitroxyl radical (A). [129] A catalytic amount of TCCA reacts with TEMPO to form *N*-oxoammonium ion (B). The formed *N*-oxoammonium ion is attached to the nucleophilic alcohol (R-CH_2-OH) (C). The aldehyde (D) and hydroxylamine (E) are formed by elemination. The hydroxylamine can be reoxidized by the secondary oxidant TCCA to form hypochlorous acid (F) in aqueous

media and the prior nitrosonium ion (B). The hypochlorous acid (F) can oxidize the aldehyde (D) to form the carboxylic acid function (G) and acetic acid (H).

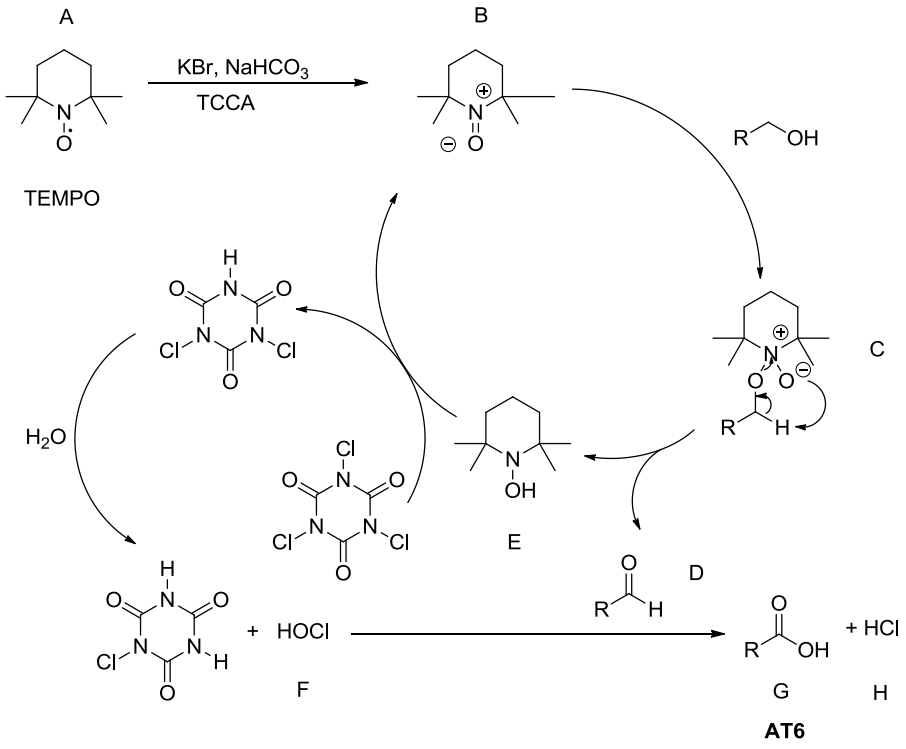

Scheme 28: Oxidation of 2-[2-(2-chloroethoxy)ethoxy]ethanol with TEMPO[128]

After the carboxylated compound **AT6** was synthesized with a yield of 56%, the ester **AT7** was synthesized. This was done by alkylation of a carboxylate anion with methyl iodide in DMF (Scheme 27). The yield was 57%. Afterwards compound **AT7** was treated with sodiumazide to substitute the chlorine with the azide function. This yielded in compound **AT8** (95%). The last step was the hydrolysis of the ester (**AT8**). In the hydrolysis the ester reacts with sodium hydroxide in aqueous methanolic environment. The product was achieved in 63% yield. The coupling between the spacer molecule **AT9** and the Boc-protected compound **AT4** (4-{10-[4-(2-Hydrody-ethyl)-phenyoxy]-decyloxy}-benzamidine hydrochloride) was done in dry DCM. To couple a carboxylic acid with an alcohol, the Steglich estification is a convenient method.[130] *Tert*-butyl esters in presence of DCC (dicyclohexylcarbodiimide) and DMAP (4-dimethylaminopyridine) were formed this way. The yield of compound **AT9** was 63%.

The synthesis of the alkyne terminated sialic acid follows the publication of Jean-Marie Beau and Long Jiang.[131,132] Both groups started with the commercially available compound *N*-acetylneuraminic acid (also called sialic acid or Neu5Ac) (Scheme 29). Esterification of

sialic acid was done under acidic conditions to protect the carboxylic acid function. Compound **AT12** was obtained in 98% yield. The chlorination of compound **AT12** was done with HCl-gas. The acetyl protective groups were introduced using acetylchoride. Product **AT13** was obtained in 97% yield. The chlorination was necessary for the next step in the route. Subsequently, butagylalcohol was coupled with the sialic acid derivate to achieve the clickable compound **AT 16**. Silver triflate was used in this step to substitute the chlorine by butagylalcohol.[133] Silver chloride as insoluble component was filtered off. The compound **AT14** had to be purified by column chromatography. This reaction yielded 48% of compound **AT14**. The next two steps were required to deprotect the sialic acid derivate.[134] Sodiummethoxide was used as first step to remove the acetyl- protecting group from the hydroxyl function. The first deprotection step required column chromatographic purification, which resulted in a yield of 50% (**AT15**). In a second step sodiumhydroxide was used to deprotect the carbonyl function. The product from the second deprotection step was obtained in 98% yield (**AT16**).

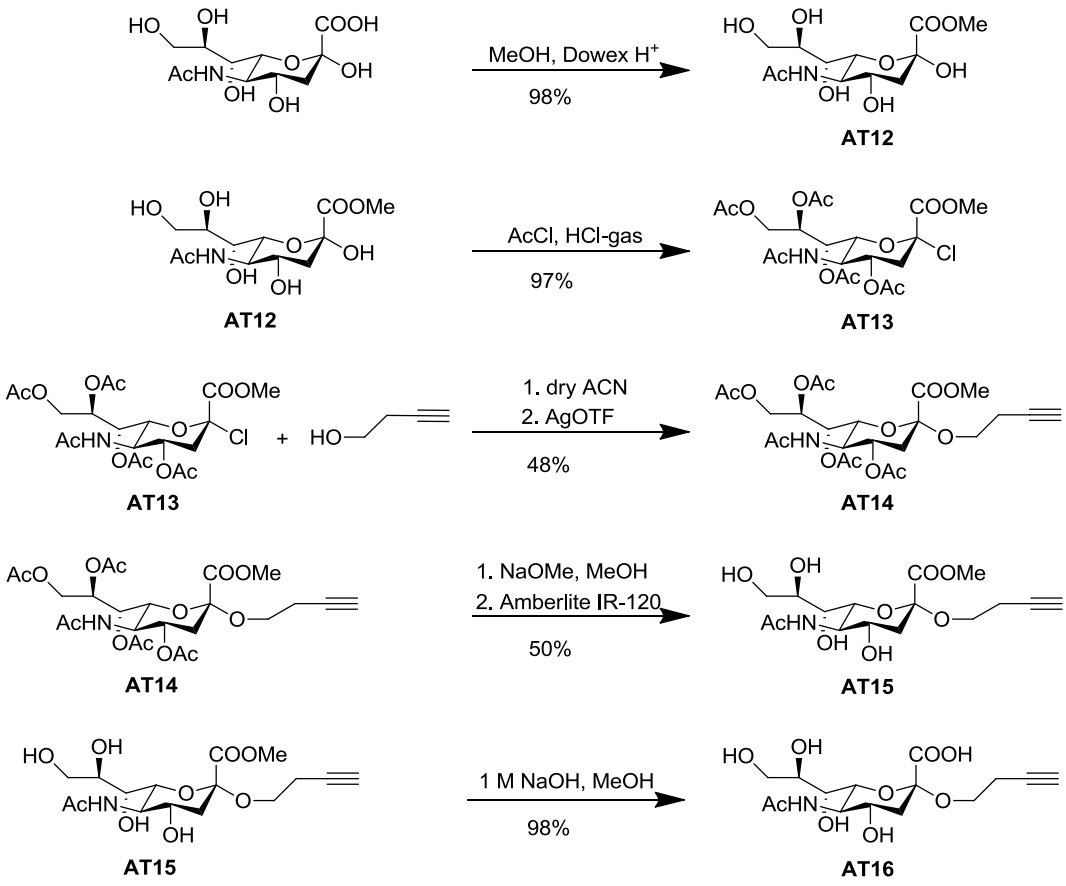

Scheme 29: Synthesis of alkyne terminated sialic acid AT17

The final step in the synthesis route of the sialic acid terminated amidine was a click-reaction. The difficulty in the click-reaction was the solubility of the reactants in water. Since it was not possible to click in mild reaction conditions, toluene had to be chosen as solvent. This is not a common solvent for click-reactions, since click-reactions should be environmentally friendly.[125,135] The click-reaction is a Husigen cycloaddition.[136] Herein the azide **(AT11)** reacts in a 1,3-dipolar cycloaddition with an alkyne **(AT16)** to result in a 1,2,3-triazole **(AT17)**. Cu(II)SO_4 was used to catalyze the reaction.[137] Sodium ascorbate was added to reduce the copper(II)sulfate to copper(I). The mechanism of the reaction is shown in Scheme 30.

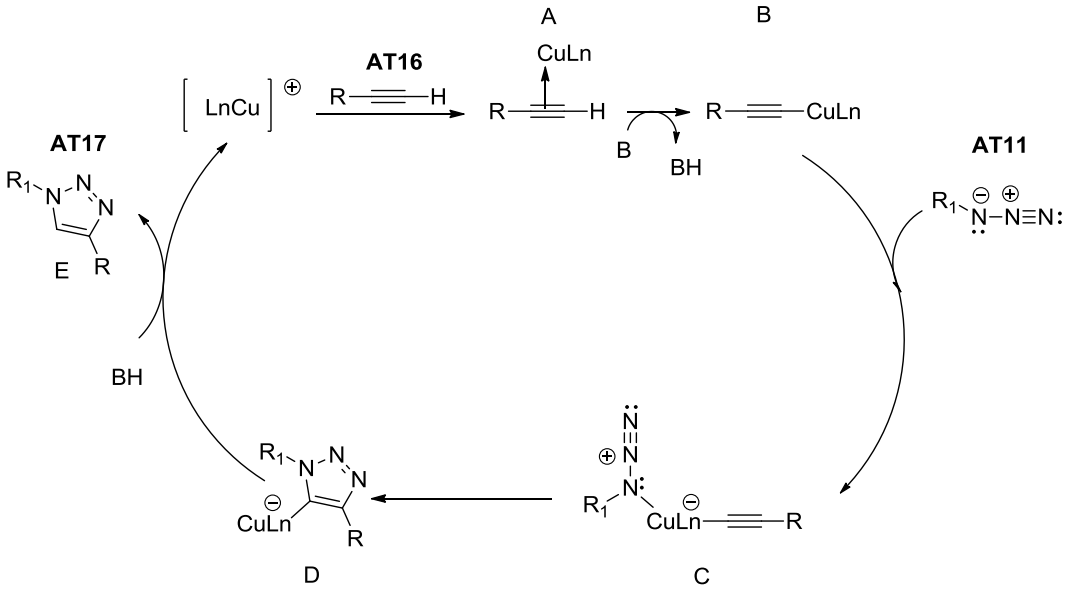

Scheme 30: Mechanism of the Husigen cycloaddition in presence of a copper catalyst[137]

At first a π - complex (A) is formed between the alkyne and the copper(I). This π - complex increases the acidity of the alkyne (**AT16**). In this condition, the π- complex can be deprotonated. The formed copper(I)acetylid (B) can couple to the azide and build an azide-copper(I) acetylide-complex (C). This complex reacts through intramolecular cyclization to a copper containing 1,2,3-triazole (D). As a last step the catalyst is protonated, which yields in the substituted 1,2,3-triazole (E). The yield of the compound **AT17** is 38%. When the crude product was worked up, it was necessary to recrystallize the compound twice, with an additional filtration step, respectively. This could be a reason for the low yield. In general, click-reactions tend to be quantitative. With infrared spectroscopy we have proven that the click-reaction was successful.[138] Figure 45 shows the azide bond at 2100 cm^{-1} disappearing during the click-reaction. This is due to the conversion of that azide into a 1,2,3-triazole ring.

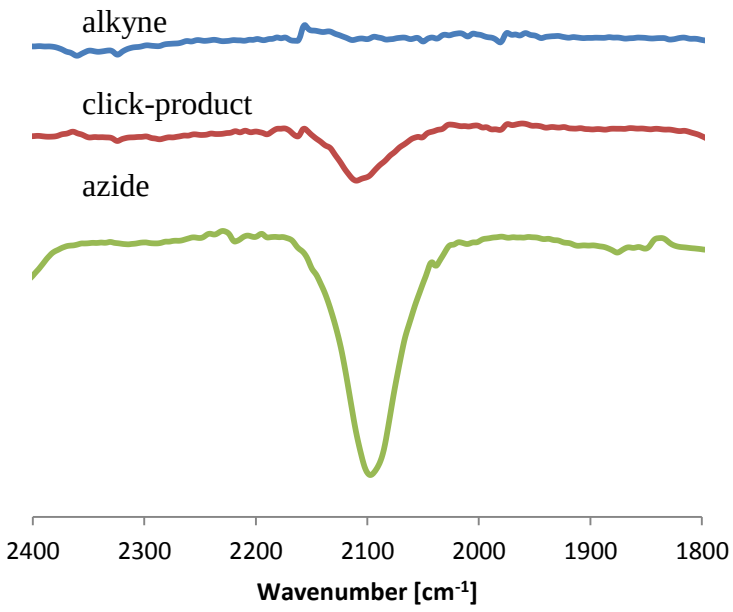

Figure 45: ATR-IR spectrum of the alkyne AT16, the azide AT11 and product of the click-reaction the 1,2,3-triazole AT17

3.3.1 In-situ ellipsometry of sialic acid terminated amphiphiles

We confirmed the assembly of the sialic acid terminated amphiphile with *in-situ* ellipsometry. The sialic acid terminated molecule was used to subsequently bind hemagglutinin, which is usually present on the surface of influenza virus.[139] After a first series of experiments, where the binding of the protein hemagglutinin was displayed, we moved to influenza virus like particles (VLPs). In Scheme 31 a schematic representation of the influenza virus binding to the sensor is shown.

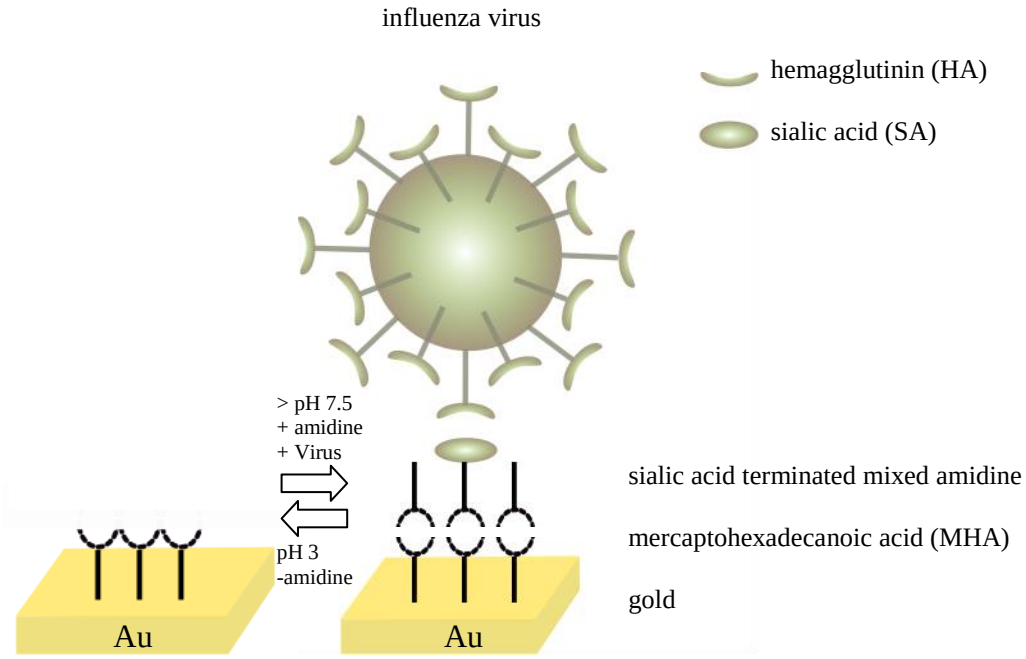

Scheme 31: Reversible biosensor consisting of MHA, sialic acid terminated mixed amidin and influenza virus; reversibility is achieved by changing the pH of the environmental solution to 3

In order to achieve optimal hemagglutinin (HA) packing on the sialic acid terminated amphiphile layer, different ratios of sialic acid terminated amphiphile to hydroxylated amphiphile were tested. The ratios were 0/100, 10/90, 20/80, 40/60, 60/40, 80/20 and 100/0. The ratios were displayed as molar ratio X_B in the same way as above. The gold substrates were prepared as described in chapter 4.2. After gold deposition, the substrates were immersed in freshly prepared piranha solution for 1 min, rinsed with copious amounts of water and 5 mL ethanol, and dried under nitrogen flow. The substrates were immersed in 0.02 mM ethanolic MHA overnight, rinsed with absolute ethanol and dried under nitrogen flow. After MHA assembly, the substrate was mounted in the ellipsometer cuvette and the latter was filled with pH 9 buffer. The different mixed amphiphiles were added in a concentration of 50 µM. The molar ratio of sialic acid terminated amphiphile to

hydroxylated amphiphile in dependence of the thickness are displayed in Figure 46. The kinetics of the amphiphile attachment are depicted in Figure 47 .

As one can observe, the achieved thickness of the SAM with only sialic acid terminated amphiphile is 3.0 ± 1.2 nm (X_B = 1). If we calculate the thickness via ChemBioDraw 3D (Version 12.0 Ultra) the molecule would be ~4.8 nm in its stretched configuration. This difference is an indication for a disordered orientation on the MHA SAM. The reason could be the voluminous sialic acid head group of the molecule, which could sterically hinder closed packing. When only the hydroxylated amphiphile was assembled, the thickness measured was in good agreement with the thickness estimated. The layer with a sialic acid content of X_B = 0.1 yielded in a thickness of 4.5 ± 0.7 nm. A sialic acid content of X_B = 0.2 and X_B = 0.4 yielded in 4.2 ± 1.1 nm and 5.4 ± 1.4 nm, respectively. The higher thicknesses with a low amount of functional head group in the mixture is an indication for the closer packing of the sialic acid terminated amphiphiles on the MHA SAM, driven by van der Waals interaction.[140] Lower dilution with spacer molecules (X_B = 0.6, X_B = 0.8) yielded in thicknesses of 0.96 ± 0.60 nm and 0.66 ± 0.62 nm, respectively. This is an indication for low ordering on the MHA SAM as explained above. Mixing the amphiphiles also results in a broader distribution of the sialic acid head group in the film, which is optimal for close hemagglutinin and VLP packing.

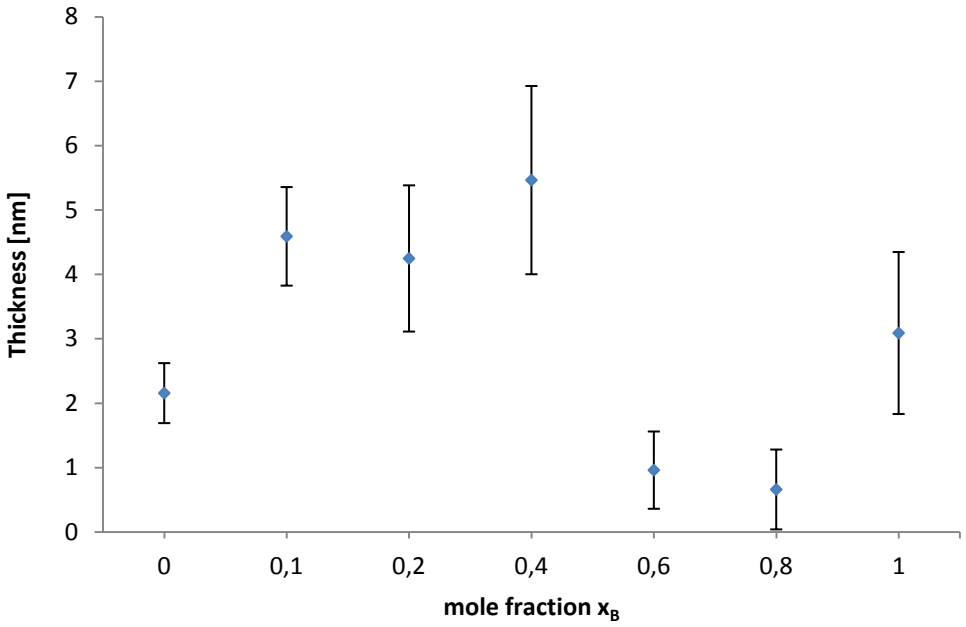

Figure 46: Film thickness measured by *in-situ* ellipsometry versus mole fraction of sialic acid terminated amidine. Data points are the monolayer thickness of amphiphiles on MHA; the thickness of the different monolayers is shown as a function of the mole fraction X_B of sialic acid terminated amidine to OH terminated amidine in the adsorption solution

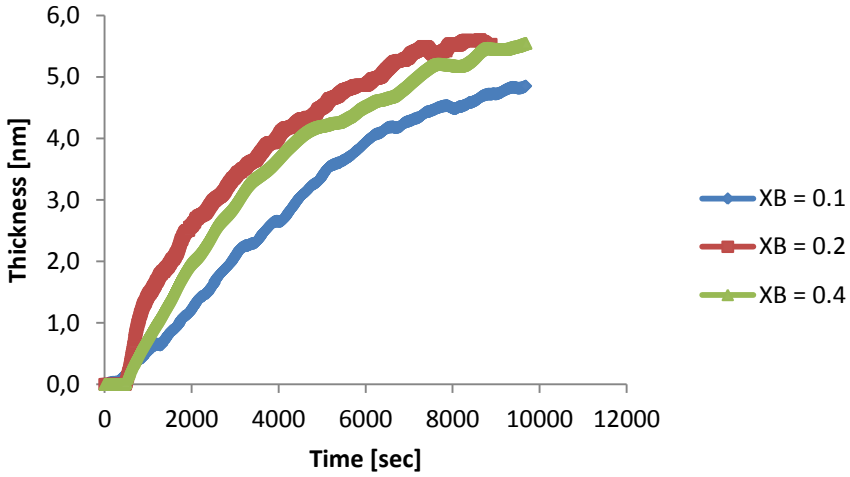

Figure 47: Three examples for assembly kinetics at different mole fractions of sialic acid terminated amidine achieved with mixed amphiphiles on MHA

In order to find the optimal packing condition for hemagglutinin assembly, different ratios of sialic acid terminated to hydroxylated amphiphiles were studied. In the following figures, the amount of bound protein, as well as the thickness of those films are shown.

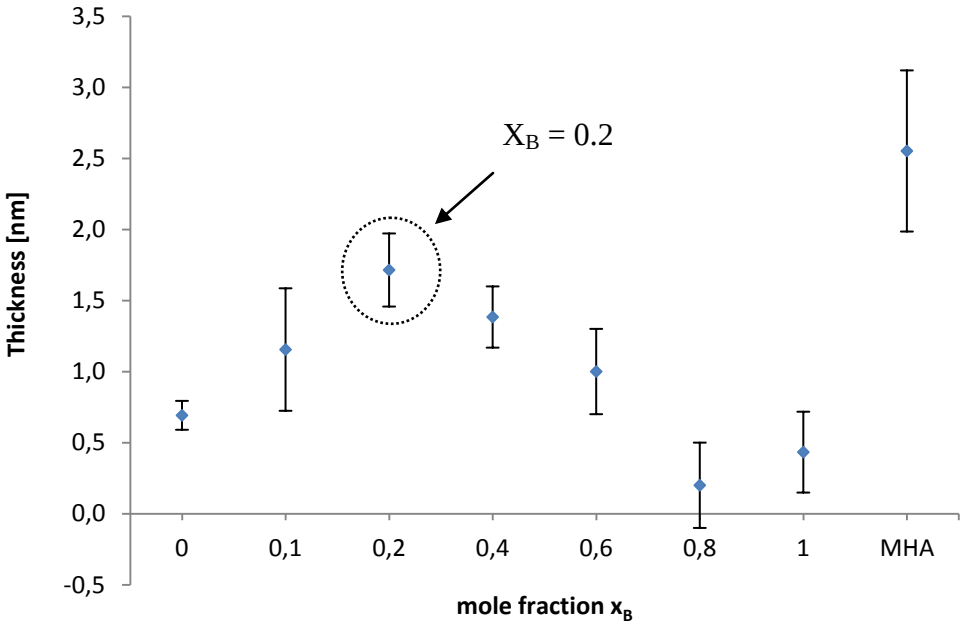

Figure 48: Film thickness of of hemagglutinin (420 nM) on the mixed amphiphiles measured by *in-situ* ellipsometry versus mole fraction of sialic acid terminated amidine

After assembling the amphiphiles in borate buffer (pH 9, 10 mM boric acid), the cuvette was rinsed with pH 8 borate buffer to get better biological compatibility for protein assembly (pH 8 is closer to physiological pH). Different concentrations of hemagglutinin were studied. The first concentration tested was 420 nM which was reported by Sun and coworkers in a system using hemagglutinin on irreversible sialic acid SAMs.[49] Lower concentrations up to 42 nM were investigated here.

Present literature does not offer much information about ellipsometric thickness data for HA adsorption onto SAMs. But we found for example Pereira et al. who tried to assemble HA on Si/SiO_2 wafers.[141] They found film thicknesses of about 3.4 ± 0.2 nm, but concluded that these values are too small for a fully covered surface, since the size of hemagglutinin protein measured by X-ray diffraction is 6.6 nm x 11.6 nm x 11.8 nm.[142] The film thickness of 1.7 ± 0.3 nm is a measure of the protein size in our case when a sialic acid content of X_B = 0.2 was used in the amphiphile mixture (Figure 48). This is the highest film thickness reached with the amphiphile mixtures. Lower sialic acid contents in

the mixture show a size of 1.2 ± 0.4 nm. A higher content of $X_B = 0.4$, $X_B = 0.6$ and $X_B = 0.8$ also shows decreasing film thicknesses. This is why the optimal condition for hemagglutinin binding was considered to be at $X_B = 0.2$. Since the thickness measured by *in-situ* ellipsometry is still lower than the size measured by X-ray diffraction, we have to considerer that there is no dense hemagglutinin packing on the mixed SAM. This can have several reasons. For example, the size difference of the spacer molecule and the sialic acid terminated molecule. In the previously introduced sensor containing biotin, the spacer molecule is able to make only the head group of the biotin accessible for the streptavidin binding site. Here the molecule containing sialic acid is significantly longer than the spacer (Scheme 32). The size difference of the two molecules makes it possible for the sialic acid head group to bend. The upper part of the molecule (glycol chain) is not stabilized by van der Waals interaction and able to bend down. For further investigations a longer spacer molecule should be synthesized.

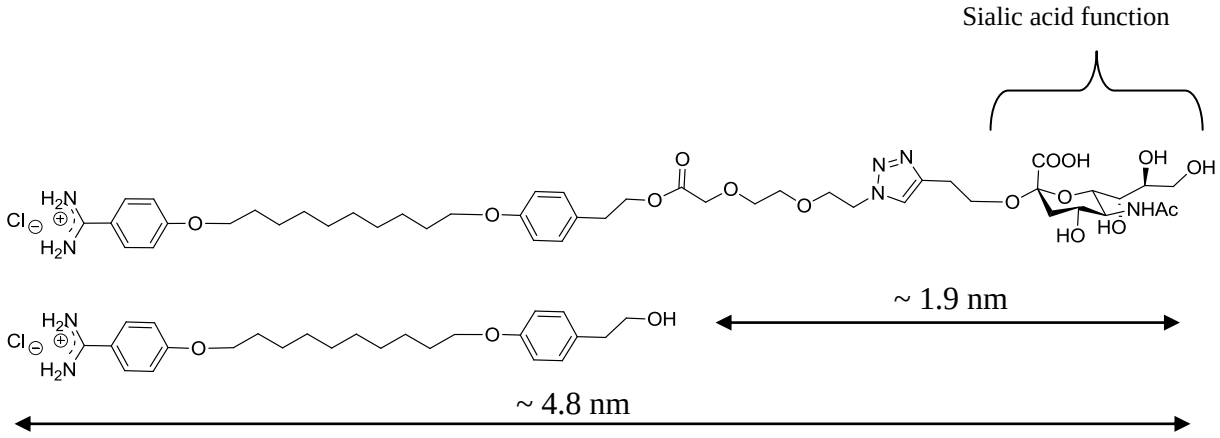

Scheme 32: Sialic acid terminated amphiphile and hydroxylated amphiphile and estimated size (ChemBioDraw 3D Version 12.0 Ultra)

Based on the results from *in-situ* ellipsometry, a model has been developed (Scheme 33).[93] This model shows how important the spacer molecule is for protein adsorption. The protein is sterically hindered when the head-group packing is too dense (a). Optimal protein adsorption can be achieved when the spacer molecule and the receptor molecule molar ratio are mixed efficiently (b). The right spacer size is important to allow only the head group of the receptor to stick out of the surface (c).[93,143] In Juan and Carmichaels paper it is pointed out that too short alkyl chains as spacer molecules disrupt the van der Waals

interactions among the chain. Those short molecules are just not long enough to stabilize the alkyl chains of the functional molecule (c).[143]

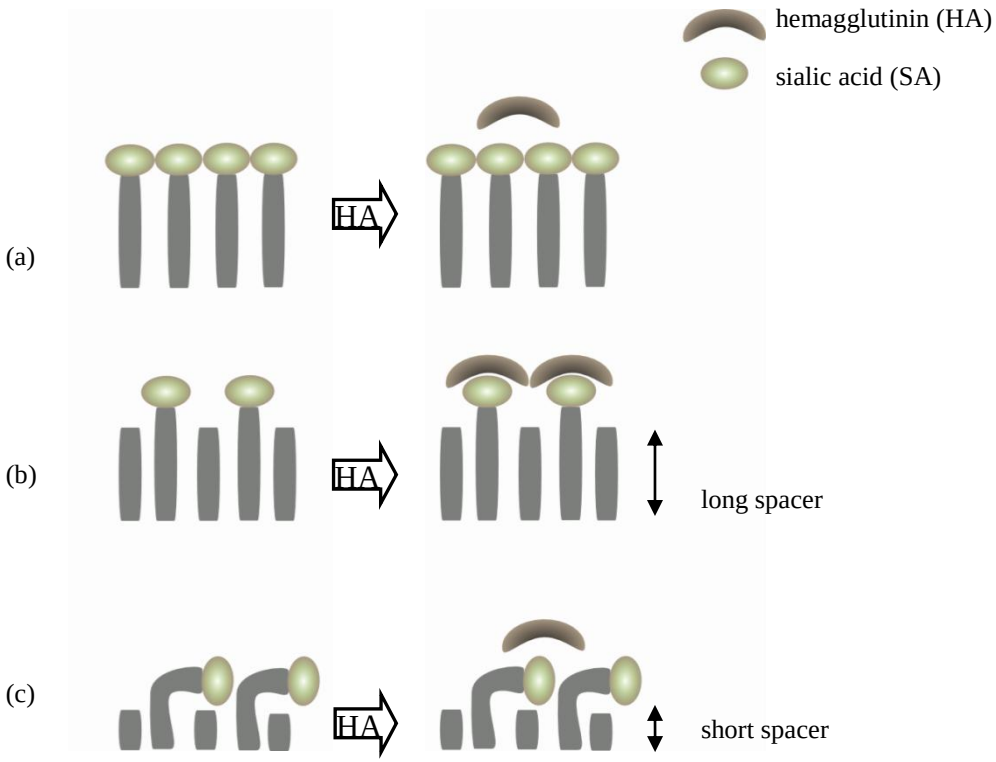

Scheme 33: Schematic representation of the mixed sialic acid terminated amphiphile SAM and the binding to hemagglutinin; a) top scheme shows the pure sialic acid terminated SAM. Binding of hemagglutinin is sterically hindered; b) middle scheme, a layer of optimal packed amphiphiles with hemagglutinin binding is shown; c) possible assembly of molecule AT 3 and AT17. The spacer AT3 is too short[93,143]

Interestingly, a high film thickness was observed when hemagglutinin was assembled on the pure mercaptohexadecanoic acid (MHA) surface (2.5 ± 0.6 nm). The surface of a protein contains different domains, it has hydrophobic parts, hydrophilic parts, positively and negatively charged parts.[144] Furthermore, hemagglutinin has an isoelectric point (pI) of 3.5 [145], but it still binds on the negatively charged carboxylic acid terminated surface. The low pI of hemagglutinin, leads to the conclusion that the protein has a negative charge when dissolved in pH 8 borate buffer. Rabe et al. explained the adsorption of proteins with a net negative charge to hydrophilic surfaces as follows: The adsorbed protein can expose its positively charged domains to the negatively charged surface. The negatively charged domains are oriented in the opposite direction.[144] This would explain the preferred assembly of HA on MHA. The kinetic data of the hemagglutinin adsorption can be found in Figure 49-54.

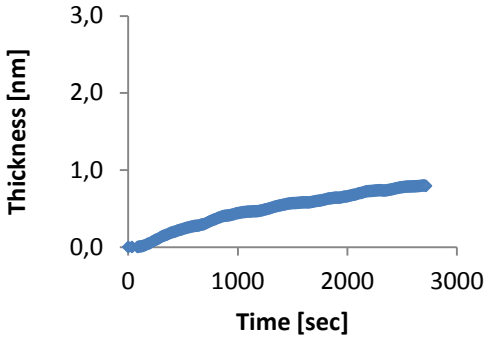

Figure 49: Assembly kinetic of 420 nM HA on hydroxylated SAM (X_B = 0)

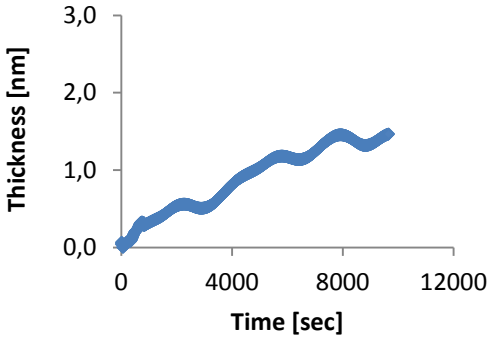

Figure 50: Assembly kinetic of 420 nM HA on mixed sialic acid terminated SAM (X_B = 0.1)

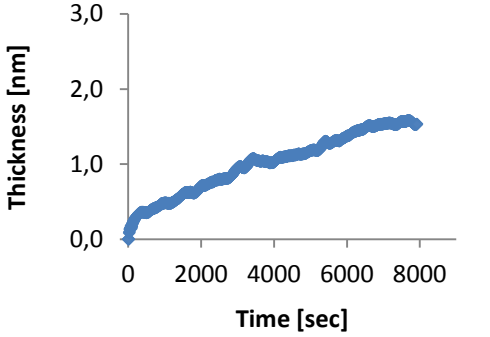

Figure 51: Assembly kinetic of 420 nM HA on mixed sialic acid terminated SAM (X_B = 0.2)

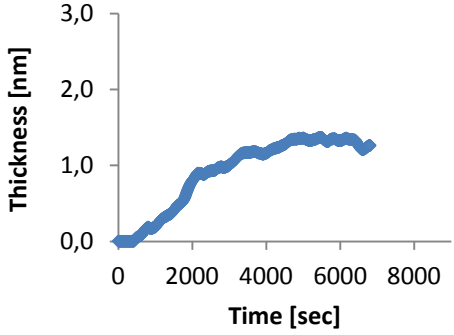

Figure 52: Assembly kinetic of 420 nM HA on mixed sialic acid terminated SAM (X_B = 0.4)

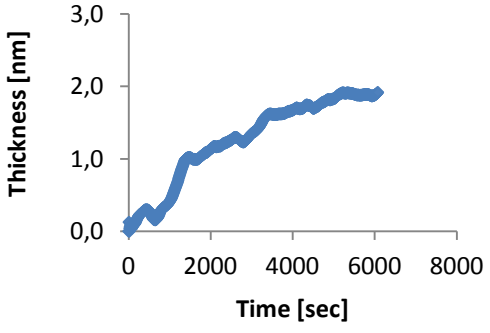

Figure 53: Assembly kinetic of 420 nM HA on MHA

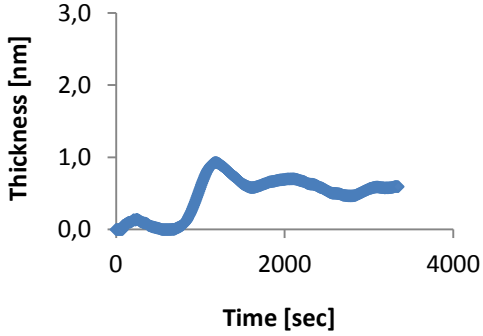

Figure 54: Assembly kinetic of 420 nM HA on sialic acid SAM (X_B = 1)

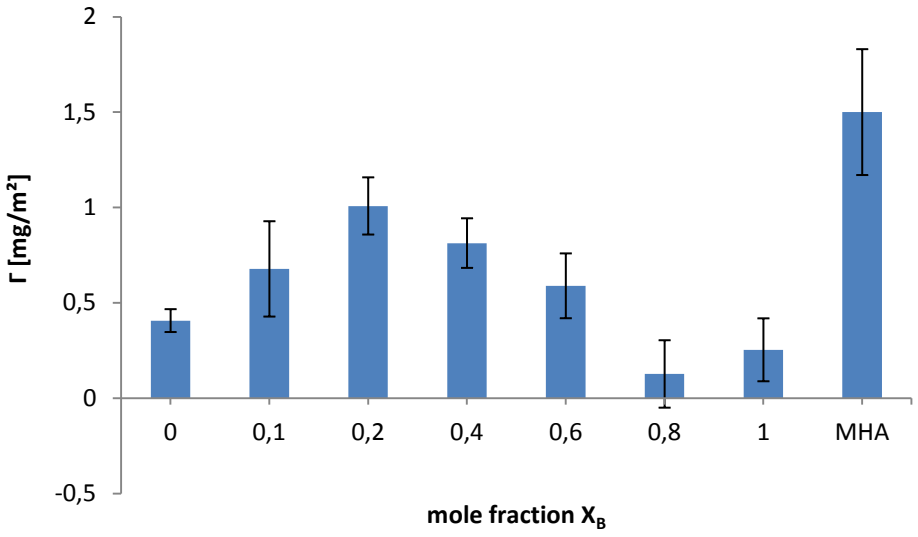

Figure 53: Amount of bound hemagglutinin on different mixed amphiphiles as a function of the mole fraction X_B of sialic acid terminated to -OH terminated amidine in the adsorption solution

The amount of bound hemagglutinin on the mixed reversible SAM was explored as well (Figure 53). It was calculated via the Feijter equation[114] (introduced in chapter 3.2.1). The results from the thickness measurements and the calculation of the amount of protein are in good agreement. It was found that most hemagglutinin was bound with a sialic acid content of $X_B = 0.2$. As discuss above, the carboxylic acid terminated hydrophilic surface attracts the hemagglutinin as well. The amount of bound HA is 1.5 ± 0.3 mg/m². The amount of bound hemagglutinin on a SAM has not been reported in literature to our knowledge. But the thickness we measured was smaller than the protein size achieved with X-ray diffraction. Therefore we can assume that the amount of bound hemagglutinin did not form a monolayer, but is immobilized in a lower density.

Reversibility of above described system was tested by acidifying the ellipsometer cuvette. Upon the pH switchability of the amidinum – carboxylate interaction, the layer consisting of hemagglutinin and mixed amphiphiles was removable. For assembly, 50 µM amphiphile solution ($X_B = 0.2$) was added to the MHA coated substrate. After a stable baseline was achieved, the cell was rinsed with pH 8 HEPES buffer (10 mM) and a 42 nM hemagglutinin solution was added. After this assembly kinetic was completed, the cell was rinsed with buffer again. Furthermore, the cell was acidified with pH 3 solution and a removal of the assembled hemagglutinin and amphiphile layer was displayed (Figure 54).

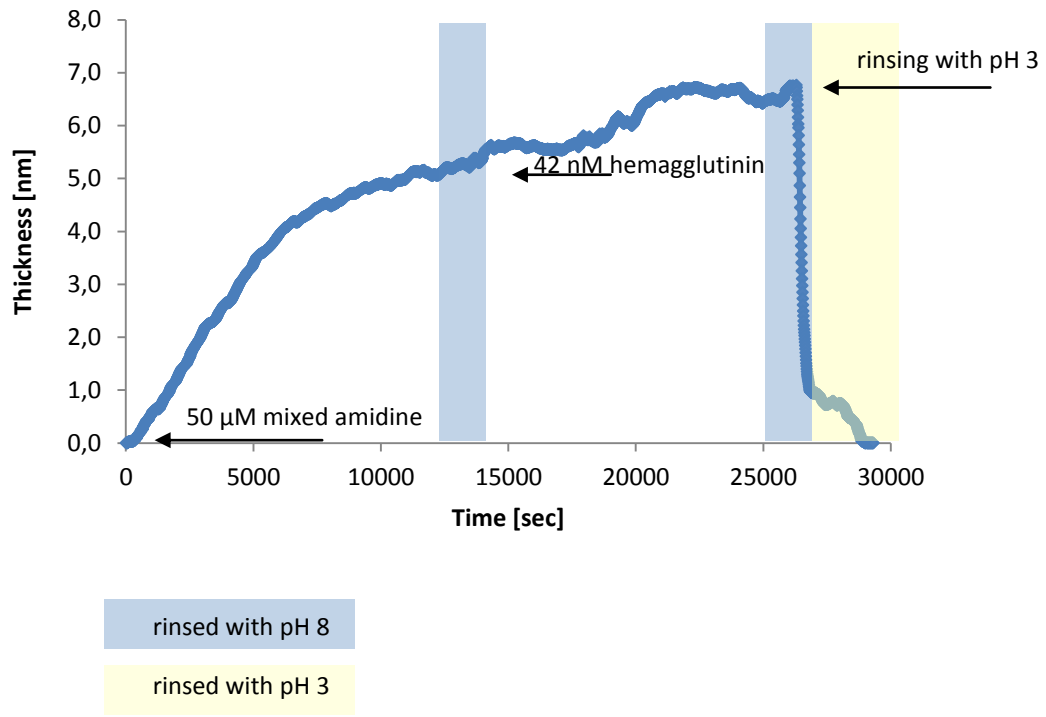

Figure 54: Assembly and disassembly of 50 µM mixed amphiphile solution (X_B = 0.1) and 42 nM hemagglutinin

3.3.2 Contact angle investigation of sialic acid terminated amphiphiles

In order to proof the adsorption of the mixed amphiphiles and the assembly of hemagglutinin on the latter, we carried out contact angle measurements with water droplets. The samples were prepared as follows: The gold slides were immersed in 0.02 mM ethanolic MHA solution overnight, rinsed with ethanol and dried under nitrogen flow. The MHA coated substrate was immersed in 50 µM amphiphile solution (pH 9 borate buffer) for > 1h and rinsed with the buffer. Then they were dried under nitrogen flow and examined. For the hemagglutinin assembly, the amphiphile coated substrates were immersed in 420 nM HA solution (pH 8 borate buffer), rinsed, dried and examined.

The results achieved with contact angle measurement have proven the hydrophobic nature of the sialic acid terminated molecule assembled on the MHA. The mixed SAMs with a sialic acid content from 10% to 100% show decreasing contact angles with increasing sialic acid content (63° to 41°). The contact angle decreases, which is a result of the increasing hydrophilicity. When hemagglutinin was added, the contact angles changed slightly in comparison to the contact angles for the mixed amphiphile layers underneath. Comparing the hemagglutinin values with each other, they show very similar values (50.9° ± 2.0°). The contact angle of the pure hydroxylated SAM shows a value of 22° ± 5.4°. Assembling hemagglutinin on top increases the value by only 0.7°. This is hinting low hemagglutinin density. These contact angle data are in excellent agreement with *in-situ* ellipsomety.

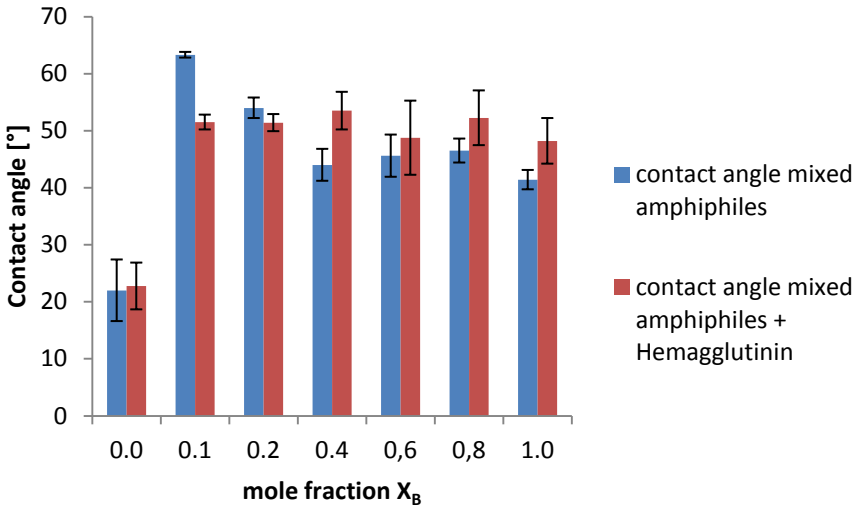

Figure 55: Contact angle measurements of mixed amphiphiles and assembled hemagglutinin

3.3.3 IRRAS of sialic acid terminated amphiphiles

To investigate the spectroscopic behavior of the assembled films infrared reflection adsorption spectroscopy (IRRAS) measurements were carried out. The spectroscopic behavior of the assembled MHA layer was discussed in chapter 3.2.2. The sample preparation of the amphiphile films as well as the preparation of the protein films were done as described in the previous chapter 3.3.2. First, the amphiphile films were examined in order to find evidence for a crystalline like orientation of the thin films. [4,38,94] The -CH_2 asymmetric and symmetric stretch peaks are the most important hint for a good film orientation. The peaks can be found at $\nu_a(CH_2)$ 2921 cm^{-1} and $\nu_s(CH_2)$ 2849 cm^{-1}. We only show the spectra of the mixed amphiphile film with a sialic acid content of X_B = 0.2 in here (Figure 56).

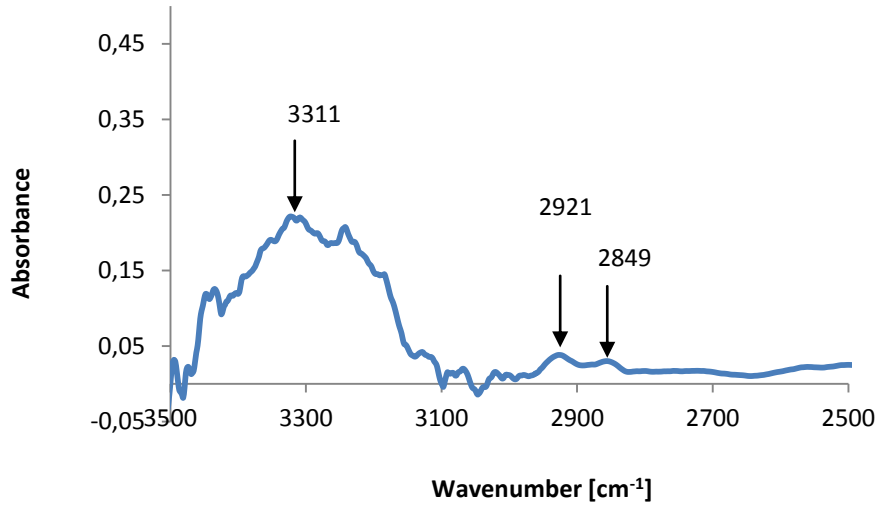

Figure 56: IRRAS spectrum of the high frequency region of mixed sialic acid terminated amphiphile film (X_B = 0.2)

The characteristic broad OH band of the sialic acid can be found between 3100 cm^{-1} and 3500 cm^{-1}. The low frequency region of the mixed SAM shows characteristic bands between 1200 cm^{-1} and 1000 cm^{-1}. This peaks can be assigned to carbohydrate residues, which give coinciding, broad modes of the asymmetric stretch C-O-C band (Figure 57).[95]

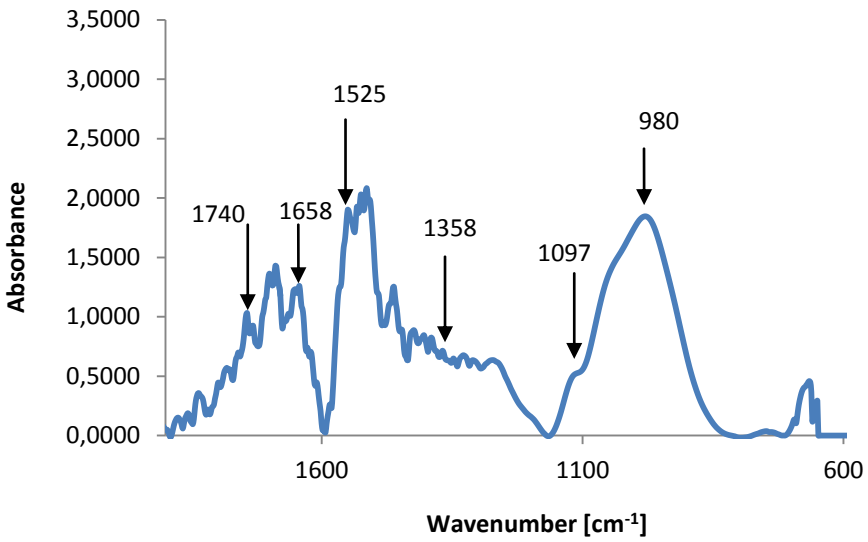

Figure 57: IRRAS spectrum of the low frequency region of mixed sialic acid terminated amphiphile film (X_B = 0.2)

The peaks at 1658 cm^{-1} and 1525 cm^{-1} can be assigned to the amide I and amide II vibration of the sialic acid. The carbonyl peak at 1740 cm^{-1} can also be attributed to the sialic acid molecule.[95,146] The in-plane bending of the of the -C-H group was found between 1100 cm^{-1} – 970 cm^{-1}. The IRRAS spectrum shows the presence of all functional groups found for sialic acid terminated SAMs in literature.

Optimal hemagglutinin binding was examined by taking a close look at the amide I and amide II bands in the presented spectra. By comparing the height of the absorbance one can estimate on which of the amphiphile mixtures, the most hemagglutinin was bound.

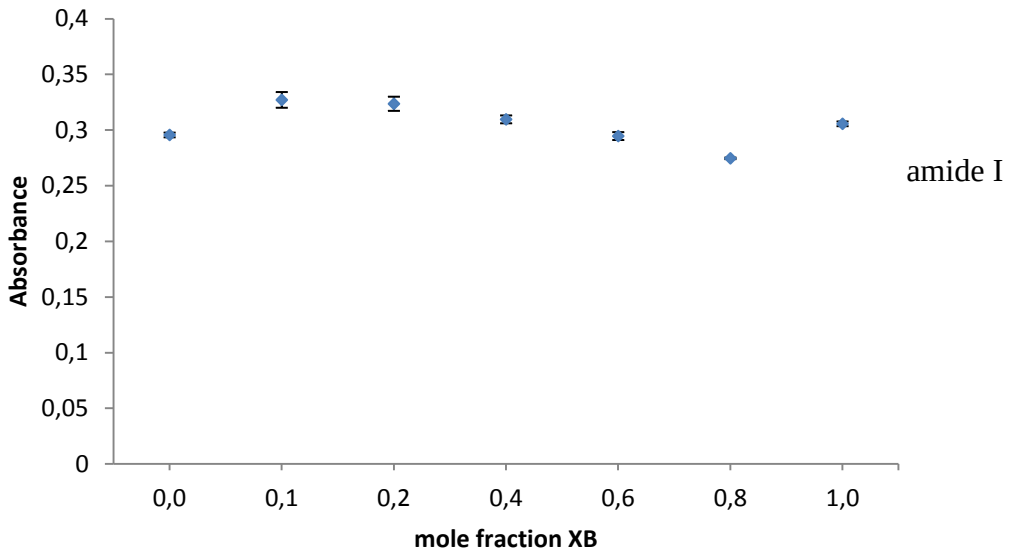

Figure 58: Absorption peak height of the amide I band of hemagglutinin as a function of the mole fraction X_B of sialic acid terminated amidine to -OH terminated amidine in the adsorption solution; the error bars are the standard deviation of three measurements on different substrates

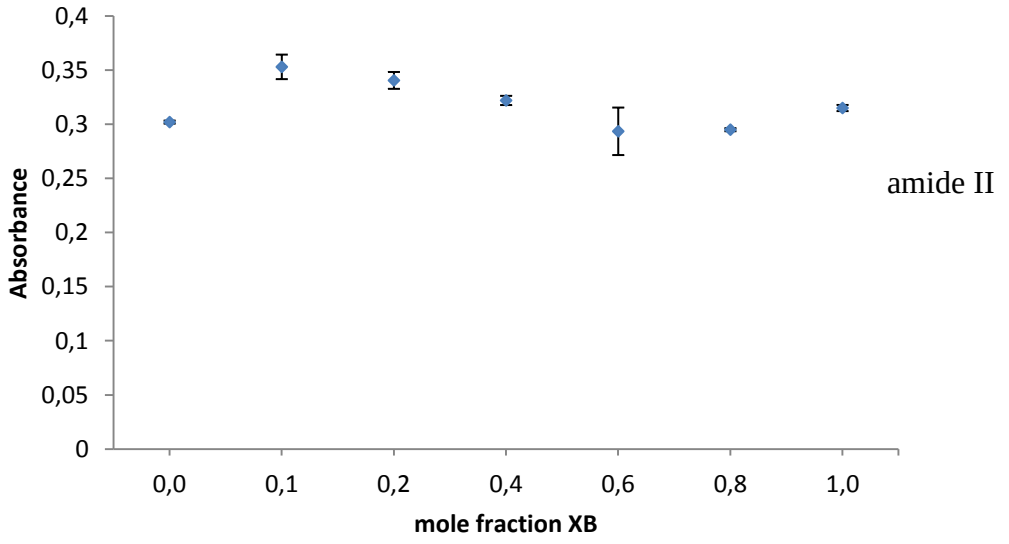

Figure 59: Absorption peak height of the amide II band of hemagglutinin as a function of the mole fraction X_B of sialic acid terminated amidine to -OH terminated amidine in the adsorption solution, the error bars are the standard deviation of three measurements on different substrates

One can observe that a sialic acid content of $X_B = 0.1$ yields in the highest intensity of the amide I and amide II band. Furthermore, the amide I band of the mixed SAMs with a sialic acid content of $X_B = 0.1$ and $X_B = 0.2$ have nearly the same absorption intensity (0.327 and 0.324). However, we can conclude that similar amounts of hemagglutinin are adsorbed. Looking at the amide II band, all mixed amphiphile layers show similar values for the absorption intensity (0.294 – 0.353). Only the layer without sialic acid (hydroxylated layer) shows a decrease in absorption intensity. This results are in comparison with the *in-situ* ellipsometry results, where we could achieve the highest hemagglutinin film thickness with a sialic acid content of $X_B = 0.2$.

3.4 Detection of influenza virus like particles (VLPs) with sialic acid terminated amphiphile SAMs

To investigate detection of influenza viruses with the biosensor system, viruses like particles were chosen as model analytes. They mimic the structure and binding sites of the authentic influenza virus particles,[147] including the important protein for binding: hemagglutinin (HA).[148] VLPs do not contain the genetic material of the pathogen and therefore they are not infectious and safe to use.[149] The influenza VLPs were kindly provided by Prof Dr. Reingard Grabherr from the Institute of Applied Microbiology in Vienna, Austria. The original concentration of H5N1 virus like particle was approximately 32 HA units per 50 µL. For further investigations the VLPs were diluted with HEPES buffer to the desired concentrations (pH 8, 10 mM). In a first series of measurements the optimal sialic acid content for VLP binding was investigated. The MHA coated substrate was mounted into the ellipsometer cuvette and HEPES buffer (pH 8, 10 mM) was added. Subsequently, 50 µM of amphiphile solution was added. The ratios tested contained 0, 10, 20, 40, 60, 80 and 100% of sialic acid terminated to hydroxylated amidine (X_B = 0, 0.1, 0.2, 0.4, 0.6, 0.8 and 1), respectively. For this experiments, the H5N1 titer was 29 HA units per 1.7 mL cuvette volume. Influenza VLPs are 30 - 100 nm in diameter.[141,28,150] The *in-situ* ellipsometry results show a maximum film thickness for influenza VLPs of 4.1 ± 0.1 nm when a sialic acid content of X_B = 0.2 was used (Figure 62). Pereira et al. investigated influenza VP binding on functionalized Si/SiO_2 wafer substrates.[141] Pereira used a carbohydrate binding protein (concanavalin A) as an anchor for VP. They achieved film thicknesses of about 3.0 - 3.5 nm, and concluded that the surface is not fully covered with virus particles. Our results for the achieved thicknesses are in the same range as Pereira's.[141]

Reversibility was tested by rinsing the cuvette with a buffer at pH 3. The film thicknesses of the other rSAM mixtures are summarized in Figure 63.

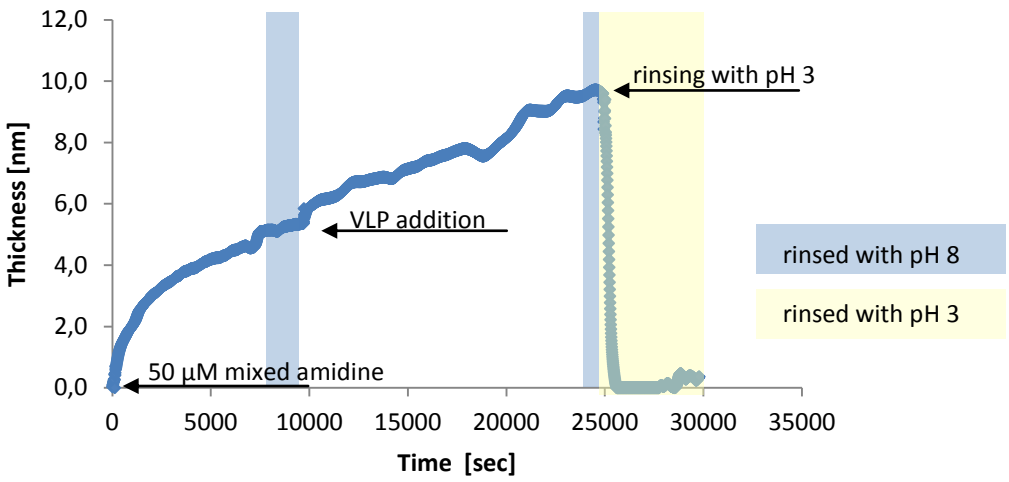

Figure 60: Assembly and disassembly kinetics of influenza virus like particles (29 HA units) on sialic acid terminated rSAM (X_B = 0.2)

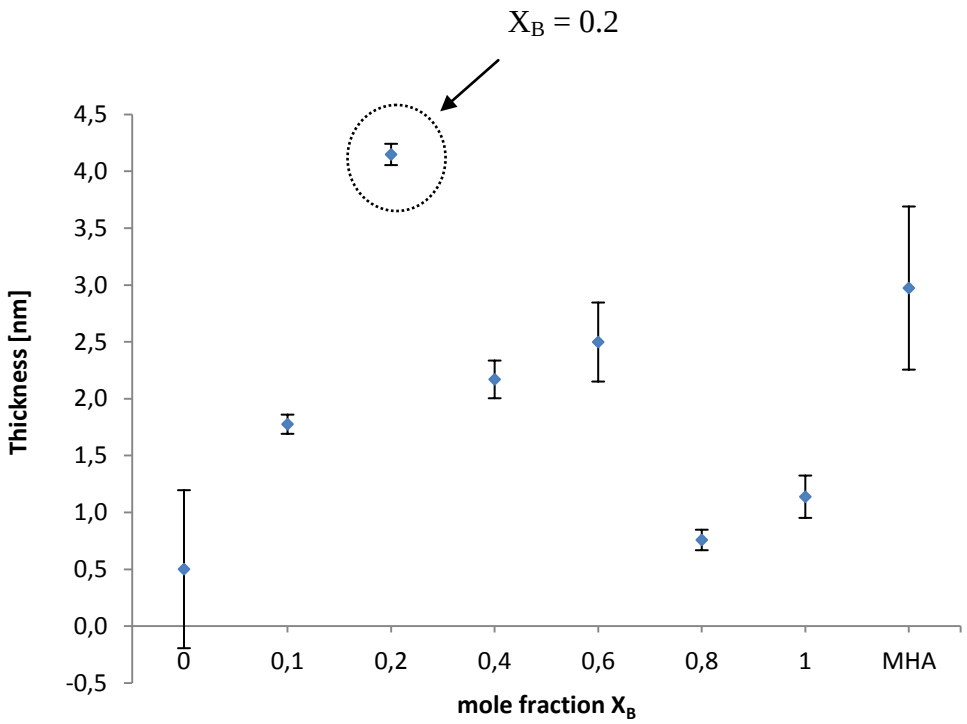

Figure 61: Film thickness of VLPs on different mixed amphiphiles measured by *in-situ* ellipsometry versus mole fraction X_B. The error bar is a result of measuring three replicates

The mixed rSAMs with a sialic acid content of X_B = 0.1 resulted in 1.8 ± 0.1 nm film thickness for VLP assembly. When a sialic acid content of X_B = 0.4 was used it resulted in a film thickness of 2.2 ± 0.2 nm. However, the hydroxylated sample showed a film thickness of only 0.5 nm with a high standard deviation.

VLP assembly on mercaptohexadecanoic acid (MHA) resulted in 2.9 ± 0.7 nm. The increase of film thickness of VLPs for the MHA layer can be attributed to unspecific binding. Huang et al. report similar observations.[151] They tried to assemble influenza virus particles on negatively and positively charged surfaces and found that the virus particles bind unspecifically to both surfaces in the same manner. In conclusion, they wrote that influenza VPs, which have a pI of 5, carry local positive charges.

In order to examine the topography and the surface coverage with VLPs we used AFM for further investigations. Atomic force microscopy measurements were carried out with the help of Nico Zamarelli from the Technische Universität Dortmund. The measurements were carried out in dynamic contact mode (tapping mode). Samples were prepared by immersion in 0.02 mM MHA in ethanolic solution overnight. After assembly the substrates were rinsed with copious amounts of ethanol and dried under nitrogen flow. Samples containing a mixed rSAM (X_B = 0.2) were prepared by immersion of MHA coated substrate in 50 µM amidine solution for > 2h (pH 8, HEPES buffer). Subsequently, the substrate was rinsed with buffer and dried under nitrogen flow. HEPES solution containing 29 HA units in 1.7 mL were used to assemble the VLPs. The sample was rinsed with buffer and dried under nitrogen flow. The AFM image (Figure 62) shows that VLPs are sparsely distributed on the substrate. In the section analysis a height of about 60 - 70 nm was observed. This height was attributed to influenza virus like particles which are 30 - 100 nm in diameter. [28,141,150]

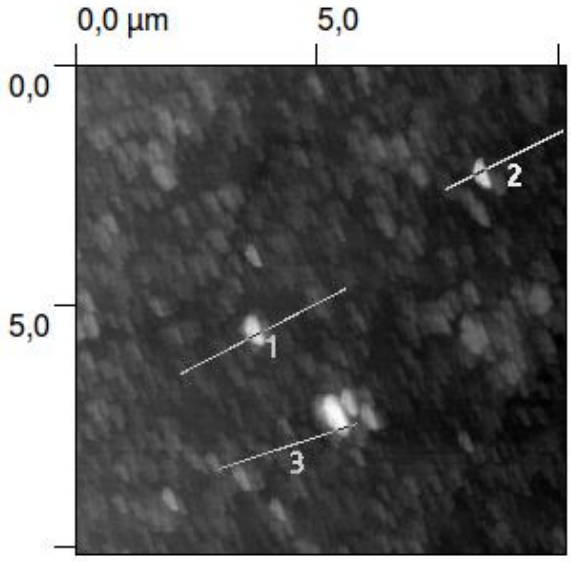

Figure 62: AFM image of surface section of 1 µm x 1 µm of influenza VLP on sensor surface

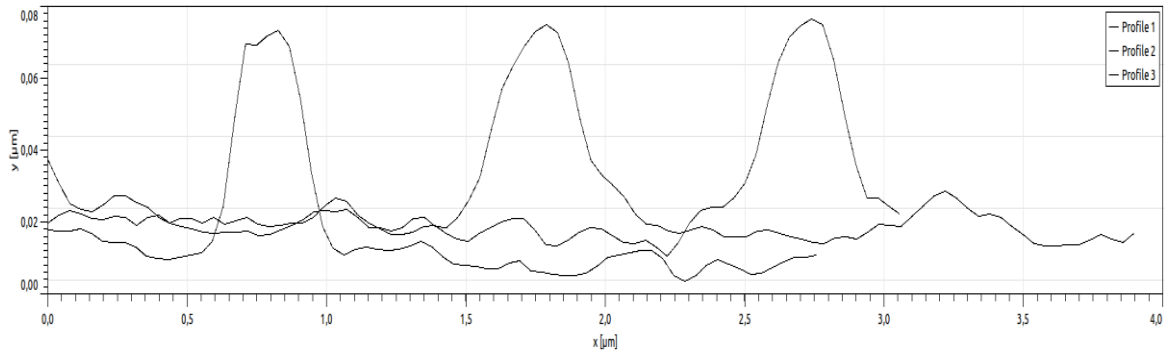

Figure 63: Section analysis of the VLPs. Profile numbers correspond to line numbers in Figure 64

3.4.1 Conclusion sialic acid terminated SAMs

By introducing the biologically active ligand sialic acid to the amphiphile, a sensor for hemagglutinin was generated. Hemagglutinin, which is present on the surface of influenza viruses, was detected subsequently. Following, we tested the detection of influenza virus-like-particles (VLPs) by the biosensor.

In a first series of experiments the sialic acid terminated molecule was investigated. The molecule size estimated by ChemDraw was ~ 4.8 nm in stretched configuration. The thickness observed with *in-situ* ellipsometry was 3.0 ± 1.2 nm when only sialic acid terminated molecules were assembled. Diluting the latter with the hydroxylated spacer molecule increased the film thickness due to higher organization within the film. Without the spacer, the voluminous sialic acid head groups sterically hinder a close and therefore ordered packing. In order to find the optimal conditions for HA assembly, different ratios of sialic acid terminated to hydroxylated amphiphiles (X_B) were tested. The ratio, which resulted in the highest HA binding was 2;8 (X_B = 0.2). The film thickness of HA here was 1.7 ± 0.3 nm. This film thickness is not equivalent to a complete monolayer coverage. From X-ray diffraction we know that the molecule has a size of 6.6 nm x 11.6 nm x 11.8 nm.[142] Therefore, we have to conclude that the density of HA on the film is low. We developed a model which can explain the low HA density. The most reasonable explanation would be that the hydroxylated spacer molecule is too short to stabilize the sialic acid terminated amphiphile via van der Waals interactions among the chain. Therefore, the sialic acid terminated molecule might bend and hinder the accessibility needed for the binding between SA and HA. To avoid this problem, longer spacer molecules should be synthesized, which could stabilize the entire alkyl chain.

The stability of the sensor was confirmed by rinsing the films with a solution at pH 8 after the addition. Decreasing the pH of the solution to 3 triggers a disassembly of the biosensor. The covalently bound mercaptohexadecanoic acid SAM was stable and the sensor sample could be reused several times. After the binding behavior of the free HA had been studied, virus like particle binding upon addition to mixed amphiphile assemblies was explored. The optimal condition for the binding of VLPs was tested by assembly of different ratios for sialic acid terminated to hydroxylated amphiphile. The optimal ratio for VLP binding was the same as for HA binding. The molar ratio X_B = 0.2 turned out to be the best. The film thickness obtained was 4.1 ± 0.1 nm. We compared this size with dimensions reported in literature (30 - 100 nm diameter). [28,141,150] Since the film thickness is lower than the dimension reported, we have to assume that the density of VLPs which is assembled on the

rSAM is not optimal. The surface coverage seems to be only 4 - 13% (calculated from the average film thickness measured by ellipsometry). These conclusions are supported by AFM investigations. VLPs could be identified with AFM with a size of ~ 60 nm. The stability of the sensor was tested by rinsing the films with solutions at pH 8 after the assembly. When the sample solution was acidified to pH 3 the biosensor assembly consisting of amphiphile and VLP was removed. Hence the mercaptohexadecanoic acid SAM was stable and the sensor could be reused several times.

IRRAS experiments proofed the assembly of HA, since we could identify the most common peaks for proteins. Typically, one should observe amide I and amide II bands.[32,33] Herein, the band at ~1658 cm^{-1} was assigned to the amide I band , whereas the amide II band could be detected at ~1525 cm^{-1}, respectively. Contact angle measurements proofed the hydrophobicity after protein assembly. The hydrophobic behavior of this protein can be attributed to the hydrophobic interactions and the low polarity of the protein.[35]

3.4.2 Comparison of the sensor devices and Outlook

If we compare the first sensor, which is based on antibody/antigen interactions, with the second sensor based on SA/HA interactions, we have to point out that the first sensor seems to be more effective. The reason could be the strong affinity of the binding between antibodies and antigens with K_a values of $>10^{11}$ L/mol.[59] Association constants of sialic acid to hemagglutinin are lower than the values for antibodies and antigens. They are in the range of $\sim 2 * 10^3$ L/mol.[152] We also observed that the second sensor needs a longer assembly time (the time until HA or VLP equilibrium is reached). This effect can also be attributed to the significantly lower association constant. One of the advantages of the second sensor is the simple architecture. Only three different chemical molecules are used to set up this sensor for detection. The sensor can be built up in two immersion steps and is ready for detection. The first sensor on the other hand has an architecture, which requires not only the chemical compounds, but also biomolecules such as biotin, STV and a biotinylated antibody for antigen detection. Disadvantages using antibodies for capturing is the high cost of antibodies and the preparation method.[64]

In this thesis we could demonstrate the usage of rSAMs as biosensing device; with the great advantage of substrate reusability. By applying two different functionalized amphiphiles, we could produce two biosensors with outstanding sensing applications, which are the detection of prostate cancer markers from real samples and the detection of influenza virus like particles. Further studies should now focus on the more effective binding of influenza VLPs on the sialic acid terminated device. One should focus on the polyvalence of viruses and therefore on the addition of further functionalized amphiphiles, for example with an oseltamivir functional group. Oseltamivir is a compound, which is also known to interact with influenza viruses.[153] The lateral mobility of the rSAMs could make polyvalent binding to the device possible.

4 Experimental Section

4.1 Synthesis of α,ω-hetero-functionalized amphiphiles

4.1.1 Synthesis of 4-((10-bromodecyl)oxy)benzonitrile (AT1)

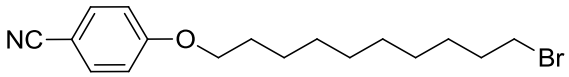

To a dry, nitrogen filed two neck flask, equipped with a stir bar, 25.19 g (83.9 mmol, 1 eq.) of 1,10 dibromodecane and 5 mL dry acetone were added. The mixture was heated to 40°C and 1 g (8.39 mmol, 0.1 eq.) of 4-cyanolphenol and 2.3 g (16.8 mmol, 0.2 eq.) K_2CO_3 were added. After reflux for 48h the K_2CO_3 was filtered off and washed with dry acetone. The crude product was purified by column chromatography (1:10 ethylacetate/n-hexan). The organic fraction was concentrated *in vacuo*. The product **AT1** was obtained as a white solid in 84.4% yield.

^{1}H NMR (300 MHz, Chloroform-d) δ 7.56 (d, *J* = 8.8 Hz, 2H), 6.92 (d, *J* = 8.9 Hz, 2H), 3.98 (t, *J* = 6.5 Hz, 2H), 3.40 (d, *J* = 6.8 Hz, 2H), 1.87 – 1.76 (m, 4H), 1.43 – 1.24 (m, 12H).

HR-ESI-MS: calc. $C_{17}H_{24}BrNO$ $[M+H]^+$ m/z 338.1114 found 338.1116.

4.1.2 Synthesis of 2-[4-(8-Bromo-octyloxy)-phenyl]-ethanol (AT2)

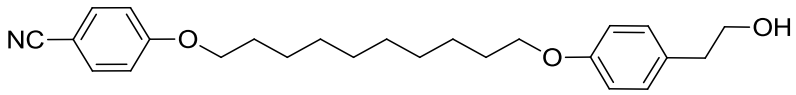

To a dry, nitrogen filed two neck flask, equipped with a stir bar, **AT1** (4-((10-bromodecyl)oxy)benzonitrile) (0.053g, 0.16 mmol) and 5 mL of dry acetone was added. At 40°C, K_2CO_3 (0.044g, 0.32mmol) and 4-(2-hydroxyethyl)phenol (0.043g, 0.32mmol) were added. After 24h under reflux, K_2CO_3 was filtered off and resulting solution was dried under reduced pressure at 40°C to yield in crude product. The crude product was purified by column chromatography (3:8 ethylacetate/n-hexan). The product **AT2** was obtained as a white solid in 81.6% yield.

^{1}H NMR (300 MHz, Chloroform-d) δ 7.56 (d, *J* = 8.9 Hz, 2H), 7.12 (d, *J* = 8.6 Hz, 2H), 6.92 (d, *J* = 8.9 Hz, 2H), 6.83 (d, *J* = 8.4 Hz, 2H), 3.97 (t, *J* = 6.4 Hz, 2H), 3.91 (t, *J* = 6.4 Hz, 2H), 3.82 (t, *J* = 6.4 Hz, 2H), 2.81 (t, *J* = 6.5 Hz, 2H), 1.86 – 1.70 (m, 4H), 1.54 – 1.48 (m, 12H).

HR-ESI-MS: calc $C_{25}H_{33}NO_3$ $[M+H]^+$ m/z 396.2544 found 396.2533.

4.1.3 Pinner-Synthesis of 4-{10-[4-(2-Hydrody-ethyl)-phenyoxy]-decyloxy}-benzamidine hydrochloride (AT3)

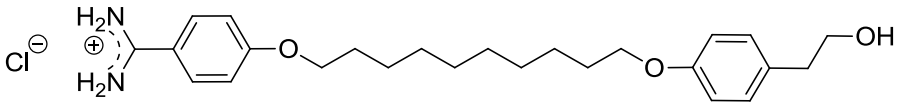

To a two neck flask equipped with a stir bar, **AT2** (4-(10-(4-(2-hydroxyethyl) phenoxy) decaloxy) benzonitril) (0.5g, 1.26mmol), dry benzene (50 mL) and dry methanol (5 mL). An addition funnel filled with 80 mL sulfuric acid was attached to a 250 mL 2-neck round bottom flask with sodium chloride (16 g, 0.54 mol). Sulfuric acid was slowly dropped into the NaCl to generate HCl. The produced HCl was bubbled into the reaction mixture for 30 min at 0°C. The mixture was stirred for 3 days under nitrogen atmosphere at RT. The final solution was concentrated *in vacuo* at 40°C to yield in the crude product. Pinner-salt was dissolved in 5 mL MeOH, precipitated with diethylether and Schlank-filtered. The salt was dissolved in 50 mL of dried MeOH and 50 mL of 7N methanolic ammonia. The solution was heated at 60°C for 6h. The product was concentrated *in vacuo* and precipitated in diethylether. The product **AT3** was obtained as a white solid in ~100% yield.

^{1}H NMR (400 MHz, DMSO-d6) δ 9.11 (s, 2H), 8.76 (s, 2H), 7.77 (d, *J* = 8.9 Hz, 2H), 7.11 (d, *J* = 8.9 Hz, 2H), 7.05 (d, *J* = 8.5 Hz, 2H), 6.76 (d, *J* = 8.5 Hz, 2H), 4.56 (t, *J* = 5.2 Hz, 1H), 4.04 (t, *J* = 6.5 Hz, 2H), 3.86 (t, *J* = 6.4 Hz, 2H), 3.54 – 3.44 (m, 2H), 2.59 (t, *J* = 7.2 Hz, 2H), 1.71 – 1.62 (m, 4H), 1.37 – 1.26 (m, 12H).

HR-ESI-MS: calc $C_{25}H_{36}N_2O_3$ $[M+H]^+$ m/z 413.2799 found 413.2795.

4.1.4 Synthesis of [(4-{10-[4-(2-Hydroxy-ethyl)-phenoxy]-decyloxy}- phenyl)-imino-methyl]-carbamic acid *tert*-butyl ester (AT4)

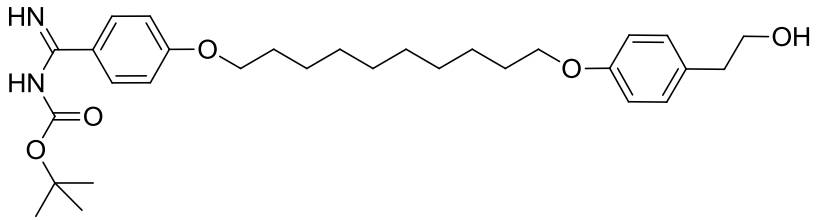

To a two neck flask equipped with a stir bar, **AT3** 4-10-[4-(2 hydroxyethyl)phenoxy]decoxybenzamidinehydrochloride) (0.0514g, 0.114 mmol), 20 mL of DI water, 2 mL NaOH (3N) and 22 mL THF were added. At 0°C, boc anhydride (Boc_2O) (0.250 g, 1.14 mmol) was added drop wise to the solution which was stirred for 3 hours. The reaction mixture was concentrated *in vacuo* and extracted with EtOAc and H_2O. Organic phase was dried with sodium sulfate and concentrated under reduced pressure to yield in 67% of the yellowish solid product **AT4**. The product was used without further purification.

^{1}H NMR (400 MHz, DMSO-d6) δ 7.84 (dd, *J* = 44.5, 8.5 Hz, 1H), 7.68 (d, *J* = 8.5 Hz, 2H), 7.05 (d, *J* = 8.5 Hz, 2H), 6.92 (d, *J* = 8.4 Hz, 2H), 6.76 (d, *J* = 8.5 Hz, 2H), 3.96 (t, *J*=6.40 Hz, 2 H), 3.86 (t, *J*=6.40 Hz, 2 H);), 3.51-4.47 (m, 3H), 2.61 – 2.47 (m, 2H), 2.49 (m, 4H), 1.70 – 1.33 (m, 9H), 1.33 – 1.13 (m, 12H).

^{13}C NMR (101 MHz, Chloroform-d) δ 162.37, 157.70, 130.03, 129.81, 128.97, 114.50, 114.25, 68.10, 67.87, 63.72, 38.15, 29.32, 29.18, 28.97, 28.10, 25.91, 25.83.

HR-ESI-MS: calc $C_{30}H_{44}N_2O_5$ $[M+H]^+$ m/z 513.3323 found 513.3330.

4.1.5 Synthesis of 5-(2-Oxo-hexahydro-thieno[3,4-*d*]imidazol-6-yl)-pentanoic acid 2-{4-[10-(4-carbamimidoyl-phenoxy)-decyloxy]-phenyl}-ethyl ester triflouro acetic acid (biotinylated amphiphile) (AT5)

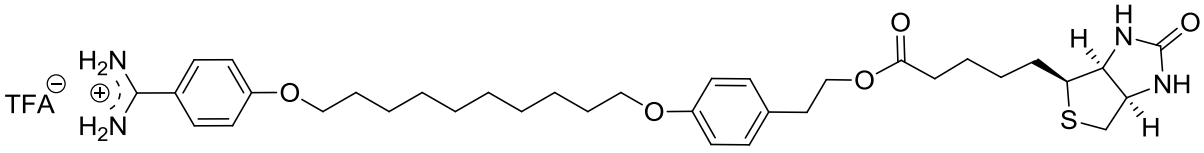

To a N_2 flushed round bottom flak equipped with a stir bar, **AT4** [(4-{10-[4-(2-hydroxy-ethyl)-phenoxy]-decyloxy}-phenyl)-imino-methyl]-carbamic acid tert-butyl ester (0.4 g, 0.78 mmol), 10 mL dry acetone and 10 mL dry toluene were added. A solution of biotin chloride (0.226 g, 0.858 mmol), 5 mL dry acetone and K_2CO_3 (0.7g, 5.1 mmol) were added to the above mixture. The reaction mixture was heated to 50°C for 12h. The solution was filtered and concentrated *in vacuo*. The crude product **AT5** was dissolved in 10 mL DCM, and 3 mL TFA was added drop wise at 0°C. Reaction mixture was allowed to warm up to RT and stirred for 2 h. The crude product was concentrated *in vacuo* before recrystallization with ethanol. The product **AT5** was obtained as a yellow solid in a yield of 34%.

^{1}H NMR (400 MHz, DMSO-d6) δ 9.08 (s, 2H), 8.68 (s, 2H), 7.76 (d, *J* = 8.8 Hz, 2H), 7.20 – 7.04 (m, 4H), 6.80 (d, *J* = 8.5 Hz, 2H), 6.41 (s, 1h), 6.33 (s, 1H), 4.26 (t, 8.0 Hz, 1H), 4.10 – 4.01 (m, 4H), 3.87 (t, 8.0 Hz, 2H), 3.39 (d, *J* = 13.8 Hz, 2H), 2.77-2.74 (m, 4H), 2.16 (t, *J* = 8.0 Hz, 2H), 1.71 - 1.62 (m, 6H), 1.44 – 1.14 (m, 14H).

MALDI TOF MS: $C_{35}H_{52}N_4O_5S$ $[M+Na]^+$ m/z = 664.748, $C_{35}H_{52}N_4O_5S$ $[M+2Na]^+$ m/z = 686.752, $C_{35}H_{52}N_4O_5S$ $[M+3Na]^+$ m/z = 708.866

4.1.6 Synthesis of 2-(2-(2-chloroethoxy)ethoxy)acetic acid (AT6)

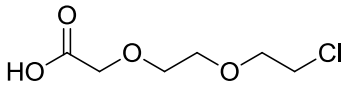

To a round bottom flask, equipped with a stir bar, 2-[2-(2-chloroethoxy) ethoxy] ethanol (6.6 g, 39.14 mmol, 1.0 eq.), $NaHCO_3$-solution (120 mL, 15 wt%), acetone (250 mL) were added. At 0°C KBr (0.93 g, 7.8 mmol, 0.19 eq.) and TEMPO (0.12 g, 0.77 mmol, 0.02 eq.) were added. Trichlorisocyanuric acid (TCCA) (18.30 g, 78.7 mmol, 2.0 eq.) was dissolved in acetone (80 mL), and dripped into the reaction mixture over 20 min at 0°C. The reaction was allowed to reach RT, and was stirred for additional 28h. The reaction was determined over by TLC. 2-Propanol (50 mL) was added and stored overnight. Afterwards, the mixture was filtered over Celite 545. The mixture was concentrated *in vacuo*, and the crude product was treated with Na_2CO_3-solution until pH 10. The byproduct was extracted with EtOAc (2x100 mL). The aqueous phase was acidified with 1M HCl until pH 2. Then the mixture was extracted with EtOAc (2x150 mL). Organic phase was dried with sodium sulfate and concentrated under reduced pressure. The product **AT6** obtained as a pink liquid in 56% yield.

^{1}H NMR (400 MHz , Chloroform-d) δ 10.93 (s, 1H), 4.16 (s, 2H), 3.73 – 3.70 (m, 4H), 3.68 – 3.66 (m, 2H), 3.58 (t, *J* = 5.8 Hz, 2H).

^{13}C NMR (101 MHz, Chloroform-d) δ 174.82, 71.20, 70.87, 70.36, 68.17, 42.48.

HR-ESI-MS: calc $C_6H_{11}O_4Cl$ $[M+H]^+$ m/z 183.0419 found 183.0419.

4.1.7 Synthesis of methyl 2-(2-(2-chloroethoxy)ethoxy)acetate (AT7)

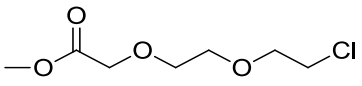

To a flask, equipped with a stir bar, **AT6** 2-(2-(2-chloroethoxy)ethoxy)acetic acid (3.9 g, 21.6 mmol, 1 eq.) was dissolved at 0°C in dry methanol (40 mL). NaOMe (1.2 g, 22 mmol, 1 eq.) was added and stirred for 20 min without further cooling. Reaction was dried *in vacuo* at 40°C. The crude product was dissolved in dry DMF at 0°C under nitrogen atmosphere, and MeI (6.13 g, 43.2 mmol, 2 eq.) was added drop wise. The reaction mixture was stirred for 40h at RT. The crude product was concentrated *in vacuo* and dissolved in chloroform (120 mL). The organic solution was washed with 20 mL of 1 M HCl, 20 mL sat. $NaHCO_3$ and 20 mL of brine. Organic phase was dried with sodium sulfate and concentrated under reduced pressure. The product **AT7** was purified with gradient flash chromatography, ($CHCl_3$/MeOH, 1:0→10:1) to yield in 57% of the yellowish oily product.

^{1}H NMR (500 MHz, Chloroform-d) δ 4.07 (s, 1H), 3.71 – 3.58 (m, 9H), 3.53 (t, *J* = 5.8 Hz, 2H).

^{13}C NMR (126 MHz, Chloroform-d) δ 170.66, 71.20, 70.76, 70.55, 68.47, 51.60, 42.65.

HR-ESI-MS: calc $C_7H_{13}O_4Cl$ $[M+H]^+$ m/z 197.0575 found 197.0627.

4.1.8 Synthesis of methyl 2-(2-(2-azidoethoxy)ethoxy)acetate (AT8)

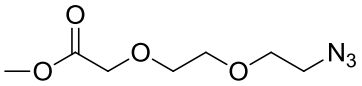

To a dry, nitrogen filled two neck flask, equipped with a stir bar, **AT7** methyl 2-(2-(2-chloroethoxy)ethoxy)acetate (0.82 g, 4.17 mmol, 1 eq.) and dry DMF (70 mL) were added. NaN_3 (1.35 g, 20.85 mmol, 5 eq.) was added to the solution and was stirred at 70 °C for 24 h. Reaction mixture was allowed to cool to RT, filtered and was washed with 5 mL chloroform. The organic solution was washed with 20 mL of 1 M HCl, sat. $NaHCO_3$ and brine, respectively.The organic phase was dried with sodium sulfate, filtered and concentrated under reduced pressure. The product **AT8** was obtained as a yellow oil in 95% yield.

^{1}H NMR (400 MHz, Chloroform-d) δ 4.04 (s, 2H), 3.61 (s, 3H), 3.60 -3.58 (m, 2H), 3.57 – 3.54 (m, 4H), 3.26 (t, J = 4.0 Hz, 2H)

^{13}C NMR (500 MHz, Chloroform-d) δ 170.77, 70.96, 70.68, 70.01, 68.63, 51.72, 50.64.

HR-ESI-MS: calc $C_7H_{13}O_4N_3$ $[M+H]^+$ m/z 204.0979 found 204.0982.

4.1.9 Synthesis of 2-(2-(2-azidoethoxy)ethoxy)acetic acid (AT9)

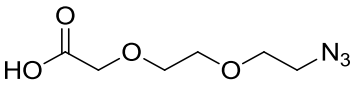

To a flask, equipped with a stir bar, **AT8** methyl 2-[2-(2-Azidoethoxy) ethoxy]acetate (0.080 g, 4.06 mmol, 1 eq.), DI water (5 mL) and MeOH (5 mL) were added. The reaction mixture was stirred at RT for 18 h. The mixture was neutralized with 1 N HCl and concentrated under reduced pressure at 40°C. The crude product was dissolved in chloroform and filtered. The organic fraction was washed with 20 mL of 1 N HCl and 3x 20 mL brine. The organic phase was dried with $MgSO_4$ and the solvent was evaporated at 40°C. The product **AT9** was obtained as a green/yellow oil in 63% yield.

^{1}H NMR (400 MHz, Chloroform-d) δ 10.55 (s, 1H), 4.15 (s, 2H), 3.66 – 3.62 (m, 6H), 3.36 – 3.34 (m, 2H).

^{13}C NMR (101 MHz, Chloroform-d) δ 174.68, 70.96, 70.38, 69.91, 68.20, 50.44.

HR-ESI-MS: calc $C_6H_{11}O_4N_3$ $[M+H]^+$ m/z 190.0822 found 190.0828.

4.1.10 Synthesis of 4-((10-(4-(N-(tert-butoxycarbonyl)carbamimidoyl) phenoxy) decyl)oxy) phenethyl 2-(2-(2-azidoethoxy)ethoxy)acetate (AT10)

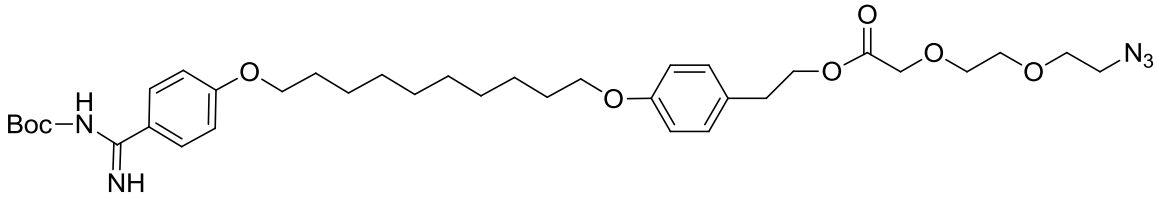

To a dry, nitrogen filled two neck flask, equipped with a stir bar, **AT4** (tert-butyl ((4-((10-(4-(2-hydroxyethyl)phenoxy)decyl)oxy)phenyl)(imino)methyl)carbamate) (0.189 g, 0.36 mmol, 1 eq.), **AT 9** (2-(2-(2-azidoethoxy)ethoxy)acetic acid) (0.08 g, 0.4 mmol, 1.1 eq.) and dry DCM (40 mL) were added. At 0°C, DMAP (0.0094 g, 0.08 mmol) and DCC (0.080g, 0.4 mmol) were added. The reaction was stirred for 2h. The byproducts were filtered off, and the organic fraction was washed with 20 mL of 1 M HCl and 3x 20 mL of brine. The product was dried under reduced pressure at 40°C. The product **AT10** was obtained as a yellowish solid in 75% yield.

^{1}H NMR (400 MHz, $CDCl_3$) δ 7.80 (d, *J* = 8.9 Hz, 2H), 7.07 (d, *J* = 8.6 Hz, 2H), 6.95 (s, 1H), 6.86 (d, *J* = 8.9 Hz, 2H), 6.79 (d, *J* = 8.6 Hz, 2H), 4.29 (t, *J* = 7.1 Hz, 2H), 4.10 (s, 2H), 3.95 (t, *J* = 6.5 Hz, 2H), 3.88 (t, *J* = 6.5 Hz, 2H), 3.72-3.62 (m, 4H), 3.35 (t, 7.1 Hz, 2H), 2.86 (t, *J* = 7.1 Hz, 2H), 1.78 – 1.67 (m, 6H), 1.47 – 1.37 (m, 9H), 1.30 – 1.22 (m, 12H).

^{13}C NMR (101 MHz, MeOD-d_4) δ 170.71, 166.67, 162.91, 157.81, 151.09, 129.86, 129.40, 124.96, 114.02, 113.78, 81.43, 70.27, 70.14, 69.61, 67.75, 67.41, 65.09, 50.22, 33.63, 33.24, 29.08, 28.90, 28.70, 26.83, 25.64, 25.23, 24.55.

HR-ESI-MS: $C_{36}H_{53}N_5O_8$ $[M+H]^+$ m/z calc 684.3967 found 684.3966.

4.1.11 Synthesis of 4-{10-[2-(2-(2-azidoethoxy)ethoxy)acetate-phenyoxy]-decyloxy}-benzamidine hydrochloride (AT11)

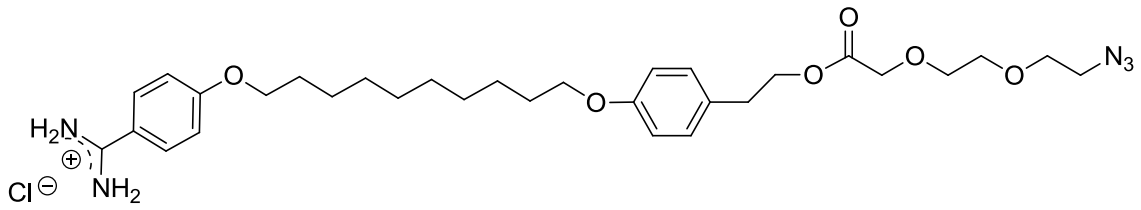

To a nitrogen purged round bottom flask, equipped with a stir bar, **AT10** (4-((10-(4-(N-(tert-butoxycarbonyl)carbamimidoyl)phenoxy)decyl)oxy)phenethyl2-(2-(2-azidoethoxy) ethoxy) acetate) (182 mg, 0.266 mmol, 1 eq.) and dry chloroform (15 mL) were added. At 0°C, TFA (200 µL, 0.266 mmol, 1 eq.) was added to solution and stirred for 3h. The product was dried *in vacuo* at 40°C. The crude product was dissolved in 2 mL of acetone and recrystallized with 10 mL diethylether. The product **AT 11** was obtained as a white solid in 27% yield.

^{1}H NMR (500 MHz, $CDCl_3$) δ 7.80 (s, 2H), 7.50 (d, J = 8.8 Hz, 2H), 7.04 (d, J = 7.7 Hz, 2H), 6.89 (s, 2H), 6.86 (d, J = 10 Hz, 2H), 6.76 (d, J = 8.4 Hz, 2H), 4.26 (t, J = 7.0 Hz, 2H), 4.07 (s, 2H), 3.95 – 3.84 (m, 4H), 3.65 – 3.61 (m, 4H), 3.34 – 3.30 (m, 2H), 2.82 (t, J = 7.1 Hz, 2H), 1.71 (m, 6H), 1.39 (m, 4H), 1.26-1.19 (m, 8H).

^{13}C NMR (101 MHz, Chloroform-d) δ 170.28, 157.80, 133.84, 129.71, 129.07, 115.04, 114.43, 114.40, 70.86, 70.61, 69.96, 68.63, 68.27, 67.85, 65.38, 50.59, 34.05, 29.18, 25.81.

HR-ESI-MS: $[C_{31}H_{46}N_5O_6]^+$ m/z calc 584.3443 found 584.3443.

4.1.12 Synthesis of methyl 5-acetamido-2,4-dihydroxy-6-(1,2,3-trihydroxypropyl)tetrahydro-2H-pyran-2-carboxylate (AT12)

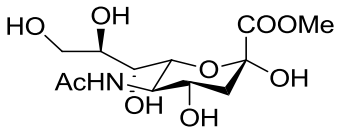

To nitrogen purged flask, equipped with a stir bar, in absence of light, sialic acid (0.530 g, 1.71 mmol, 1eq.) and dry MeOH (35 mL) were added. At RT, Dowex 50 (H^+) (0.147 g) was added and stirred for 24h. Reaction mixture was filtered and washed with 5 mL of dry MeOH. Organic phase was dried *in vacuo* and the product **AT12** was obtained as a white solid in 98% yield.

^{1}H NMR (400 MHz, MeOD-d_4) δ 4.07 – 3.92 (m, 2H), 3.82 – 3.77 (m, 2H), 3.76 (d, *J* = 4.0 Hz, 3H), 3.72 – 3.64 (m, 1H), 3.59 (dd, *J* = 11.2, 5.7 Hz, 1H), 3.45 (d, *J* = 10.4 Hz, 1H), 2.19 (dd, *J* = 12.9, 4.9 Hz, 1H), 1.99 (s, 3H), 1.89 (t, *J*=12.17 Hz, 1 H).

^{13}C NMR (101 MHz, MeOH-d_4) δ 173.57, 170.22, 95.14, 70.56, 70.11, 68.66, 66.33, 63.31, 52.80, 51.60, 39.18, 21.11.

HR-ESI-MS: $C_{13}H_{21}NO_{10}$ $[M+H]^+$ calc m/z 324.1289 found 324.1288.

4.1.13 Synthesis of 3-acetamido-4-acetoxy-6-chloro-6-(methoxycarbonyl)tetrahydro-2H-pyran-2-yl)propane-1,2,3-triyl triacetate (AT13)

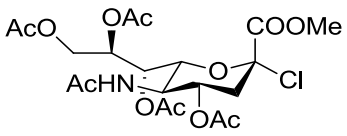

To a nitrogen purged flask, equipped with a stir bar, **AT12** (methylated sialic acid) (0.056 g, 0.17 mmol, 1eq.) and dry AcCl (3.5 mL, 0.049 mol) were added. The reaction mixture was cooled to 0°C and saturated with HCl-gas for 20 min. Mixture was stirred for 3 days at RT under nitrogen atmosphere. The reaction mixture was filtered over Celite and washed with 5 mL of dry toluene. Product **AT13** was dried *in vacuo* to obtain a white foam in 97% yield.

^{1}H NMR (500 MHz, $CDCl_3$) δ 7.25 (s, 1H), 6.06 (d, *J* = 8.8 Hz, 1H), 5.42 (d, *J* = 6.1 Hz, 1H), 5.35 – 5.31 (m, 1H), 5.12 – 5.10 (m, 1H), 4.40 – 4.32 (m, 2H), 4.03 – 4.00 (m, 1H), 3.81 (s, 3H), 2.72 (dd, *J* = 13.9, 4.3 Hz, 1H), 2.21 (d, *J* = 11.4 Hz, 1H), 2.06 – 1.98 (m, 12H), 1.85 (s, 3H).

^{13}C NMR (126 MHz, Chloroform-d) δ 170.90, 170.63, 169.92, 166.41, 165.58, 96.65, 73.87, 70.14, 68.80, 66.99, 53.72, 48.52, 40.60, 22.97, 22.13, 20.66.

HR-ESI-MS: [$C_{20}H_{28}ClNO_{12}$] calc m/z 509.2359 found 509.2340.

4.1.14 Synthesis of 3-acetamido-4-acetoxy-6-(but-3-yn-1-yloxy)-6-(methoxycarbonyl) tetrahydro-2H-pyran-2-yl) propane-1,2,3-triyl triacetate (AT14)

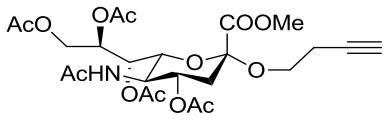

To a dry, nitrogen filled round bottom flask, acetylated sialic acid **(AT13)** (0.787 g, 1.55 mmol, 1 eq.), dry acetonitrile (45 mL, 0.8 mmol, 0.5 eq.) and 2 g of 0.45 Å molecular sieves were added. Butagylalcohol (1.16 mL, 15.5 mmol, 10 eq.) was added, and the reaction mixture was shaken for 1h. Sequentially, in the dark, triflat (0.720 g, 4.8 mmol, 3 eq.) was added, and the mixture was shaken for 16h. The reaction mixture was filtered over Celite and washed with 50 mL of dry ACN. Product was dried *in vacuo* and dissolved on 80 mL chloroform. The organic fraction was washed with 40 mL of $NaHCO_3$ and 50 mL brine. The organic phase was dried with Na_2SO_4 and the solvent was evaporated at 40°C. The product was purified with column chromatography, (Petrolether/DCM/iso-Propanol, 8:4:1). The product **AT14** was achieved in 48% yield as a yellowish oil.

^{1}H NMR (400 MHz, Chloroform-d) δ 7.24 (s, 1H), 5.48 (s, 1H), 5.38 (s, 1H), 5.38 - 5.30 (m, 1H), 5.25 - 5.20 (m, 1H), 4.80 (d, *J* = 14.7 Hz, 1H), 4.18 (d, *J* = 10.5 Hz, 1H), 4.11 - 4.06 (m, 1H), 3.77 (s, 3H), 3.61 – 3.44 (m, 2H), 2.57 (dd, *J* = 12.8, 4.7 Hz, 1H), 2.46 – 2.41 (m, 2H) 2.11 – 1.98 (m, 15H), 1.85 (s, 3H).

^{13}C NMR (101 MHz, Chloroform-d) δ 170.96, 170.72, 170.53, 170.30, 170.11, 167.09, 125.76, 98.23, 81.36, 72.11, 71.54, 70.13, 68.75, 68.11, 62.26, 62.04, 52.70, 49.12, 37.25, 31.80, 25.21, 23.03, 21.02, 20.69, 19.57.

HR-ESI-MS: $C_{24}H_{33}NO_{13}$ $[M+H]^+$ calc for m/z 544.2033 found 544.2031.

4.1.15 Synthesis of 5-acetamido-2-(but-3-yn-1-yloxy)-4-hydroxy-6-(1,2,3-trihydroxypropyl) tetrahydro-2H-pyran-2-carboxylate (AT15)

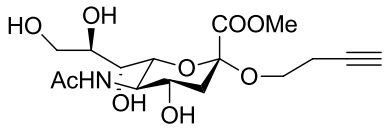

To a dry, nitrogen filled round bottom flask, **AT14** (methyl 5-acetamido-2-(but-3-yn-1-yloxy)-4-hydroxy-6-(1,2,3-trihydroxypropyl)tetrahydro-2H-pyran-2-carboxylate) (0.048 g, 0.0088 mmol, 1.0 eq.) and dry MeOH (2 mL) were added. At 0°C, NaOMe (0.5 M in methanol, 0.04 mL, 0.0199 mmol, 0.23 eq.) was added. After 3h of stirring, the reaction mixture was neutralized with Amberlite IR-120. The mixture was filtered through Celite and rinsed with 5 mL dry MeOH. The crude product was concentrated *in vacuo* and purified with gradient flash chromatography, ($CHCl_3$/MeOH, 7:1 → 4:1). The product **AT15** was achieved in 50% yield as yellowish oil.

^{1}H NMR (400 MHz, CD_3CD) δ 5.62 (s, 1H), 4.34 - 4.31 (m, 1H), 4.08 (d, *J* = 10.9 Hz, 1H), 4.00 - 3.95 (m, 1H), 4.01 – 3.95 (m, 1H), 3.86 – 3.74 (m, 9H), 3.64 – 3.59 (m, 3H), 3.49 - 3.45 (m, 1H), 2.66 (dd, *J* = 12.8, 4.6 Hz, 1H), 2.02 – 1.98 (m, 4H), 1.87 (s, 3H).

^{13}C NMR (101 MHz, $CDCl_3$) δ 170.55, 169.72, 165.42, 96.54, 73.92, 70.02, 68.83, 66.92, 62.11, 60.49, 53.98, 48.15, 40.58, 23.61, 21.26.

HR-ESI-MS: $C_{16}H_{25}NO_9$ $[M+H]^+$ calc m/z 376.1602 found 376.1603.

4.1.16 Synthesis of 5-acetamido-2-(but-3-yn-1-yloxy)-4-hydroxy-6-(1,2,3-trihydroxypropyl)tetrahydro-2H-pyran-2-carboxylic acid (AT16)

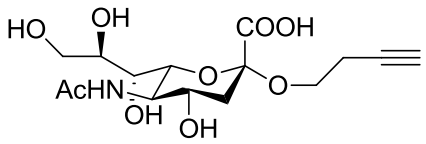

To a round bottom flask equipped with a stir bar, **AT 15** (5-acetamido-2-(but-3-yn-1-yloxy)-4-hydroxy-6-(1,2,3-trihydroxypropyl) tetrahydro-2H-pyran-2-carboxylate) (0.191 g, 0.53 mmol, 1 eq.) and MeOH (8 mL) were added. 1M NaOH (0.7 mL) was added, and reaction mixture was stirred for 16h. The mixture was neutralized with 1 M HCl and NaCl precipitated out. Product was filtered and dried *in vacuo*. The product **AT16** was obtained as a yellow solid in 98% yield.

^{1}H NMR (400 MHz, d6-DMSO) δ 8.21 (s, 1H), 8.05 (s, 1H), 5.55 (s, 1H), 5.21 (s, 1H), 4.68 (s, 1H), 4.27 (d, J = 9.0 Hz, 1H), 4.13 (s, 1H), 3.83 (d, J = 10.8 Hz, 1H), 3.57 (m, 7H), 3.12 (s, 1H), 2.75 – 2.60 (m, 2H), 2.37 – 2.19 (m, 1H), 1.85 (m, 3H).

^{13}C NMR (101 MHz, d6-DMSO) δ 172.25 , 170.24 , 100.58 , 82.29 , 76.58 , 72.32 , 71.65 , 68.95 , 66.34 , 63.76 , 61.95 , 53.38 , 51.06 , 22.96, 19.98 .

HR-ESI-MS: $C_{15}H_{23}NO_9$ $[M+H]^+$ calc m/z 362.1446 found 362.1444.

4.1.17 Synthesis of (4-((10-(4-(2-(2-(2-(2-(4-(2-((-5-acetamido-2-carboxy-4-hydroxy-6-(1,2,3-trihydroxypropyl)tetrahydro-2H-pyran-2-yl)oxy)ethyl)-1H-1,2,3-triazol-1-yl)ethoxy)ethoxy)acetoxy) methyl)phenoxy)decyl)oxy)- benzamidine hydrochloride (AT17)

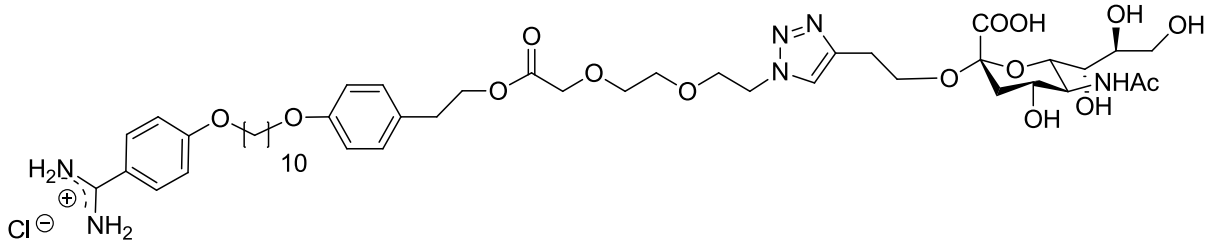

To a round bottom flask, equipped with a stir bar, **AT16** (5-acetamido-4-hydroxy-2-(prop-2-yn-1-yloxy)-6-((1R,2R)-1,2,3-trihydroxypropyl)tetrahydro-2H-pyran-2-carboxylic acid) (0.1 g, 0.27 mmol, 1 eq.), **AT11** (4-{10-[2-(2-(2-azidoethoxy) ethoxy) acetate-phenyoxy]-decyloxy}-benzamidine hydrochloride) (0.161 g, 0.27 mmol, 1 eq.) EtOH (3 mL) and toluene (3 mL) were added. Sodium ascorbate (20 mg, 0.1 mmol, 0.3 eq.), copper (II) sulfate (10 mg, 0.04 mmol, 0.15 eq.) and EtOH (0.6 mL) were added to the reaction mixture. The mixture was stirred at RT for 48h. Solution was filtered, washed with 2 mL toluene and dried *in vacuo*. The product was recrystallized in MeOH and then in chloroform. The product **AT17** was obtained as a yellow solid in 38% yield.

^{1}H NMR (400 MHz, CD_3CD) δ 7.81 (d, J = 8.8 Hz, 2H), 7.74 (d, J = 8.9 Hz, 2H), 7.11 (s, 1H), 7.09 (d, J = 2.7 Hz, 2H), 7.07 (d, J = 8.2 Hz, 2H), 6.94 (d, J = 8.7 Hz, 2H), 6.79 (d, J = 7.7 Hz, 2H), 4.26 (t, J = 6.8 Hz, 2H), 4.14 (s, 2H), 4.05 (t, J = 6.5 Hz, 4H), 3.99 (t, J = 6.2 Hz, 1H), 3.87-3.90 (m, 4H), 3.69 – 3.66 (m, 2H), 3.62-3.59 (m, 10H), 3.45 – 3.39 (m, 2H), 3.32 – 3.28 (m, 4H), 2.83 (t, J = 6.7 Hz, 4H), 2.70 (t, J = 7.2 Hz, 1H), 1.83– 1.66 (m, 9H), 1.25 – 1.09 (m, 12H).

^{13}C NMR (101 MHz, CD_3CD) δ 170.69, 166.63, 165.70, 164.64, 162.90, 157.80, 130.55, 129.90, 129.42, 114.79, 114.03, 113.80, 85.55, 81.45, 77.98, 70.39, 70.06, 69.58, 67.83, 67.41, 65.12, 50.23, 33.65, 33.25, 26.60.

HR-ESI-MS: $[C_{46}H_{70}N_6O_{15}]^+$ calc m/z 946.4696 found 946.4647.

4.2 Sample preparation

4.2.1 Preparation of gold substrates

Glass slides (1.4 x 1.8 cm^2) were cleaned by sonication in a 2% Hellmanex solution for 15 min, following an additional sonication step for 15 minutes in absolute ethanol. The slides were rinsed 10 times with Milli-Q water ($\rho \geq 18$ MΩcm) prior to each treatment and finally dried under nitrogen flow. Chromium (20 nm) was deposited by plasma sputtering at a pressure of 0.133 Pa followed by gold (99.99%) (200 nm thickness). For further sample processing, all slides were immersed in thiol solution as follows.

4.2.2 Self-assembly solution to fabricate carboxylated surfaces

Gold slides prepared as previously described (1.4 x 1.8 cm^2) were immersed in freshly prepared piranha solution (4:1 H_2SO_4/H_2O_2) for 1 min, washed with copious amounts of Milli-Q water, and dried with N_2. Subsequently, the gold slides were immersed in a 0.02 mM solution of MHA in absolute ethanol for ≥18h. The slides were removed from the thiol solution and rinsed with ethanol. The slides were dried under nitrogen flow. Contact angle measurements confirmed the hydrophilicity of the surface: $\theta < 30°$.

4.2.3 Sample preparation for *in-situ* ellipsometry

Ellipsometry experiments were performed using a DRE Riss Ellipsometer, Ratzeburg, Germany, with a liquid cuvette (cuvette volume: 1.7 mL). Using the setup shown in Scheme 18, the MHA terminated gold substrate was mounted in the cuvette with pH 9 borate buffer-solution (10 mM) and a magnetic stirrer. Biotinylated (**AT5**) and hydroxylated (**AT3**) amidine (50 µM) were added to the cuvette in different ratios to assemble the second layer. After equilibrium was observed, surface was rinsed with 20 mL pH 9 borate buffer and the solution was exchanged to pH 8 borate buffer. Streptavidin solution (5 µM in pH 8 borate buffer) was added to assemble the third layer. After the saturation point was observed, the surface was rinsed with pH 8 buffer. Biotinylated anti-HSA (5 µM in pH 8 borate buffer) was added and rinsed after a plateau could be observed to generate layer number four. Different concentrations of Human-Serum-Albumin (1.5 pM to 5 µM) were added to test the sensor surface. Also the nonspecific protein IgG was tested

in different concentration and mixtures on the above described surface. To test the detection in real samples, 5 µM biotinylated anti-PSA was added to the layer-system made from MHA, mixed amidines and streptavidin. PSA with concentrations of 40 fM to 5 µM were injected to the cuvette filled with pH 8 HEPES buffer (10 mM).

The human serum samples were prepared as follows. The human serum was filtered with a 0.45 µm syringe filter, diluted with pH 8 HEPES buffer 200 times before loaded with different concentrations of PSA (100 fM – 10 nM). The different solutions were tested on the anti-PSA assemblies to determine the detection limit of biological solutions.

The sialic acid terminated SAMs were prepared in the same manner. After MHA adsorption, the substrates were mounted into the ellipsometer cuvette. 50 µM amidine solution with different ratios of sialic acid terminated amidine **(AT17)** to hydroxylated amidine **(AT3)** was added. After equilibrium was observed, surface was rinsed with 20 mL pH 9 borate buffer and solution was exchanged to pH 8 HEPES buffer. Different concentrations of hemagglutinin (42 – 420 nM) were added to test the sensor surface. In order to test the detection of virus like particles (VLPs) we prepared samples in HEPES buffer with 29 HA units per 1.7 mL.

4.2.4 Sample preparation for contact angle investigation / IRRAS

An OCA 15 from Data-Physics was used to measure the contact angle with water droplets (Milli-Q water, $\rho \geq 18$ MΩcm). This measurement was carried out upon every above described layer addition. The samples were dried under nitrogen flow and measured immediately.

4.2.5 Sample preparation for atomic force microscopy (AFM)

Atomic force microscopy was carried out with a Nanoscope IIIa equipped with a 10 µm scanner from Veeco Instruments. The samples were examined with standard cantilevers equipped with a tip with10 nmradius. The AFM samples were prepared in a similar wayas described above for ellipsometry, but from MICA-substrates covered by electron sputtered

gold (200 nm) for the first series of measurements (biotinylated rSAMs). MICA was obtained from "Ssenes", Netherlands. The second series of measurement (sialic acid terminated rSAMs) was carried out with SF-10 glass slides form Phasis in Geneva. The substrates were coated with 200 nm gold by magnetron sputtering.

4.2.6 Apparatus for molecule characterization

^{1}H-NMR and ^{13}C-NMR spectra were obtained using a Bruker Advance DRX spectrometer using MestReNova Software. HR-ESI-MS spectra were obtained with a Thermo Scientific LTQ-Orbitrap mass spectrometer. MALDI TOF MS, was performed using a Autoflex II mass spectrometer from Bruker Daltonics.

4.2.7 Chemicals

Acetyl chloride, 1,10-dibromdecan, dimethylaminopyridin, 4-cyanophenol, sodium carbonate, sodium hydrogen carbonate, sulfuric acid, biotinylated human serum albumin, human serum albumin, human serum from male AB plasma, streptavidin immunoglobulin G and toluene were obtained from Sigma Aldrich. 4-(2-hydroxyethyl)phenol, di-*tert*-butyl dicarbonate (Boc_2O), D(+)-Biotin, 7N methanolic ammonia, potassium carbonate, diethylether, dry aceton, dry acetonitrile, dry dimethylformamide, potassium bromide, potassium carbonate, tetrahydrofuran and trifluoracetic acid were purchased from Acros Organics. Sodium azide was purchased from Alfa Aesar. 3-Butyn-1-ol, iodomethane, sodium ethanolate, 2-propanol, silver trifluoromethanesulfonate, *2,2,6,6-Tetramethyl*-piperidin-1-yl)oxyl, trichloroisocyanuric acid and triethylene glycol monochloride were ordered from *ABCR*. Thionylchloride, N-actylneuraminic acid, Amberlite IR-120 (H^+), Celite 545 and benzene were obtained from Merck. Methanol, ethanol, ethyl acetate and acetic acid were purchased from J.T. Barker. Dichloromethane, sodium sulfate, sodium hydroxide, sodium sulfate, dichloromethane, DOWEX50w 8x mesh 100-200, hexane, dry methanol, sodium ascorbate, N,N'-dicyclohexylcarbodiimide and sodium chloride and HEPES dry powder were purchased from Applichem. 2-(2-(2-azidoethoxy)ethoxy)acetic acid was obtained for TCI. Biotinylated prostate specific antigen and prostate specific antigen were purchased from antikoerper-online.de. Influenza A H5N1 (A/Anhui/1/2005)

hemagglutinin was obtained from Hölzel Diagnostika. Deuterated solvents for NMR were purchased from Deutero GmbH. Influenza virus like particles were a gift from Prof. Dr. Reingard Grabherr from the Institute of Applied Microbiology at the University of Vienna.

5 Literature

1. Ulman, A. *An Introduction to Ultrathin Organic Films: from Langmuir - Blodgett to Self Assembly*. (Academic Press: Boston, MA, 1991).

2. Nuzzo, R. G., Dubois, L. H. & Allara, D. L. Fundamental studies of microscopic wetting on organic surfaces. 1. Formation and structural characterization of a self-consistent series of polyfunctional organic monolayers. *Journal of the American Chemical Society* **112**, 558–569 (1990).

3. Nuzzo, R. G., Fusco, F. a. & Allara, D. L. Spontaneously organized molecular assemblies. 3. Preparation and properties of solution adsorbed monolayers of organic disulfides on gold surfaces. *Journal of the American Chemical Society* **109**, 2358–2368 (1987).

4. Porter, M. D., Bright, T. B., Allara, D. L. & Chidsey, C. E. D. Spontaneously organized molecular assemblies. 4. Structural characterization of n-alkyl thiol monolayers on gold by optical ellipsometry, infrared spectroscopy, and electrochemistry. *Journal of the American Chemical Society* **109**, 3559–3568 (1987).

5. Bain, C. B. *et al.* Formation of Monolayer Films by the Spontaneous Assembly of Organic Thiols from Solution onto Gold. *Journal of American Chemical Society* **111**, 321–335 (1989).

6. Laibinis, P. E. *et al.* Comparison of the structures and wetting properties of self-assembled monolayers of n-alkanethiols on the coinage metal surfaces, copper, silver, and gold. *Journal of the American Chemical Society* **113**, 7152–7167 (1991).

7. Dubois, L. H. & Nuzzo, R. G. Synthesis, Structure, and Properties of Model Organic Surfaces. *Annual Review of Physical Chemistry* **43**, 437–463 (1992).

8. Fenter, P. *et al.* Structure of octadecyl thiol self-assembled on the silver(111) surface: an incommensurate monolayer. *Langmuir* **7**, 2013–2016 (1991).

9. Love, J. C. *et al.* Formation and structure of self-assembled monolayers of alkanethiolates on palladium. *Journal of the American Chemical Society* **125**, 2597–609 (2003).

10. Carvalho, A., Geissler, M., Schmid, H., Michel, B. & Delamarche, E. Self-Assembled Monolayers of Eicosanethiol on Palladium and Their Use in Microcontact Printing. *Langmuir* **18**, 2406–2412 (2002).

11. Li, Z., Chang, S. & Williams, R. S. Self-Assembly of Alkanethiol Molecules onto Platinum and Platinum Oxide Surfaces. *Langmuir* **19**, 6744–6749 (2003).

12. Muskal, N., Turyan, I. & Mandler, D. Self-assembled monolayers on mercury surfaces. *Journal of Electroanalytical Chemistry* **409**, 131–136 (1996).

13. Love, J. C., Estroff, L. a, Kriebel, J. K., Nuzzo, R. G. & Whitesides, G. M. Self-assembled monolayers of thiolates on metals as a form of nanotechnology. *Chemical reviews* **105**, 1103–69 (2005).

14. Nuzzo, R. G. & Allara, D. L. Adsorption of Biofunctional Organic Disulfides on Gold Surfaces. *Journal of the American Chemical Society* **105**, 4481–4483 (1983).

15. Whitesides, G. M. & Laibinis, P. E. Wet Chemical Approaches to the Characterization of Organic Surfaces: Self- Assembled Monolayers, Wetting, and the Physical-Organic Chemistry of the Solid-Liquid Interface. 87–96 (1990).

16. Tenboll, A. Abscheidung von orientiertem Kollagen. (2008).

17. Nakashima, M. & Adamson, A. W. Photocalorimetry. 2. Enthalpies of ligand substitution reactions of some group 6 metal carbonyl complexes in solution. *The Journal of Physical Chemistry* **86**, 2905–2909 (1982).

18. Piguet, C. Enthalpy-entropy correlations as chemical guides to unravel self-assembly processes. *Dalton transactions (Cambridge, England : 2003)* **40**, 8059–71 (2011).

19. Knoll, W., Liley, M., Piscevic, D., Spinke, J. & Tarlov, M. J. Supramolecular architectures for the functionalization of solid surfaces. *Advances in biophysics* **34**, 231–51 (1997).

20. Rajalingam, K. *et al.* Self-assembled monolayers of benzylmercaptan and para-cyanobenzylmercaptan on gold: surface infrared spectroscopic characterization. *Physical chemistry chemical physics : PCCP* **12**, 4390–9 (2010).

21. Spinke, J., Liley, M., Angermaierj, H. G. L. & Knoll, W. Molecular Recognition at Self -Assembled Monolayers : The Construction of Multicomponent Multilayers. *Langmuir* **9**, 1821–1825 (1993).

22. Su, L.-C. *et al.* Detection of prostate-specific antigen with a paired surface plasma wave biosensor. *Analytical chemistry* **82**, 3714–8 (2010).

23. Kumbhat, S., Sharma, K., Gehlot, R., Solanki, A. & Joshi, V. Surface plasmon resonance based immunosensor for serological diagnosis of dengue virus infection. *Journal of pharmaceutical and biomedical analysis* **52**, 255–9 (2010).

24. Auer, F. *et al.* Switchable Assembly of Stable, Ordered Molecular Layers. *Chemistry - A European Journal* **5**, 1150–1159 (1999).

25. Koepf, M., Chérioux, F., Wytko, J. A. & Weiss, J. 1D and 3D surface-assisted self-organization. *Coordination Chemistry Reviews* **256**, 2872–2892 (2012).

26. Okabayashi, N., Paulsson, M. & Komeda, T. Inelastic electron tunneling process for alkanethiol self-assembled monolayers. *Progress in Surface Science* **88**, 1–38 (2013).

27. Mishina, E., Miyakita, Y., Yu, Q.-K., Nakabayashi, S. & Sakaguchi, H. Nonlinear optical properties of oligothiophene self-assembled monolayers on gold substrate. *The Journal of Chemical Physics* **117**, 4016 (2002).

28. Diltemiz, S. E., Ersöz, A., Hür, D., Keçili, R. & Say, R. 4-Aminophenyl boronic acid modified gold platforms for influenza diagnosis. *Materials Science and Engineering: C* **33**, 824–830 (2013).

29. Anderson, J. M., Defife, K., McNally, a, Collier, T. & Jenney, C. Monocyte, macrophage and foreign body giant cell interactions with molecularly engineered surfaces. *Journal of materials science. Materials in medicine* **10**, 579–88

30. Bossi, a *et al.* Synthesis of controlled polymeric cross-linked coatings via iniferter polymerisation in the presence of tetraethyl thiuram disulphide chain terminator. *Biosensors & bioelectronics* **25**, 2149–55 (2010).

31. Evans, S. D., Urankar, E., Ulman, A. & Ferris, N. Self-Assembled Monolayer of Alkanethiols Containg a Polar Aromatic Group: Effects of the Dipole Position on Molecular Packing, Orientation, and Surface Wetting Properties. *Journal of the American Chemical Society* 4121–4131 (1991).

32. Zhang, X., Gao, M., Kong, X., Sun, Y. & Shen, J. Build-up of a new type of ultrathin film of porphyrin and phthalocyanine based on cationic and anionic electrostatic attraction. *Journal of the Chemical Society, Chemical Communications* 1055 (1994).doi:10.1039/c39940001055

33. Mao, G. *et al.* Monolayers of Bolaform Amphiphiles: Influence of Alkyl Chain Length and Counterions. *Langmuir* **10**, 4174–4184 (1994).

34. Mao, G. *et al.* Interactions, Structure, and Stability of Photoreactive Bolaform Amphiphile Multilayers. *Langmuir* **11**, 942–952 (1995).

35. Auer, F., Nelles, G. & Sellergren, B. Odd-even chain length-dependent order in pH-switchable self-assembled layers. *Chemistry (Weinheim an der Bergstrasse, Germany)* **10**, 3232–40 (2004).

36. Wulff, G., Gross, T. & Schönfeld, R. Enzyme Models Based on Molecularly Imprinted Polymers with Strong Esterase Activity. *Angewandte Chemie International Edition in English* **36**, 1962–1964 (1997).

37. Hosseini, M. W., Ruppert, R., Kyritsakas, N. & Fischer, J. A Molecular Approach to Solid-state Synthesis: Prediction and Synthesis of Self-assembled Infinite Rods. *Journal of the Chemical Society, Chemical Communications* 2135–2136 (1994).

38. Arnold, R., Azzam, W., Terfort, A. & Wöll, C. Preparation, Modification, and Crystallinity of Aliphatic and Aromatic Carboxylic Acid Terminated Self-Assembled Monolayers. *Langmuir* **18**, 3980–3992 (2002).

39. Auer, F., Sellergren, B., Swietlow, A. & Offenhäuser, A. Self-Assembled Layers of Bisbenzamidines on Gold. *Langmuir* **16**, 5936–5944 (2000).

40. Sellergren, B., Auer, F. & Arnebrant, T. Selective adsorption of oligonucleotides on switchable self-assembled monolayers. *Chemical Communications* **1**, 2001–2002 (1999).

41. Auer, F. *et al.* Nanocomposites by Electrostatic Interactions: 1. Impact of Sublayer Quality on the Organization of Functionalized Nanoparticles on Charged Self-Assembled Layers. *Langmuir* **16**, 7554–7557 (2000).

42. Deshmukh, R. Switchable assembly of stable ordered molecular layers : Towards a reversible Biosensor. *Naturwissenschaften* (2006).

43. Knoll, W., Park, H., Sinner, E., Yao, D. & Yu, F. Supramolecular interfacial architectures for optical biosensing with surface plasmons. *Surface Science* **570**, 30–42 (2004).

44. Su, L.-C. *et al.* Rapid and highly sensitive method for influenza A (H1N1) virus detection. *Analytical chemistry* **84**, 3914–20 (2012).

45. Samanta, D. & Sarkar, A. Immobilization of bio-macromolecules on self-assembled monolayers: methods and sensor applications. *Chemical Society reviews* **40**, 2567–92 (2011).

46. Song, W. *et al.* Facile construction of functional biosurface via SI-ATRP and "click glycosylation". *Colloids and surfaces. B, Biointerfaces* **93**, 188–94 (2012).

47. Herrwerth, S. *et al.* Covalent Coupling of Antibodies to Self-Assembled Monolayers of Carboxy-Functionalized Poly(ethylene glycol): Protein Resistance and Specific Binding of Biomolecules †. *Langmuir* **19**, 1880–1887 (2003).

48. Spevak, W. *et al.* Polymerized liposomes containing C-glycosides of sialic acid: potent inhibitors of influenza virus in vitro infectivity. *Journal of the American Chemical Society* **115**, 1146–1147 (1993).

49. Narla, S. N. & Sun, X.-L. Immobilized sialyloligo-macroligand and its protein binding specificity. *Biomacromolecules* **13**, 1675–82 (2012).

50. Vericat, C., Vela, M. E. & Salvarezza, R. C. Self-assembled monolayers of alkanethiols on Au(111): surface structures, defects and dynamics. *Physical chemistry chemical physics : PCCP* **7**, 3258–68 (2005).

51. Malmsten, M. Ellipsometry Studies of Protein Layers Adsorbed at Hydrophobic Surfaces. *Journal of colloid and interface science* 333–342 (1994).

52. Svensson, O. & Arnebrant, T. Antibody-antigen interaction on polystyrene: an in situ ellipsometric study. *Journal of colloid and interface science* **368**, 533–9 (2012).

53. Jang, H. S. *et al.* Optical fiber SPR biosensor with sandwich assay for the detection of prostate specific antigen. *Optics Communications* **282**, 2827–2830 (2009).

54. Nelson, K. E. *et al.* Surface Characterization of Mixed Self-Assembled Monolayers Designed for Streptavidin Immobilization. *Langmuir* **17**, 2807–2816 (2001).

55. Pradier, C.-M., Salmain, M., Liu, Z. & Méthivier, C. Comparison of different procedures of biotin immobilization on gold for the molecular recognition of avidin: an FT-IRRAS study. *Surface and Interface Analysis* **34**, 67–71 (2002).

56. Misawa, N. *et al.* Orientation of avidin molecules immobilized on COOH-modified SiO2/Si(100) surfaces. *Chemical Physics Letters* **419**, 86–90 (2006).

57. Li, D. *et al.* A nanobeads amplified QCM immunosensor for the detection of avian influenza virus H5N1. *Biosensors & bioelectronics* **26**, 4146–54 (2011).

58. Seifert, M., Rinke, M. T. & Galla, H.-J. Characterization of streptavidin binding to biotinylated, binary self-assembled thiol monolayers--influence of component ratio and solvent. *Langmuir : the ACS journal of surfaces and colloids* **26**, 6386–93 (2010).

59. Holford, T. R. J., Davis, F. & Higson, S. P. J. Recent trends in antibody based sensors. *Biosensors & bioelectronics* **34**, 12–24 (2012).

60. Neish, C. S., Martin, I. L., Henderson, R. M. & Edwardson, J. M. Direct visualization of ligand-protein interactions using atomic force microscopy. *British journal of pharmacology* **135**, 1943–50 (2002).

61. Beckett, D., Kovaleva, E. & Schatz, P. J. A minimal peptide substrate in biotin holoenzyme synthetase-catalyzed biotinylation. *Protein science : a publication of the Protein Society* **8**, 921–9 (1999).

62. Cho, I.-H. *et al.* Site-directed biotinylation of antibodies for controlled immobilization on solid surfaces. *Analytical biochemistry* **365**, 14–23 (2007).

63. Baldrich, E., Laczka, O., Del Campo, F. J. & Muñoz, F. X. Gold immuno-functionalisation via self-assembled monolayers: study of critical parameters and comparative performance for protein and bacteria detection. *Journal of immunological methods* **336**, 203–12 (2008).

64. Byrne, B., Stack, E., Gilmartin, N. & O'Kennedy, R. Antibody-based sensors: principles, problems and potential for detection of pathogens and associated toxins. *Sensors (Basel, Switzerland)* **9**, 4407–45 (2009).

65. Burkert, S. *et al.* Protein resistance of PNIPAAm brushes: application to switchable protein adsorption. *Langmuir : the ACS journal of surfaces and colloids* **26**, 1786–95 (2010).

66. Goodsell, D. S. Serum Albumin. *RCSB Protein Data Bank* (2003).doi:10.2210/rcsb_pdb/mom_2003_1

67. Dirote, E. *Nanotechnology -Focus-*. (Nova Science Publishers, Inc.: Hauppauge, New York, 2005).

68. Lin, S., Shih-Yuan Lee, A., Lin, C.-C. & Lee, C.-K. Determination of Binding Constant and Stoichiometry for Antibody-Antigen Interaction with Surface Plasmon Resonance. *Current Proteomics* **3**, 271–282 (2006).

69. Frederix, F. *et al.* Enhanced Performance of an Affinity Biosensor Interface Based on Mixed Self-Assembled Monolayers of Thiols on Gold. *Langmuir* **19**, 4351–4357 (2003).

70. Van Vuuren, B. J., Read, T., Olkhov, R. V & Shaw, A. M. Human serum albumin interference on plasmon-based immunokinetic assay for antibody screening in model blood sera. *Analytical biochemistry* **405**, 114–20 (2010).

71. Yu, F., Persson, B., Löfås, S. & Knoll, W. Surface plasmon fluorescence immunoassay of free prostate-specific antigen in human plasma at the femtomolar level. *Analytical chemistry* **76**, 6765–70 (2004).

72. Zhao, X. *et al.* Interfacial immobilization of monoclonal antibody and detection of human prostate-specific antigen. *Langmuir : the ACS journal of surfaces and colloids* **27**, 7654–62 (2011).

73. Balk, S. P. Biology of Prostate-Specific Antigen. *Journal of Clinical Oncology* **21**, 383–391 (2003).

74. Lilja, H. A kallikrein-like serine protease in prostatic fluid cleaves the predominant seminal vesicle protein. *The Journal of clinical investigation* **76**, 1899–903 (1985).

75. Acevedo, B. *et al.* Development and validation of a quantitative ELISA for the measurement of PSA concentration. *Clinica chimica acta; international journal of clinical chemistry* **317**, 55–63 (2002).

76. Wang, Y., Brunsen, A., Jonas, U., Dostálek, J. & Knoll, W. Prostate specific antigen biosensor based on long range surface plasmon-enhanced fluorescence spectroscopy and dextran hydrogel binding matrix. *Analytical chemistry* **81**, 9625–32 (2009).

77. Yong, E. Influenza: Five questions on H5N1. *Nature* **486**, 456–8 (2012).

78. Portela, A. & Digard, P. The influenza virus nucleoprotein: a multifunctional RNA-binding protein pivotal to virus replication. *The Journal of general virology* **83**, 723–34 (2002).

79. Amano, Y. & Cheng, Q. Detection of influenza virus: traditional approaches and development of biosensors. *Analytical and bioanalytical chemistry* **381**, 156–64 (2005).

80. Stamboulian, D., Bonvehi, P. E., Nacinovich, F. M. & Cox, N. INFLUENZA. *Infectious Disease Clinics of North America* **14**, 141–166 (2000).

81. Woolcock, P. R. & Cardona, C. J. Commercial immunoassay kits for the detection of influenza virus type A: evaluation of their use with poultry. *Avian diseases* **49**, 477–81 (2005).

82. He, Q. *et al.* Detection of H5 avian influenza viruses by antigen-capture enzyme-linked immunosorbent assay using H5-specific monoclonal antibody. *Clinical and vaccine immunology : CVI* **14**, 617–23 (2007).

83. Ho, H.-T. *et al.* Rapid detection of H5N1 subtype influenza viruses by antigen capture enzyme-linked immunosorbent assay using H5- and N1-specific monoclonal antibodies. *Clinical and vaccine immunology : CVI* **16**, 726–32 (2009).

84. Xu, J., Suarez, D. & Gottfried, D. S. Detection of avian influenza virus using an interferometric biosensor. *Analytical and bioanalytical chemistry* **389**, 1193–9 (2007).

85. Bañuls, M.-J., González-Pedro, M.-V., Puchades, R. & Maquieira, Á. Influenza A virus infection diagnosis based on DVD reader technology. *Analytical Methods* **4**, 3133 (2012).

86. Gamblin, S. J. & Skehel, J. J. Influenza hemagglutinin and neuraminidase membrane glycoproteins. *The Journal of biological chemistry* **285**, 28403–9 (2010).

87. Charych, D. H., Nagy, J. O., Spevak, W. & Bednarski, M. D. Direct colorimetric detection of a receptor-ligand interaction by a polymerized bilayer assembly. *Science (New York, N.Y.)* **261**, 585–8 (1993).

88. Spevak, W., Nagy, J. O. & Charych, D. H. Molecular assemblies of functionalized polydiacetylenes. *Advanced Materials* **7**, 85–89 (1995).

89. Tompkins, H. G. *A User's Guide to Ellipsometry*. 1–260 (Dover Publications, Inc.: Mineola, New York, 1993).

90. Drude, P. Annalen der Physik. *Annalen der Physik* **36**, 1889 (1889).

91. Fujiwara, H. *Spectroscopic Ellipsometry: Principles and Applications*. (Maruzen Co. Ltd, Tokyo, Japan: West Sussex, England, 2007).

92. Busse, S., Käshammer, J., Krämer, S. & Mittler, S. Gold and thiol surface functionalized integrated optical Mach–Zehnder interferometer for sensing purposes. *Sensors and Actuators B: Chemical* **60**, 148–154 (1999).

93. Mittler-Neher, S. *et al.* Spectroscopic and surface-analytical characterization of self-assembled layers on Au. *Biosensors and Bioelectronics* **10**, 903–916 (1995).

94. Myrskog, A., Anderson, H., Aastrup, T., Ingemarsson, B. & Liedberg, B. Esterification of self-assembled carboxylic-acid-terminated thiol monolayers in acid environment: a time-dependent study. *Langmuir : the ACS journal of surfaces and colloids* **26**, 821–9 (2010).

95. Röefzaad, M., Klüner, T. & Brand, I. Orientation of the GM1 ganglioside in Langmuir-Blodgett monolayers: a PM IRRAS and computational study. *Physical chemistry chemical physics : PCCP* **11**, 10140–51 (2009).

96. Blanke, J. F., Vincent, S. E. & Overend, J. Infrared spectroscopy of surface species ; instmlmental considerations. *Spectrochimica Acta Part A: Molecular Spectroscopy* **32**, 163–173 (1976).

97. Arndt, T., Bubeck, C. & Schouten, A. J. FTIR Spectroscopy of Monomolecular Layers and Multilayers of Organic Molecules on Solid Substrates. *Mikrochimica Acta* **II**, 7–9 (1988).

98. Young, T. An Essay on the Cohesion of Fluids. *Philosophical Transactions of the Royal Society of London* **95**, 65–87 (1805).

99. Korayem, M. H., Ebrahimi, N. & Korayem, A. H. Modeling and Simulation of Tapping-mode Atomic Force Microscopy in Liquid. *Nanoscience and Nanotechnology* **1**, 14–21 (2012).

100. Nelles, G. *et al.* Two-Dimensional Structure of Disulfides and Thiols on Gold(111). *Langmuir* **14**, 808–815 (1998).

101. Gaczynska, M. & Osmulski, P. A. AFM of biological complexes: What can we learn? *Current opinion in colloid & interface science* **13**, 351–367 (2008).

102. Kasson, P. M. Receptor binding by influenza virus: using computational techniques to extend structural data. *Biochemistry* **51**, 2359–65 (2012).

103. Klein, F. & Pinner, A. Umwandlung der Nitrile in Imide. (1889).

104. Wood, D. H. 1,5-Bis(4-amidinophenoxy)pentane (pentamidine) is a potent inhibitor of []idazoxan binding to imidazoline I2 binding sites. *European Journal of Pharmacology* **353**, 97–103 (1998).

105. Molla, A. FULL PAPER A Constrained Diketopiperazine as a New Scaffold for the Synthesis of. 853–859 (1998).

106. Tamada, K. *et al.* Structure and Growth of Hexyl Azobenzene Thiol SAMs on Au(111). *Langmuir* **14**, 3264–3271 (1998).

107. Tenboll, A. *et al.* Controlled deposition of highly oriented type I collagen mimicking in vivo collagen structures. *Langmuir : the ACS journal of surfaces and colloids* **26**, 12165–72 (2010).

108. Hsu, H.-J., Sheu, S.-Y. & Tsay, R.-Y. Preferred orientation of albumin adsorption on a hydrophilic surface from molecular simulation. *Colloids and surfaces. B, Biointerfaces* **67**, 183–91 (2008).

109. Choi, E. J. *et al.* Effect of Flow on Human Serum Albumin Adsorption to Self-Assembled Monolayers of Varying Packing Density. *Langmuir* **19**, 5464–5474 (2003).

110. Lee, M., Martin, K., Emerson, D. L. & Galbraith, R. M. Antibodies to Polymerized Human Serum Albumin in Acute and Chronic Liver Disease. *HEPATOLOGY* **7**, 906–912 (1987).

111. Martins, M. C. L., Ratner, B. D. & Barbosa, M. a Protein adsorption on mixtures of hydroxyl- and methyl-terminated alkanethiols self-assembled monolayers. *Journal of biomedical materials research. Part A* **67**, 158–71 (2003).

112. Hosseini, M. W. *et al.* A molecular approach to solid-state synthesis: prediction and synthesis of self-assembled infinite rods. *Journal of the Chemical Society, Chemical Communications* **0**, 2135 (1994).

113. Sellergren, B., Swietlow, A., Arnebrant, T. & Unger, K. Consecutive Selective Adsorption of Pentamidine and Phosphate Biomolecules on a Self-Assembled Layer: Reversible Formation of a Chemically Selective Coating. *Analytical Chemistry* **68**, 402–407 (1996).

114. Engström, S. & Bäckström, K. Ellipsometry as a Tool To Study Detergency at Hard Surfaces. *Langmuir* **3**, 568–574 (1987).

115. Tumolo, T., Angnes, L. & Baptista, M. S. Determination of the refractive index increment (dn/dc) of molecule and macromolecule solutions by surface plasmon resonance. *Analytical biochemistry* **333**, 273–9 (2004).

116. Wojciechowskil, P. W. Fibrinogen and albumin adsorption from human blood plasma and from buffer onto chemically functionalized silica substrates ". *Colloids and surfaces. B, Biointerfaces* 7–13 (1993).

117. Lensen, H. G. ., Bargeman, D., Bergveld, P., Smolders, C. a & Feijen, J. High-performance liquid chromatography as a technique to measure the competitive adsorption of plasma proteins onto latices. *Journal of Colloid and Interface Science* **99**, 1–8 (1984).

118. Heinrich, L., Mann, E. K., Voegel, J. C., Koper, G. J. M. & Schaaf, P. Scanning Angle Reflectometry Study of the Structure of Antigen−Antibody Layers Adsorbed on Silica Surfaces. *Langmuir* **12**, 4857–4865 (1996).

119. Road, T. C., Kingdom, U. & Genetics, M. AFM Studies of Protein Adsorption. **601**, 586–601 (1996).

120. Kunitake, T., Kurihara, K. & Sasaki, D. Y. Specific, Multiple-Point Binding of ATP and AMP to a Guanidinium-Functionalized Monolayer. *Journal of the American Chemical Society* **113**, 9685–9686 (1991).

121. Colthup, N. B., Daly, L. H. & Wiberley, S. E. *Introduction to Infrared and Raman Spectroscopy*. 547 (Elsevier, Academic press: New York, 1990).

122. Krishnan, A., Liu, Y.-H., Cha, P., Allara, D. & Vogler, E. a Interfacial energetics of globular-blood protein adsorption to a hydrophobic interface from aqueous-buffer solution. *Journal of the Royal Society, Interface / the Royal Society* **3**, 283–301 (2006).

123. Buriak, J. M. Organometallic chemistry on silicon and germanium surfaces. *Chemical reviews* **102**, 1271–308 (2002).

124. Iijima, K., Matsubara, T. & Sato, T. Selective Precipitation of Salts on the Surface of a Gel State Phosphatidylcholine Membrane. *Chemistry Letters* **36**, 860–861 (2007).

125. Kolb, H. C., Finn, M. G. & Sharpless, K. B. Click Chemistry: Diverse Chemical Function from a Few Good Reactions. *Angewandte Chemie (International ed. in English)* **40**, 2004–2021 (2001).

126. Wang, L. *et al.* Covalent immobilization of redox protein via click chemistry and carbodiimide reaction: direct electron transfer and biocatalysis. *Journal of colloid and interface science* **350**, 544–50 (2010).

127. Kato, H., Böttcher, C. & Hirsch, A. Sugar Balls: Synthesis and Supramolecular Assembly of [60]Fullerene Glycoconjugates. *European Journal of Organic Chemistry* **2007**, 2659–2666 (2007).

128. Luca, L. De, Giacomelli, G., Masala, S., Porcheddu, A. & Chimica, D. Trichloroisocyanuric / TEMPO Oxidation of Alcohols under Mild Conditions : A Close Investigation is a topic of current interest . However , direct conversion is still a challenge , and the most commonly used methods reported a very mild and chemoselective. 4999–5001 (2003).

129. Van Bekkum, H., Besemer, A. C. & De Nooy, A. E. J. On the Use of Stable Organic Nitroxyl Radicals for the Oxidation of Primary and Secondary Alcohols. *Synthesis* **10**, 1153–1174 (1996).

130. Neises, B. & Steglich, W. Simple Method for the Esterification of Carboxylic Acids. *Angewandte Chemie (International ed. in English)* **553**, 12–14 (1978).

131. Malapelle, A., Coslovi, A., Doisneau, G. & Beau, J.-M. An Expeditious Synthesis ofN-Acetylneuraminic Acid α-C-Glycosyl Derivatives ("α-C-Glycosides") from the Anomeric Acetates. *European Journal of Organic Chemistry* **2007**, 3145–3157 (2007).

132. Deng, J. *et al.* Construction of effective receptor for recognition of avian influenza H5N1 protein HA1 by assembly of monohead glycolipids on polydiacetylene vesicle surface. *Bioconjugate chemistry* **20**, 533–7 (2009).

133. Shelke, S. V *et al.* A fragment-based in situ combinatorial approach to identify high-affinity ligands for unknown binding sites. *Angewandte Chemie (International ed. in English)* **49**, 5721–5 (2010).

134. Buchini, S., Buschiazzo, A. & Withers, S. G. A new generation of specific Trypanosoma cruzi trans-sialidase inhibitors. *Angewandte Chemie (International ed. in English)* **47**, 2700–3 (2008).

135. Gil, M., Arévalo, M. & López, Ó. Click Chemistry - What's in a Name? Triazole Synthesis and Beyond. *Synthesis* **2007**, 1589–1620 (2007).

136. Rostovtsev, V. V, Green, L. G., Fokin, V. V & Sharpless, K. B. A stepwise huisgen cycloaddition process: copper(I)-catalyzed regioselective "ligation" of azides and terminal alkynes. *Angewandte Chemie (International ed. in English)* **41**, 2596–9 (2002).

137. Meldal, M. & Tornøe, C. W. Cu-catalyzed azide-alkyne cycloaddition. *Chemical reviews* **108**, 2952–3015 (2008).

138. Cummins, D. *et al.* Click chemistry as a means to functionalize macroporous PolyHIPE. *Soft Matter* **5**, 804 (2009).

139. Wiley, D. C. & Skehel, J. J. The Structure and Function of the Hemagglutinin Membrane Glycoprotein of Influenza Virus. *annual Reviews Biochemistry* **56**, 365–394 (1987).

140. Cheng, N. & Cao, X. Photoactive SAM surface for control of cell attachment. *Journal of colloid and interface science* **348**, 71–9 (2010).

141. Pereira, E. M. a, Dario, A. F., França, R. F. O., Fonseca, B. a L. & Petri, D. F. S. Binding of dengue virus particles and dengue proteins onto solid surfaces. *ACS applied materials & interfaces* **2**, 2602–10 (2010).

142. Xu, R., McBride, R., Nycholat, C. M., Paulson, J. C. & Wilson, I. a Structural characterization of the hemagglutinin receptor specificity from the 2009 H1N1 influenza pandemic. *Journal of virology* **86**, 982–90 (2012).

143. San Juan, R. R. & Carmichael, T. B. Formation of self-assembled monolayers with homogeneously mixed, loosely packed alkyl groups using unsymmetrical dialkyldithiophosphinic acids. *Langmuir : the ACS journal of surfaces and colloids* **28**, 17701–8 (2012).

144. Rabe, M., Verdes, D. & Seeger, S. Understanding protein adsorption phenomena at solid surfaces. *Advances in colloid and interface science* **162**, 87–106 (2011).

145. D'Attoma, A., Grivel, C. & Heinisch, S. On-line comprehensive two-dimensional separations of charged compounds using reversed-phase high performance liquid chromatography and hydrophilic interaction chromatography. Part I: Orthogonality and practical peak capacity considerations. *Journal of chromatography. A* **1262**, 148–59 (2012).

146. Bonnin, S., Besson, F., Gelhausen, M., Chierici, S. & Roux, B. A FTIR spectroscopy evidence of the interactions between wheat germ agglutinin and N-acetylglucosamine residues. *FEBS letters* **456**, 361–4 (1999).

147. Noad, R. & Roy, P. Virus-like particles as immunogens. *Trends in microbiology* **11**, 438–444 (2003).

148. Mammen, M., Choi, S.-K. & Whitesides, G. M. Polyvalente Wechselwirkungen in biologischen Systemen: Auswirkungen auf das Design und die Verwendung multivalenter Liganden und Inhibitoren. *Angewandte Chemie* **110**, 2908–2953 (1998).

149. Yamaji, H. *et al.* Production of Japanese encephalitis virus-like particles using the baculovirus-insect cell system. *Journal of bioscience and bioengineering* **114**, 657–62 (2012).

150. Skehel, J. J. & Wiley, D. C. RECEPTOR BINDING AND MEMBRANE FUSION IN VIRUS ENTRY : The Influenza Hemagglutinin. (2000).

151. Huang, R. T. Adsorption of influenza virus to charged groups on natural and artificial surfaces. *Medical microbiology and immunology* **159**, 129–35 (1974).

152. Takemoto, D. K., Skehel, J. J. & Wiley, D. C. A surface plasmon resonance assay for the binding of influenza virus hemagglutinin to its sialic acid receptor. *Virology* **217**, 452–8 (1996).

153. Fraser, B. H. *et al.* Synthesis of 1,4-triazole linked zanamivir dimers as highly potent inhibitors of influenza A and B. *MedChemComm* **4**, 383 (2013).

6 Appendix

6.1 List of abbreviations

AcCl	acetylchloride
ACN	acetonitrile
AFM	Atomic Force Microscopy
AgOTF	silvertriflat
anti-HSA	human serum albumin antibody
anti-PSA	prostate serum albumin antibody
Boc	*tert*.-butyloxycarbonyl
Boc_2O	di-*tert*.-butyldicarbonate
c-PSA	complexed prostate specific antigen
$CuSO_4$	copper sulfate
DCC	N,N'-dicyclohexylcarbodiimide
DCM	dichloromethane
DMAP	4-dimethylaminopyridine
DMF	dimethylformamide
DMSO	dimethylsulfoxide
ELISA	enzyme-linked immunosobent assay
eq.	equivalents
EtOH	ethanol
f-PSA	free prostate specific antigen
FTIR	Fourier Transform Infrared Spectroscopy
HA	hemagglutinin
HCG	human chorionic gonadotrophin
HCl	hydrogen chloride
HEPES	4-(2-hydroxyethyl)-1-piperazineethanesulfonic acid
HS	human serum
HSA	human serum albunin
HR-ESI-MS	high resolution electrospray ionization mass spectroscopy

IgG	immunoglobulin G
IRRAS	infrared reflection absorption spectroscopy
K_2CO_3	potassium carbonate
KBr	potassium bromide
LOD	limit of detection
M	molar
MeOH	methanol
MHA	mercaptohexadecanoic acid
n	refractive index
NA	neuraminidase
NaAsc	sodium ascorbate
NaOH	sodium hydroxide
NH_3	ammonia
-OH	hydroxyl rest
pI	isoelectric point
p-polarized	parallel polarized
PSA	prostate specific antigen
QCM	quartz crystal microbalance
RNA	ribonucleic acid
rSAM	reversible self-assembled monolayer
RT	room temperature
SA	sialic acid
SAGA	specular apertured grazing angle
SAM	self-assembled monolayer
s-polarized	senkrecht/perpendicular polarized
SPR	surface plasmon resonance spectroscopy
STV	streptavidin
TCCA	Trichloroisocyanuric acid
TDM	transition dipole moment
TEMPO	(*2,2,6,6-tetramethyl*-piperidin-1-yl)oxyl

TLC	thin layer chromatography
TFA	trifluoro acetic acid
THF	tetrahydrofuran
VLP	virus like particle
VP	virus particle
WHO	world health organization
X_B	molar ratio
ΔH	enthalpy
ΔG	Gibbs free energy
T	temperature
ΔS	entropy
Γ	amount of bound protein
d	thickness
v_a	asymmetric vibration
v_s	symmetric vibration
Δ	delta
Ψ	psi
N	complex refractive index
r	reflection coefficient

6.2 Spectra

^{1}H-NMR of 4-((10-bromodecyl)oxy)benzonitrile (AT1)

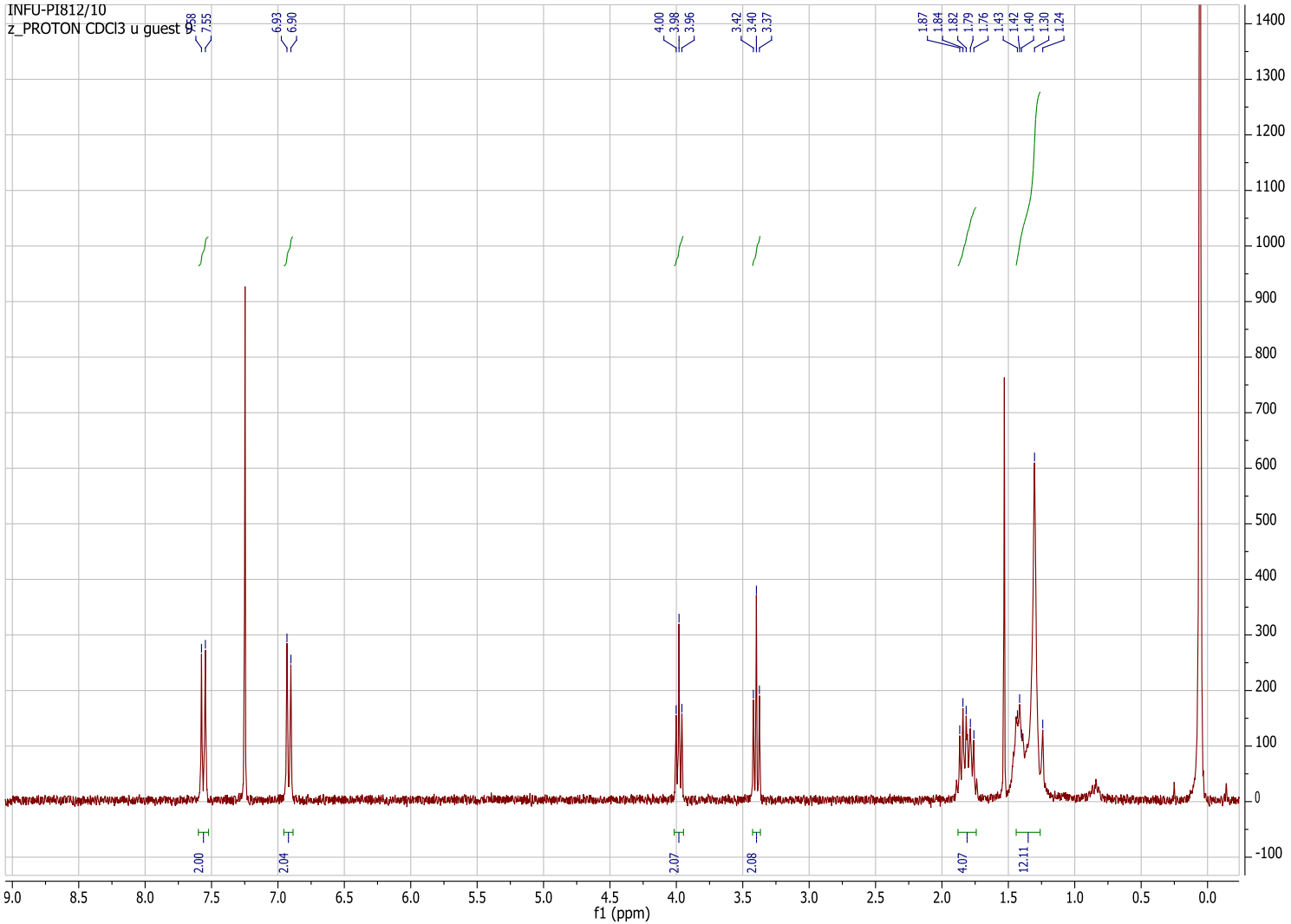

HR-ESI-MS of 4-((10-bromodecyl)oxy)benzonitrile (AT1)

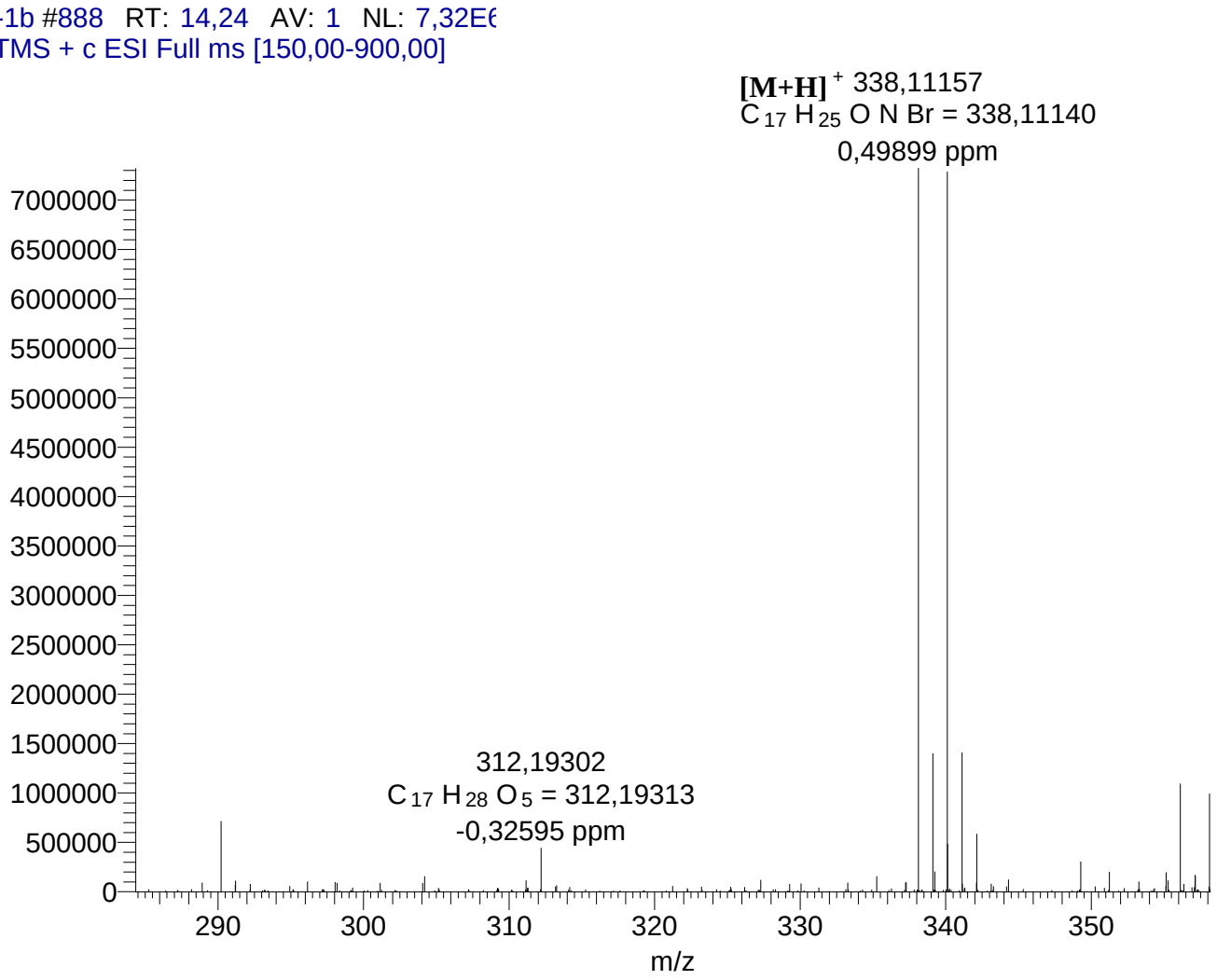

^{1}H-NMR of 2-[4-(8-Bromo-octyloxy)-phenyl]-ethanol (AT2)

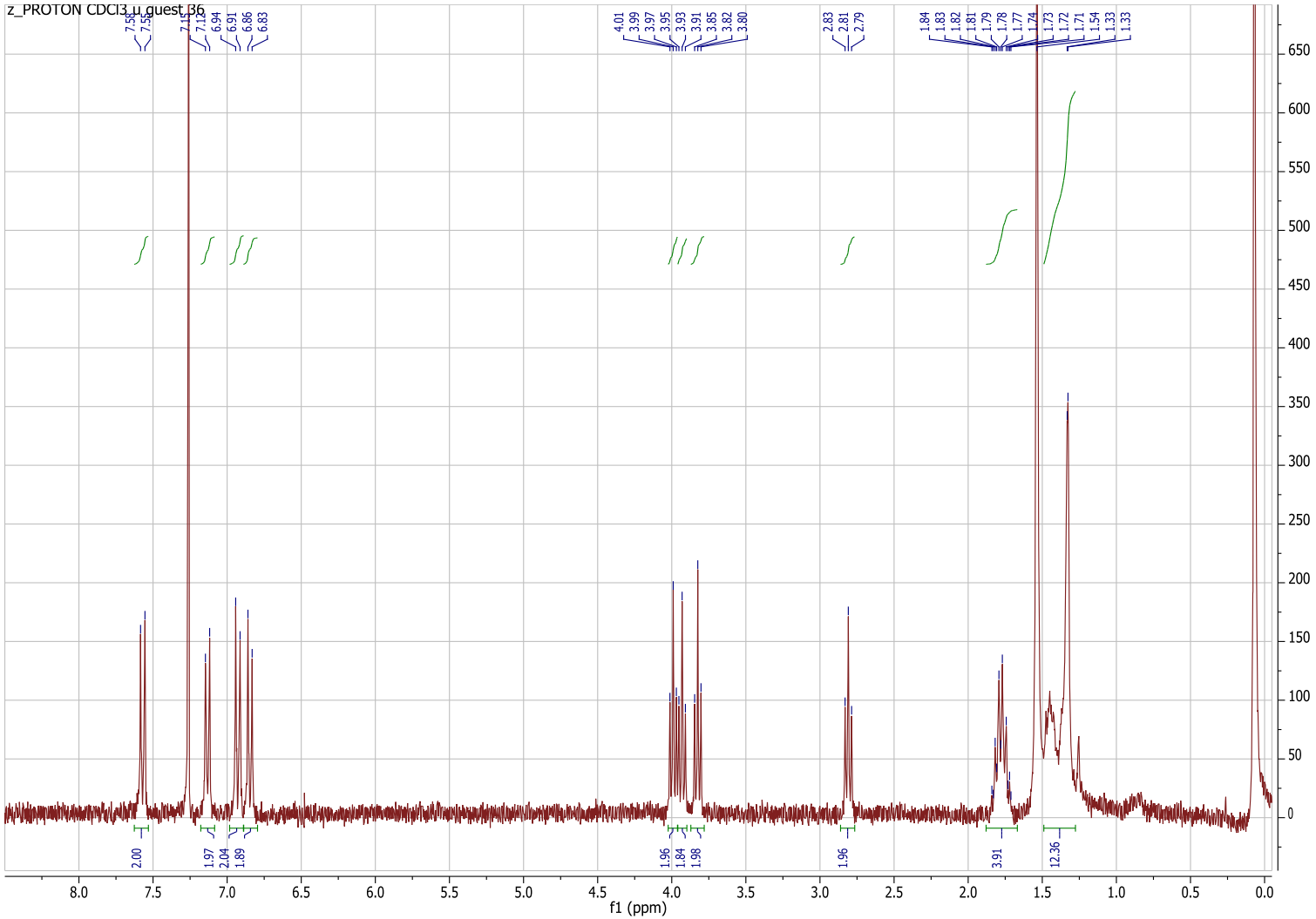

HR-ESI-MS of 2-[4-(8-Bromo-octyloxy)-phenyl]-ethanol (AT2)

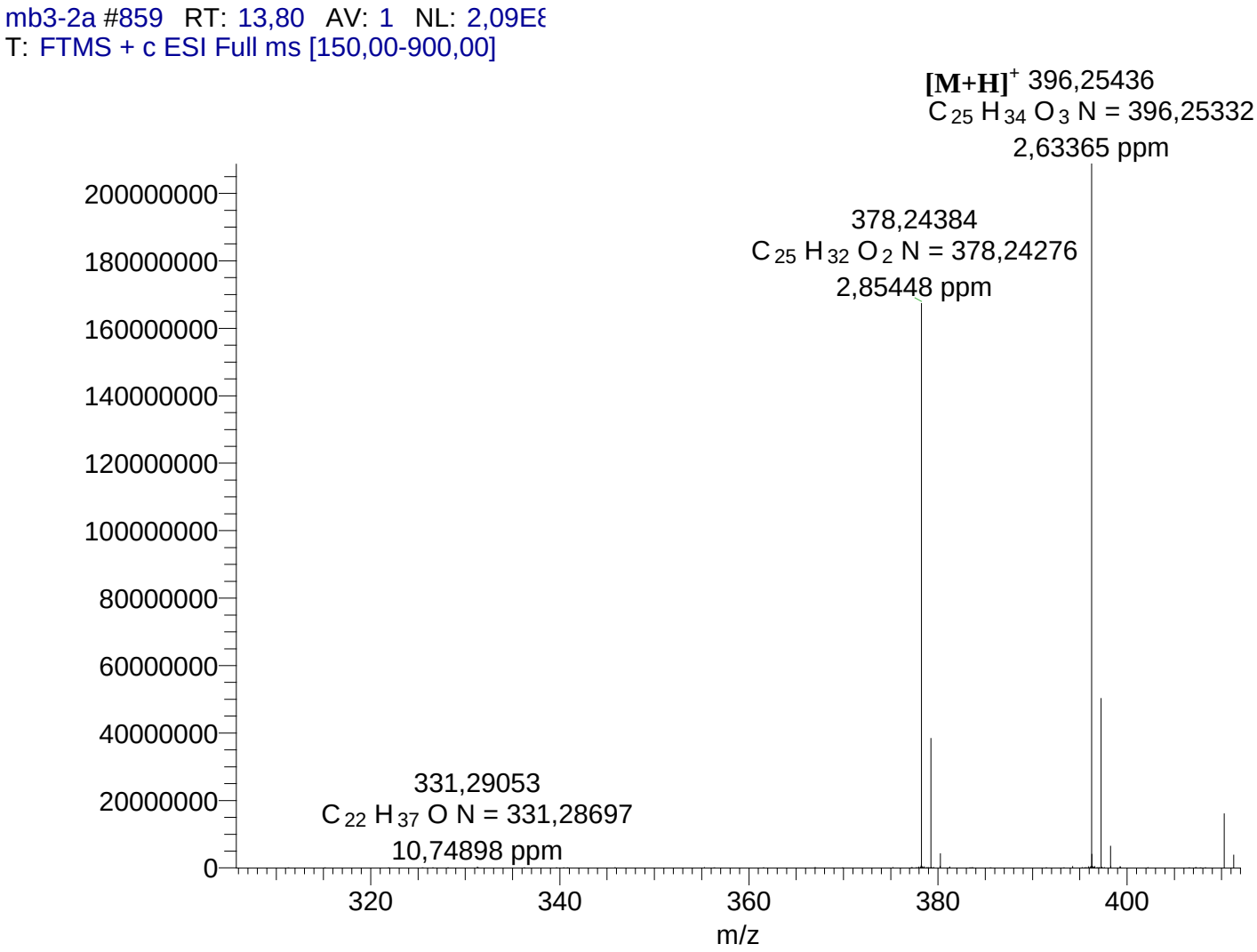

^{1}H-NMR of 4-{10-[4-(2-Hydrody-ethyl)-phenyoxy]-decyloxy}-benzamidine hydrochloride (AT3)

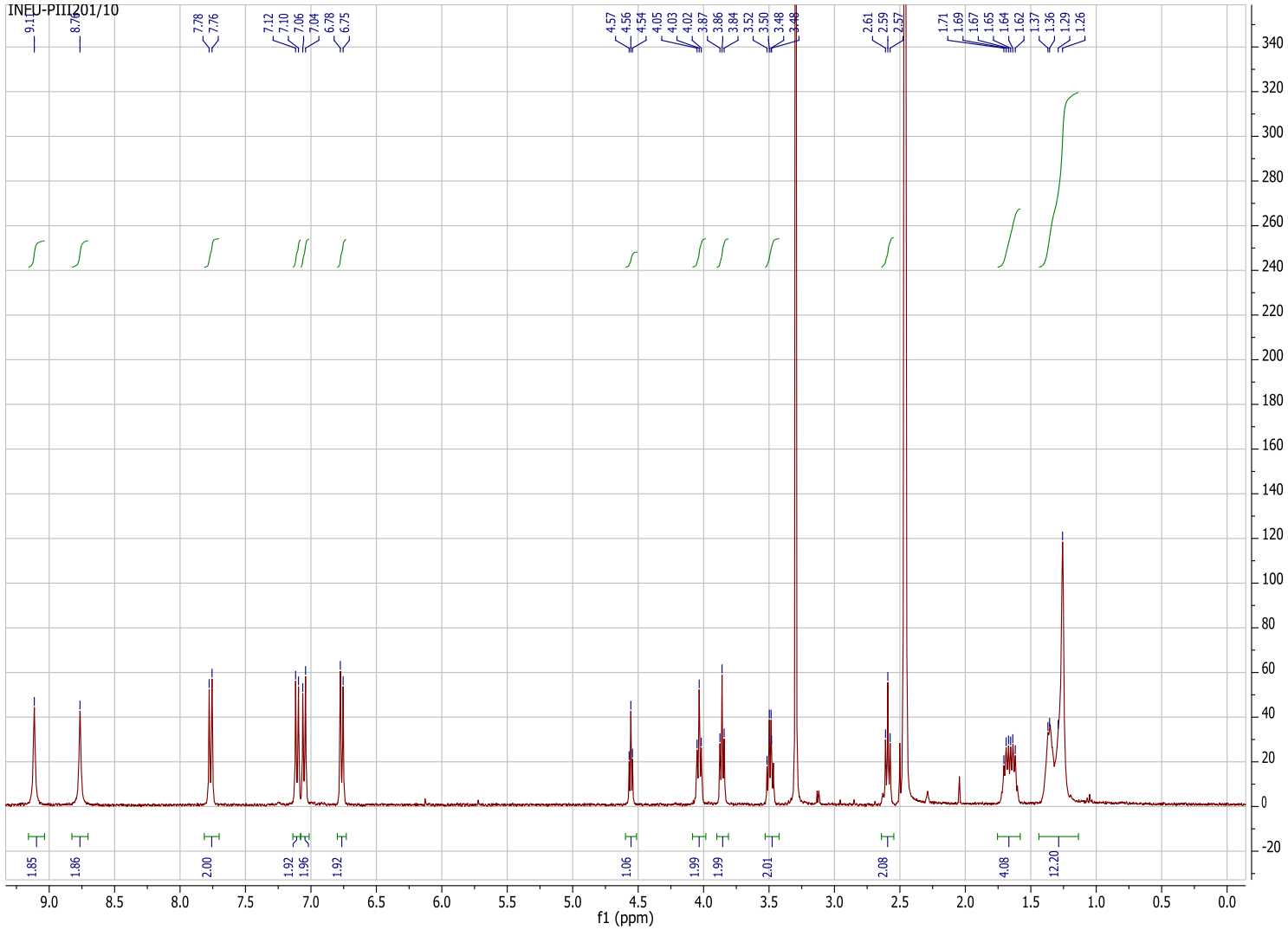

HR-ESI-MS of 4-{10-[4-(2-Hydrody-ethyl)-phenyoxy]-decyloxy}-benzamidine hydrochloride (AT3)

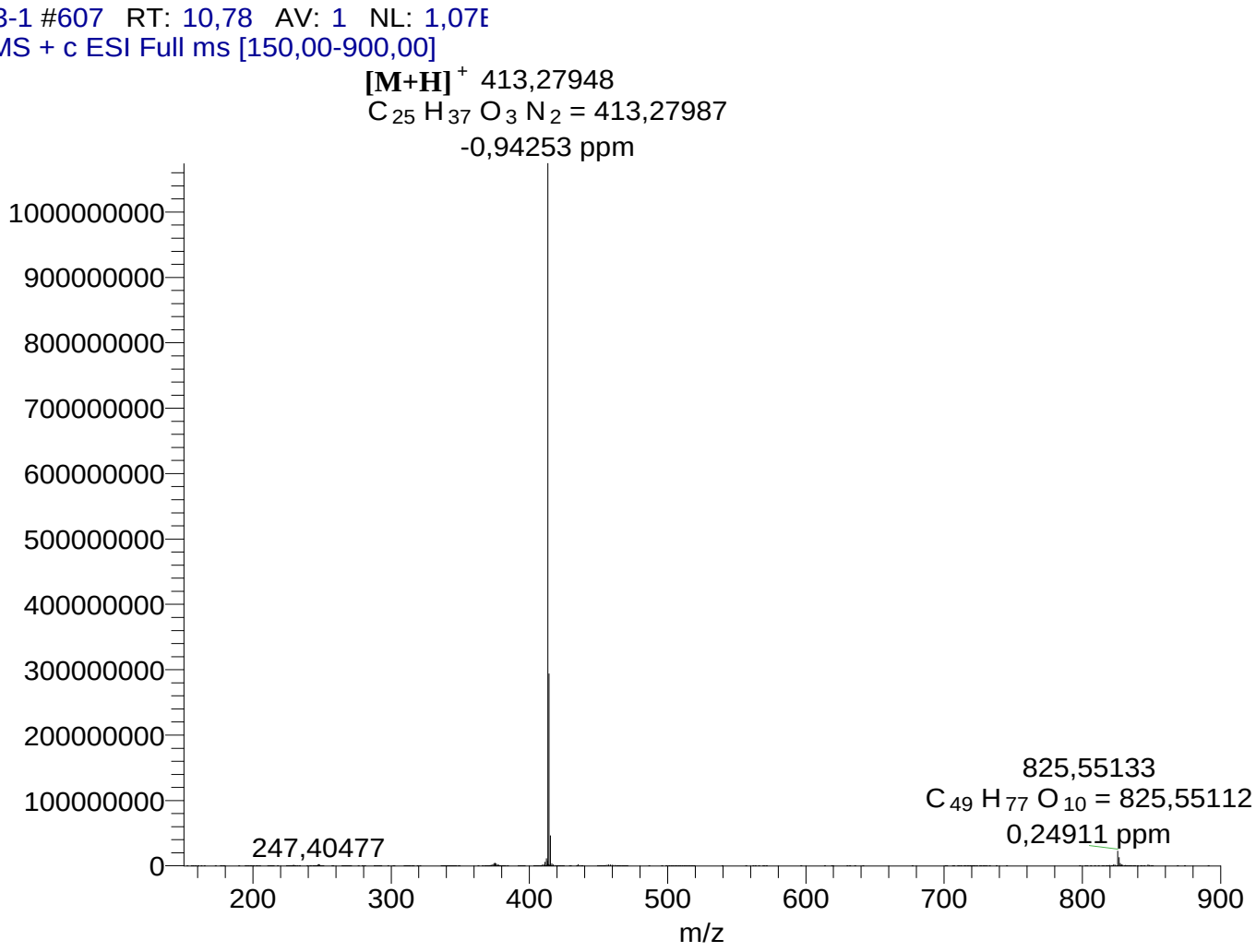

^{1}H-NMR of [(4-{10-[4-(2-Hydroxy-ethyl)-phenoxy]-decyloxy}- phenyl)-imino-methyl]-carbamic acid *tert*-butyl ester (AT4)

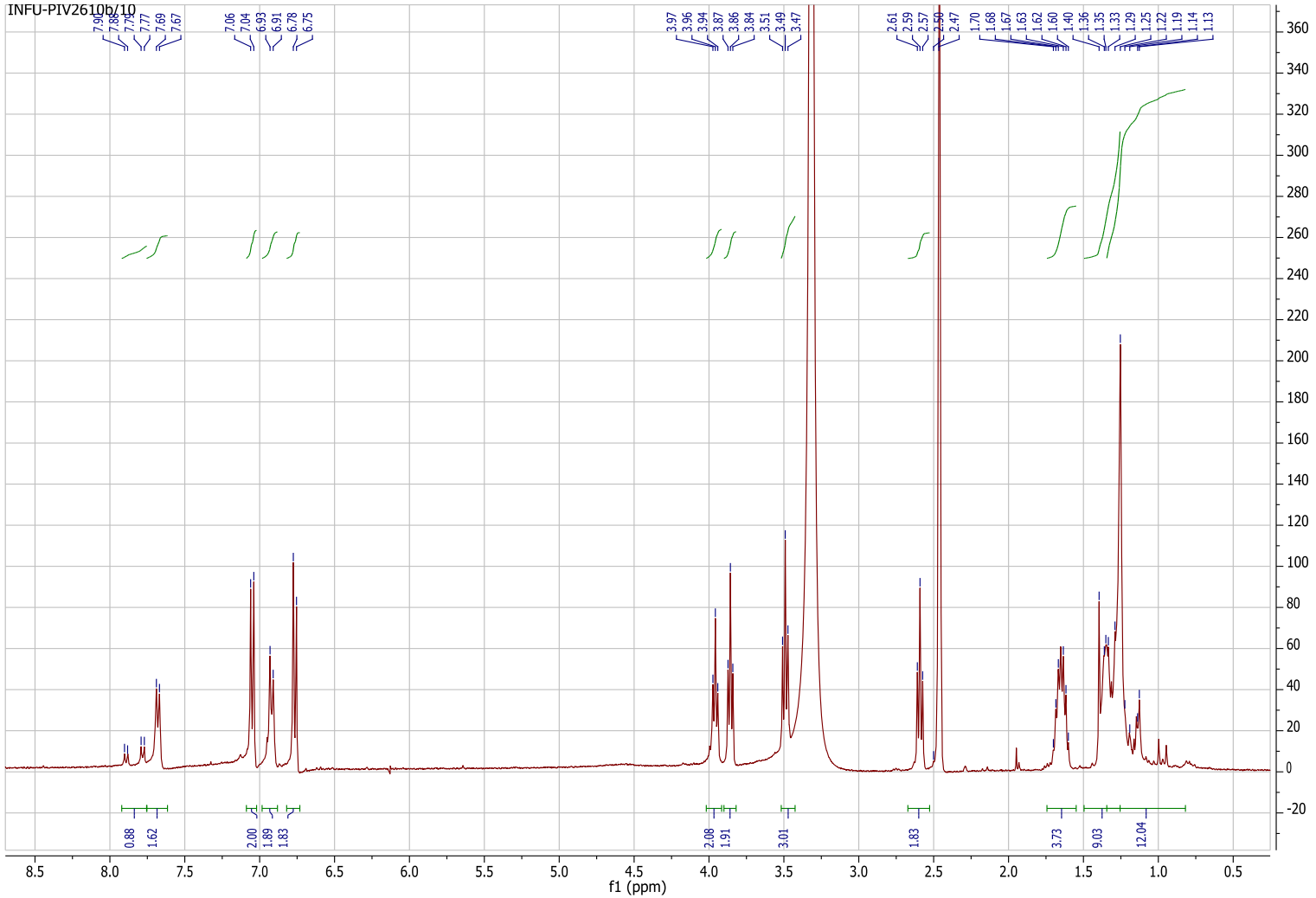

^{13}C-NMR of [(4-{10-[4-(2-Hydroxy-ethyl)-phenoxy]-decyloxy}- phenyl)-imino-methyl]-carbamic acid *tert*-butyl ester (AT4)

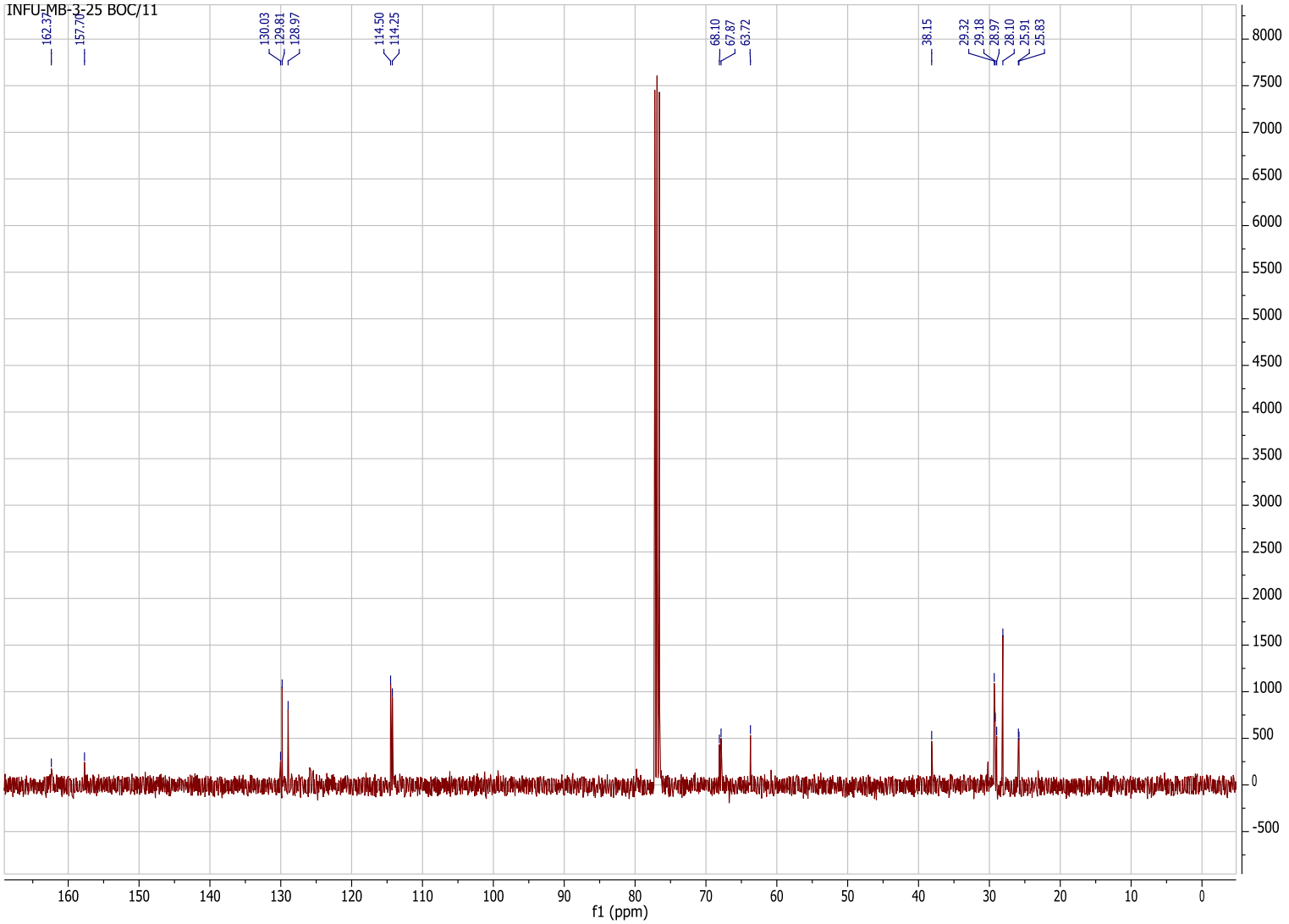

HR-ESI-MS of [(4-{10-[4-(2-Hydroxy-ethyl)-phenoxy]-decyloxy}- phenyl)-imino-methyl]-carbamic acid *tert*-butyl ester (AT4)

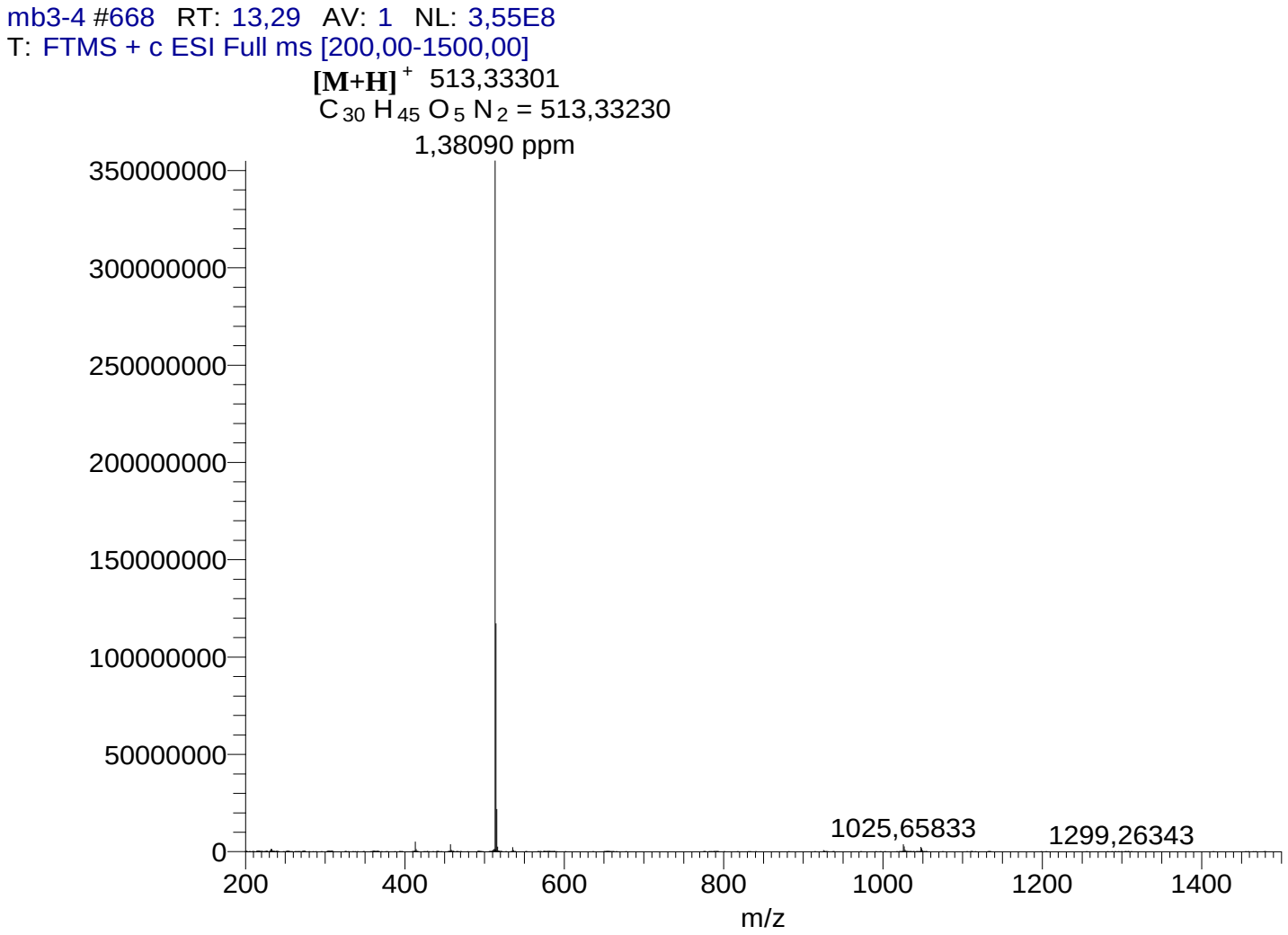

^{1}H-NMR of 5-(2-Oxo-hexahydro-thieno[3,4-*d*]imidazol-6-yl)-pentanoic acid 2-{4-[10-(4-carbamimidoyl-phenoxy)-decyloxy]-phenyl}-ethyl ester triflouro acetic acid (biotinylated amphiphile) (AT5)

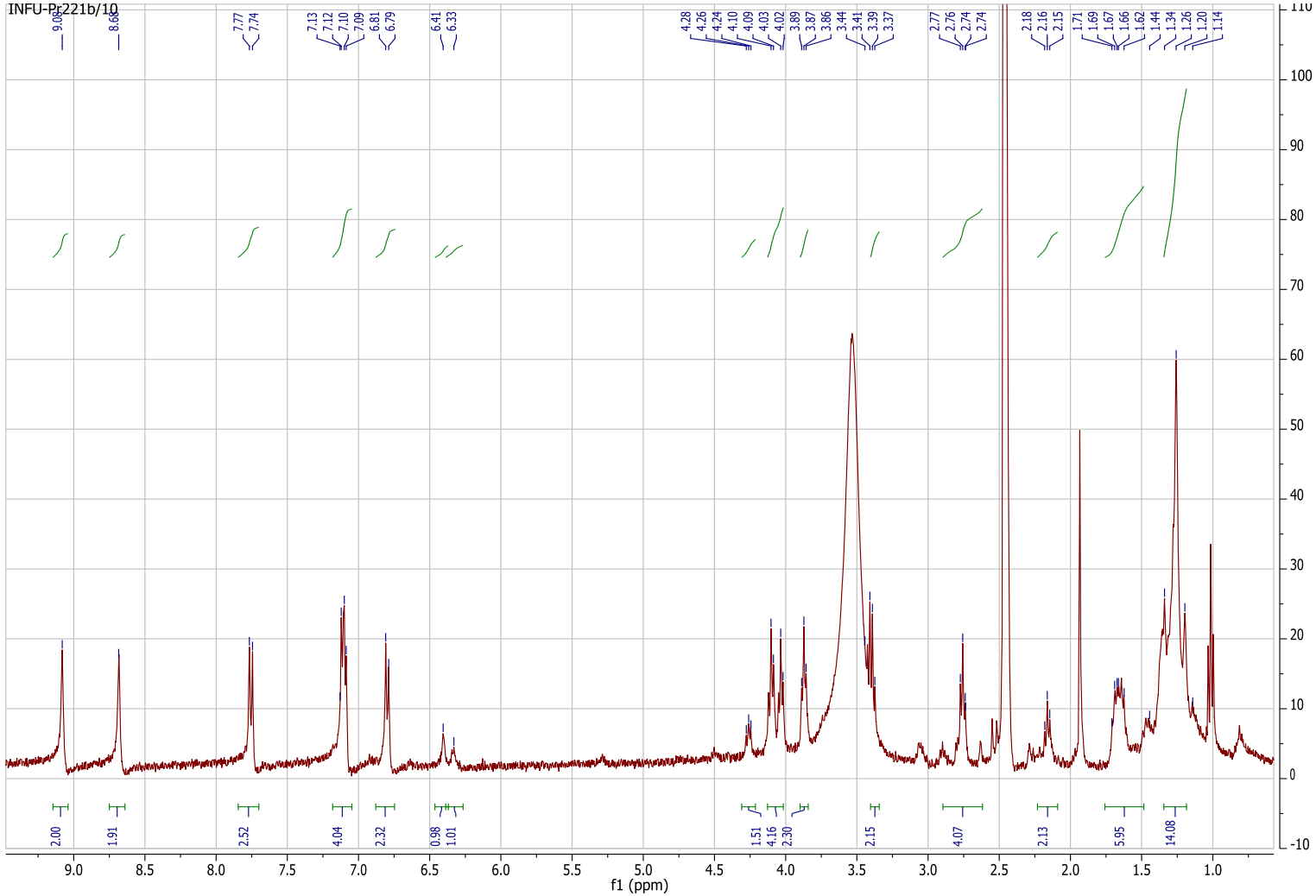

MALDI of 5-(2-Oxo-hexahydro-thieno[3,4-*d*]imidazol-6-yl)-pentanoic acid 2-{4-[10-(4-carbamimidoyl-phenoxy)-decyloxy]-phenyl}-ethyl ester triflouro acetic acid (biotinylated amphiphile) (AT5)

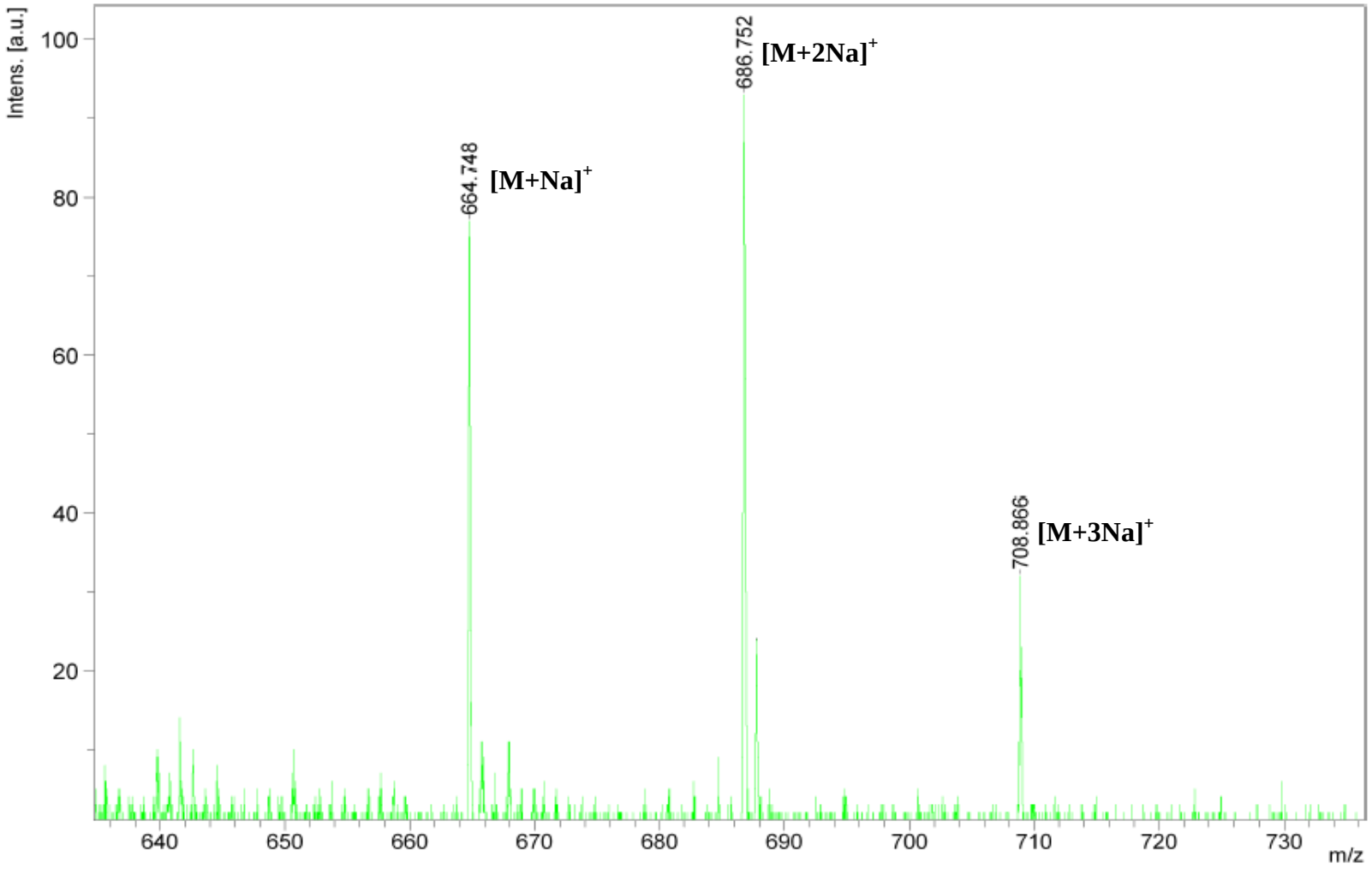

^{1}H-NMR of 2-(2-(2-chloroethoxy)ethoxy)acetic acid (AT6)

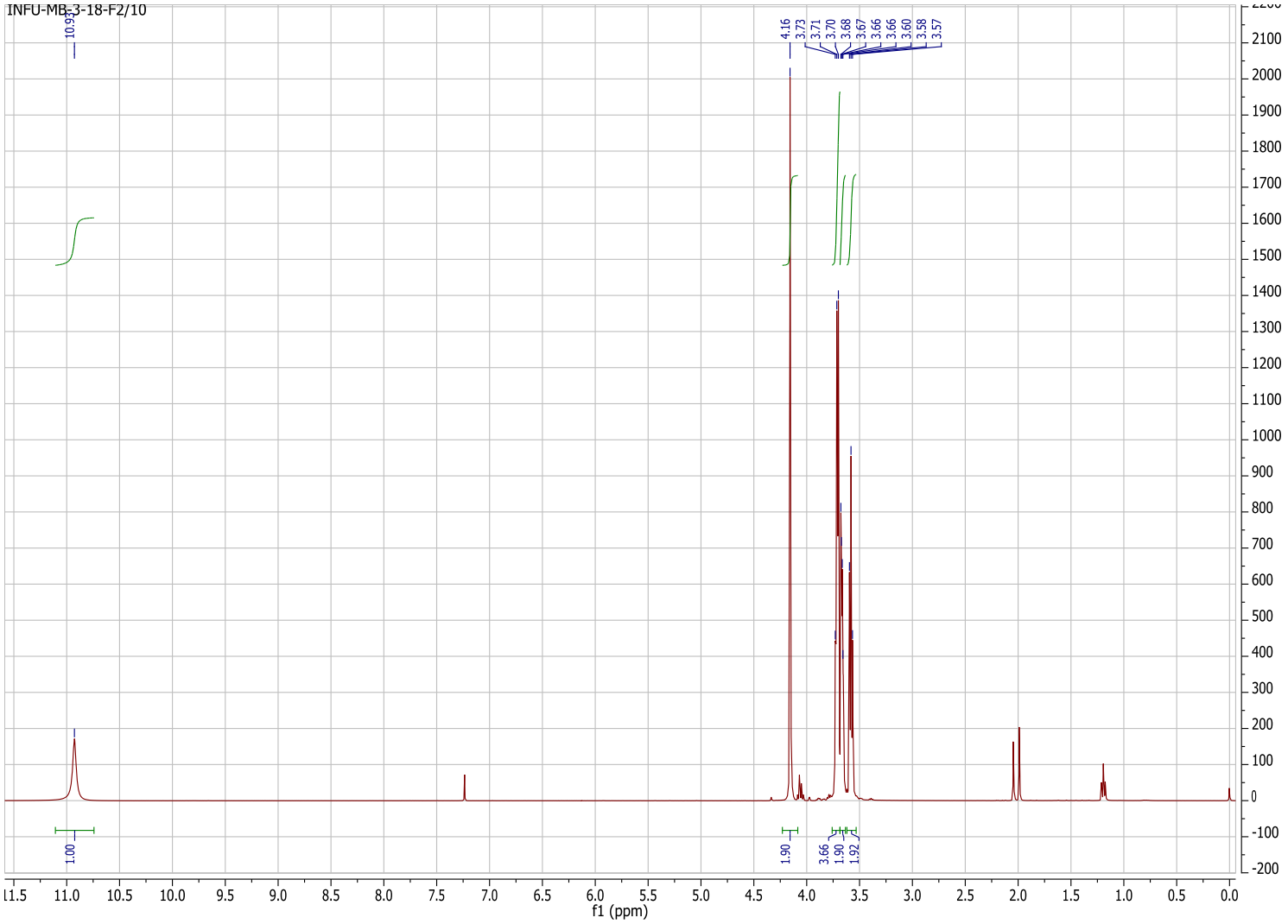

^{13}C-NMR of 2-(2-(2-chloroethoxy)ethoxy)acetic acid (AT6)

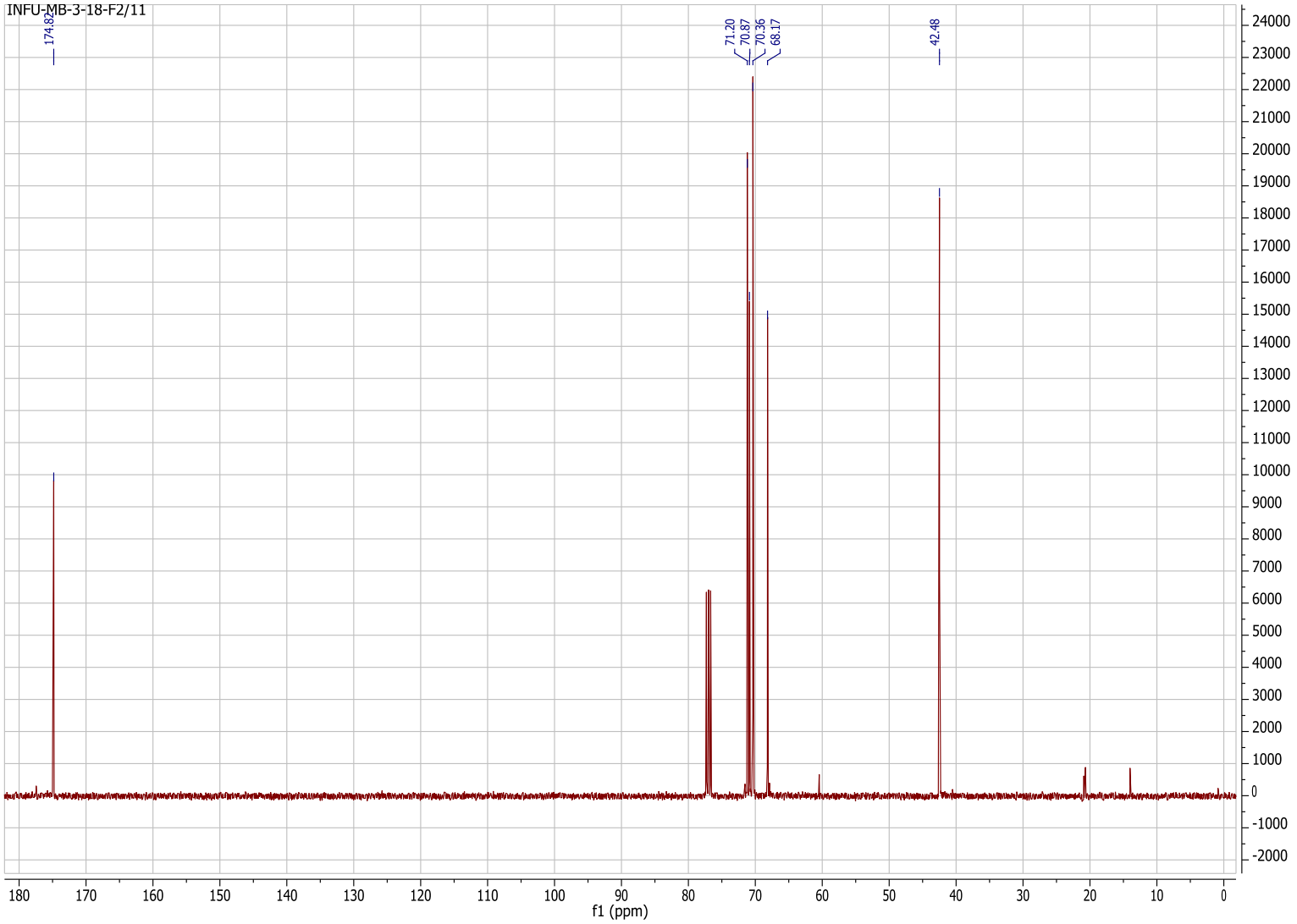

HR-ESI-MS of 2-(2-(2-chloroethoxy)ethoxy)acetic acid (AT6)

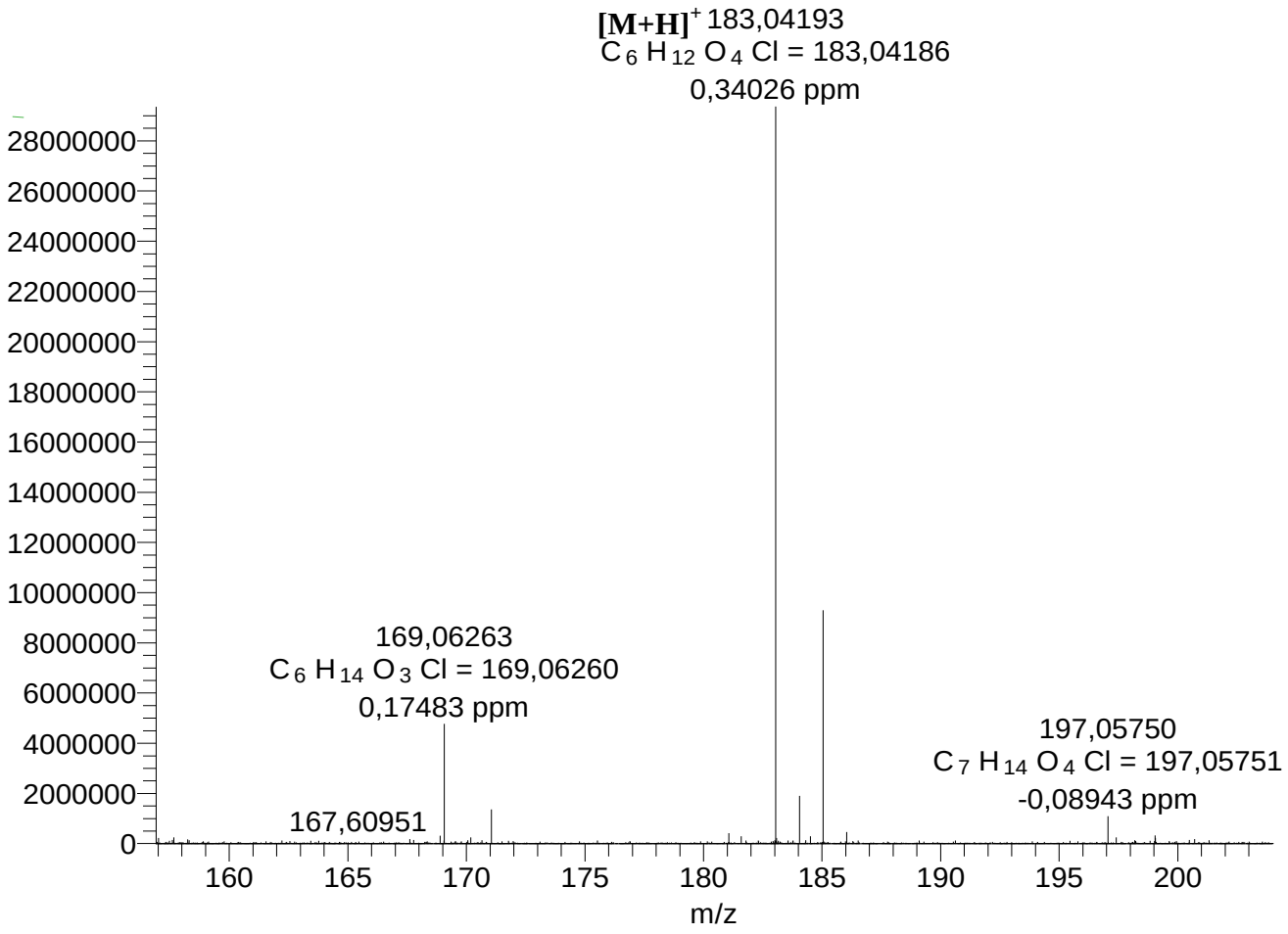

^{1}H-NMR of methyl 2-(2-(2-chloroethoxy)ethoxy)acetate (AT7)

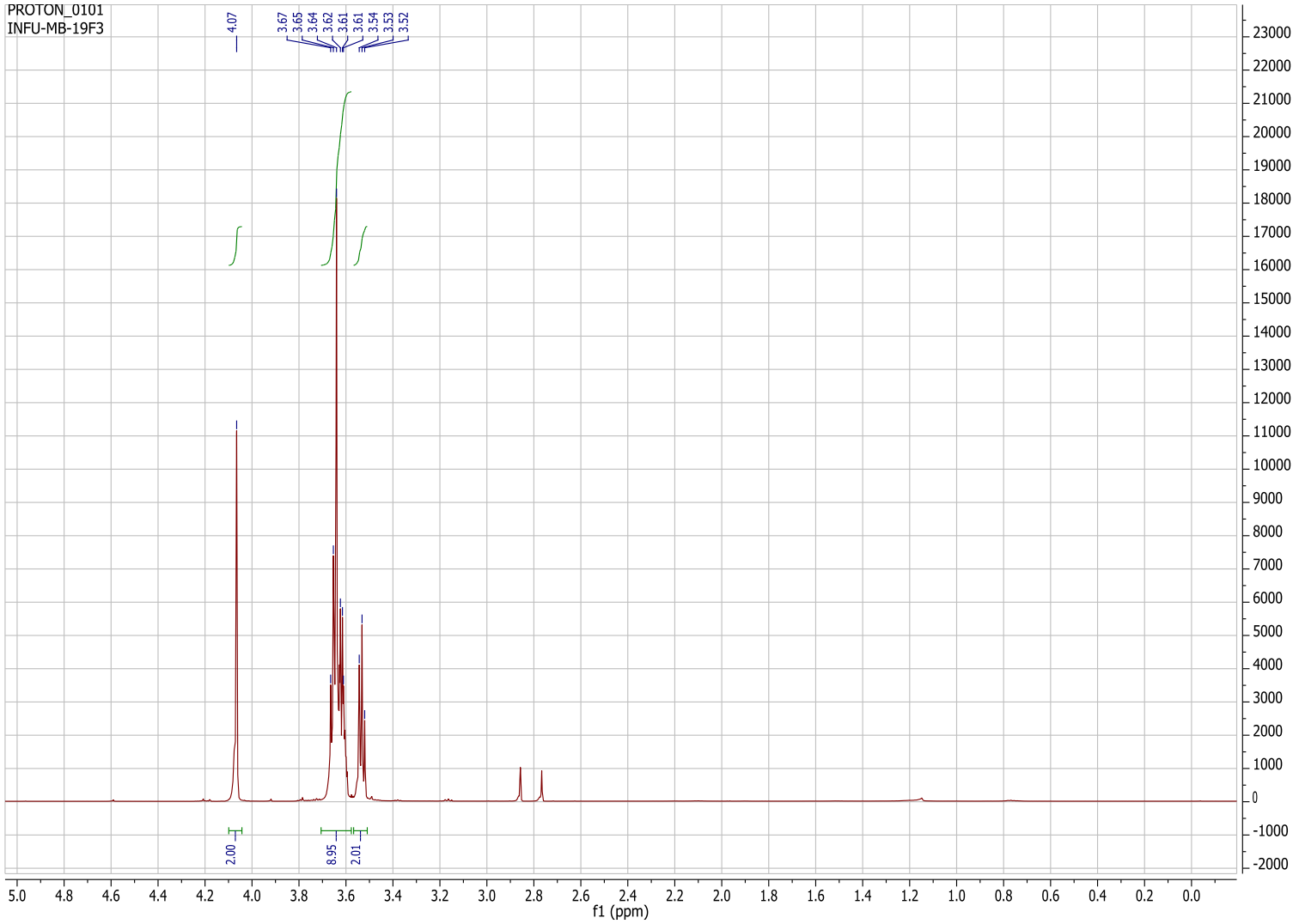

^{13}C-NMR of methyl 2-(2-(2-chloroethoxy)ethoxy)acetate (AT7)

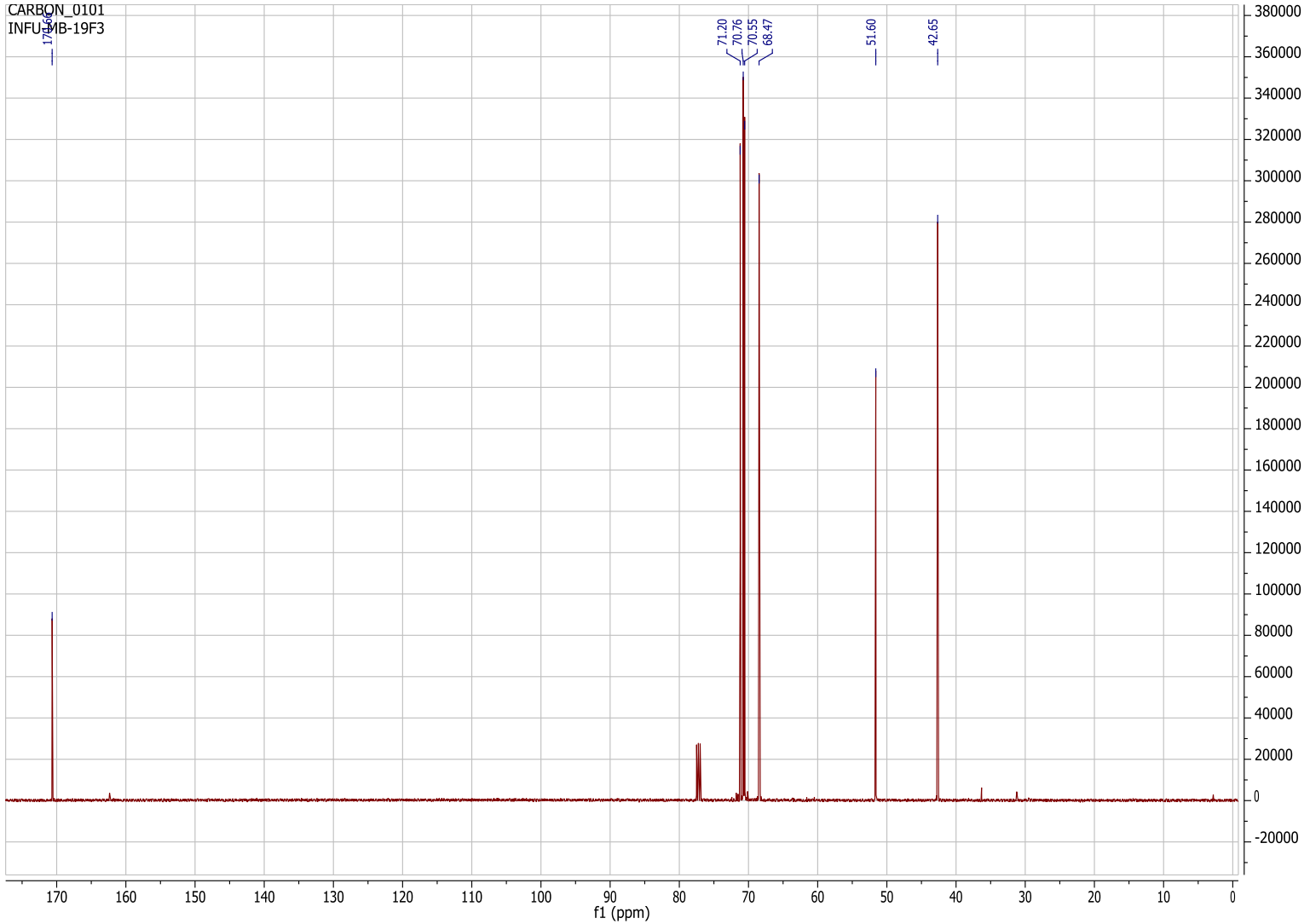

HR-ESI-MS of methyl 2-(2-(2-chloroethoxy)ethoxy)acetate (AT7)

MB-3-18F1 #787-820 RT: 12,10-12,59 AV: 7
T: FTMS + p ESI Full ms [65,00-350,00]

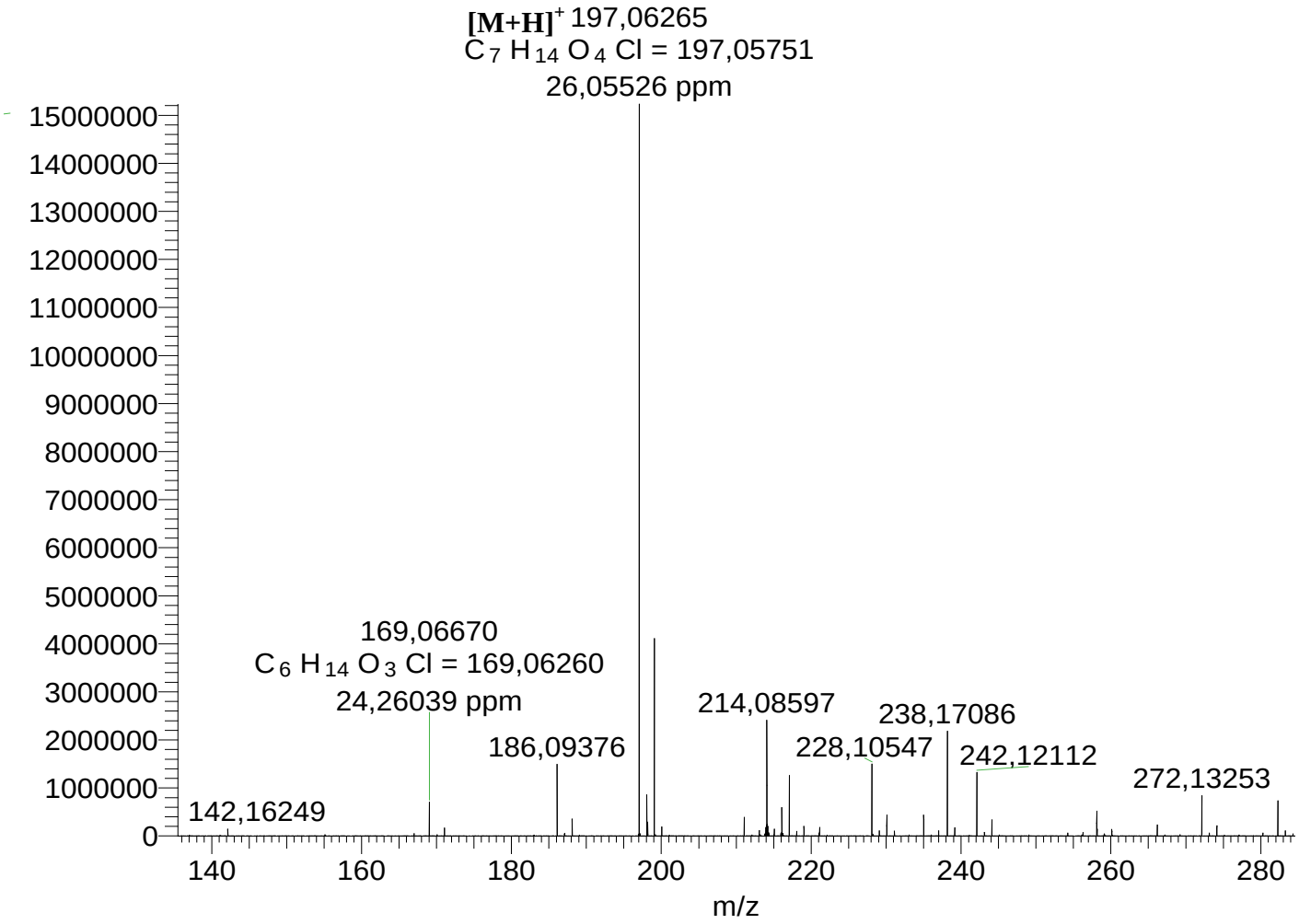

^{1}H-NMR of methyl 2-(2-(2-azidoethoxy)ethoxy)acetate (AT8)

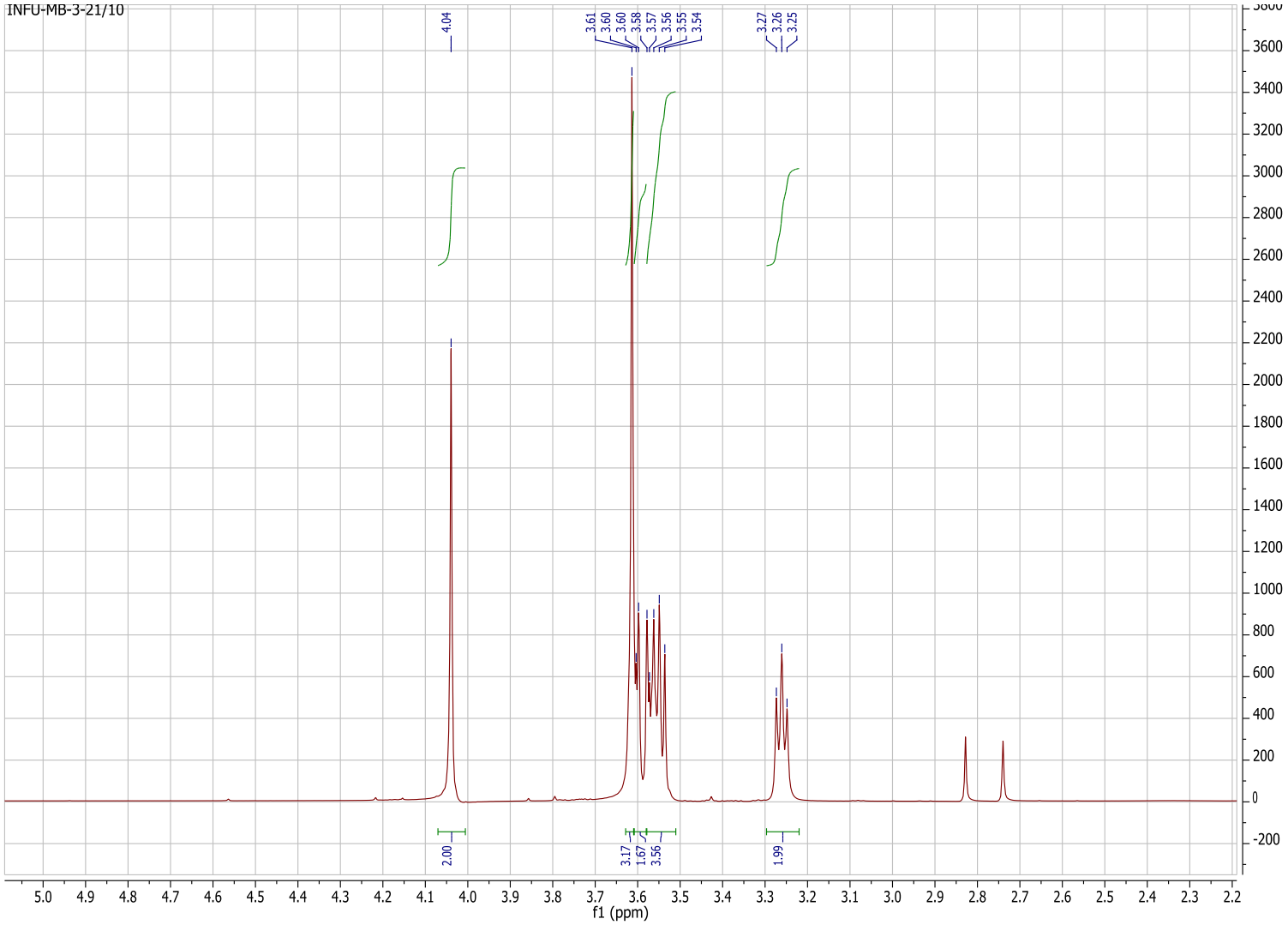

^{13}C-NMR of methyl 2-(2-(2-azidoethoxy)ethoxy)acetate (AT8)

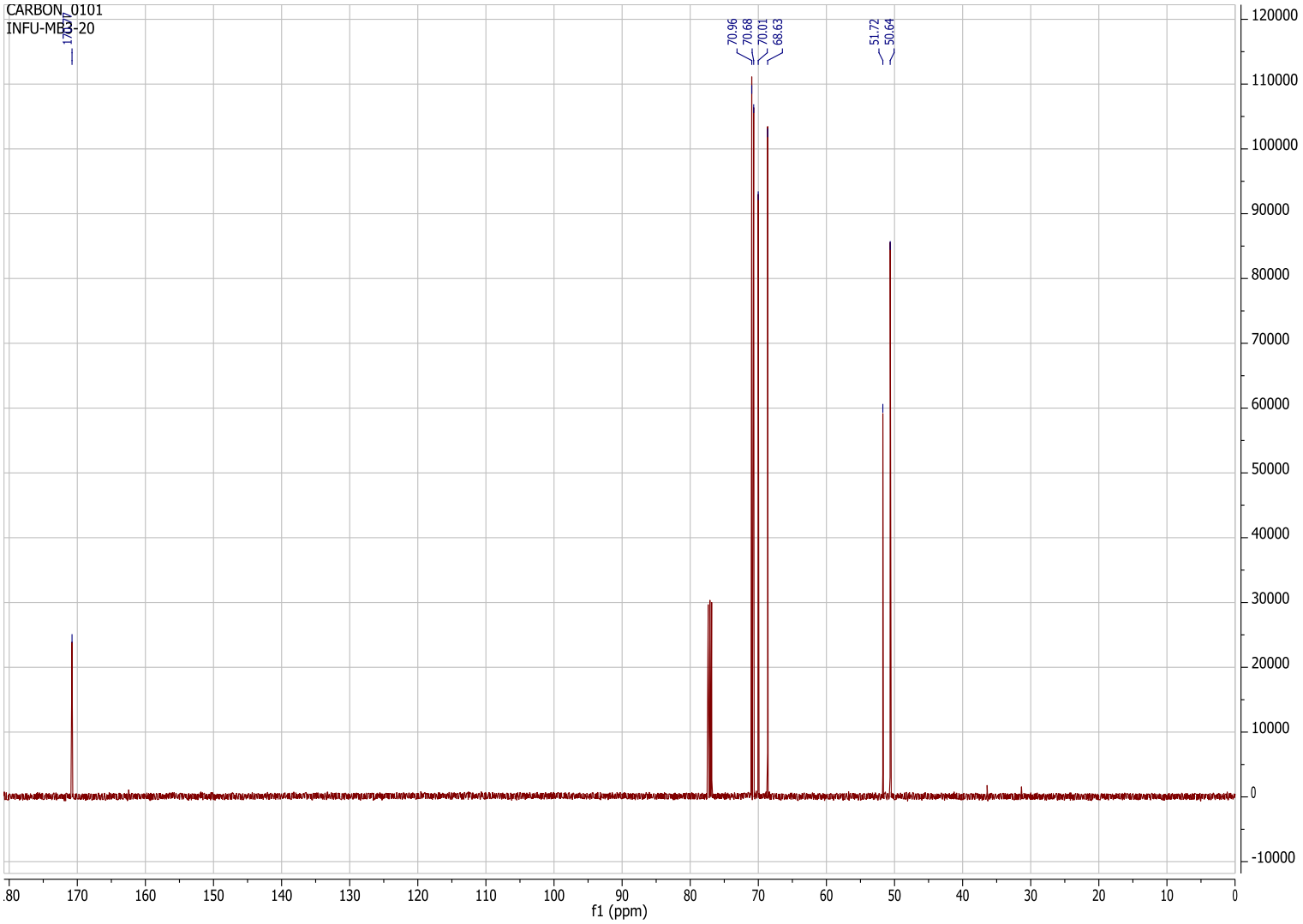

HR-ESI-MS of methyl 2-(2-(2-azidoethoxy)ethoxy)acetate (AT8)

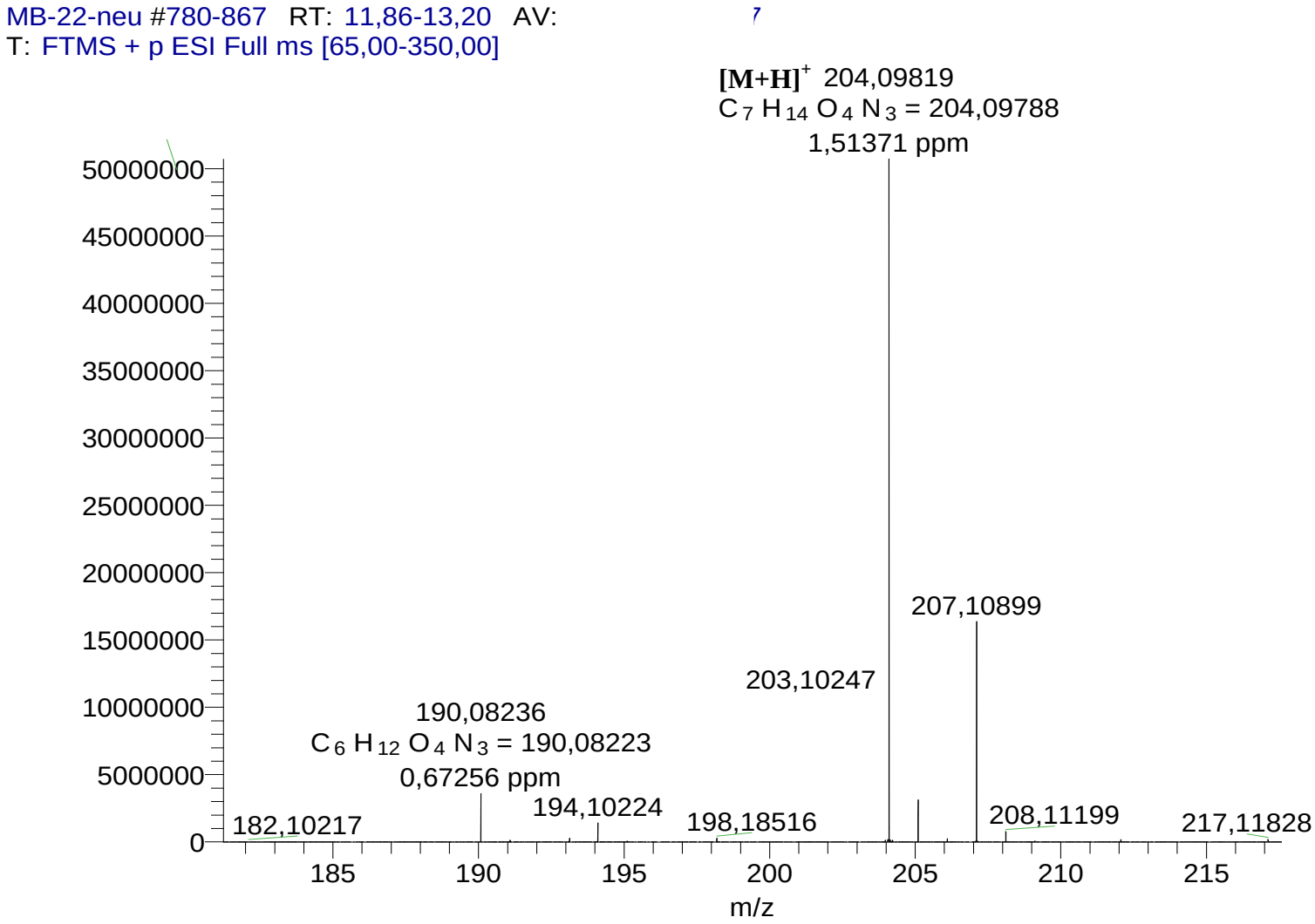

^{1}H-NMR of 2-(2-(2-azidoethoxy)ethoxy)acetic acid (AT9)

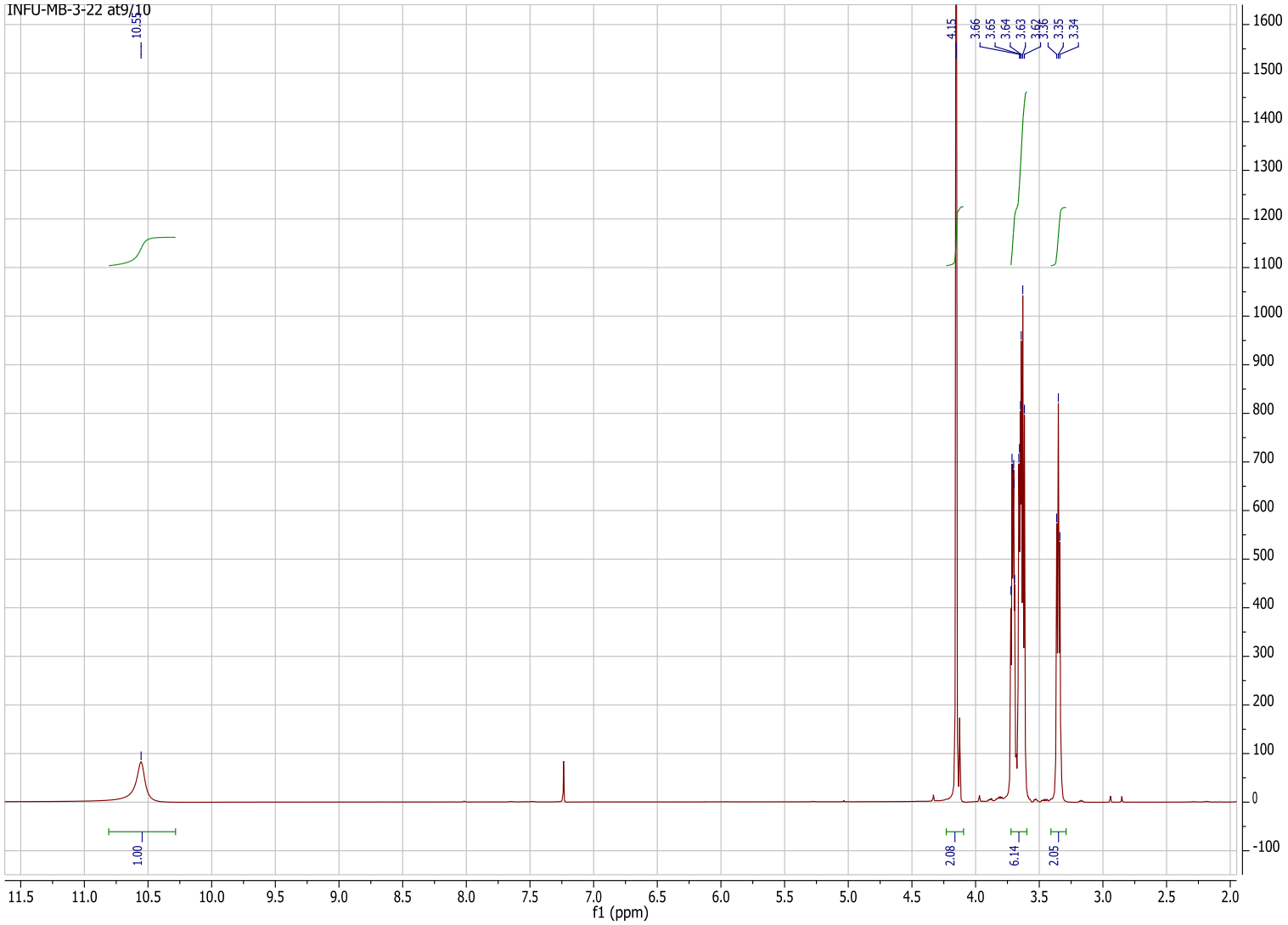

^{13}C-NMR of 2-(2-(2-azidoethoxy)ethoxy)acetic acid (AT9)

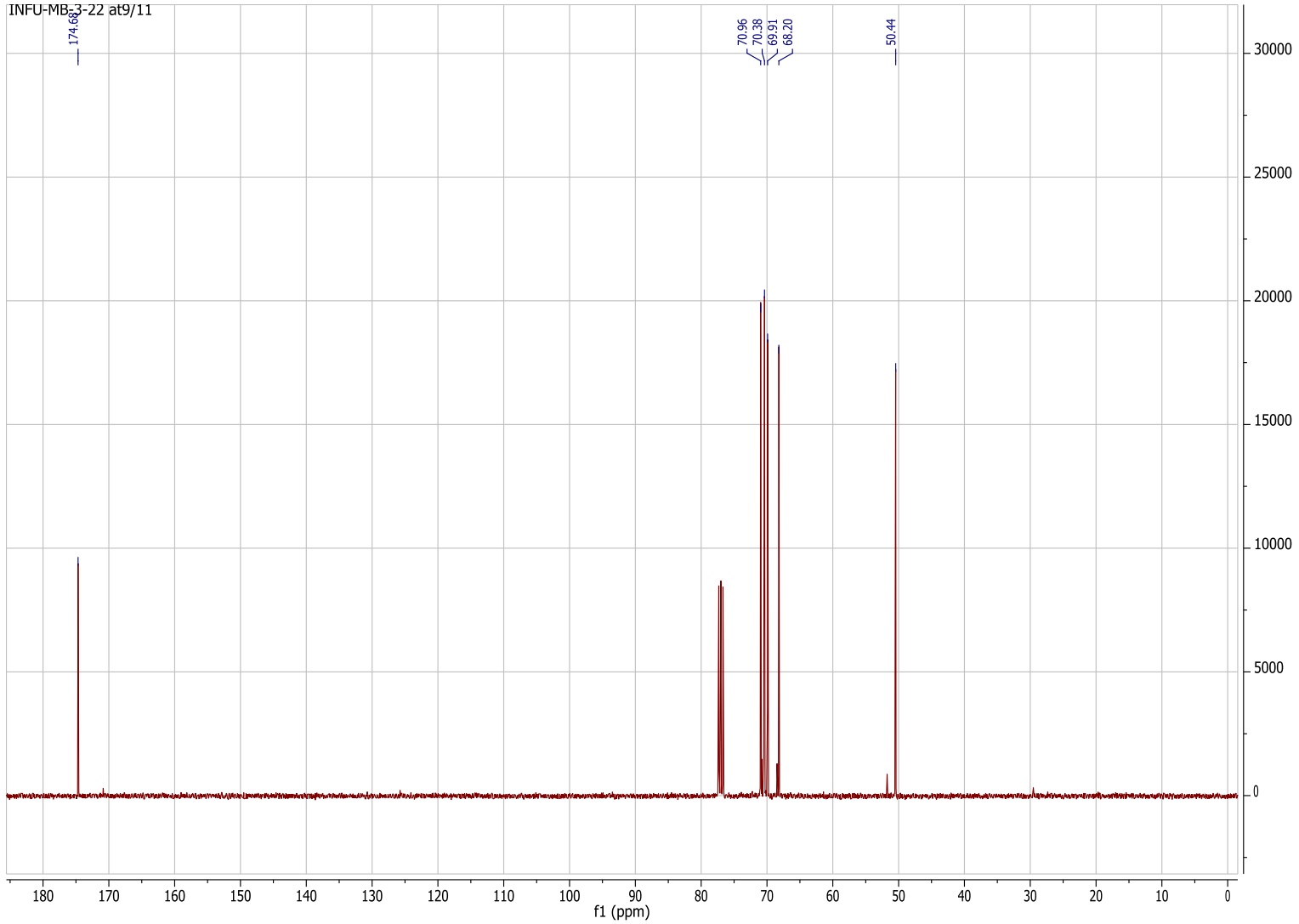

HR-ESI-MS of 2-(2-(2-azidoethoxy)ethoxy)acetic acid (AT9)

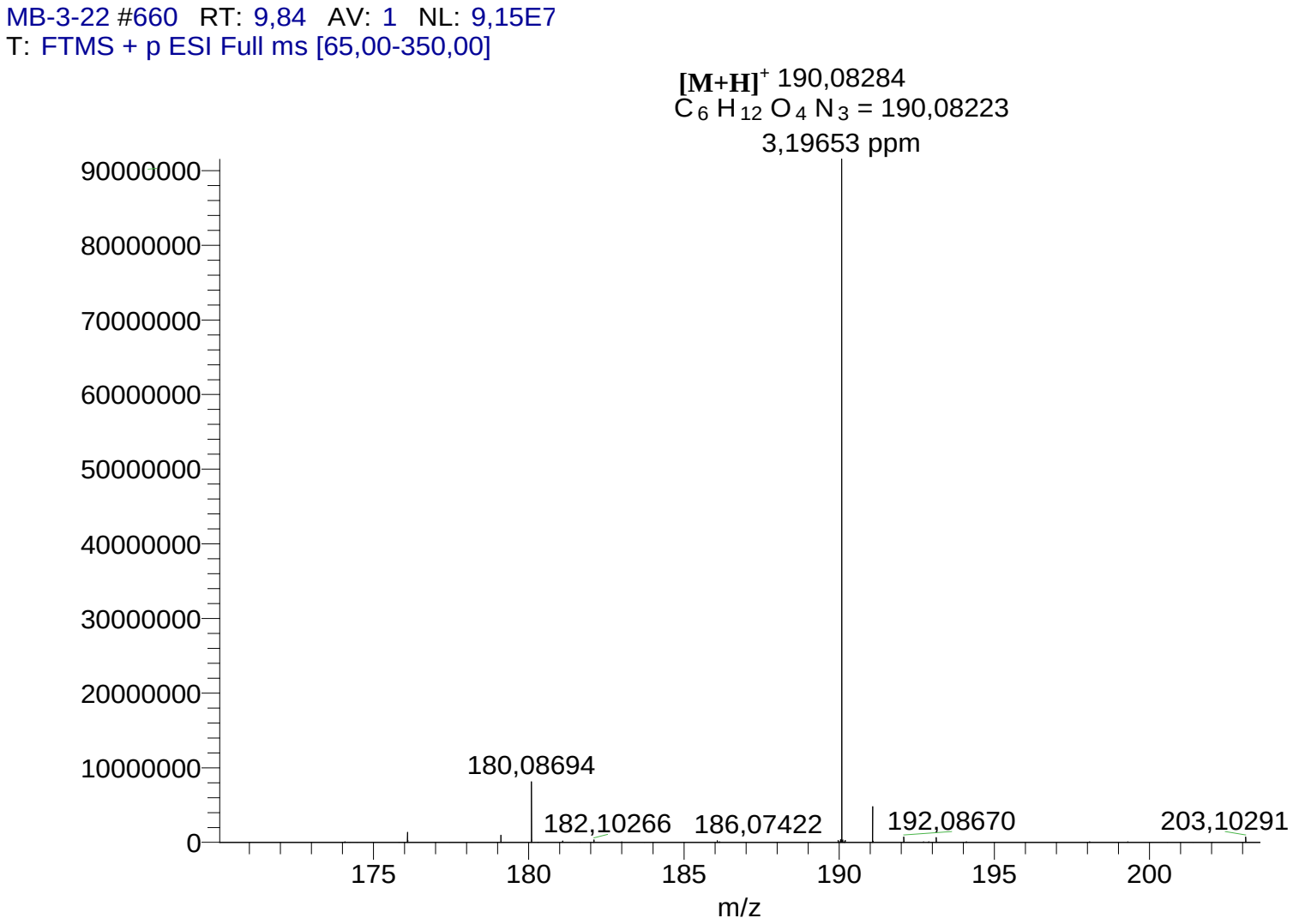

^{1}H-NMR of 4-((10-(4-(N-(tert-butoxycarbonyl)carbamimidoyl) phenoxy) decyl)oxy) phenethyl 2-(2-(2-azidoethoxy)ethoxy)acetate (AT10)

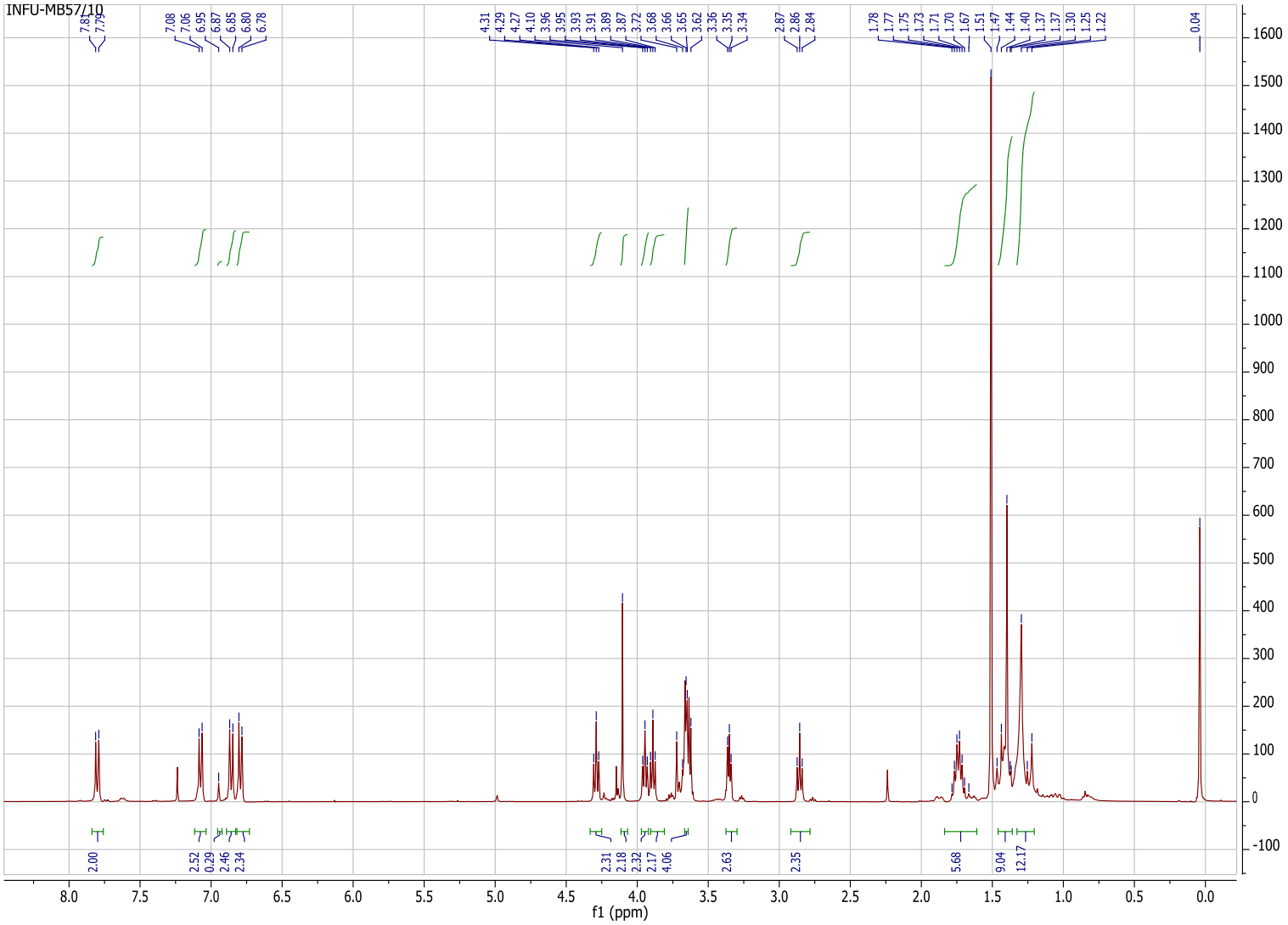

^{13}C-NMR of 4-((10-(4-(N-(tert-butoxycarbonyl)carbamimidoyl) phenoxy) decyl)oxy) phenethyl 2-(2-(2-azidoethoxy)ethoxy)acetate (AT10)

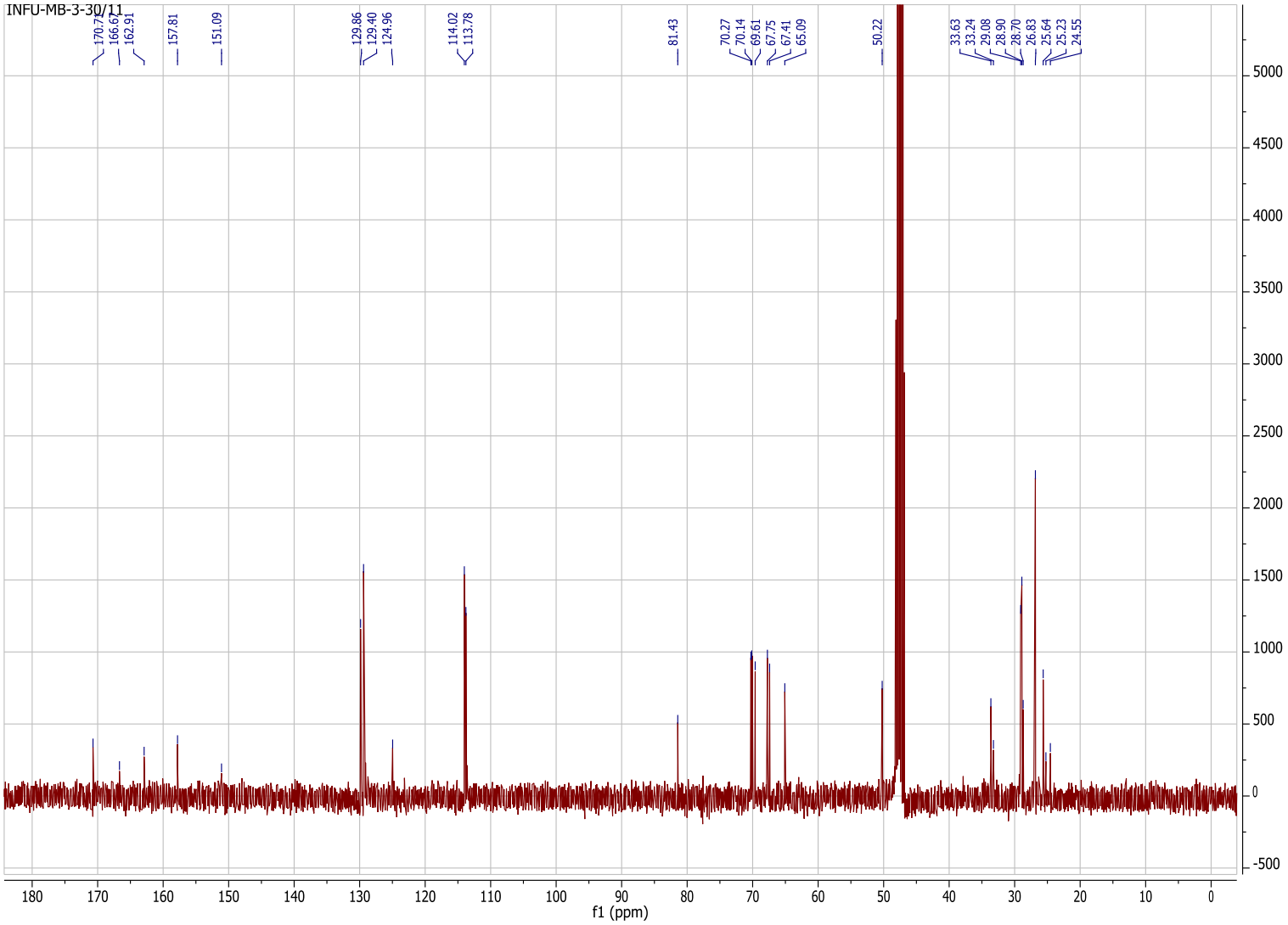

HR-ESI-MS of 4-((10-(4-(N-(tert-butoxycarbonyl)carbamimidoyl) phenoxy) decyl)oxy) phenethyl 2-(2-(2-azidoethoxy)ethoxy)acetate (AT10)

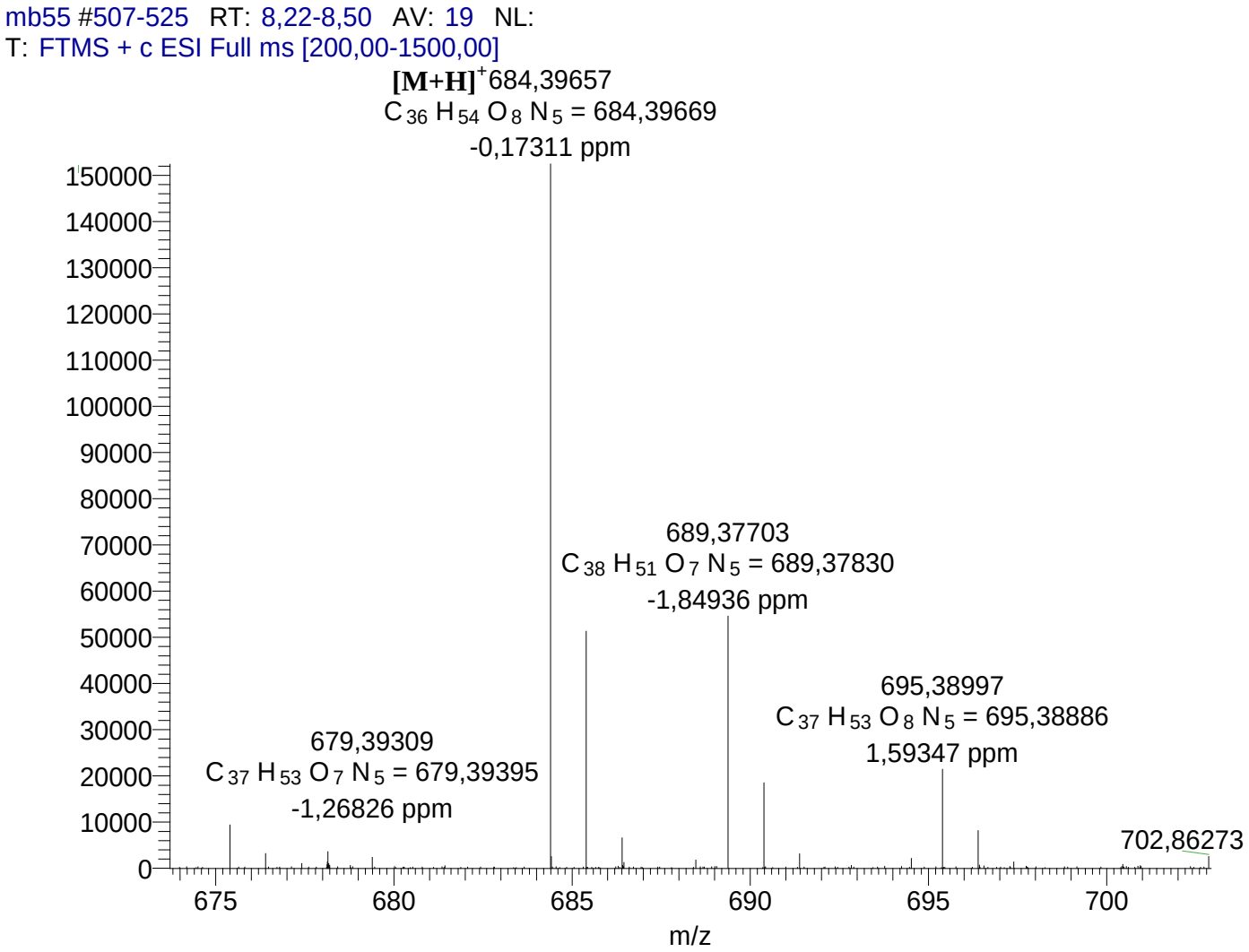

^{1}H-NMR of 4-{10-[2-(2-(2-azidoethoxy)ethoxy)acetate-phenyoxy]-decyloxy}-benzamidine hydrochloride (AT11)

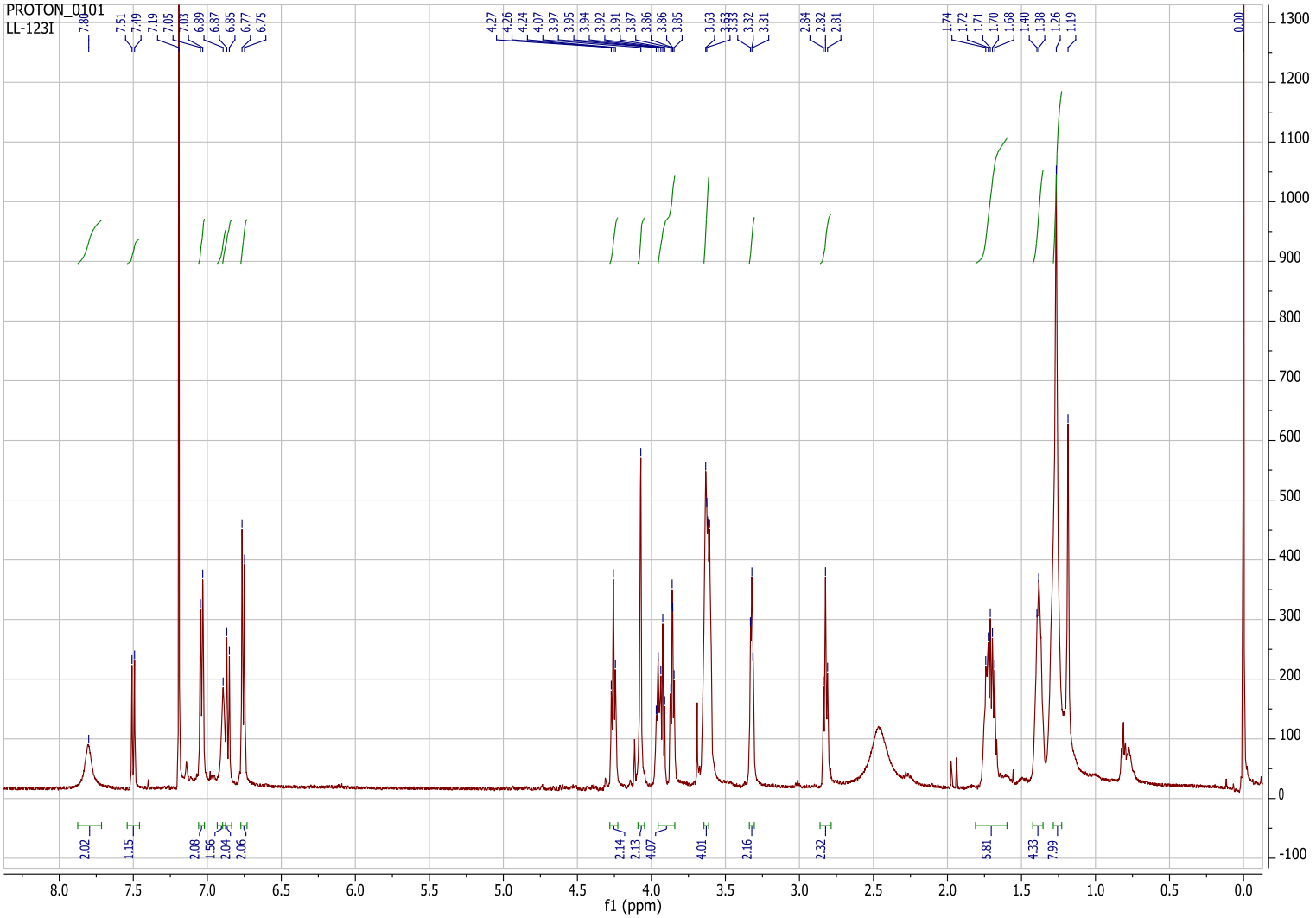

^{13}C-NMR of 4-{10-[2-(2-(2-azidoethoxy)ethoxy)acetate-phenyoxy]-decyloxy}-benzamidine hydrochloride (AT11)

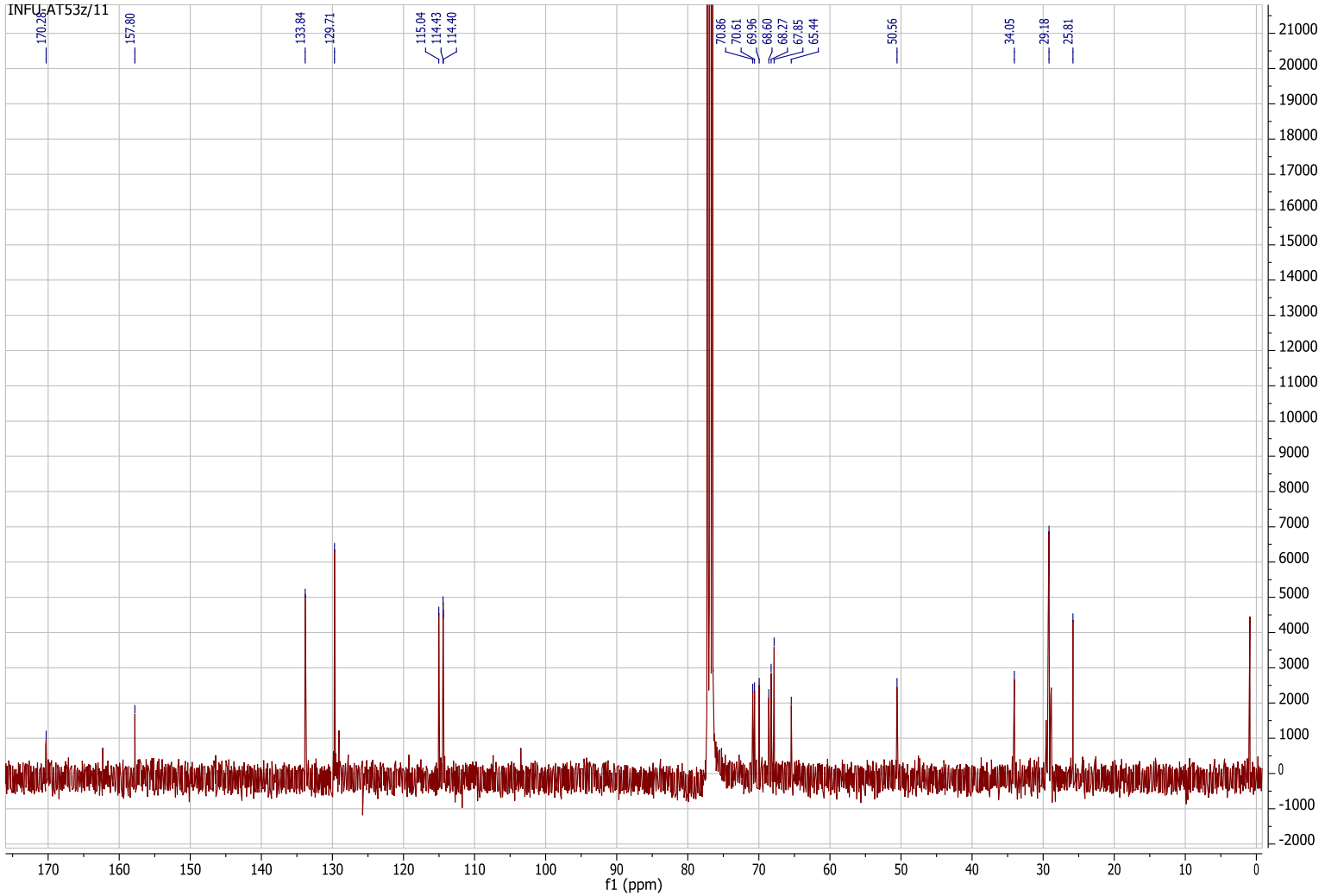

HR-ESI-MS of 4-{10-[2-(2-(2-azidoethoxy)ethoxy)acetate-phenyoxy]-decyloxy}-benzamidine hydrochloride (AT11)

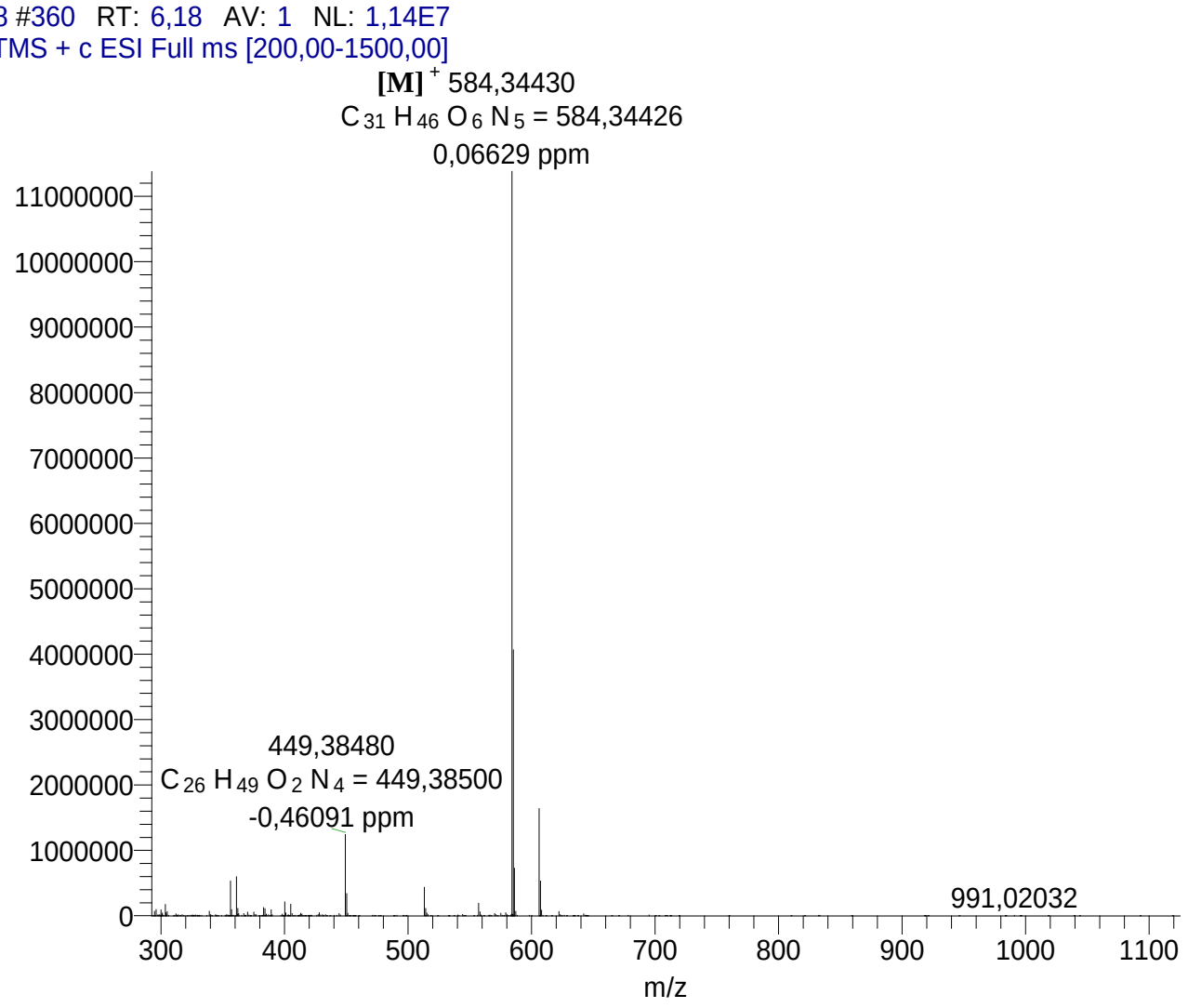

^{1}H-NMR of methyl 5-acetamido-2,4-dihydroxy-6-(1,2,3-trihydroxypropyl)tetrahydro-2H-pyran-2-carboxylate (AT12)

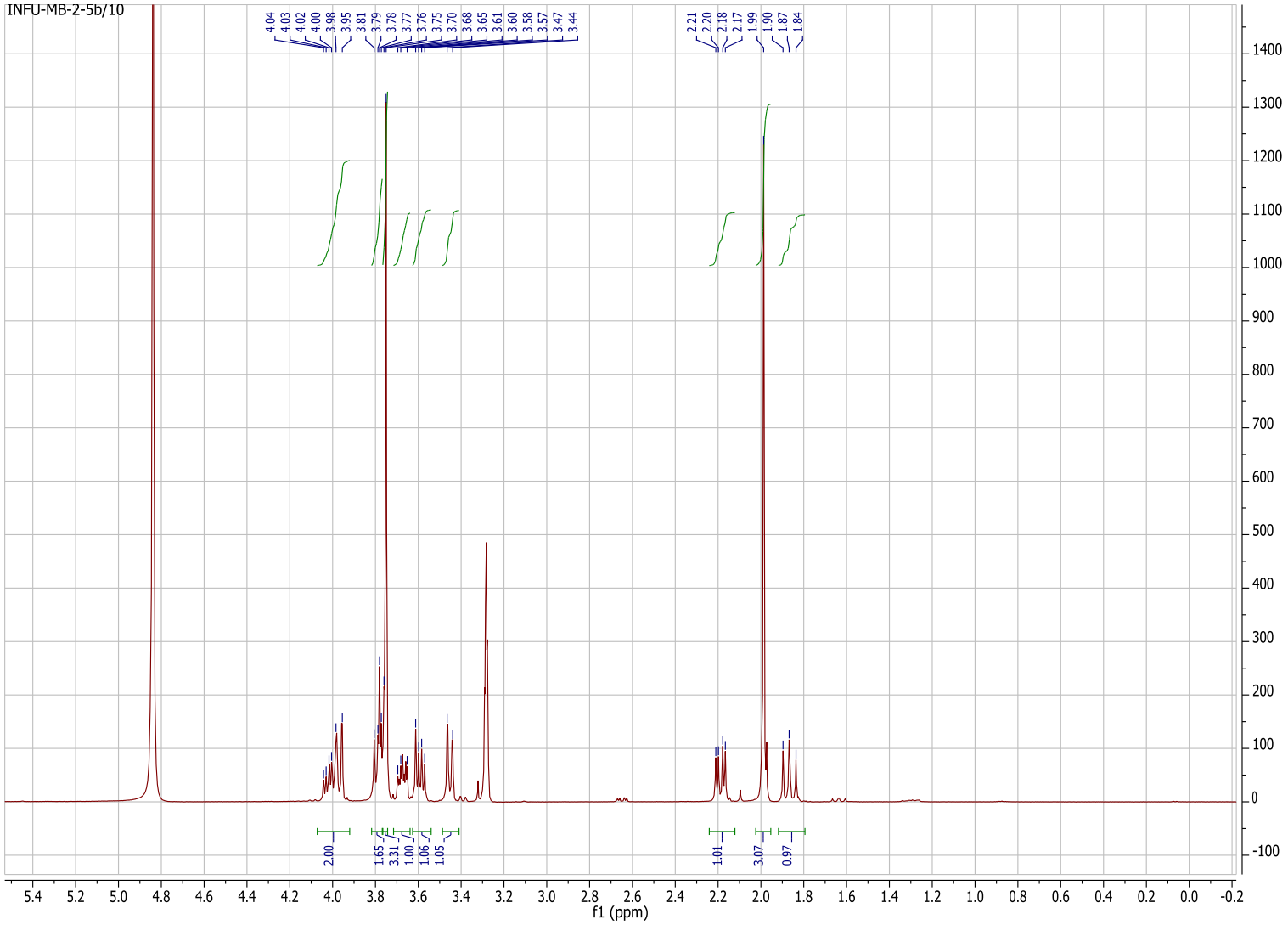

^{13}C-NMR of methyl 5-acetamido-2,4-dihydroxy-6-(1,2,3-trihydroxypropyl)tetrahydro-2H-pyran-2-carboxylate (AT12)

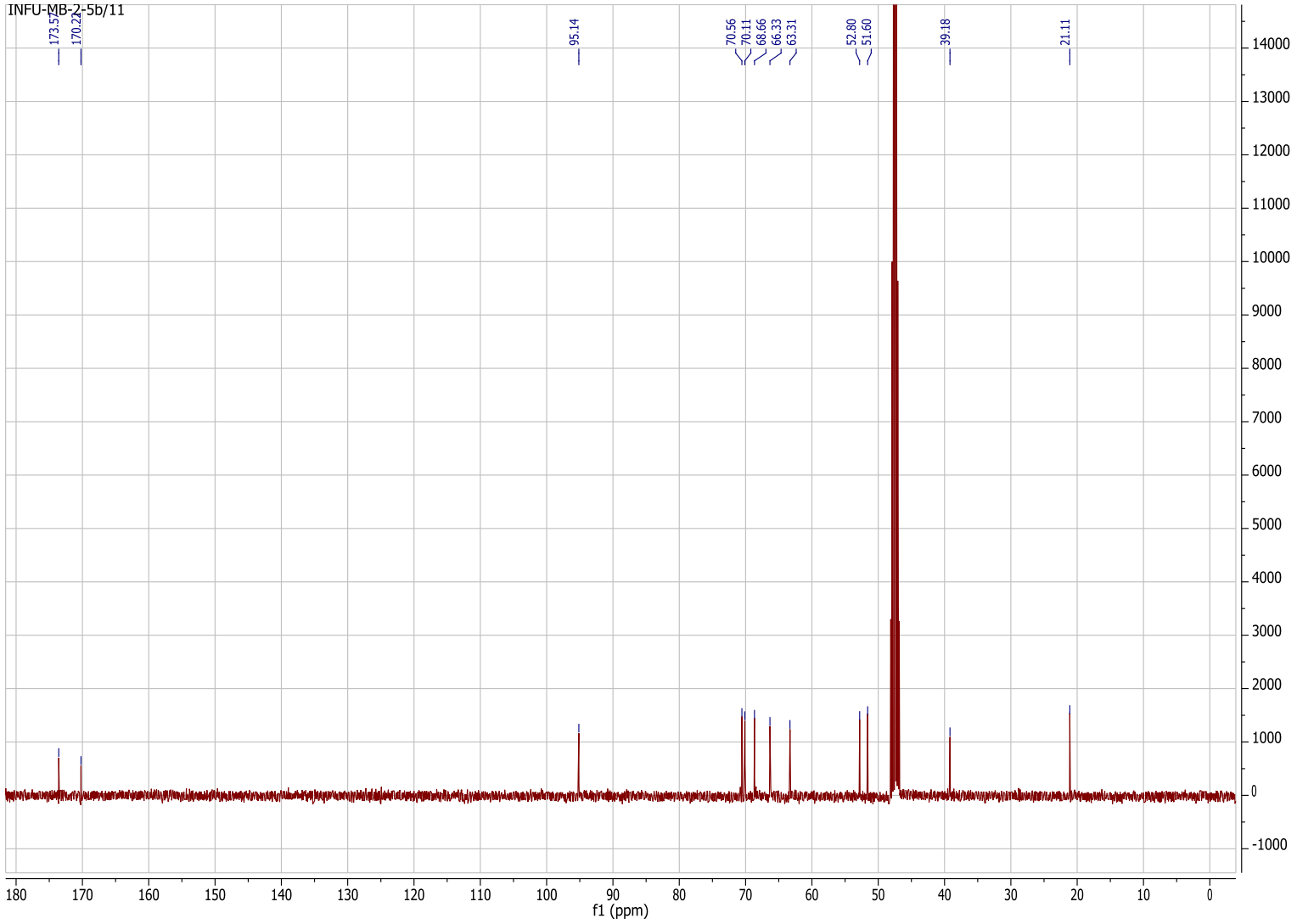

HR-ESI-MS of methyl 5-acetamido-2,4-dihydroxy-6-(1,2,3-trihydroxypropyl)tetrahydro-2H-pyran-2-carboxylate (AT12)

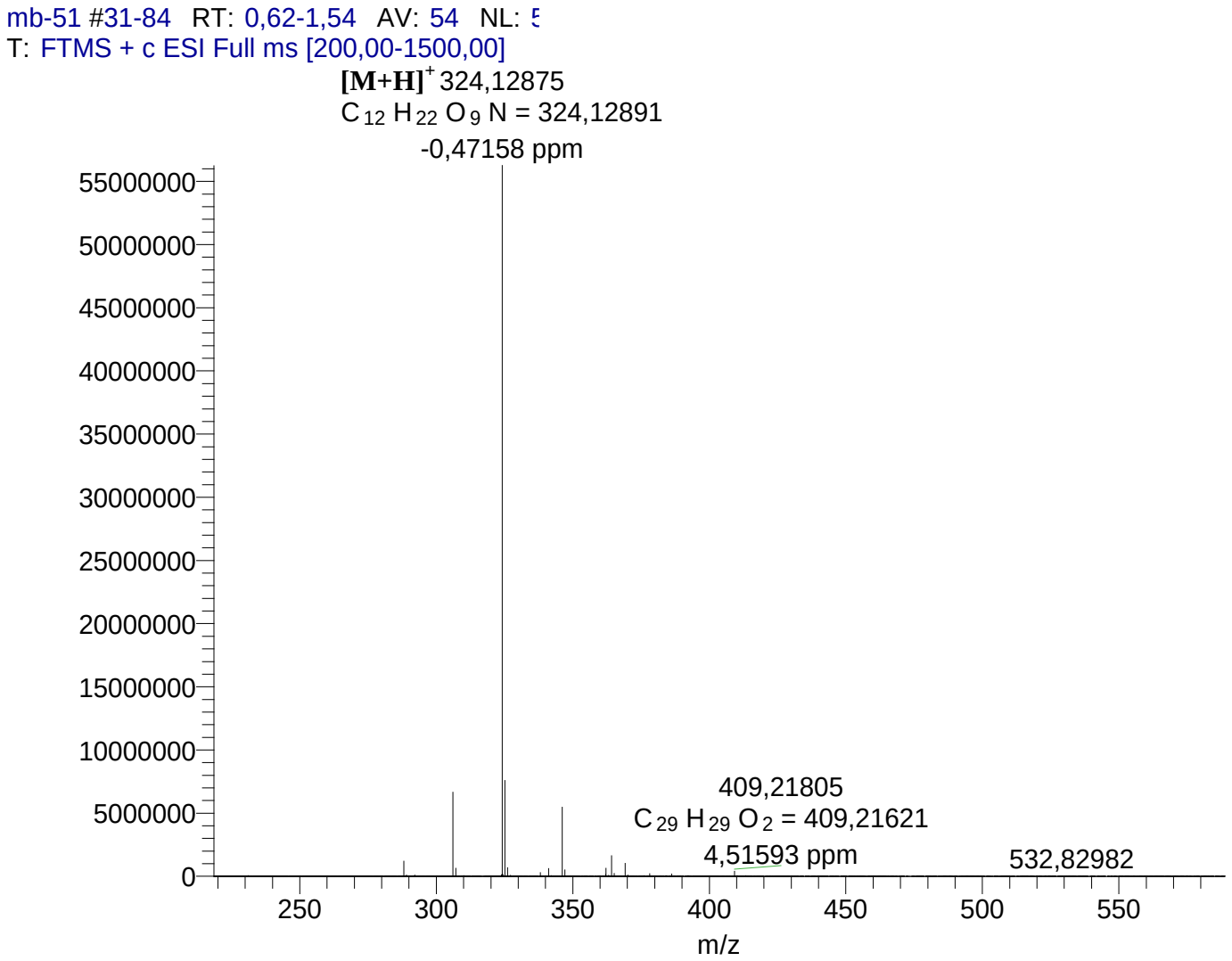

^{1}H-NMR of 3-acetamido-4-acetoxy-6-chloro-6-(methoxycarbonyl)tetrahydro-2H-pyran-2-yl)propane-1,2,3-triyl triacetate (AT13)

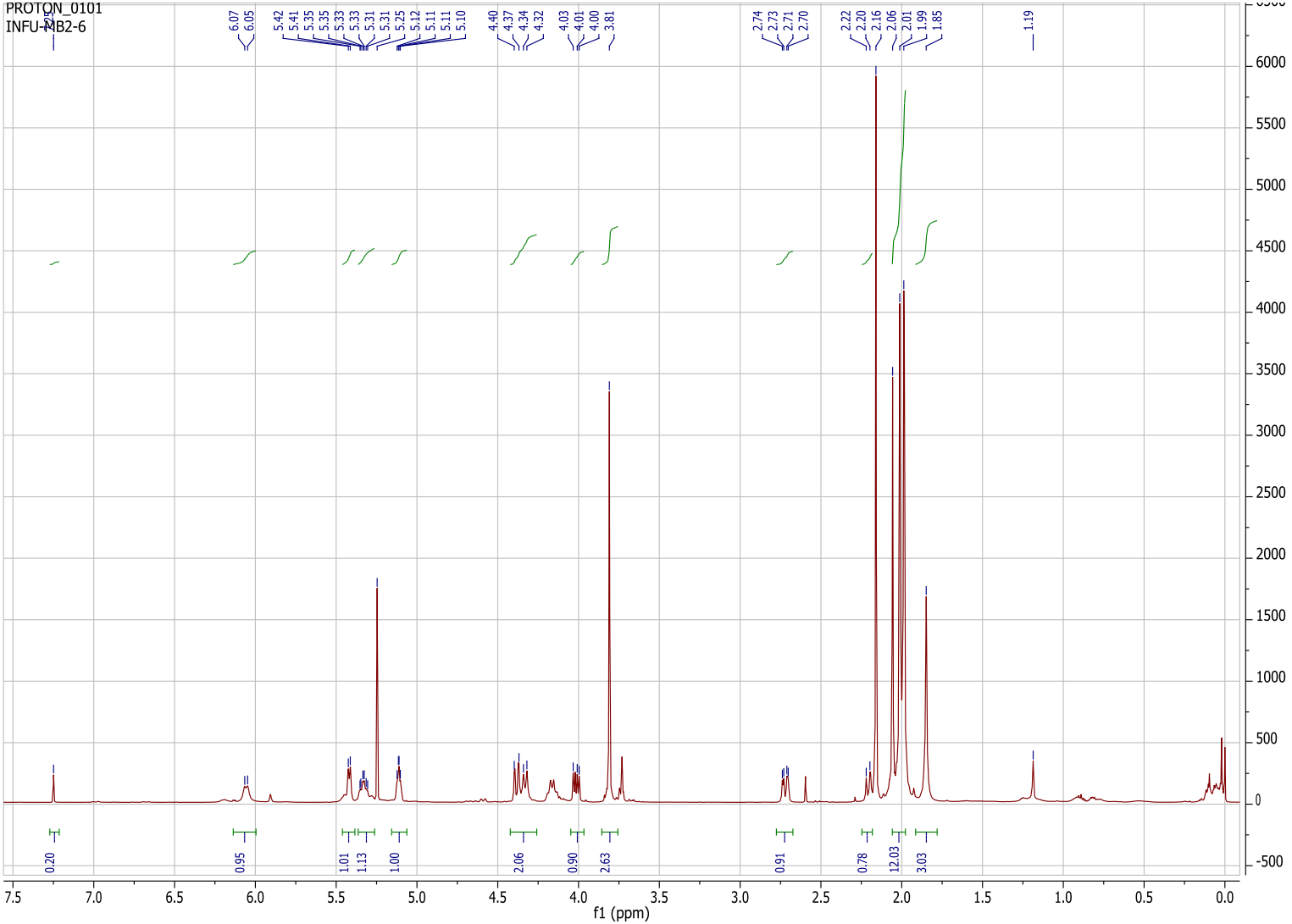

^{13}C-NMR of 3-acetamido-4-acetoxy-6-chloro-6-(methoxycarbonyl)tetrahydro-2H-pyran-2-yl)propane-1,2,3-triyl triacetate (AT13)

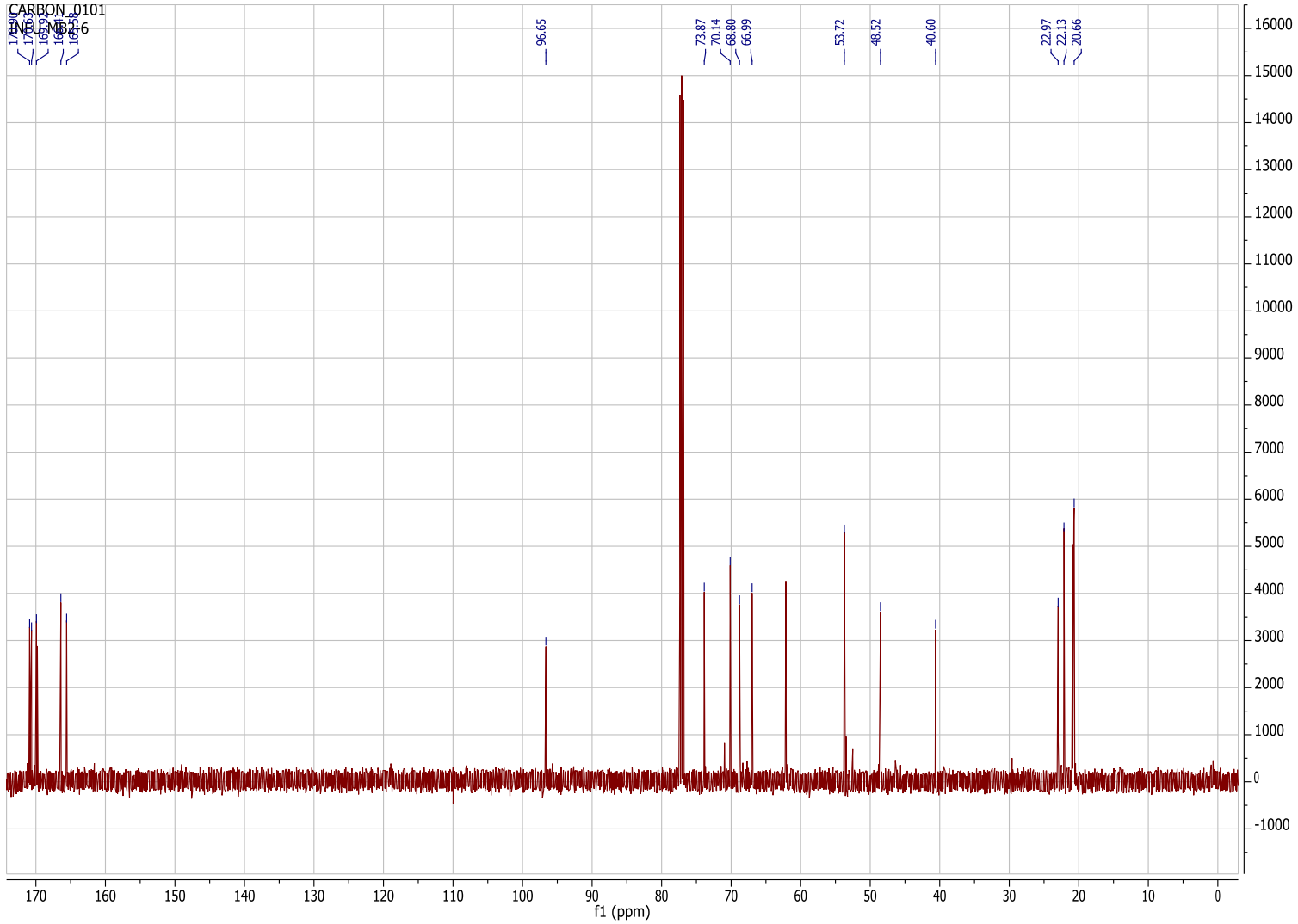

HR-ESI-MS of 3-acetamido-4-acetoxy-6-chloro-6-(methoxycarbonyl)tetrahydro-2H-pyran-2-yl)propane-1,2,3-triyl triacetate (AT13)

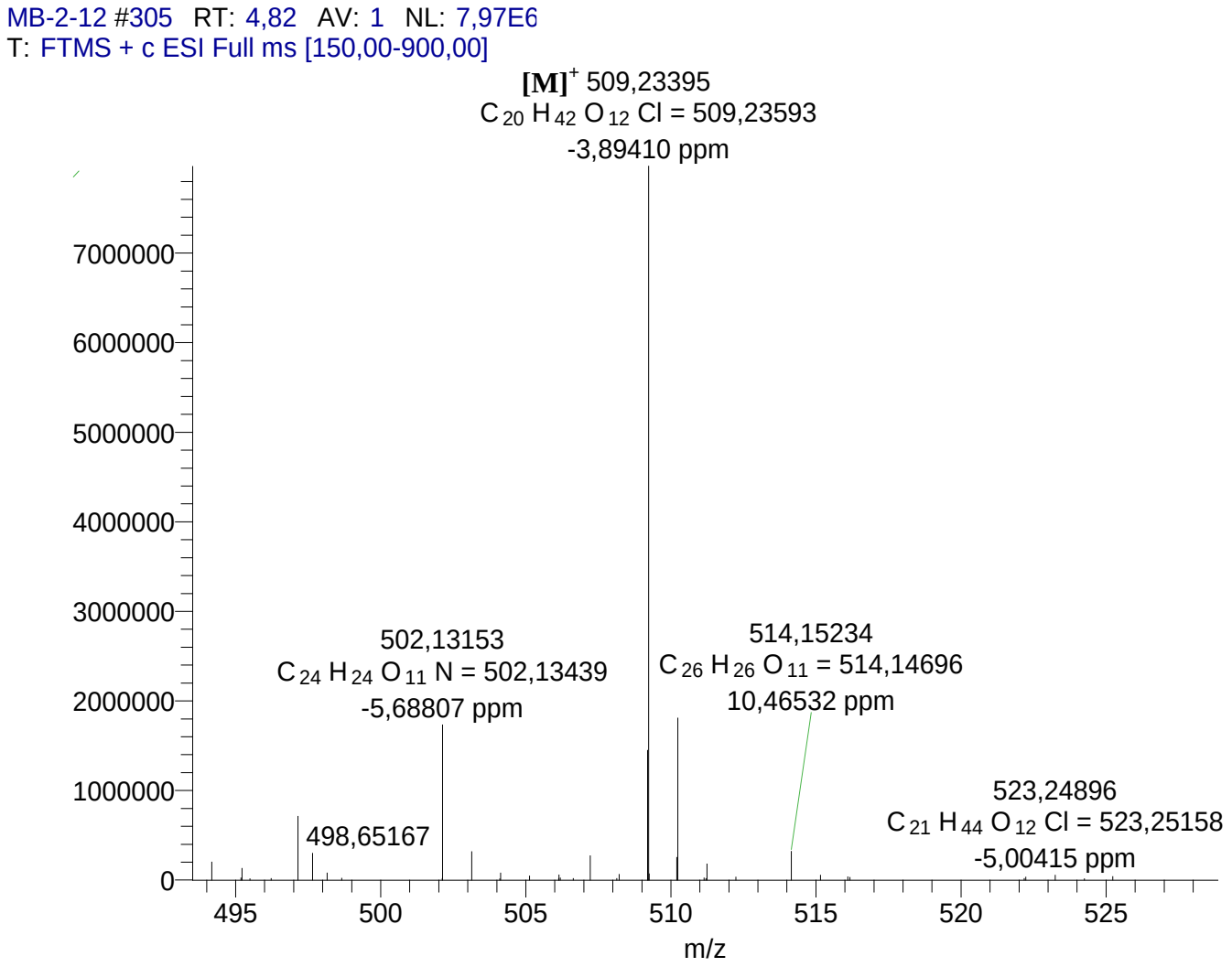

^{1}H-NMR of 3-acetamido-4-acetoxy-6-(but-3-yn-1-yloxy)-6-(methoxycarbonyl) tetrahydro-2H-pyran-2-yl) propane-1,2,3-triyl triacetate (AT14)

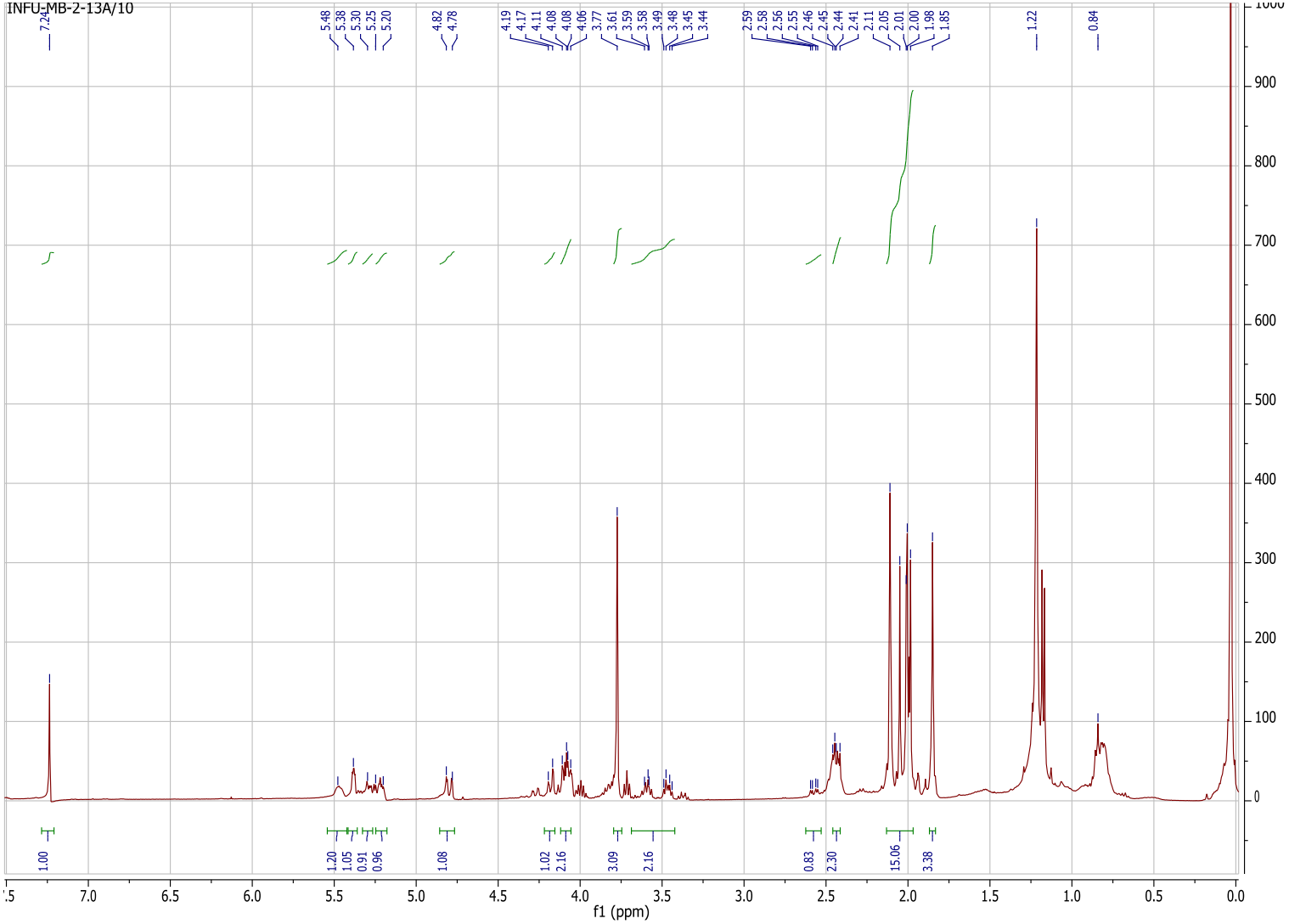

^{13}C-NMR of 3-acetamido-4-acetoxy-6-(but-3-yn-1-yloxy)-6-(methoxycarbonyl) tetrahydro-2H-pyran-2-yl) propane-1,2,3-triyl triacetate (AT14)

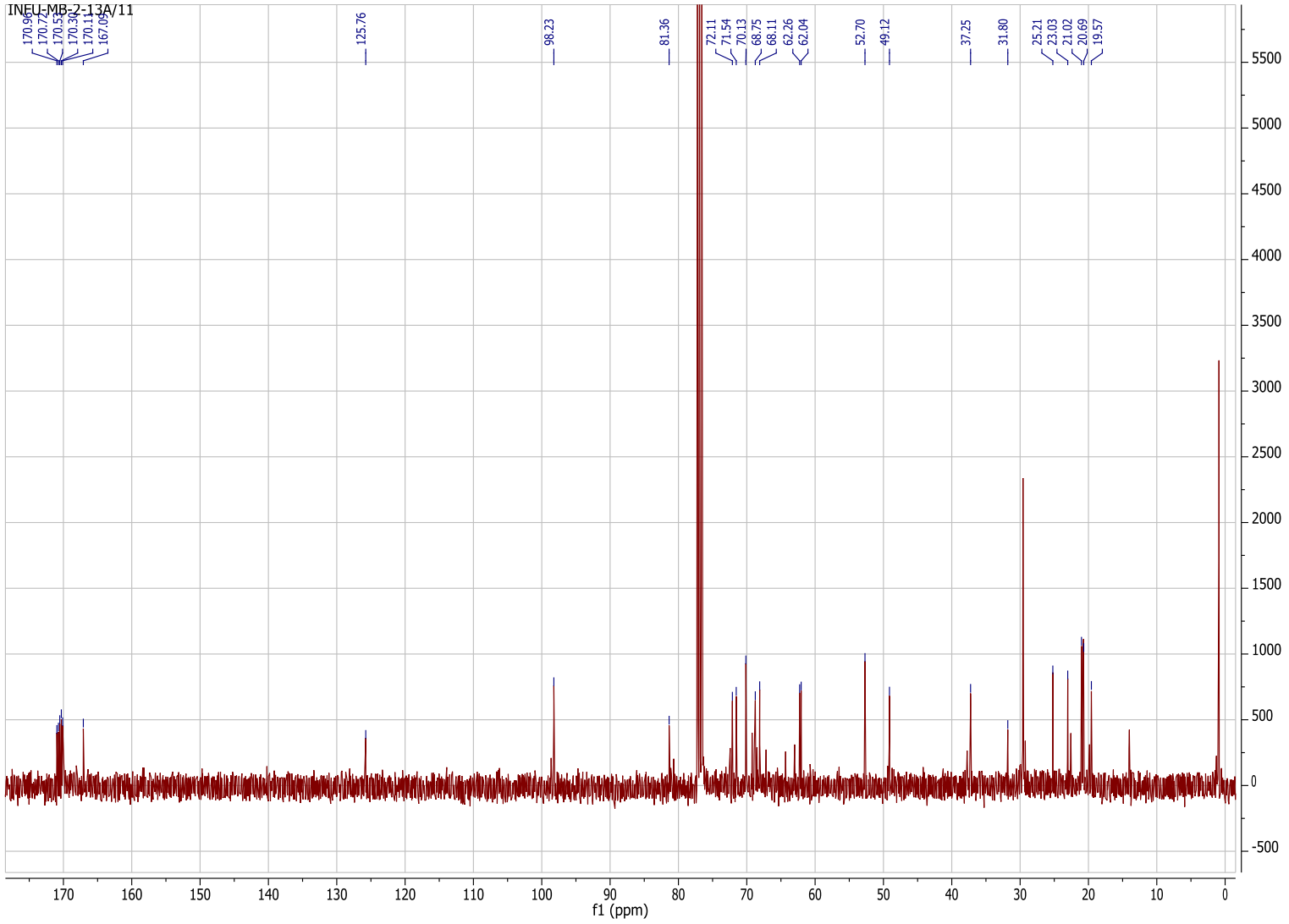

HR-ESI-MS of 3-acetamido-4-acetoxy-6-(but-3-yn-1-yloxy)-6-(methoxycarbonyl) tetrahydro-2H-pyran-2-yl) propane-1,2,3-triyl triacetate (AT14)

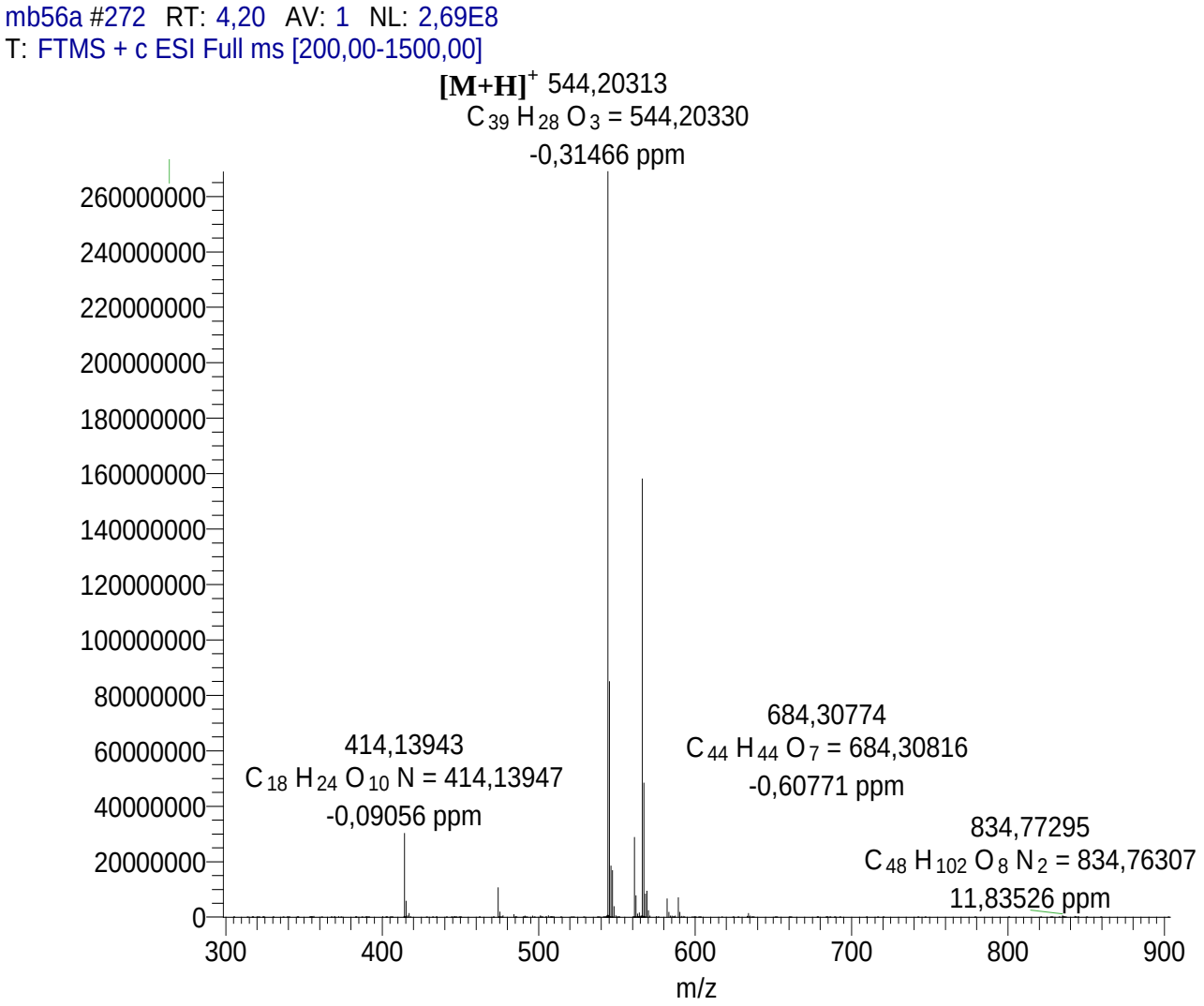

^{1}H-MNR of 5-acetamido-2-(but-3-yn-1-yloxy)-4-hydroxy-6-(1,2,3-trihydroxypropyl) tetrahydro-2H-pyran-2-carboxylate (AT15)

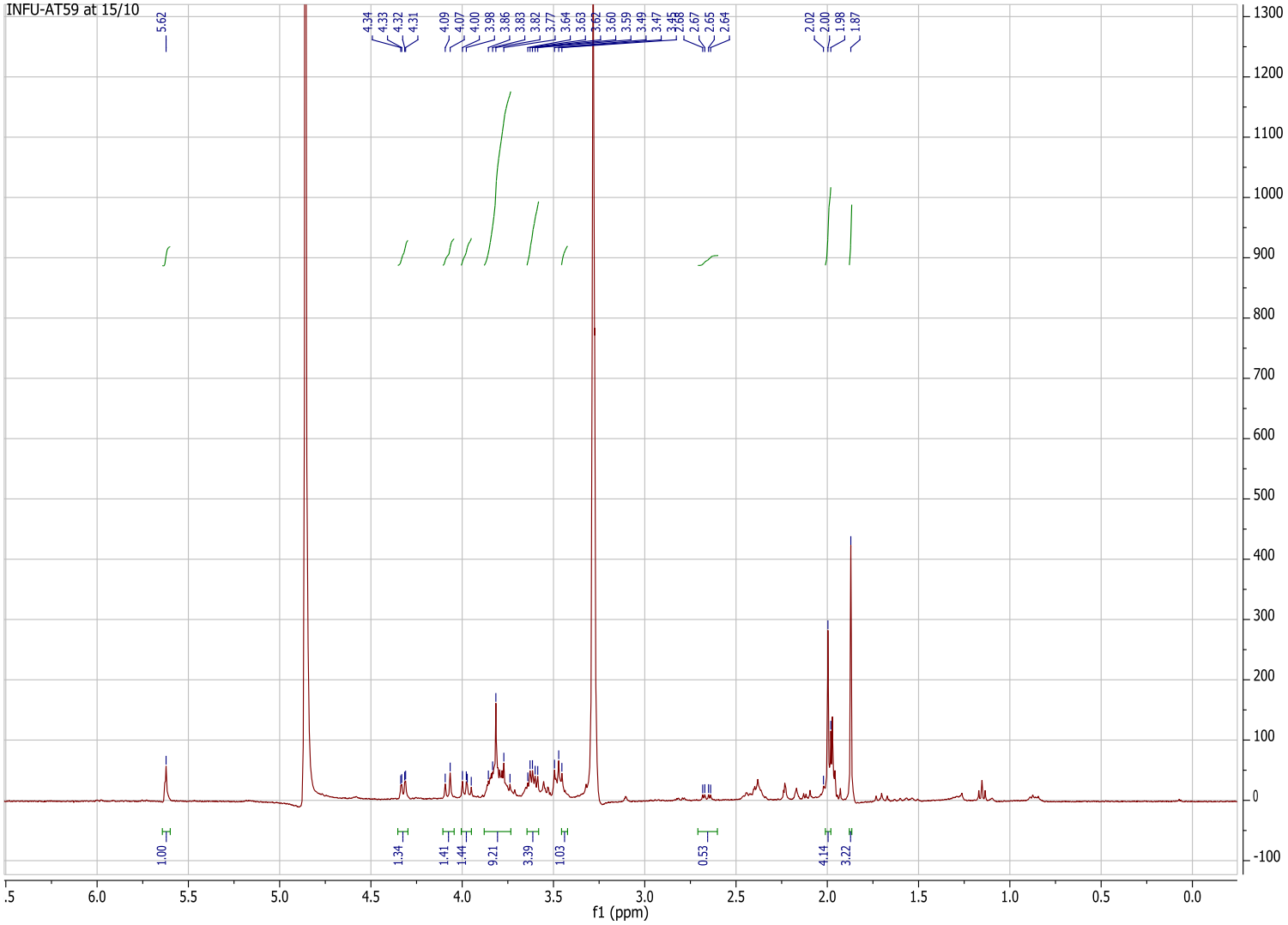

^{13}C-NMR of 5-acetamido-2-(but-3-yn-1-yloxy)-4-hydroxy-6-(1,2,3-trihydroxypropyl) tetrahydro-2H-pyran-2-carboxylate (AT15)

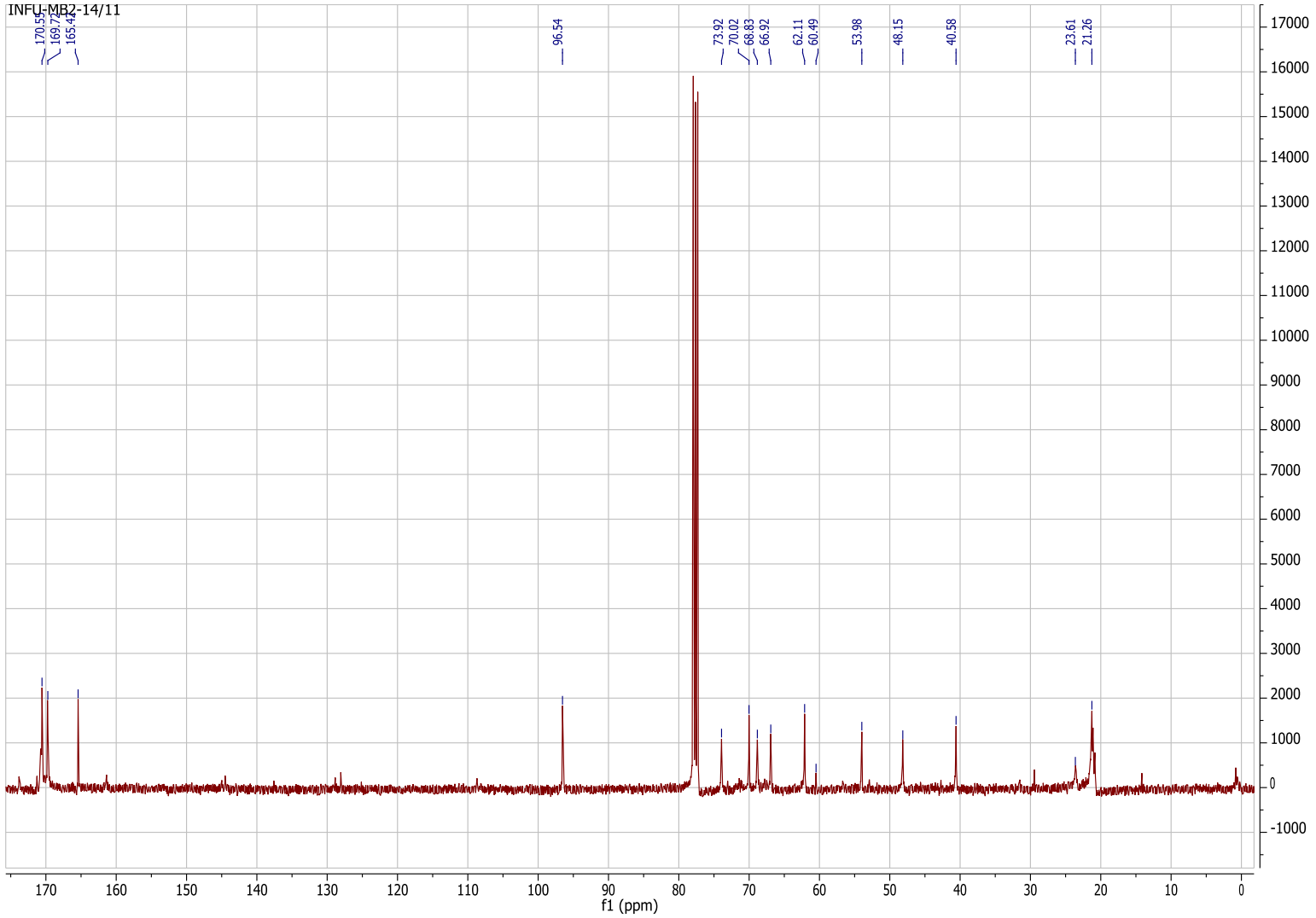

HR-ESI-MS of 5-acetamido-2-(but-3-yn-1-yloxy)-4-hydroxy-6-(1,2,3-trihydroxypropyl) tetrahydro-2H-pyran-2-carboxylate (AT15)

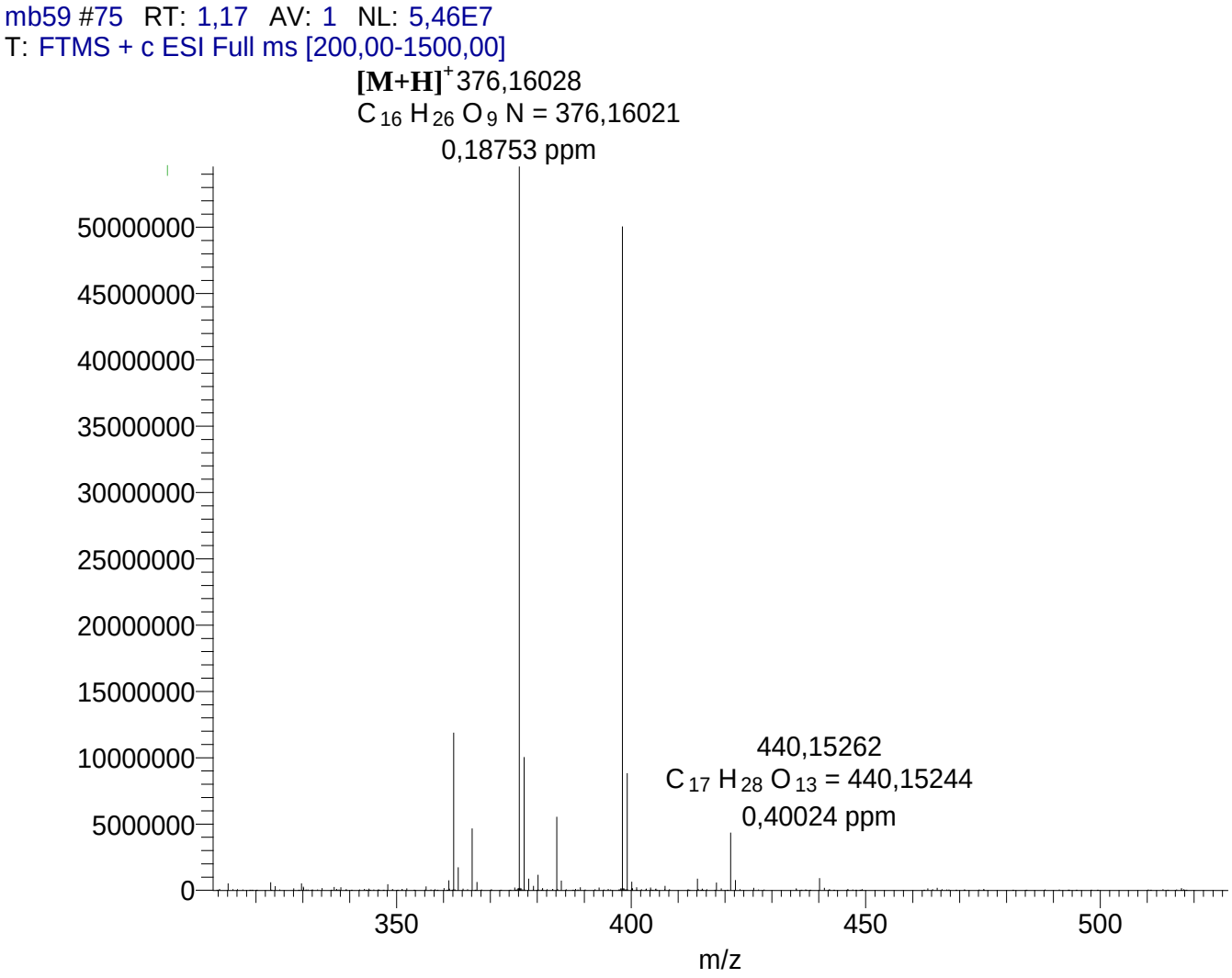

^{1}H-NMR of 5-acetamido-2-(but-3-yn-1-yloxy)-4-hydroxy-6-(1,2,3-trihydroxypropyl)tetrahydro-2H-pyran-2-carboxylic acid (AT16)

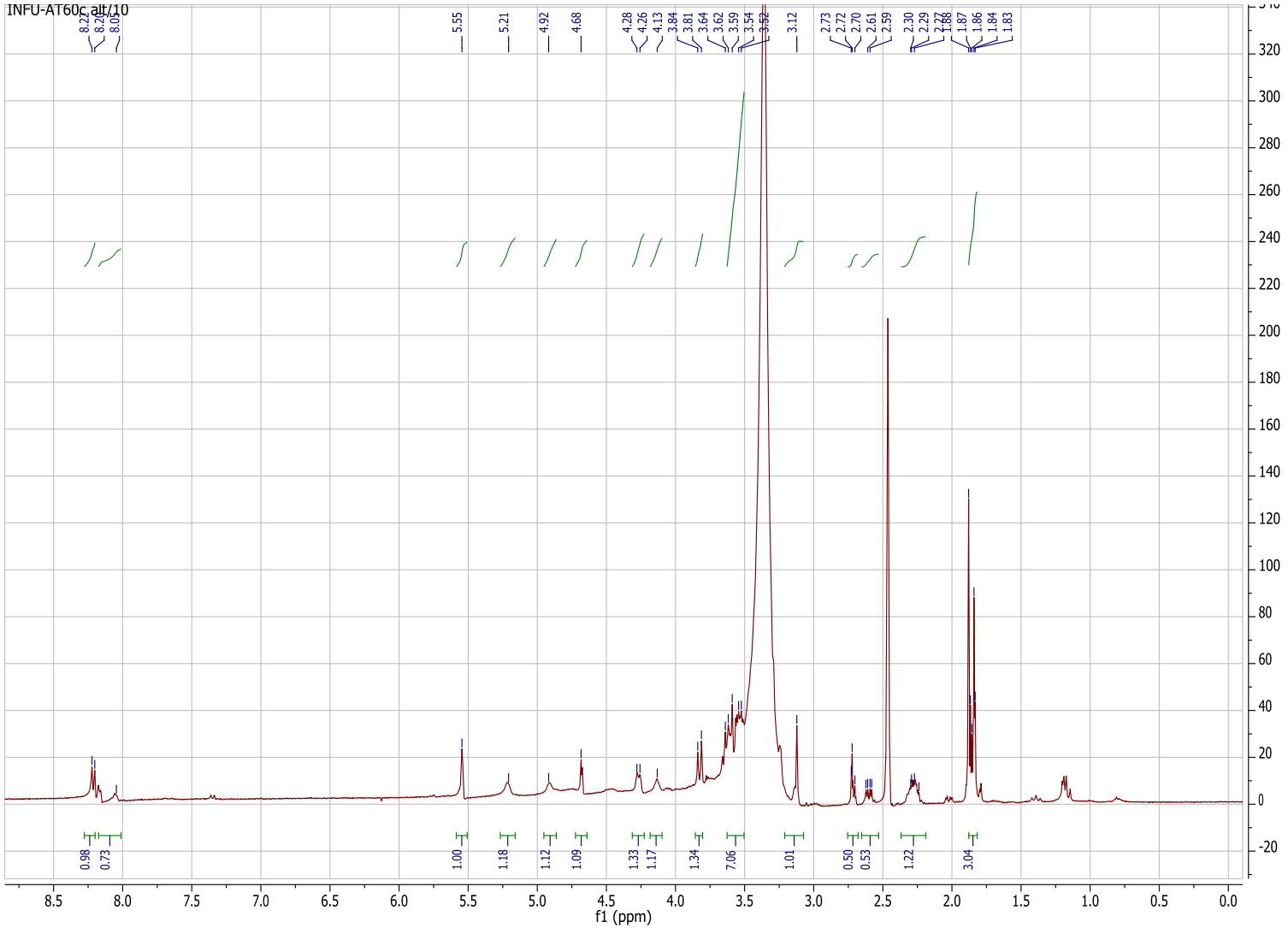

^{13}C-NMR of 5-acetamido-2-(but-3-yn-1-yloxy)-4-hydroxy-6-(1,2,3-trihydroxypropyl)tetrahydro-2H-pyran-2-carboxylic acid (AT16)

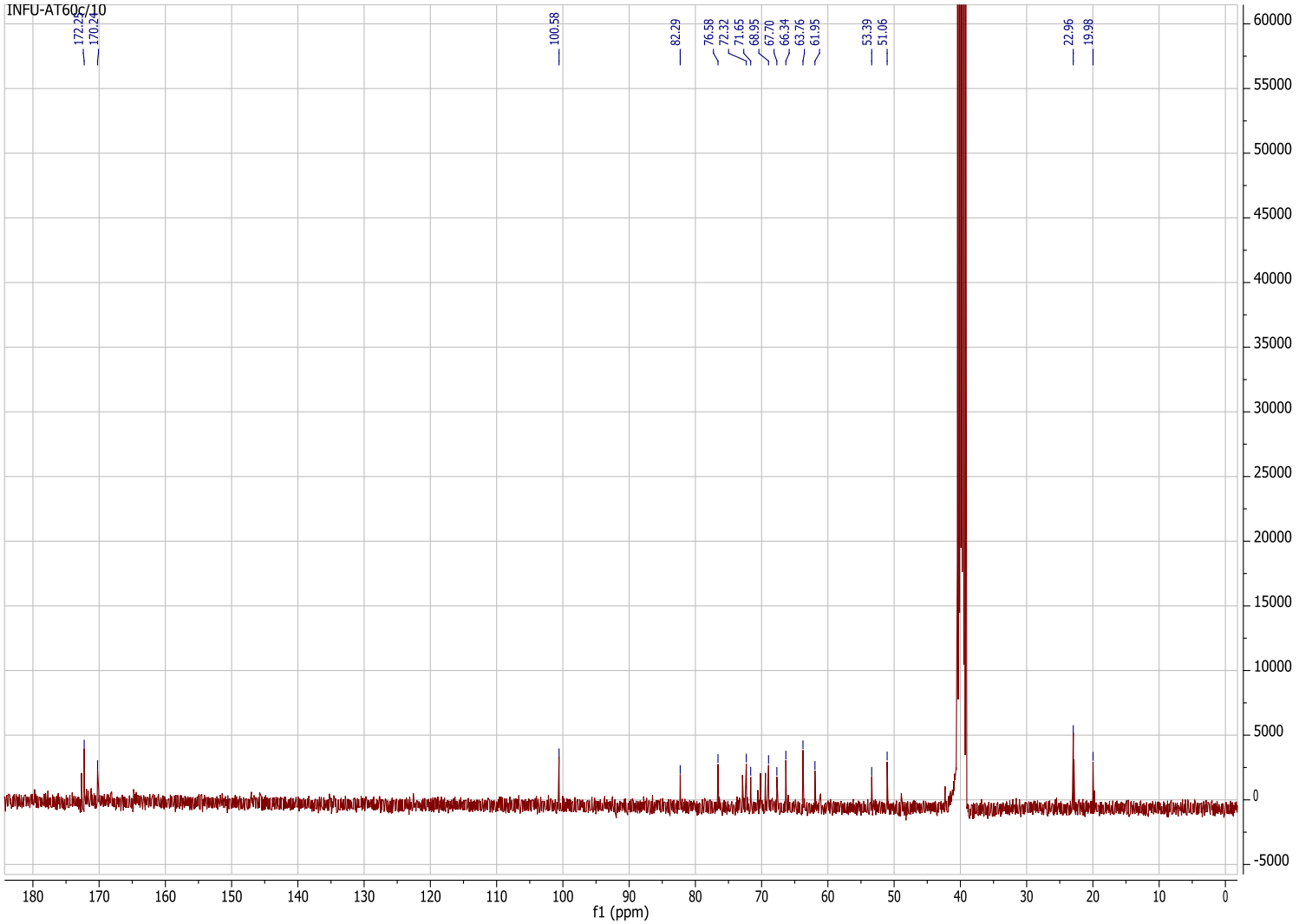

HR-ESI-MS of 5-acetamido-2-(but-3-yn-1-yloxy)-4-hydroxy-6-(1,2,3-trihydroxypropyl)tetrahydro-2H-pyran-2-carboxylic acid (AT16)

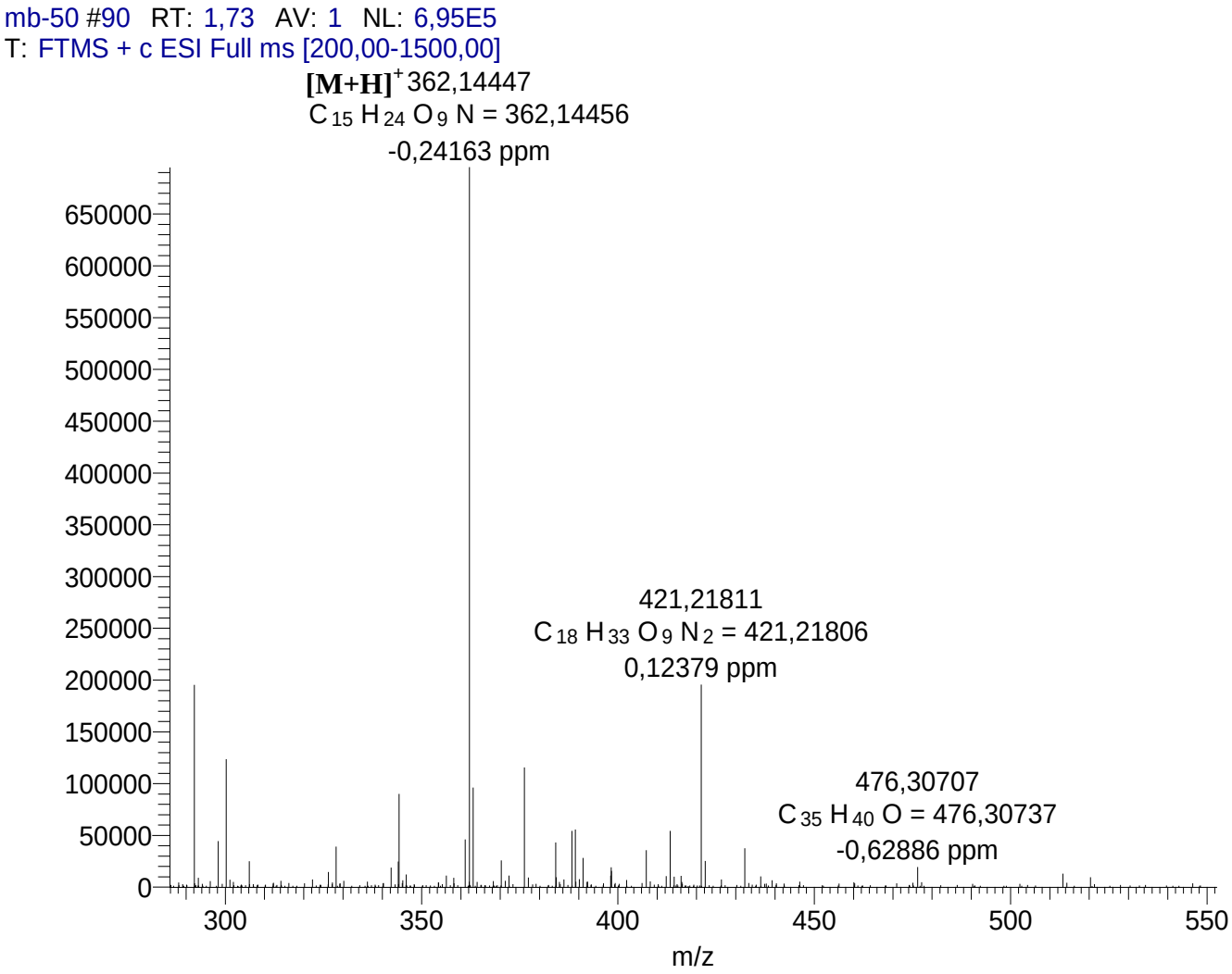

^{1}H-NMR of (4-((10-(4-(2-(2-(2-(2-(4-(2-((-5-acetamido-2-carboxy-4-hydroxy-6-(1,2,3-trihydroxypropyl)tetrahydro-2H-pyran-2-yl)oxy)ethyl)-1H-1,2,3-triazol-1-yl)ethoxy)ethoxy)acetoxy) methyl)phenoxy)decyl)oxy)- benzamidine hydrochloride (AT17)

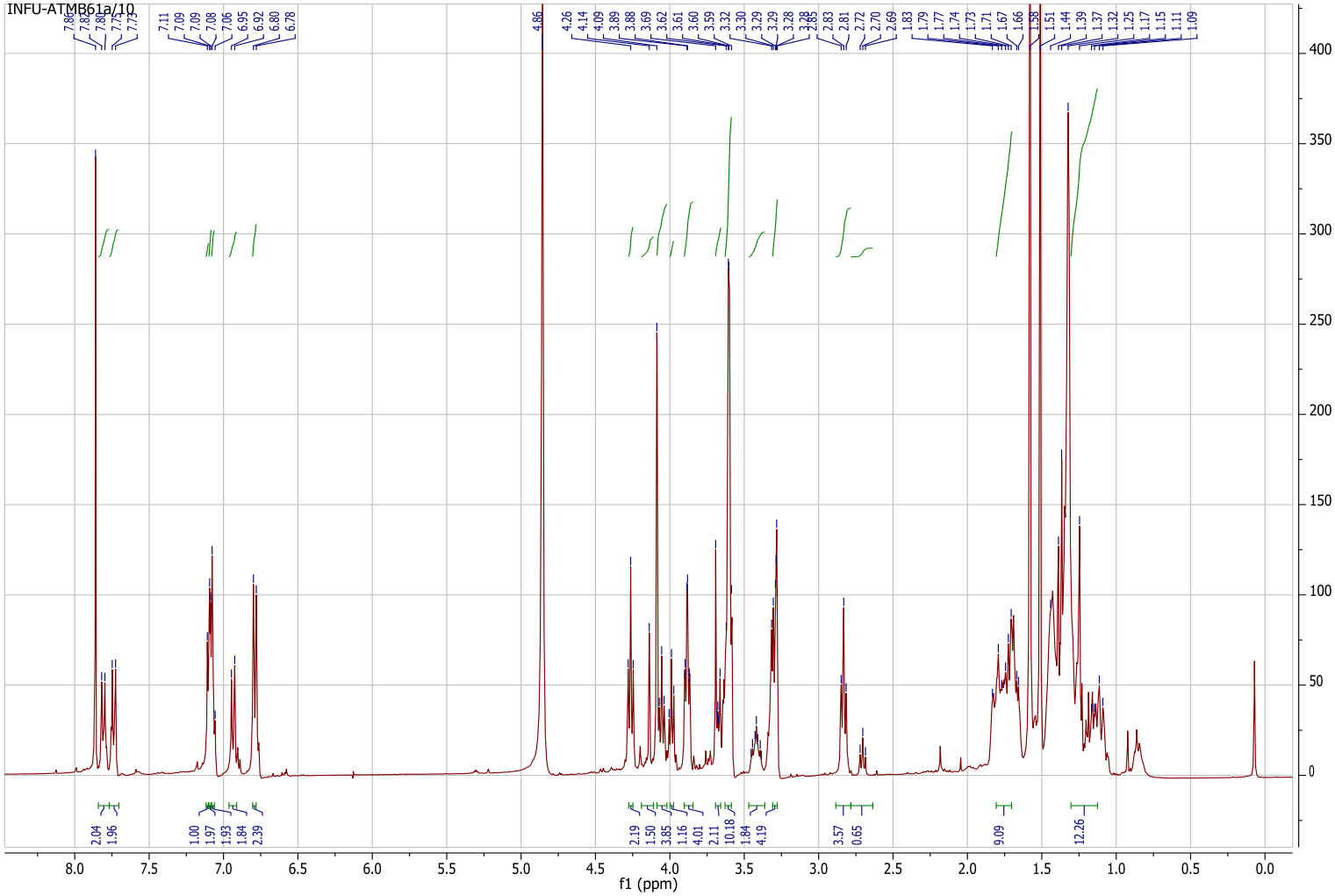

^{13}C-NMR of (4-((10-(4-(2-(2-(2-(2-(4-(2-((-5-acetamido-2-carboxy-4-hydroxy-6-(1,2,3-trihydroxypropyl)tetrahydro-2H-pyran-2-yl)oxy)ethyl)-1H-1,2,3-triazol-1-yl)ethoxy)ethoxy)acetoxy) methyl)phenoxy)decyl)oxy)- benzamidine hydrochloride (AT17)

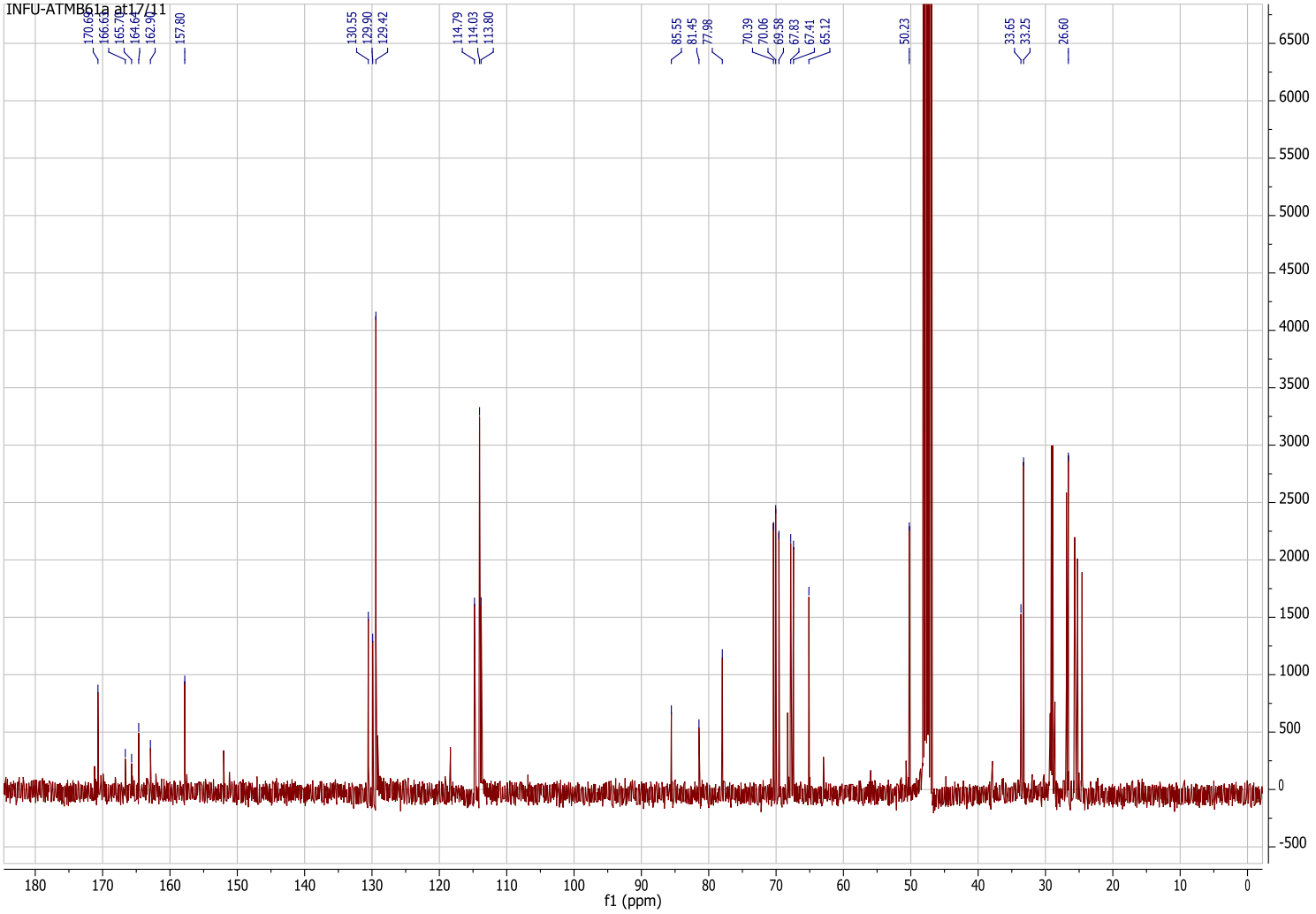

HR-ESI-MS of (4-((10-(4-(2-(2-(2-(2-(4-(2-((-5-acetamido-2-carboxy-4-hydroxy-6-(1,2,3-trihydroxypropyl)tetrahydro-2H-pyran-2-yl)oxy)ethyl)-1H-1,2,3-triazol-1-yl)ethoxy)ethoxy)acetoxy) methyl)phenoxy)decyl)oxy)- benzamidine hydrochloride (AT17)

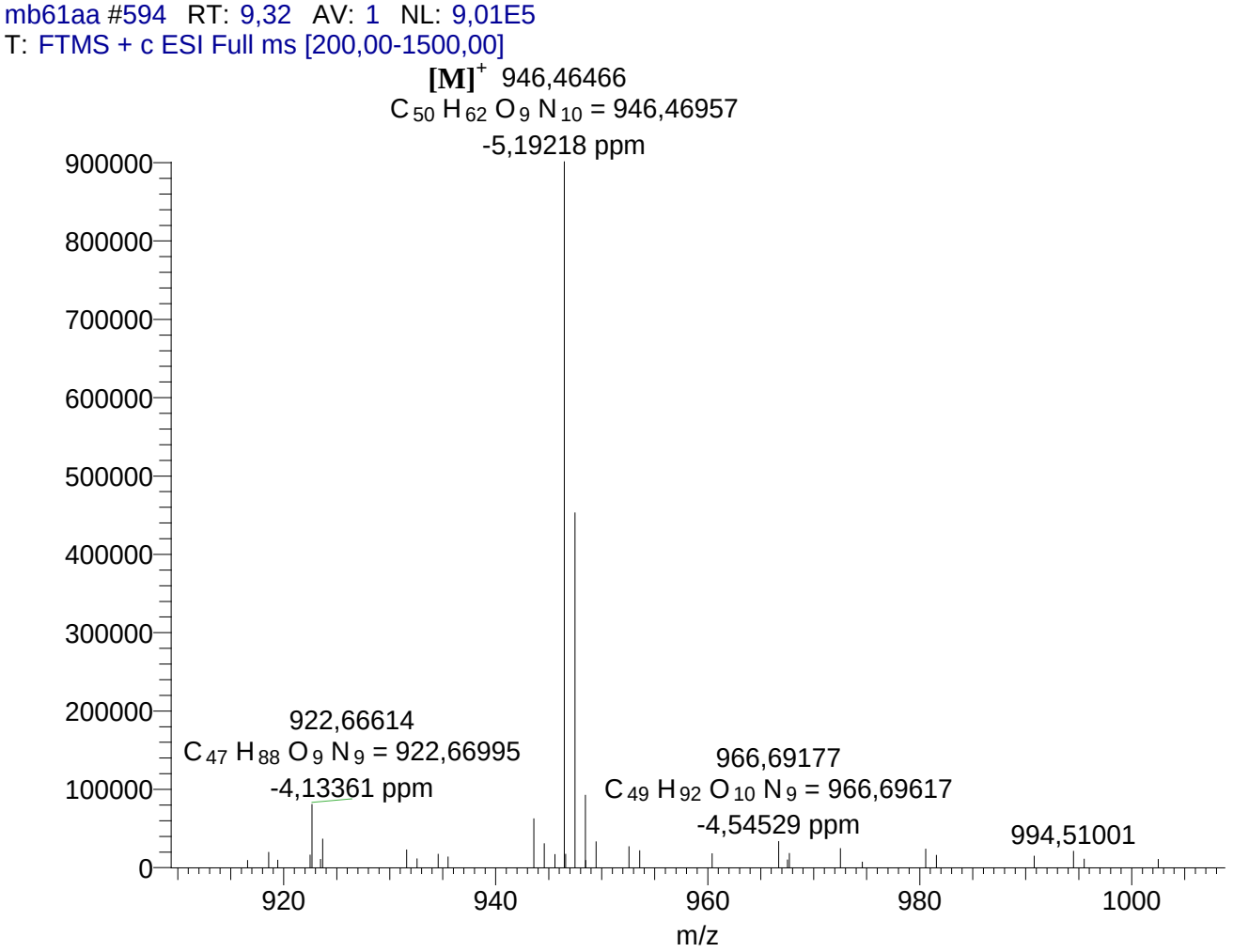

6.3 Pubilcations

Journals

Tenboll et al., Controlled deposition of highly oriented type I collagen mimicking in vivo collagen structures. *Langmuir,* **26** (14), 12165- 12172 (2010)

Poster

Tenboll et al., "Mixed monolayers of ω-biotin functionalized α-(4-amidinophenoxy)alkanes as reversible and adaptable platforms for molecular recognition and biosensing", 3. Tag der Chemie, TU Dortmund, 2010

Tenboll et al., "Switchable assembly of ω-biotin functionalized α-(4-amidinophenoxy) alkanes and its application as reversible and adaptable surfaces in molecular recognition and biosensing", 3rd EuCheMS Chemistry Congress Nürnberg 2010

Tenboll et al., "Ultrasensitive biosensors via reversible mixed SAMs", 2. Junges Chemie Symposium Ruhr, Universität Essen, 2011

Tenboll et al., "Ultrasensitive biosensors via reversible mixed self-assembed monolayers", 5. Tag der Chemie, TU Dortmund, 2012

Tenboll et al. "Adaptable Monolayers in Biosensors or as Platform for 2D Imprinting", International conference of Molecularly Imprinted Polymers - Science and Technology, Paris, Frankreich, 2012

Presentations

Tenboll et al., "Mixed monolayers of ω- functionalized α-(4-amidinophenoxy)alkanes as reversible & adaptable platforms for molecular recognition and biosensing", 4. Tag der Chemie, TU Dortmund, 2011

Tenboll et al., "Mixed bola-SAMs as adaptable platforms for molecular recognition and biosensing", MIP Summer School, La Rochelle, France, 2011

Tenboll et al. "Ultrasensitive biosensors via reversible mixed self-assembed monolayers", 243rd ACS National Meeting, San Diego, USA, 2012

6.4 Curriculum Vitae

Der Lebenslauf ist in der Online-Version aus Gründen des Datenschutzes nicht enthalten.

Erklärung

Hiermit versichere ich, dass ich die vorliegende Arbeit mit dem Titel

„Reversible Self-Assembled Monolayers as Biosensor Platforms”

selbst verfasst und keine außer den angegebenen Hilfsmitteln und Quellen benutzt habe, und dass die Arbeit in dieser oder ähnlicher Form noch bei keiner anderen Universität eingereicht wurde.

6.5 Acknowledgement

Als erstes Danke ich Herrn Prof. Dr. Börje Sellergren für die Betreuung meiner Doktorarbeit und die Aufnahme in seine Arbeitsgruppe. Die interessanten fachlichen Diskussionen und Ratschläge haben sehr zum Erfolg dieser Arbeit beigetragen.

Als zweites danke ich Herrn Prof. Dr. Thomas Schrader für die Übernahme des Gutachtens und die Möglichkeit an der Universität Essen zu promovieren.

Des weiteren Danke ich Frau Prof. Dr. Silvia Mittler für die anregenden Diskussionen über meine Arbeit und die Unterstützung in vielen Belangen meines Lebens. Silvia ist mir zu einer guten Freundin geworden.

I would like to thank all members of the Sellergren group for their friendship and help. The scientific discussion, the international lunches, the kicker-competitions, the BBQs, the Swedish-Kubb-afternoons and the interesting discussions about culture, made these years an unforgettable time of my life. Especially I would also like to thank Emelie Fritz, who became a very close friend of mine during my PhD. Special thanks also to Ricarda Wagner, Jennifer Hesse and Melanie Berghaus for their friendship and advises during this time. I will miss our girls nights. Thanks also to the PostDocs Dr. Sun Wei and Dr. Robert Sulc. Wei welcomed me very warmly to this group and was of great help during my first year. I would also like to thank my master student Malak Boutrus for the good collaboration.

Dank gebührt ebenfalls Herrn Nico Zammarelli für die Hilfe mit dem AFM-Messungen, Herrn Dr. Marc Lamshöft für die Hilfe mit den MS-Messungen, sowie den Mitarbeitern der NMR-Abteilung und den Werkstätten.

Ebenfalls möchte ich mich bei Herrn Dr. Metternich und Herrn Rockahr von Evonik Industries bedanken. Die Ratschläge und Begleitung auf meinem Karriereweg haben mir sehr geholfen.

Ein besonderer Dank geht an meinen Freund Domenic Mucha und meine Mutter Anna-Maria, die mich während meines gesamten Studiums und meiner Doktorarbeit unterstützt haben und immer ein offenes Ohr hatten. Deswegen möchte ich diese Arbeit Ihnen widmen.